Development and Optimization of Fast Single Particle Inductively Coupled Plasma Mass Spectrometry as a Tool for Nanomaterial Analysis in Environmental Waters

DISSERTATION

to obtain the degree of
Doctor of Science

submitted by Annika Schardt, M.Sc.

submitted to the School of Science and Technology
of the University of Siegen
Siegen 2025

Supervisor and first appraiser

Prof. Dr. Carsten Engelhard

University of Siegen / Bundesanstalt für Materialforschung und -prüfung

Second appraiser

Prof. Dr. Manuela Killian

University of Siegen

Date of the oral examination

11.7.2025

Summary

Single particle inductively coupled plasma mass spectrometry (spICP-MS) is an instrumental analysis method that enables the determination of the size, size distribution, and particle number concentration of nanoparticles (NP) in suspensions. Due to its comparatively short total analysis time of a few minutes and minimal required sample preparation, spICP-MS has evolved to a routine research tool to characterize NP in aqueous samples, as *e.g*. surface water, sea water, and waste water. Because nanoparticle toxicity can be size dependent (among other factors), it is crucial to be able to detect NP in the largest possible size range. This thesis reports novel instrumental developments and data processing pathways that aim to decrease the lower size detection limit of spICP-MS with a quadrupole mass analyzer and to further enhance analysis and data evaluation speed.

First, a novel data acquisition unit is tested that provides nanosecond time resolution spICP-MS (4 ns, nanoDAQ). In contrast to previous spICP-MS analysis methods with milli- or microsecond time resolution, this fast measurement mode enables not only the detection of individual NP, but even the detection of individual atoms that make up each NP. Because the structure of the obtained data differs from conventional spICP-MS, a data processing workflow is developed to determine NP sizes and particle number concentrations. It is shown that the prototype nanoDAQ achieves a size detection limit for gold NP in bi-distilled water samples of *ca*. 7 nm. Subsequently, an optimized version of the nanoDAQ prototype is evaluated, which was developed to reduce measurement artifacts. The figures of merit of the improved system are showcased.

In order to reduce and facilitate data processing steps, an automated ion cloud recognition algorithm is tested and described, which had been tailor-made to detect, characterize, and count NP signals in the nanosecond time-resolved data from the nanoDAQ. The algorithm is first tested on model suspensions of spherical gold NP (4.7–125 nm diameter) in bi-distilled water samples and is compared to the previously used, elaborate data processing workflow. After careful evaluation of the method capabilities, the nanoDAQ system and the automated algorithm are utilized for the analysis of surface water and waste water samples from a field study. With the novel method, NP containing Ag, Ce, and Zr could be detected successfully in regional surface water samples from the area of Siegen and their particle number concentrations (PNC) could be estimated. The estimated PNC agree well with comparative values that were reported in the literature for river systems in Europe and North America.

Zusammenfassung

Die Massenspektrometrie mit induktiv gekoppeltem Plasma im Einzelpartikel-Modus (spICP-MS) ist eine instrumentelle Analysenmethode, welche die Bestimmung von Größe, Größenverteilung und Partikelanzahlkonzentration von Nanopartikeln (NP) in Suspensionen ermöglicht. Aufgrund der vergleichsweise kurzen Gesamtanalysezeit von wenigen Minuten und der minimalen erforderlichen Probenvorbereitung hat sich spICP-MS zu einer in der Forschung routinemäßig-verwendeten Methode zur Charakterisierung von NP in wässrigen Proben, wie z.B. Oberflächenwasser, Meerwasser und Abwasser, entwickelt. Da die Toxizität von NP (neben anderen Faktoren) von deren Größe abhängt, ist es entscheidend, sie in einem größtmöglichen Größenbereich nachweisen zu können. In dieser Arbeit werden neue instrumentelle Entwicklungen und Datenverarbeitungswege vorgestellt, die darauf abzielen, die untere Nachweisgrenze von spICP-MS in Kombination mit einem Einzel-Quadrupol-Massenanalysator zu senken und die Analyse- und Datenauswertungsgeschwindigkeit weiter zu erhöhen.

Zunächst wird eine neuartige Datenerfassungseinheit getestet, welche spICP-MS mit einer Zeitauflösung im Nanosekundenbereich (4 ns, nanoDAQ) ermöglicht. Im Gegensatz zu bisherigen spICP-MS-Methoden erlaubt dieser schnelle Messmodus nicht nur den Nachweis einzelner NP, sondern sogar die Detektion einzelner Atome, aus welchen jeder NP besteht. Da sich die Struktur der erhaltenen Daten von denen der konventionellen spICP-MS unterscheidet, wird ein Datenverarbeitungsworkflow entwickelt, um Partikelgrößen und -anzahlkonzentrationen zu bestimmen. Es wird gezeigt, dass der nanoDAQ-Prototyp eine Größennachweisgrenze für Gold-NP in bi-destilliertem Wasser von *ca*. 7 nm erreicht. Anschließend wird eine optimierte Version des nanoDAQ-Prototyps getestet, welche entwickelt wurde um Messartefakte zu reduzieren. Die Leistungsdaten des verbesserten Systems werden vorgestellt.

Zur Reduzierung und Vereinfachung der Datenverarbeitungsschritte wird ein automatischer Algorithmus zur Erkennung von Ionenwolken getestet und beschrieben, der speziell für das Erkennen, Charakterisieren und Zählen von NP-Signalen in den Nanosekunden-zeitaufgelösten Daten des nanoDAQ entwickelt wurde. Der Algorithmus wird zunächst an Modell-Suspensionen sphärischer Goldnanopartikel (4.7–125 nm Durchmesser) in bi-destilliertem Wasser getestet und mit dem zuvor verwendeten, aufwendigen Datenverarbeitungsprozess verglichen. Nach sorgfältiger Evaluierung der Leistungsfähigkeit der Methode werden das nanoDAQ-System und der automatisierte Algorithmus für die Analyse von Oberflächenwasser- und Abwasserproben aus einer Feldstudie eingesetzt. Mit der neuen Methode konnten Ag-, Ce- und Zr-enthaltende Nanopartikel erfolgreich in regionalen Oberflächengewässerproben aus der Region Siegen detektiert werden und deren Partikelanzahlkonzentration (PNC) konnte abgeschätzt werden. Die abgeschätzten PNC stimmen gut mit vergleichbaren Werten überein, welche in der Literatur für Flusssysteme in Europa und Nordamerika berichtet wurden.

Table of Contents

Summary IV
Zusammenfassung V
Table of Contents VI
1. Aims and Scope of the Thesis 1
1.1. Introduction 2
1.2. Aims and scope 6
2. State of the Art and Theory 8
2.1. State of the art 9
2.2. Theory 22
3. Experimental Section 37
3.1. Chemicals and materials 38
3.2. Nanoparticle sample preparation 41
3.3. Environmental water sampling campaign 42
3.4. Scanning transmission electron microscopy 45
3.5. Single particle ICP-MS 47
4. Results and Discussion 54
4.1. Structure of nanosecond time-resolved spICP-MS data 56
4.2. Capabilities of nanoparticle characterization with the nanoDAQ MK1 62
4.3. Figures of merit of improved nanoDAQ MK2 71
4.4. Evaluation of an automated ion cloud recognition algorithm 87
4.5. Feasibility test: Nanoparticle screening in surface and waste waters 105
5. Concluding Remarks and Future Perspectives 119
Appendix 123
I. Supplementary tables 123
II. Supplementary figures 127
III. Supplementary equations 133
References 134
List of Abbreviations 145
Contributions to this Thesis 147
Acknowledgements 148

1. Aims and Scope of the Thesis

Based on:

A. Schardt, J. Schmitt, C. Engelhard, Single particle inductively coupled plasma mass spectrometry with nanosecond time resolution, *J. Anal. At. Spectrom*., 2024, **39**, 389–400.
DOI: 10.1039/D3JA00373F.

1.1. Introduction

Engineered nanomaterials (ENM) are used in over 11000 different products and are produced in 68 countries according to a nanotechnology products database. Important application fields include electronics, medicine, construction, and cosmetics.[1–3]

With the rise and success of the nanotechnology industry came the increasing concern about the fate and potential risk of ENM. Many beneficial possibilities of the implementation of ENM in medicine[4], agriculture[5,6], automotive industry[7], cosmetics[8,9], food science[10], and textiles industry[11] are well known and desired. Today (2025), more than 5000 consumer products are listed in an online database (The Nanodatabase) that was set up in 2012 to provide the public with information on the content of nanomaterials (as declared by the manufacturer or other stakeholders) in products available on the European market.[3,12] For the majority of the listed consumer products (including the categories health and fitness, home and garden, automotive, electronics and computers, food and beverage, appliances, and goods for children), the type of incorporated nanomaterial is unknown (70%).[12] Within the portion of consumer products that contain an identified type of nanomaterial, the most common nanomaterials are silver (35.0%), titanium and titanium dioxide (21.6%), carbon (7.2%), carbon nanotubes (5.9%), gold (4.7%), and silicon dioxide (4.6%).[13] Another database (Nanotechnology Products Database) names silver, silicon dioxide, titanium dioxide, graphene, and tungsten disulfide as the most frequently used nanomaterials among more than 11000 listed products.[1] The comprehensible reason for the world´s demand for ENM is that they possess a variety of useful features, such as *e.g.* special optical, magnetic, or electrical properties that differ from the corresponding bulk material´s[14], they show antibacterial behavior[15], and their small size makes them useful carriers for precisely-targeted drug transport *via* (bio)functionalization[16].

Considering those remarkable and beneficial opportunities that the use of ENM offers, their production, use, and release into the environment can be expected to increase in the future. It is therefore imperative to provide a definition for this relatively new compound class, to study their compositional and geometrical variety, and to assess potential risks.

A nanomaterial is defined as a “natural, incidental or manufactured material containing particles, in an unbound state or as an aggregate or as an agglomerate and where, for 50% or more of the particles in the number size distribution, one or more external dimensions is in the size range 1 nm–100 nm”[17]. In the field, the expression “engineered” nanomaterials is often used analogously to the term “manufactured” nanomaterials. According to the definition, only one of three dimensions has to be in the size range of 1–100 nm.[17] This indicates that nanomaterials occur in a plethora of shapes and sizes, which in turn can be composed of a variety of different chemical

elements. Optical, magnetic, and electrical properties of ENM are largely defined by the combination of these three parameters (size, shape, composition).[14] Many (intended or unintended) biological or chemical reactions of ENM depend on surface interactions that are influenced by specially-tailored ENM surface coatings or naturally acquired (protein-) coronas.[18]

Well-defined synthesis parameters allow for the manufacturing of specific ENM shapes, as *e.g.* spheres with defined diameters, porous spheres, rods with defined diameter-to-length aspect ratios, wires, cubes, triangular plates, pyramids, stars, core/shell particles, hollow shells, and bimetallic shells.[19–24] A survey among experts in the nanomaterial sector in 2011 indicated that relevant compositions of ENM with highest worldwide production quantities are mainly SiO_2 (5500 t/a, estimated median), TiO_2 (3000 t/a), ZnO (550 t/a), carbon nanotubes (300 t/a), FeO_X (55 t/a), AlO_X (55 t/a), CeO_2 (55 t/a), Ag (55 t/a), quantum dots (0.6 t/a), and fullerenes (0.6 t/a).[25] In many research studies, (spherical) gold nanoparticles are used as model particles, presumably because they are commercially available with well-defined diameters across a broad size range. Silver and TiO_2 nanoparticles are often used in environmental studies and are considered by the authors as representative model nanomaterials. They deliver important insights on particle-organism-interactions,[26,27] and models predict that they are widely distributed in many ecosystems either as geogenic or anthropogenic nanomaterials.[28]

The fact that nanoparticles (NP) are released into many environmental systems is a cause for concern. ENM may be taken up into cells,[29] cross the blood-brain-barrier,[30–32] or penetrate the skin[33,34]. Once the particles entered a vulnerable system such as a plant/animal/human cell, they can cause severe damage by inducing the generation of reactive oxygen species (ROS) or releasing dissolved metal ions, which can induce oxidative stress in the affected cells and lead to mitochondrial dysfunction, DNA damage, inflammation and/or eventual cell death.[35–37]

It is therefore the aim of numerous research groups worldwide to assess the various pathways that these potentially or demonstrably harmful substances take in the environment.[38,39] Research interests are focused on ENM´s fates in the aquatic and terrestrial environment and the atmosphere.[40–42] Particluar attention is paid to the influence of municipal waste water treatment plants (WWTP) on the distribution of ENM in the environment.[43–49] In 2013, Gottschalk *et al*. reviewed multiple reported concentrations of nanomaterials in WWTP effluents. The reported TiO_2NP mass concentrations were in the range of *ca*. 1–1000 µg L^{-1} (modeled data) and *ca*. 2–20 µg L^{-1} (experimentally determined), while AgNP were reported to tend to lower mass concentrations (approx. 0.1 µg L^{-1} (modeled) and *ca*. 0.001–100 µg L^{-1} (measured).[28]

The underlying requirement for most of those studies is the availability of a measurement tool, which is able to detect and characterize NP (engineered or natural NP alike) in the sample of interest. During the last decades, several instrumental methods have been employed for the detection of nanomaterials in aquatic environmental samples.[50–52] Important characteristics of NP in aqueous samples that need to be known to assess their toxicity are their particle size, aspect ratio, morphology, composition, surface properties, and particle number concentration.[53,54] Each NP analysis method has its own advantages and limitations regarding the different properties that have to be determined. The specific tools and their capabilities will be discussed in more detail in Chapter 2.1.1.

The legal regulation of ENM still bears many challenges due to their diverse nature and the need for robust and standardized characterization methods for a variety of complex matrices.[55] In the last few years, efforts have been undertaken by the IUPAC (International Union of Pure and Applied Chemistry) Division Analytical Chemistry to form a consent on method metrology and sample preparation techniques and to pave the way for legal limits.[13,56] The ultimate goal for all nanoanalysis method developers is therefore to increase their technique's sensitivity and robustness, to improve selectivity, to lower size detection limits and measurement times, to broaden the application range, and to fully exploit the obtained information depth

One particular method that has gained increasing popularity among NP researchers over the last two decades is single particle inductively coupled plasma mass spectrometry (spICP-MS). This technique allows to determine the mass of nanoparticles, to provide chemical information on their elemental composition, as well as to estimate their size and particle number concentration.[57] To obtain those information on the NP characteristics, several assumptions about their density and morphology have to be made and an appropriate calibration strategy has to be applied. Since the first observation of transient signals from colloids with an ICP-MS setup in 1993 by Nomizu *et al.*,[58] spICP-MS has developed into a widely used tool for nanomaterial analysis in water, soil, air, biological, food, and consumer product samples.[59–61] Instrumental parameters and guidelines on data processing for reliable detection, characterization, and quantification of nanomaterials in aqueous suspensions *via* spICP-MS have been specified in an ISO technical specification in 2017, which was recently updated to the ISO/TS 19590:2024.[62,63] The basic principles of spICP-MS will be presented in Chapter 2.1.2 and specific physical processes that provide explanations for the data observed in this work will be discussed in Chapter 2.2.

Part of the previous work in this group focused on spICP-MS method development. In particular, Strenge *et al*. developed hardware and software and adapted a prototype with microsecond time resolution to a state-of-the-art ICP mass spectrometer.[64] As a result, a calculated size detection limit of 3.9 to 4.6 nm for gold NP was achieved and gold NP with a size of 10 nm were successfully detected in bi-distilled water.[64] Subsequently, the system was coupled to capillary electrophoresis to separate mixtures of silver nanoparticles with different coatings (branched polyethylenimine (BPEI), polyethylene glycol (PEG), polyvinylpyrrolidone (PVP), and citrate) and sizes (20, 40, or 60 nm) prior to spICP-MS analysis.[65–67] Thirdly, the home-built system was applied to the detection and characterization of silver nanoparticles (AgNP) and titanium dioxide nanoparticles (TiO_2NP) in water samples from Austrian WWTP and a mountain lake.[47]

In this thesis, two home-built modified versions of the first data acquisition system (DAQ) were tested as a proof-of-concept,[68] a suitable data processing method was developed, and their figures of merit were compared. The conceptualization and construction of the hardware as well as the conceptualization and programming of the tailored software were done by Johannes Schmitt.[68–70] Because the modified DAQs provided significantly improved size detection powers for nanoparticles, the latest version of the system was field-tested in a nanoparticle analysis study with surface and waste waters from the area of Siegen.

1.2. Aims and scope

This thesis is dedicated to the advancement of spICP-MS as a tool for nanoparticle characterization in environmental samples. This work includes the methodological evaluation of novel spICP-MS data acquisition hardware systems with nanosecond time resolution and assesses their capabilities to improve nanoparticle detection. Additionally, a manual data processing workflow is developed to enable the characterization of detected NP in model samples. This manual approach is then used to evaluate an automated data processing software, which had been developed for high-throughput NP analysis. A proof-of-principle study is conducted to showcase the automated method's ability for NP detection, counting, and sizing in surface water and waste water treatment plant effluent.

After a brief introduction in Chapter 1, the state of the art in spICP-MS is reviewed in Chapter 2.2. This includes the discussion of the theoretical background of physical processes that occur during ion generation, ion extraction, ion selection, and ion detection. The chapter is intended to provide critical information that is needed to understand and evaluate the results that were obtained from the experiments in this thesis.

In Chapter 3, the procedures of conducted experiments are described. This includes sample preparation, instrumental settings, measurement optimization steps, and the design of the environmental water sampling campaign. Special sections are dedicated to the data acquisition and data processing with the evaluated hardware and software systems.

The results of the experiments in this thesis are presented and critically discussed in Chapter 4. Chapter 4.1 describes the first use of the nanoDAQ MK1 for spICP-MS data acquisition with a time resolution of 4 ns. This combination enables the detection and recording of ion clouds on a single-ion basis. The structure of the acquired raw data is described and visualized in detail. For the first time, it was demonstrated that it is possible to derive information on nanoparticle properties from the temporal gap (event gap) between ions that strike the detector during the detection of an ion cloud. A nomenclature for the novel type of spICP-MS data is established in this chapter.

In Chapter 4.2, the capabilities of the novel nanoDAQ MK1 system are determined. A size calibration approach based on the event gap between ions is developed and the resulting size accuracy and limit of detection of the method and workflow are evaluated. It is shown that the novel system with the tailored software lowers the size detection limit for AuNP to 7 nm. Additionally, a particle number concentration calibration approach is presented, which showed a

linear range from 10^3–10^7 particles per mL. Current challenges of the method are discussed, which are the detection of NP in the presence of dissolved analyte and the size resolution of NP mixtures.

Chapter 4.3 presents a modified version of the data acquisition system, the nanoDAQ MK2, which enables a time resolution of 2 ns and includes a filter function for false positive detector event signals. The effect of this improved filter function on the particle characterization is discussed. In addition, a new particle-by-particle approach is developed and the resulting particle sizing accuracy is compared to the previously presented data processing workflow's figures of merit.

In Chapter 4.4, an automated ion cloud recognition (ICRA) program is tested on data that is acquired with the nanoDAQ MK2. The analysis software had been designed to automatically identify, count, and characterize particle signals in data files from the nanoDAQ MK2 and was intended to significantly speed up the data processing time for high-throughput analysis. In comparison to conventional spICP-MS, this software processes the acquired data based on the calculated ion density instead of counts. The core feature of the program is an algorithm that automatically determines an ion density threshold, above which a series of signals is flagged as a nanoparticle. The capability of this feature is tested with model NP solutions is and critically discussed.

In Chapter 4.5, the developed tools, nanoDAQ MK2 (Chapter 4.3) and ICRA (Chapter 4.4), are combined and applied to the first feasibility study to screen environmental water samples for NP. Specifically, surface water from twenty sampling sites and waste water effluent samples from ten different waste water treatment plants were collected and characterized by spICP-MS. The possibilities and current limits regarding matrix (*i.e.* dissolved analyte) content in environmental water are investigated. This small-scale field study provides a first insight into the NP load in a river system in the area of Siegen and helps to assess the impact of waste water discharges into the surface water.

Chapter 5 summarizes the results of this thesis and discusses challenges and future perspectives in the field of nanosecond time resolution spICP-MS. Suggestions are provided for the improvement of the current nanoDAQ system and the corresponding data processing with regard to high-throughput nanoparticle analysis in environmental water samples.

2. State of the Art and Theory

Based on:

A. Schardt, J. Schmitt, C. Engelhard, Single particle inductively coupled plasma mass spectrometry with nanosecond time resolution, *J. Anal. At. Spectrom*., 2024, **39**, 389–400.
DOI: 10.1039/D3JA00373F.

2.1. State of the art

The range of applications for nanomaterials and their occurrence in the environment is immense (*cf*. Chapter 1.1). Due to their diverse nature and even more complex sample matrices, different methods for their characterization and detection are used today. The focus of this chapter is to provide a brief overview over the available tools to detect metal or metal oxide nanoparticles in liquid environmental samples as, *e.g.*, surface or ground waters, waste waters, and drinking water. Depending on the analyte, matrix, and nanoparticle property of interest, certain analysis methods prove to be more suitable than others. A more detailed discourse on the evolution and capabilities of single particle inductively coupled plasma mass spectrometry is presented.

2.1.1. Nanomaterials in aqueous environments

Concentration and size of particles in surface waters and WWTP effluents. The occurrence of engineered nanomaterials in environmental water samples is an area of increasing research. Nanomaterials under investigation have been mostly metal-containing NP, but carbon-based nanomaterials in the environment are gaining interest.[71] Among the metal-containing NP, silver-, titanium-, and cerium-bearing NP are the most frequently investigated types. Nanomaterial characteristics, which are important for toxicological risk assessments, are particle size and number concentration. The methods to determine these properties quantitatively in complex aqueous matrices are, however, limited. Particle size may be determined very accurately *via* microscopy-based techniques, yet they are not suitable for routine quantification in liquid samples. Particle number concentrations (PNC) are accessible through light spectroscopic methods, though on an element-specific level only. One compromise is to filter the liquid samples and retrieve a filtrate with a defined maximum particle size (*i.e*. smaller than the filter pore size). These filtrates are digested appropriately and the total element mass concentration of the particulate matter in the defined particle size fraction is determined (*e.g*. by ICP-MS). As a consequence, studies on particles that were detected in environmental samples sometimes provide either particle size, particle number concentration, or mass concentration, but not all three parameters.

Even within these parameters, reporting is not standardized, and comparability can be challenging. For example, reported particle sizes can represent the mean of a size distribution, an average of all detected sizes, the most frequently detected size, or a detected size range. Sometimes it is simply stated that particle sizes were lower than the used filter pore size.[31]. Particle number concentrations can be either analyzed directly or they represent indirectly calculated values from total mass concentrations and particle size. Moreover, the particle sizes could have been determined directly or be derived from analyzed particle masses using several assumptions.

In the case of metals that are known to appear as oxides (*e.g*. CeO_2, TiO_2)[72,73] or sulfides (*e.g.* Ag_2S)[74] in environmental samples, particle sizes from spICP-MS may be reported as the corresponding oxide or sulfide, or alternatively as the diameter of a hypothetical particle that only contains the respective metal. All in all, the variety of possibilities to report on nanoparticle characteristics and the plethora of methods to obtain those values complicate the comparison and evaluation of nanomaterials in environmental samples.

In **Figure 1**, the ranges of reported values are presented to give at least an approximate overview on the orders of magnitude of particle size, particle number concentration, and mass concentration of nanomaterials that were found in surface water samples and samples of WWTP effluents with discharges into a nearby water body. The spread of the reported values for identical nanomaterial types is explained by the variety of applied methods (spICP-MS, AF4-ICP-MS (asymmetric flow-field flow fractionation ICP-MS), CPE-GFAAS (cloud-point extraction-graphite furnace atomic absorption spectroscopy), ultrafiltration followed by ICP-MS, EDX (energy dispersive X-ray spectroscopy), HR-TEM (high-resolution transmission electron microscopy), SEM (scanning electron microscopy), or XPS (X-ray photoelectron spectroscopy)) but also, of course, by the natural variety of the analyzed samples and sampling regions. Data to create this figure was collected from several studies that are listed in **Table S1** (Appendix) and **Table 6**.

The summarized data show that for most particle types the reported sizes, mass concentration, and PNC ranges more or less overlap for surface water and waste water effluent. Apart from regional variations, this underlines that the number of evaluated studies for the creation of **Figure 1** is not substantial enough to draw general conclusions about the (anthropogenic or non-anthropogenic) origin of the nanometer-sized materials. However, many of the individual studies investigate the influence of specific WWTP discharges into receiving rivers or basins. Sanchìs *et al*. found that a WWTP with discharge into the Ebro River Delta (Spain) significantly mitigates the concentration of nanometer-sized particulates bearing Ti, Ag, and Ce by 76%, 76%, and 66%, respectively.[75] Li *et al*. demonstrated that two WWTP in Germany removed more than 96% of AgNP from the influent waste water.[46] Nevertheless, the authors point out that an increase in AgNP concentration in the River Isar can be clearly attributed to the discharge from the WWTP.[46] Similarly, Shi *et al*. investigated the removal of TiO_2NP by two WWTP that discharge treated waste water into the Binhe River and Minxin River (China) and found that, while the major part of TiO_2NP was retained by the WWTP (85% and 74%, respectively), relatively high total concentrations of 27–43 µg L^{-1} Ti remained in the effluent.[76]

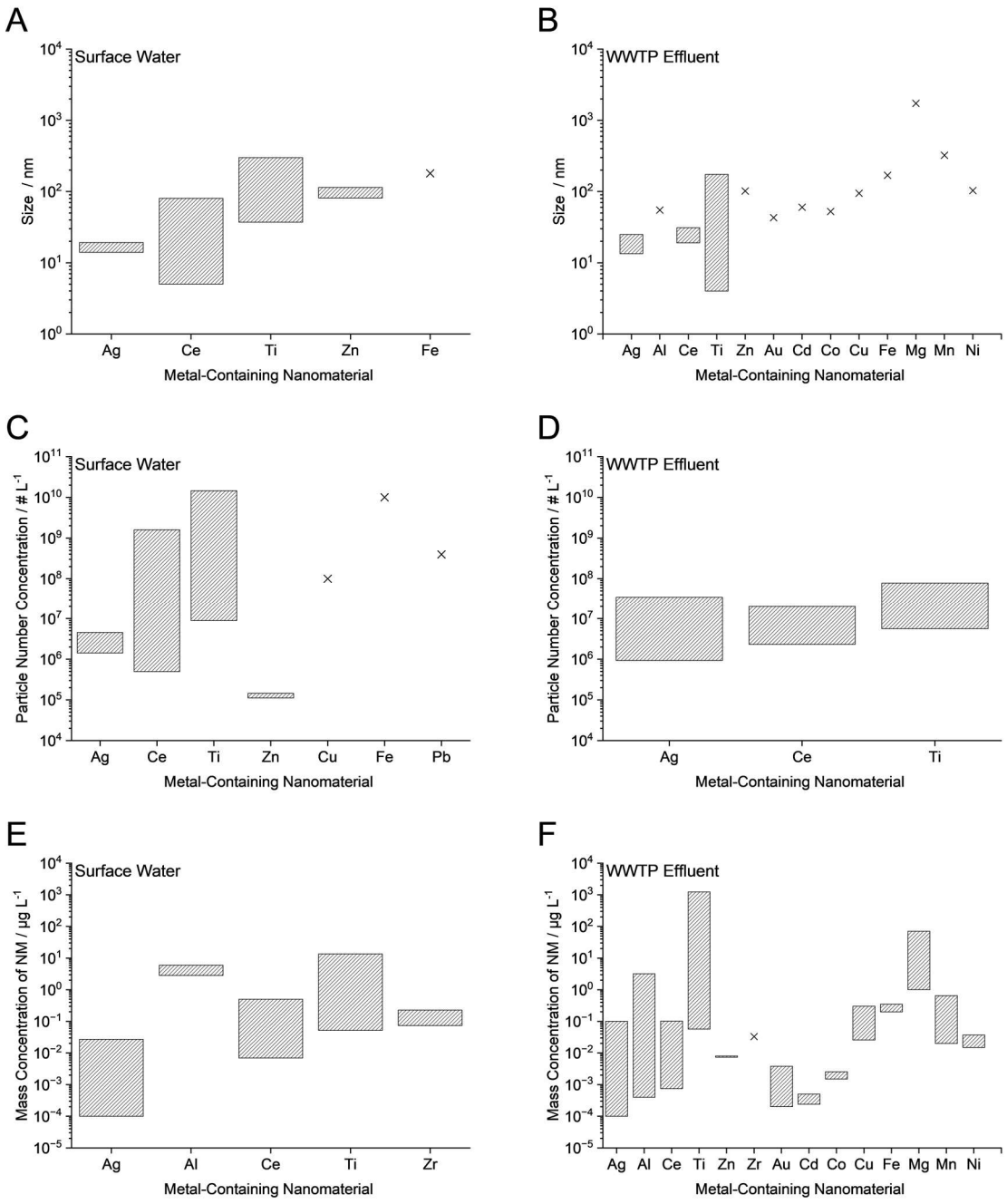


Figure 1. Sizes (**A**, **B**), particle number concentrations (**C**, **D**), and mass concentrations (**E**, **F**) of different types of nanomaterials that were reported for surface waters or waste water treatment plant (WWTP) effluent in the studies listed in **Table S1** and **Table 6**. Gray boxes indicate the total range of values reported in the reviewed studies, while individual values of only one study are marked by an "x", respectively.

Relevant information drawn from those studies for the method development in this thesis is that nanomaterials can be expected to occur in PNCs between *ca*. 10^5–10^9 particles per liter (# L^{-1}), and sizes range from a few nanometers to several hundred nanometers (excluding Mg). While size determination above 100 nm requires element-specific method optimization for spICP-MS, it should be possible to detect particles especially in the smaller nanometer range at the expected

concentrations in a fast, quasi-multi-element screening with the nanosecond time-resolved spICP-MS method.

Analysis Methods. In general, the method of choice for the characterization of nanomaterials largely depends on the property that is to be examined and on the physical state and complexity of the medium that contains the particles. A detailed list of instrumental tools that can be used to analyze properties of many types of nanomaterial in a large range of samples is given in a IUPAC Technical Note by Labuda *et al*.[56] A review from Leopold *et al*. specifically highlighted the importance of offline and online separation techniques as a pretreatment for NP characterization.[50] In **Table 1**, typical examples of important nanoparticle characteristics are presented next to suitable instrumental methods that have been employed to analyze nanomaterials explicitly in environmental water samples.

Table 1. Nanomaterial characterization methods commonly used for the analysis in complex environmental waters.

Nanomaterial Property	Method
Size	TEM, DLS, MALS, spICP-MS (SF, Q, QQQ, or TOF), UV-Vis, AF4, HDC
Particle size distribution	TEM, DLS, spICP-MS, AF4, HDC
Mass	Ultracentrifugation
Shape	TEM, MALS
Agglomeration	DLS, TEM, UV-Vis, AF4, HDC
Dispersion/ dispersibility	TEM, MALS, DLS, SPE
Optical properties	UV-Vis
Elemental composition	ICP-MS, (TEM-EDX), sp-ICP-ToF-MS
Concentration	spICP-MS, UV-Vis, MALS
Surface charge	LPE, CPE, SPE
Solubility	ICP-MS, spICP-MS, CPE

Methods and purposes modified from Labuda *et al*., 2023 (2)[56] and Leopold et al., 2016[50]. Acronyms are defined in the text below and in the list of abbreviations.

Microscopy-based techniques as *e.g.* TEM or SEM have the advantage that actual images of the colloids provide direct information on particles size, morphology, and shape. Also, a wide range of particle sizes is accessible with electron microscopy analysis due to the high spatial resolution of below 1 nm (TEM). In combination with EDX, the chemical composition of the particles can be investigated. However, electron microscopy requires the separation of NP from their surrounding matrix prior to the analysis, *e.g.* by CPE of the NP into another medium.[77] Following the purification, the NP need to be deposited onto thin microscopy grids. The pre-treatment and deposition processes are very time consuming and prone to introduce bias. The applied extraction or separation conditions might favor certain sizes or particles with specific surface coatings. Additionally, it is very cumbersome to find a sufficient number of particles on the grids for valid

particle size statistics. Efforts have been made to develop a validated PNC determination method based on TEM, but the process required ultracentrifugation prior to TEM analysis and at least 20 to 30 images (depending on the concentration) have to be taken per sample to achieve a stable average PNC value.[78]

Dynamic light scattering (DLS), multi-angle light scattering (MALS), and nanoparticle tracking analysis (NTA) can be used to directly analyze particle size and size distribution in liquid samples, but the presence of a high matrix content in environmental samples complicates the interpretation of the obtained data. The optical analysis methods cannot distinguish between different types of particles, *e.g.* between the metal nanoparticles of interest and natural organic matter (NOM). Additionally, precise information on the refractive index and viscosity of the sample medium need to be known to derive accurate particle sizes. These parameters are usually not available for unknown environmental water samples without preceding analysis.

Common methods for the separation of nanoparticles and matrix components are separation techniques, *e.g.* field flow fractionation (FFF), asymmetric flow-field flow fractionation (AF4), or hydrodynamic chromatography (HDC), ultrafiltration/-centrifugation, dialysis, solid phase extraction (SPE), liquid phase extraction (LPE), or CPE, which are operated offline or online coupled to a suitable detector.[50] Here, ICP-MS, ICP optical emission spectroscopy (ICP-OES), UV-Vis spectroscopy, or DLS are the most commonly used detection systems. Additionally, sample fractions from FFF or AF4 can be collected for subsequent microscopic analysis, *e.g. via* TEM.

In the last two decades, spICP-MS has evolved to a widely used and powerful technique for nanoparticle characterization in environmental waters, both as a standalone method or in combination with preceding size separation.[60,79,80] A relatively new tool is the combination of spICP-MS with time-of-flight (ToF) mass spectrometers. In brief, ToF mass analyzers separate analyte ions with different mass-to-charge number (m/z) values according to their flight times in a field-free drift tube. The time span between the detection of the lightest ion and the heaviest ion is in the range of nano- to microseconds, depending on the mass range.[81] Therefore, ion detection in a ToF-MS can be regarded as quasi-simultaneous (in contrast to a scanning quadrupole) and a complete m/z spectrum from $^{7}Li^{+}$ to $^{238}U^{+}$ can be recorded within 33 µs.[82] Because of this fast multi-element detection, single particle ICP-ToF-MS (spICP-ToF-MS) enables to investigate the elemental fingerprint of individual nanoparticles and to distinguish between engineered and natural colloids by classification according to the prevalence of certain elements (*e.g.* Zr and Ti) in each NP.[83–85] Unfortunately, ToF mass spectrometers remain relatively expensive in comparison to quadrupole mass analyzers, and the latter are already widely available in many water analysis laboratories worldwide. The evolution and capabilities of spICP-MS will be presented in Chapter 2.1.2.

2.1.2. Single particle inductively coupled plasma mass spectrometry

History. The development of single particle inductively coupled plasma mass spectrometry progressed in several stages during which existing instrumental methods were combined or their mode of usage was altered.

In the mid-1960s, the ICP was presented as an ion source for optical emission spectroscopy of elements.[86,87] About 15 years later, Houk *et al*. presented the implementation of the ICP as an ion source for mass spectrometers.[88] These methods were initially used for the analysis of traces of dissolved analytes in liquid samples. However, a few years later Kawaguchi *et al*. pioneeringly resolved "flashes" in the transient ion emission signal during the introduction of a dry aerosol containing salt particles (NaCl, $CaNO_3$, and $CuNO_3$) into the ICP by decreasing the integration time of the detection system from 10 s to 1 ms.[89] They estimated the size detection limit for copper particles to be near 300 nm. Similarly, in 1993 Nomizu *et al*. introduced a dry aerosol containing zinc- and lead-bearing particles into an ICP interfaced to a mass spectrometer and observed transient signals of the airborne particles with a digital storage oscilloscope.[58]

Ten years later, Degueldre *et al*. published a series of articles in which they presented the time-resolved detection of signals from different colloids in highly diluted liquid samples.[90–94] The extension of the field of application to colloid analysis in water samples aroused new interest in this method which dates back to the late 1980s and is now known as single particle ICP-MS. The further dissemination of the method in the atomic spectrometry community was driven by two fundamental studies on the methodology of spICP-MS by Laborda *et al*. and Pace *et al*.[57,95] Since then, spICP-MS has evolved to a routine research tool for nanoparticle analysis in environmental samples.[59–61]

Particle sizing *via* spICP-MS. In conventional ICP-MS analysis of dissolved elements in solution, the analyte is distributed homogeneously in the sample liquid, which is introduced into the plasma with a constant flow rate (in the range of 0.1-1 mL min^{-1}). Therefore, the resulting analyte ion signal intensity that is sampled at the detector is fairly constant with a certain standard deviation, which is usually well below 5% at optimized conditions (**Figure 2A**). Contrarily, inhomogeneous distribution of analytes in the sample causes significant variations of the transient signal intensity. In both cases, the signal intensity is proportional to the analyte mass flux into the plasma and hence to the concentration of the analyte element in the liquid sample.

If a highly diluted suspension of small particles is introduced into the plasma, the signal variation is large. During the time in which only solvent without particles is introduced, the detected signal intensity corresponds to the background noise level. But during the short period of time in which a particle is ionized in the plasma and forms a so-called "ion cloud", the local and temporal

analyte ion concentration becomes very high. The resulting sudden increase of the signal intensity is referred to as a signal “peak” or “flash” or “particle event” (**Figure 2**).

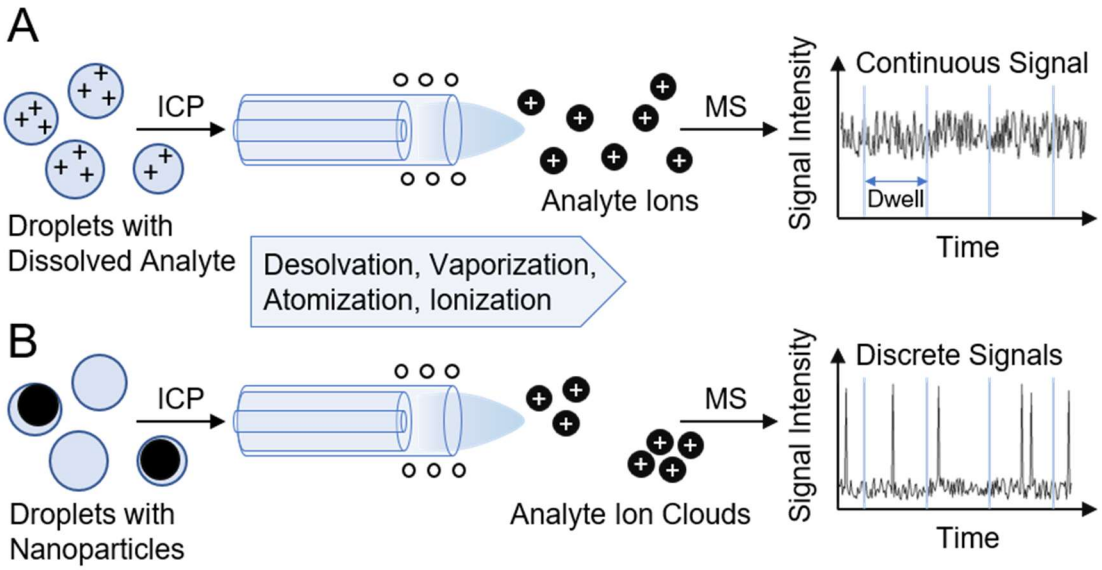


Figure 2. Schematic depiction of time-resolved ICP-MS signals from a solution (**A**) and a nanoparticle suspension (**B**) of the same element.

The detection of individual particle signals is only possible if exactly one particle flash is detected during one “detector dwell”/“integration window”. To ensure this, the particle concentration in the suspension has to be very low, *e.g.* below 10^5 # L^{-1}.[64,95] The simultaneous detection of two particles during one dwell is referred to as “particle coincidence”. Analogously, the divided signal of a single particle over two integration windows is called “split-particle event”. Both phenomena introduce a bias to the following determination of the particle size distribution.

The intensity I_{NP} of a particle signal peak is proportional to the mass of the original particle m_{NP} (Equation 1).

$$m_{\mathrm{NP}} \propto I_{NP} \qquad \text{Equation 1}$$

After converting the diagram of the transient signal intensity (**Figure 3A**) into a signal intensity histogram (**Figure 3B**), the mass distribution of the particles in the sample can be derived from this proportionality (**Figure 3C**).

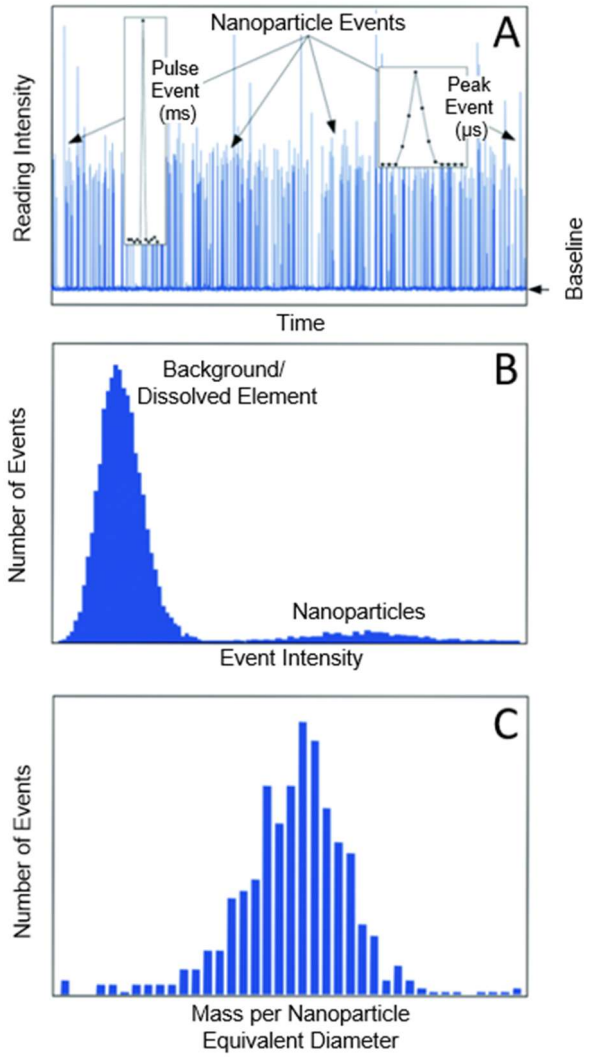


Figure 3. **A**. Time scan of suspension containing nanoparticles and dissolved forms of the same element. **B**. Event intensity histogram of data from **(A)**. **C**. Mass per nanoparticle/size distribution of spherical nanoparticles calculated from the intensity distribution on the right in **(B)**. Figure modified with permission from Bolea *et a*l. *Anal. Methods* 13 (25), **2021**, 2742–2795. [79]

Assuming a certain density ρ and ideal spherical shape of the particle, its mass can be used to calculate the corresponding diameter according to Equation 2:

$$d = \sqrt[3]{\frac{6 \cdot m_{\mathrm{NP}}}{\pi \rho}} \qquad \text{Equation 2}$$

Equation 1 and Equation 2 describe a proportional correlation between particle size and the detected signal intensity. The exact calculation of the particle size from the signal intensity is based on the fact that (in pulse-counting mode, *cf*. Chapter 2.2.4) the detector signal is directly proportional to the number of detected ions during each detection interval. In case of a NP that consists exclusively of one monoisotopic element, the number of detected ions from one ion cloud

should be directly proportional to the number of atoms *N* in the original particle and hence its diameter *d* according to Equation 3.[95]

$$N = \frac{4}{3}\pi\left(\frac{d}{2}\right)^3 \rho \frac{\mathrm{N}_{AV}}{M} \qquad \text{Equation 3}$$

Here, N_{AV} is Avogadro's number and *M* is the (mono)isotopic mass of the analyzed element of the NP. In practice however, not all atoms from a nanoparticle are completely ionized and transported through the mass spectrometer. The transmission efficiency depends on a multitude of factors (*cf*. Chapter 2.2) and varies with nanoparticle type, size, and matrix. Consequently, the absolute number of detected ions can only be used for nanoparticle sizing *via* suitable calibration.[57,95,96]

Aside from the particle number concentration, a second factor influences the occurrence of split-particle events and particle coincidence: The detector dwell time. Long dwell times in the order of 0.1–1 s, as used in conventional ICP-MS, heavily promote particle coincidence and are usually unsuitable for spICP-MS analysis. Dwell times in the order of 10 ms were commonly used in the early days of spICP-MS and allowed the recording of one signal peak for each produced ion cloud. The intensity of this peak was used for nanoparticle sizing according to Equation 1 and Equation 2.

Size detection limits that were achieved with millisecond dwell time spICP-MS (3–10 ms) in environmental water samples were *e.g.* 14 nm for AgNP[46], 19 nm for AuNP[97], and 79 nm for TiO_2NP[98]. Possibly due to the lower matrix content, size detection limits in tap water were found to be lower: 13 nm for AgNP and 75 nm for TiO_2NP.[99] The use of a high-mass resolution sector-field mass spectrometer instead of a quadrupole MS lowered the size detection limit of TiO_2NP to 42 nm, because polyatomic mass spectral interferences on the $^{48}Ti^+$ isotope could be reduced.[98]

In the early days of spICP-MS (and up to this day, to some extent), the availability of certified reference materials of different types of nanoparticles with well-defined particle sizes was very limited. Certified materials are required to perform size calibration and also to determine the size detection limit. Lee *et al*. circumvented this lack of particle standards by using dissolved element standard solutions instead. They experimentally determined the sensitivity of a quadrupole ICP-MS system (with or without use of collision cell technology (CCT)) for 40 different dissolved elements and evaluated the size detection limit (D_{min}) for 40 different hypothetical nanoparticle types according to Equation 4,

$$D_{min} = \sqrt[3]{\frac{6 \cdot 3\sigma_{BG}}{R \cdot f_a \cdot \rho \cdot \pi}}$$ Equation 4

where $3\sigma_{BG}$ [cps] is three times the standard deviation of the background signal (here: deionized water), R is the instrument sensitivity for the analyte element [cps μg^{-1}], f_a is the mass fraction of the analyte element in the particle, and ρ is the density of the particle.[100] According to their calculations, the size detection limit in spICP-MS is mainly restricted by the background noise and isobaric interferences on the analyte isotopes *m/z* values. They suggested the use of CCT to reduce polyatomic interferences and to choose isotopes with low background noise and/or high abundance to increase the signal-to-noise ratio. Lee *et al*. estimated size detection limits of 13 nm for both AgNP and AuNP in deionized water, which agreed well with the experimentally determined size limits of detection (LOD) by that time. The authors also hinted at recent promising developments by Montaño *et al*. (in 2014) that demonstrated the capability of microsecond dwell times to reduce the background signal and hence the size LOD.[101]

Due to the plethora of spICP-MS methods that have naturally evolved during its implementation in many research groups and on various instrumentation, several slightly different approaches for particle sizing have been employed. Bazo *et al*. recently compared and assessed those methods, which are either "based-on-intensity" or "based-on-time", using SiO_2NP and AuNP as model particles.[102]

Particle counting *via* spICP-MS. Because each detected count is ideally produced by an individual ion (in practice, noise also produces signals), the number of detected counts during a certain analysis time should be proportional to the concentration of particles in the sample solution. Several methods were presented to determine the so-called transport efficiency using dissolved and particulate standard solutions.[57] The transport efficiency corresponds to a mathematical correction factor between the number of detected peaks N_{NP} during a known period of time and the actual number of particles that was aspirated from the liquid sample. If the transport efficiency η_{NP} was determined accurately for a specific ICP-MS system using reference materials and the liquid flow rate v [mL min^{-1}] is known, the factor can be used to calculate the particle number concentration (PNC) [particles per mL] of unknown samples according to Equation 5. The transport efficiency usually has to be determined at least daily for each system.

$$PNC = \frac{N_{NP}}{\eta_{NP}} \cdot v$$ Equation 5

The duration of the ion cloud signal flash is in the order of several hundred microseconds, depending on particle size. This means that the time resolution with which that peak can be observed depends on the achievable dwell time of the detection system. Experiments with dwell times that are shorter than the transient profile of an individual ion cloud showed that the size detection limits could be lowered significantly. The advancement of spICP-MS with shorter dwell times will be presented in the following section.

The trend toward higher time resolution. When the concept of observing transient signals of airborne particles in an ICP was first applied to a mass spectrometer by Nomizu *et al*. in 1993,[58] most available quadrupole mass spectrometers could be operated at dwell times in the range of milliseconds. However, highly-resolved temporal profiles of singular ion clouds, which were produced from colloids and droplets in the ICP, were already reported by Olesik and Hobbs in 1992, who were able to "oversample" the ion cloud signal with a dwell time of only a few microseconds by connecting the current amplifier of the SEM to a digital oscilloscope.[103] This mode of data acquisition was initially less favourable than the usage of millisecond dwell times, because the total measurement time was limited. Since the interest in sub-millisecond time resolution has been rediscovered, researchers connected custom data acquisition systems[64,104,105] or oscilloscope solutions[106–108] to commercial ICP-MS instruments, while manufacturers adapted their hardware and software to the increasing request for fast data acquisition capabilities, as well.[101,109–112]

Sampling the detector signal with microsecond time resolution for the application in spICP-MS bears numerous benefits. A crucial factor for the establishment of spICP-MS as a routine method for NP characterization is the size detection limit, which can be lowered significantly by utilizing short dwell times, as reported by Strenge and Engelhard, who were able to detect gold nanoparticles as small as 10 nm with a single quadrupole ICP-MS by utilizing data acquisition with 5 µs time resolution.[64] The direct comparison of temporal profiles of identical ion clouds from 30 nm AuNP acquired simultaneously with 10 ms and 5 µs dwell time is demonstrated in **Figure 4**.

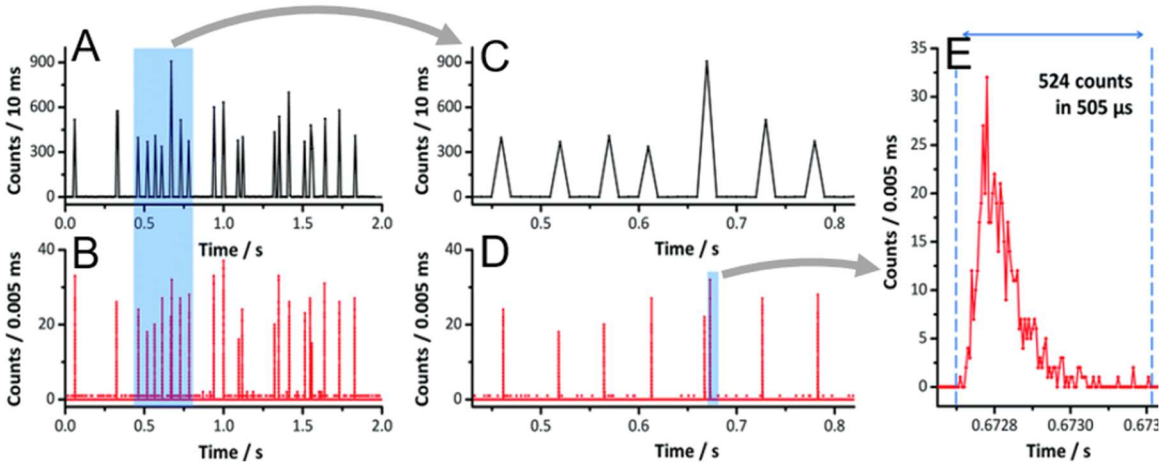


Figure 4. Representative ICP-MS signal (monitoring $^{197}Au^{+}$) due to 30 nm AuNP (PNC = $2.5 \cdot 10^{5}$ # mL^{-1}) acquired simultaneously over 2 s with (**A**) 10 ms dwell time (vendor software) and (**B**) 5 µs dwell time (home-built DAQ). First zoom level shows several particle events in (**C**) and (**D**) for 500 ms of highlighted section in (**A**) and (**B**)**.** Second zoom level E shows the temporal profile of a single particle's ion cloud identified with the home-built DAQ in (**D**). Figure taken and adapted with permission from Strenge and Engelhard, *J. Anal. Atom. Spectrom.* 31 (1), **2016**, 134–144.[64]

With a dwell time of 50 µs, Lamsal *et al*. could quantify platinum nanoparticles with a diameter of 10 nm. [113] Montaño *et al*. evaluated the advantage of employing dwell times from 25–100 µs for the detection of SiO_2 NP over the previously common method of removing the polyatomic spectral interference of $^{14}N^{14}N^{+}$ on $^{28}Si^{+}$ by use of a collision or reaction gas.[114] Additionally, Kálomista *et al*. claimed to be able to distinguish gold nanorods from spherical gold NP by comparing the shape of the oversampled ion cloud profiles of both particle types, [115] as well as the possibility to determine the structure and composition of Au-Ag bimetallic nanoparticles. [116] Because it was suggested that the cytotoxicity of gold nanoparticles and the tendency of titanium dioxide particles to permeate the blood-brain-barrier is shape-dependent, [117–119] the possibility to determine the particle shape would be a beneficial feature of the method for future investigations. Another very recently demonstrated advantage of microsecond dwell times is the significant reduction of the $^{12}C^{+}$ and $^{13}C^{+}$ background signals, which was exploited by Bolea-Fernandez *et al*., Liu *et al*., and Gonzalez de Vega *et al*. to detect microplastic particles as small as 1.0 µm, 0.8 µm, and 0.6 µm, respectively, with dwell times of 100 µs.[120–122] Mozhayeva and Engelhard showed that fast data acquisition and a tailored data processing method for spICP-MS enable to detect silver nanoparticles in the presence of up to 7.5 µg L^{-1} ionic silver.[123] Naturally, these promising results led to an increasing usage of µs-spICP-MS (microsecond spICP-MS) for a wide range of applications, which in 2021 made up for *ca*. 45% of all reported applications of spICP-MS since 2014. [79]

In 2021, Duffin *et al*. recorded time stamps of individual detector output pulses of a multicollector ICP-MS with an accuracy of 0.5 ns by means of a time-to-digital-converter and utilized

the time between two successive ion arrivals at the detector to distinguish between ions produced from particles and ions stemming from a continuous background. They observed a significant shortening of the time gap between ions during detection of an ion burst from a particle in comparison to longer gaps between background ions. The authors applied an algorithm based on boxcar averages in combination with a reasonably set threshold value to determine the beginning and the end of a detected ion cloud in transient plots that present the cumulative count of detected ions *vs*. the measurement time stamp. This approach allowed for the detection of 5 nm AuNP in a citrate-buffered solution. The correlation between the number of detected counts per ion cloud *vs*. the theoretical number of atoms per particle was shown to be linear for gold particles from 5–20 nm. Above that size, however, the response curve flattens, which the authors attribute to non-detection of ions due to pulse pile-up.[124]

In this thesis, spICP-MS data with a time resolution in the nanosecond range is recorded with a single quadrupole ICP-MS instrumentation. The possibilities of using dwell times that are significantly shorter than individual transients from AuNP and AgNP entering the ICP are investigated using a standard sample introduction system. A concept on how to process a continuous stream of nanosecond time-resolved spICP-MS (ns-spICP-MS) data for size calibration of nanomaterials is described.

2.2. Theory

The goal of each mass spectrometric method is to achieve lowest possible detection limits, ideally down to the point of "single-atom detection". In single particle ICP-MS specifically, this translates to the lowest possible particle size detection limit, where the "particle" consists of one single atom.[60] The number of ions that are detected per particle during spICP-MS measurements is orders of magnitudes smaller than the actual number of atoms in the original particle. This is a consequence of the loss of ions throughout different stages of the instrumental analysis procedure; (1) ion generation, (2) ion extraction, (3) ion selection, and (4) ion detection. These processes and their implications to the data obtained during this thesis will be presented in the following sections. The principle of ion detection is explained in more detail because it is crucial to the understanding of the presented results.

2.2.1. Implications of ion generation in the plasma on spICP-MS

In ICP-MS, ions for the subsequent mass spectrometric analysis are formed inside a plasma torch that consists of three concentric quartz glass tubes, all of which are supplied with an individual argon gas flow. The ICP itself is created by applying a radio frequency (RF) power between 750 and 1700 W to an induction coil that surrounds the tip of the torch.[125] This alternating current (AC) in the coil creates an oscillating electromagnetic field that penetrates the argon stream in the torch. To ignite the plasma, a spark from a Tesla coil introduces electrons into the argon stream. These free electrons are accelerated in the electromagnetic field and collide with neutral argon atoms, which leads to collision-induced emission of further electrons and ionization of the argon atoms. The released secondary electrons and argon ions are in turn accelerated in the electromagnetic field. This process initiates a chain reaction that continuously supplies the gas with free electrons and argon ions and therefore generates the ICP. In total, however, the plasma is considered neutral. Due to the collision process, kinetic energies of the species in the gas are extremely high and the plasma temperature varies between 6000 and 10 000 K.[125] To protect the quartz glass torch from melting, argon gas is passed through the outer tube with high flow rates of 11–15 L min^{-1}.[125] The argon stream through the middle tube sustains the plasma (at typical flow rates of 0.5–1.5 L min^{-1}) and the aerosol carrying the analyte from the nebulizer is introduced through the inner quartz tube at flow rates of 0.5–1.5 L min^{-1}, depending on sample and application.[125] The purpose of the ICP in combination with mass spectrometers is to create ions from a liquid, gaseous, or solid sample that can be selected and detected further on in the mass analyzer. To that end, *e.g.* a liquid is aspirated into a (usually pneumatic) nebulizer to create a coarse aerosol. From this primary aerosol, larger droplets or particles are removed in the spray chamber (here: glass cyclonic) to create a secondary

aerosol with a narrow droplet size distribution. These small droplets contain analyte and matrix components that are dissolved or dispersed in the solvent. The nebulizer gas stream carries the droplets into the plasma torch, where the solvent evaporates due to the high temperature. The remaining solid residue from each droplet is subsequently vaporized and atomized in the hotter regions of the plasma. In the normal analytical zone at the tip of the plasma torch, most of the ions are formed, which are then extracted into the mass spectrometer. Excitation of atoms and ions and emission of characteristic radiation also occurs in the plasma. However, the theory of optical emission in the ICP will not be discussed in detail because it is not relevant for mass spectrometric analysis.

The efficiency of the formation of ions from the original atoms in solution depends on various factors, the first one being the loss of sample during nebulization. The percentage of analyte ions that pass from the spray chamber into the plasma (transport efficiency, TE) varies with nebulizer type and liquid flow rate. With a concentric microflow nebulizer that is used in this thesis, the transport efficiency for nanoparticles is typically in the range of 1–10% at liquid flow rates of 0.1 –1 mL min^{-1}. [57,126,127] The transport efficiency for particles and cells can be increased up to 100% by using improved nebulizer and spray chamber set-ups.[128]

From the approximately 1 to 10% of analyte molecules or atoms that enter the plasma using standard sample introduction equipment, only a certain portion is ionized. As a general rule, only elements with a first ionization potential lower than that of argon (15.76 eV)[125] can be efficiently ionized in an argon plasma. Most elements in the periodic table produce singly-charged ions with ion yields between 5 and 100%,[125] while elements with ionization potentials below 8 eV are typically ionized to a degree of 90–100%[129]. Gold and silver, which are the main analytes in this thesis, typically show ionization efficiencies of 51% and 93%, respectively (at a plasma temperature of 7500 K and an electron density of 10^{15} cm^{-3}).[129]

Depending on plasma temperature, water load, and extraction (sampling) position of the ions from the plasma, competitive reactions may influence the percentage of singly-charged ions. At higher temperatures, the formation of doubly-charged ions from atoms with low second ionization energies is promoted. In contrast, low plasma temperatures might not provide sufficient energy for ionization at all and the atom-to-ion ratio increases. At high oxygen content from high water loads in the plasma, the formation of oxides is favored. Additionally, oxide formation is also observed in the plasma tail behind the tip of the torch, where lower temperatures do not break up the bonds of small molecules (*i.e.* oxides or argon adducts). As a consequence, the plasma temperature, sampling position, and gas and liquid flow rates have to be carefully tuned to obtain optimum ionization conditions for the selected analytes in the plasma.

In conventional ICP-MS, the dissolved analyte is ideally distributed homogeneously in the sample solution and is therefore delivered to the plasma in a continuous stream. At (quasi) constant plasma conditions, a mass flow of ions with a constant temporal ion density is formed in the plasma and extracted from the MS interface. If, however, the analyte is not dissolved in the sample liquid but rather present as small colloids in diluted suspension, the formation of analyte ions in the plasma is not continuous.

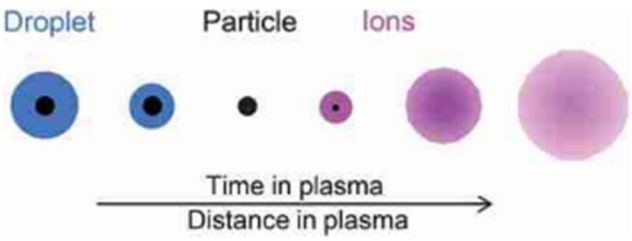


Figure 5. Schematic depiction of the processes that a particle in a droplet undergoes in the ICP. The solvent completely evaporates and subsequently, the solid particle is atomized and ionized. Each process is temperature-dependent and occurs after a certain residence time in the ICP. Simultaneously, the gas flow transports the analyte species from the torch entrance toward the MS interface. Figure reprinted with permission from Olesik and Gray, *J. Anal. Atom. Spetrom.* 27 (7), **2012**, 1143–1155.[130]

When a sufficiently diluted suspension of colloids (*e.g.* nanoparticles) is nebulized, some of the created droplets contain a single colloid, while most of the droplets are "empty". As soon as the colloid enters the plasma, it is atomized and ionized in a flash. From each droplet containing a particle, an individual cloud of ions is created during its passage through the plasma torch (**Figure 5**). Below a certain size and at optimum plasma conditions, the particle is ionized completely (also depending on the ionization potential of the element, see above). Above a critical particle diameter, however, the vaporization/ionization may be incomplete and only a fraction of the original particle's analyte atoms can be extracted as ions from the MS interface. The critical size is different for each colloid composition and upper limits in the range of 1–2 µm were reported for SiO_2 and ZrO_2 particles.[92,114,131]

In summary, both the type of spray chamber and the ionization process itself pose an upper limit on the particle size, which can be transported efficiently and completely into the mass spectrometer *via* the ICP.

2.2.2. Implications of ion extraction from the plasma on spICP-MS

After ionization of a dried droplet or particle in the plasma, the produced cations begin to repel each other due to Coulomb repulsion. Additionally, the hot temperatures in the plasma of up to 10 000 K increase their Brownian motion. These effects lead to significant spherical diffusion of the created ion cloud. Meanwhile, the ion cloud is pushed toward the sampler cone by the plasma gas flow and is equally attracted by the negative potential on the ion lenses in the MS interface. The aperture of the sampler cone is typically 1 mm in diameter. Due to diffusion, the off-axis radius of the ion cloud can be larger than this aperture; which consequently leads to the loss of a large portion of ions that are not extracted by the sampler (**Figure 6**). Fundamental studies of Niu and Houk, Stewart and Olesik, and Olesik and Gray describe these physical phenomena and other factors (*e.g.* space charge effects in the second interface stage between sampler and skimmer and further along the path toward the detector) that contribute to the ion extraction efficiency of an ICP mass spectrometer.[129,130,132]

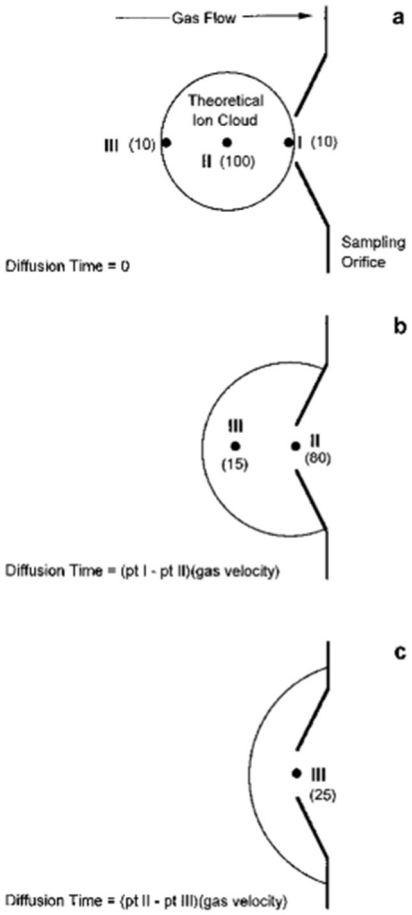


Figure 6. A cartoon depicting the dynamic effect of diffusion in the ion cloud as it flows through the mass spectrometry sampling orifice at three different times. Figure reprinted with permission from Stewart and Olesik, *J. Anal. Atom. Spectrom.* 10 (2), **1999**, 159–174.[132]

2.2.3. Implications of ion selection in the mass analyzer on spICP-MS

After extraction of the ions into the mass analyzer through the interface, they pass several ion lenses that focus the dispersed ion beam behind the skimmer. To prevent photons and neutral particles from the plasma from entering the mass analyzer region, they are separated from the ions before the entrance. This is done by different approaches, depending on the instrument type, *e.g.* by deflecting the ion beam by a 90° angle into the mass analyzer using a dedicated electromagnetic field. The neutral atoms and photons are not influenced by the field and just collide with one of the walls inside the instrument. Other manufacturers solved this issue by defocusing and refocusing the entering ion beam around a baffle plate, which serves the same purpose.

In all cases, the ion beam is very dense at certain stages in the ion optics system, which promotes the occurrence of space charge effects. Due to the high kinetic energy of high-mass ions, they induce off-axis and (to a lesser extend) axial displacement of lighter ions with lower kinetic energy from the stable path toward the mass analyzer. If the analyte of interest is a low-mass element and many high-mass elements are present in the same solution, the sensitivity for the analyte can be severely decreased. This phenomenon is observed for conventional ICP-MS of dissolved analytes, but is also a potential issue for the analysis of ion clouds from colloids, which is described in detail by Stewart and Olesik using the example of simultaneous analysis of ion clouds from $^{7}Li^{+}$ and $^{208}Pb^{+}$.[132] While this is not an issue for the analysis of a single type of nanoparticle in a pure model solution, this mass-dependent bias has severe effects on a multi-element particle screening of real water samples.

While the space-charge effects described above introduce some kind of an uncontrolled, undesirable mass pre-selection, the actual analyte mass filtering is achieved with the mass analyzer. For ICP-MS, the linear quadrupole is the most commonly used mass analyzer, because it is relatively low in cost compared to magnetic sector-field or time-of-flight mass analyzers and the quadrupole's unit mass resolution is sufficient for many inorganic mass spectrometry applications, especially when using a triple quadrupole set-up.

The principle of m/z separation of ions in the quadrupole is based on the Mathieu equations. In brief, an electromagnetic field is created between four hyperbolic or cylindrical shaped metal rods and the ion beam is directed at the center axis of the quadrupole entrance. A direct current (DC) voltage and a superimposed AC radio frequency voltage are applied to the rods. The AC voltage of two opposite rods is in the same phase, while the AC voltage of the two perpendicular rods is phase shifted by 180°.

An ion that enters the field inside the quadrupole is forced into a circular motion in x,y-direction due to the alternating attraction to different rods. Lighter ions are easily influenced by the electric field, while heavy ions have higher inertia. Singly-charged ions experience less attraction toward the electrode rods than doubly-charged ions. This mechanism provides the desired mass selectivity or mass filtering. By carefully tuning the ratio between DC and RF voltage and the offset of the DC voltage, it is possible to select ions within certain ranges of mass-to-charge number that can exit the quadrupole on a stable path along the center axis during a certain time and reach the detection system. Ions outside that range are set on unstable trajectories, eventually strike the rods and cannot be detected.

The RF *vs*. DC voltage regions for ions with a certain mass-to-charge number in which they pass the quadrupole with a stable trajectory can be determined using the Mathieu equations. If several ions with different mass-to-charge number values have to be analyzed, this has to be done in a sequential scanning manner by quickly shifting the quadrupole voltages. In between, the quadrupole requires a certain settling time until all ions with a certain *m/z* value leave the mass analyzer before the next *m/z* is chosen. Montaño *et al*. reported a settling time of 100 µs to be the minimum time their quadrupole mass analyzer required to provide stable ion intensity signals while switching between two *m/z*.[101] For conventional ICP-MS analysis of dissolved analytes in samples, the analyte mass flow through the quadrupole is assumed to be relatively constant throughout the analysis. Therefore, the settling time between isotopes does not affect the ion count rate of each isotope, which is proportional to analyte concentration, and hence the scanning of ions across a large range of *m/z*-values can be performed in quick succession.

Ionization of a colloid, however, results in the formation of an ion cloud with a short transient profile of several hundred microseconds.[64,130] The intention of single particle ICP-MS is to detect all ions from one ion cloud (or of that portion that has been transmitted to the quadrupole entrance so far) completely. If the voltages of the quadrupole were changed during the passing of a single ion cloud, all ions that entered the electrical field during the settling time would be lost. For example, 50% of the ions within an ion cloud transient of 200 µs duration would be unobserved when switching between two isotopes with a settling time of 100 µs. Since the duration of the transient signal is unknown and the ion density varies significantly across the transient itself, the loss of ions cannot be corrected by a constant, calibrated factor as in conventional analysis of dissolved analyte with a constant mass flow. Consequently, the possibility to perform quantitative multi-element single particle ICP-MS analysis on colloids using a quadrupole mass analyzer is limited by the quadrupoles specific settling time, which is determined by its instrumental design, and the duration of the ion cloud transient signal.

With the Mathieu equations, the combinations of RF and DC voltages that lead to a stable x,y-trajectory of an ion with a certain mass-to-charge number value through the quadrupole can be solved numerically. In a Mathieu diagram, it becomes apparent that the stable regions(blue regions in **Figure 7C**) for many mass-to-charge number values overlap to a large extent, which practically means that all ions within that mass-to-charge number range would pass to the detector and (almost) no mass filtering is achieved. Only small fractions of the stability regions do not overlap. In practice, sets of RF and DC voltages are dynamically adjusted in way that corresponds to a line with a certain offset and slope in the (first order) Mathieu stability diagram. In order to achieve at least unit mass resolution, the so called "scan line" is chosen to cross only the tips of each stability region.

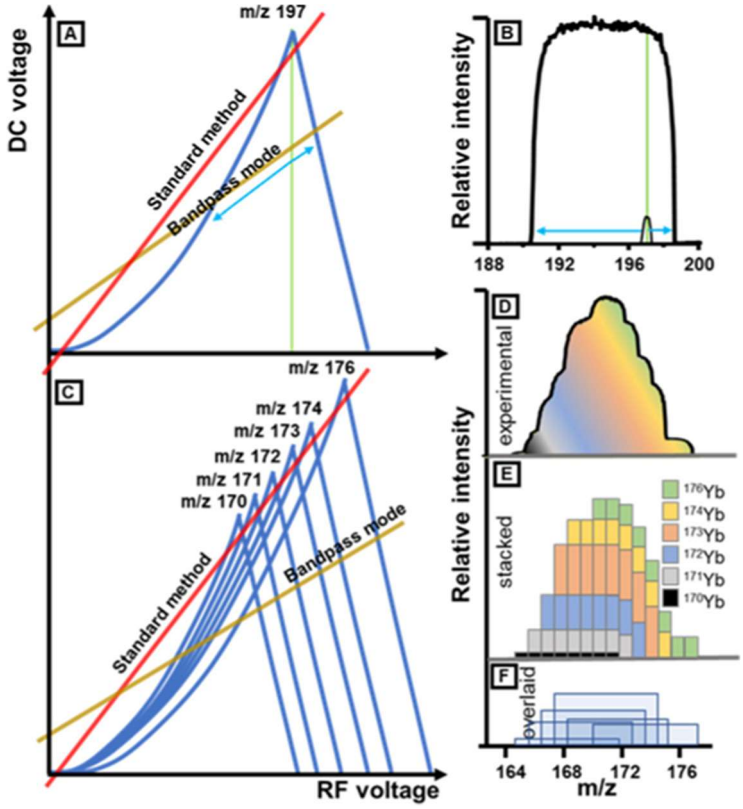


Figure 7. **A**. Schematic stability diagram for *m/z* 197. The scan lines for standard operation (unit mass resolution and for the bandpass mode are marked. **B**. Mass spectrum of Au using a standard scan line and the bandpass mode. **C**. Stability diagrams for all relevant Yb isotopes. Operating the bandpass mode results in a signal convolution. **D**. Yb mass spectrum recorded in the bandpass mode. **E, F**. Simulated convolution of Yb isotope signals. Figure reprinted with permission from Meyer *et al*. *Anal. Chem.* 92 (22), **2020**, 15007–15016.[133]

While this standard method provides a sufficient mass resolution for many applications, it comes at a loss of sensitivity. Many ions of the analyte element of interest might enter the quadrupole with slightly different kinetic energies and a large portion of them will not pass to the detector on a stable trajectory at high mass resolution settings. But if no interfering ions with neighboring *m/z* values are expected to be in the sample, the mass resolution of the quadrupole

may be decreased to the point of a mere bandpass mass filter in the favor of higher sensitivity, as shown in **Figure 7A** and **B**.[133] This reduced mass resolution is especially beneficial for the analysis of elements with several isotopes (*e.g.* Yb), because their combined signal intensity is significantly higher than the signal intensity of each individual isotope (**Figure 7C-F**). Again, this approach is only valid, if no ions from other elements interfere in the *m/z* region of interest. Especially during spICP-MS analysis of very small particles, this approach provides one possibility to increase the ion transmission and consequently to improve the size detection limit.

2.2.4. Implications of ion detection at the electron multiplier on spICP-MS

Ions that exit the quadrupole mass filter need to be detected by an appropriate system that allows for sensitive and continuous detection. In many ICP-MS instruments, discrete dynode secondary electron multipliers (SEM) are installed because of their large linear dynamic range of six orders of magnitude (10 orders of magnitude for multipliers with extended dynamic range) and (relatively) fast acquisition capability.[134]

Signal Amplification. The operating principle of the SEM is based on the ejection of secondary electrons from a metal or semiconductor surface upon impact of a primary ion. In the case of ICP-MS, an ion that passed the quadrupole is directed onto the first dynode of the SEM. The collision releases secondary electrons from the dynode's surface, which are guided onto the second dynode by electron-optics. Upon the impact of the secondary electrons, more electrons are released from the second dynode, which is held at a higher potential than the first one. This process is repeated at every stage of the SEM and a cascade of millions of electrons is produced from a single ion. Finally, the resulting current pulse is read out at the output electrode of the SEM (**Figure 8**). This operating mode of the SEM is called "pulse-counting mode" and it is especially sensitive for the analysis of low analyte concentrations due to its high gain (up to a factor of 10^{10}).[134] However, the lifetime of the semiconductor material of the SEM's dynodes is limited and depends on the potential they are held on and especially on the number of electrons that strike the surface material during operation. In order to extend its lifetime, a simultaneous mode SEM provides the possibility to automatically close an electric gate to the last dynode stages, if a specified input current threshold is exceeded. Instead, the current at a mid-stage dynode is first converted to a voltage, amplified, and eventually converted to a digital signal that can be read out.[134] This so-called "analog detection mode" consequently has a lower gain (typically 10^6)[134] and is only activated for the analysis of high analyte concentrations. The output signal intensities (counts per second) that are obtained from both operating modes for a certain ion flux are not identical, but the variance is usually corrected for by a tuned calibration factor in the ICP-MS software. During the observation

of short signal transients with varying intensity (*e.g.* ion cloud signal profiles), however, switching between the two operating modes may lead to signal loss and has to be avoided.

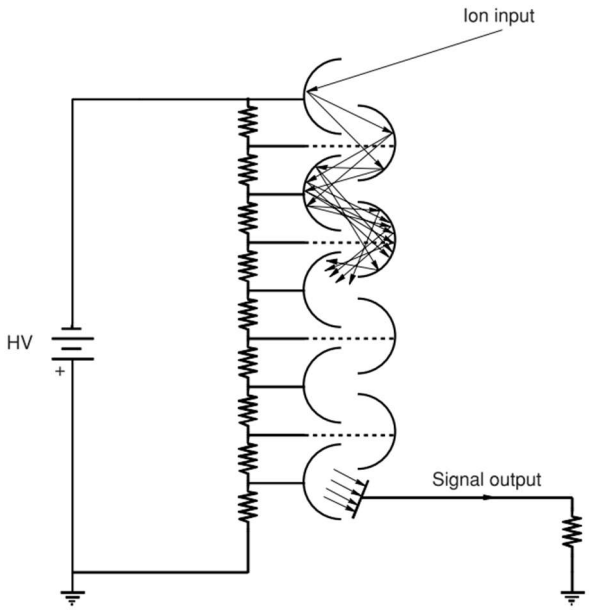


Figure 8. Schematic depiction of a discrete dynode secondary electron multiplier. Figure adapted with permission from K. Hunter and D. Stresau (**2005)**: *Ion Detection*. In: S. M. Nelms (Ed.): *Inductively coupled plasma mass spectrometry handbook*. Oxford, Boca Raton, FL: Blackwell Pub, 117–146.[134]

Pulse-Counting Statistics. When the SEM is operated in pulse-counting mode, each pulse is registered as a detector event (DE) by the pulse detection electronics (above a certain discriminator level). Accordingly, each DE is denoted as one "count". Only two logical states are possible; either a DE occurs (1 count) or it does not (0 counts). Conventional pulse-counting data acquisition systems for ICP-MS count the number of DE during certain, adjustable dwell times (nowadays as low as a few microseconds up to several seconds).[64,112] They eventually store and display an output signal as a data point (dp) with the accumulated number of counts as y-value and the measurement time of the dwell as x-value. The typical upper limit of the linear dynamic range of the pulse-counting stage of an SEM for ICP-MS is *ca*. 10^6 counts per second.[134] A simultaneous mode SEM offers the possibility to switch to the analog detection mode above that count rate, which extends the linear dynamic range to *ca*. 10^{10} counts per second. In this work, the maximum count rate was expected to be within the linear range of the pulse-counting mode and therefore, only the pulse-counting output current was sampled.

During the measurement of solutions with high analyte concentration, many analyte ions are detected during each dwell of the detector and the output signal is accordingly high. When long dwell times are set and the analyte in the solution is highly concentrated, the output signal is assumed to be normally distributed with an integer median value and a standard deviation. For

example, a measurement of the $^{115}In^{+}$ ion signal during aspiration of a 1 µg L^{-1} dissolved indium solution with a dwell time of 1 s might produce dp with a mean y-value of 350 000 counts and a typical standard deviation of ± 1% (**Figure 9**). According to Normal distribution statistics, between 360500 and 339500 DE are counted during each dwell of 1 s with a probability of 99.7% (± 3σ).

The lowest possible absolute value of the number of counts is 0. Most of the dp will be 0, when the analyte ion concentration is extremely low and DE occur rarely during the measurement, or if the dwell time is sufficiently short. At this point, the probability distribution for a certain number of counts to occur simultaneously during one dwell interval is best described by Poisson distribution statistics. Here, the expectation value λ was chosen by calculating the average number of counts during 5 µs (4.2 ns, 1.9 ns) that correspond to the mean signal intensity of 350 000 counts per second (here: λ = 1.75 (5 µs), $1.46 \cdot 10^{-3}$ (4.2 ns), $6.65 \cdot 10^{-4}$ (1.9 ns)). The probability P(k, λ) for a certain number of ions k to hit the detector during one dwell at an expected count rate λ was calculated according to Equation 6:

$$P(k,\lambda) = \frac{\lambda^k}{k!}\, e^{-\lambda} \qquad \text{Equation 6}$$

If the same indium solution as described above is measured with a dwell time of 5 µs, which can be achieved with the previously presented inhouse-built microsecond data acquisition unit (µsDAQ), [64] the probability that a dp has the y-value 0 (no DE during dwell interval) is *ca*. 17% (**Figure 9**). The probability that more than 5 analyte ions are detected during one dwell is below 1%.

The nanosecond data acquisition units nanoDAQ MK1 and MK2 allow the acquisition and storage of the pulse-counting signal with a recording time interval as low as 4.2 ns or 2.2 ns, respectively. For comparison, the same calculation as described above for 5 µs dwell time is now performed with 4.2 ns (2.2 ns) instead. According to Poisson statistics, the probability that no DE event occurs during one recording interval of 4.2 ns (2.2 ns) is *ca*. 99.85% (99,92%). The probability that exactly one ion hits the detector during one dwell is less than 0.15% (0.077%), and the coinciding detection of more than 1 ion has a probability of roughly $5 \cdot 10^{-8}$% ($8 \cdot 10^{-9}$%).

In spICP-MS measurements with dwell times shorter than the duration of an analyte ion cloud from a nanoparticle, the ion cloud signal is "oversampled", *i.e*., more than one dp is acquired per ion cloud. Different approaches have been described to identify and extract data from individual ion clouds (or particle events) from the raw data of such a time-resolved measurement. [112,123,135] In an exemplary measurement in this study ion cloud signal traces of AuNP were acquired with 5 µs time resolution using the µsDAQ (data not shown). They were found to have an average duration of 435 µs and comprised 87 dp (average values of 639 ion clouds of 80 nm AuNP). The average maximum number of DE per 5 µs (*i.e*. per dp) was 40 counts. Assuming 40 counts per 5 µs as

expectation value λ for the Poisson equation, the probability that more than one DE would occur during one dwell of 4.2 ns (2.2 ns) would be *ca*. $6 \cdot 10^{-4}$% ($9 \cdot 10^{-5}$%). So even during the measurement of nanoparticles, which produce ion clouds with very high analyte ion densities, the acquired values of 0 or 1 should be reliable for each acquired data point. In contrast, the expected average signal intensity during a 1 s dwell time for the aforementioned 80 nm AuNP would be $8 \cdot 10^{6}$ counts (**Figure 9**).

Regarding ion-coincidence, the possibility that a dp has a y-value other than 0 or 1 is virtually eliminated during data acquisition with the nanoDAQ MK1 and MK2 and the transient output signal that is obtained should in theory represent the actual pulse-counting signal of the SEM.

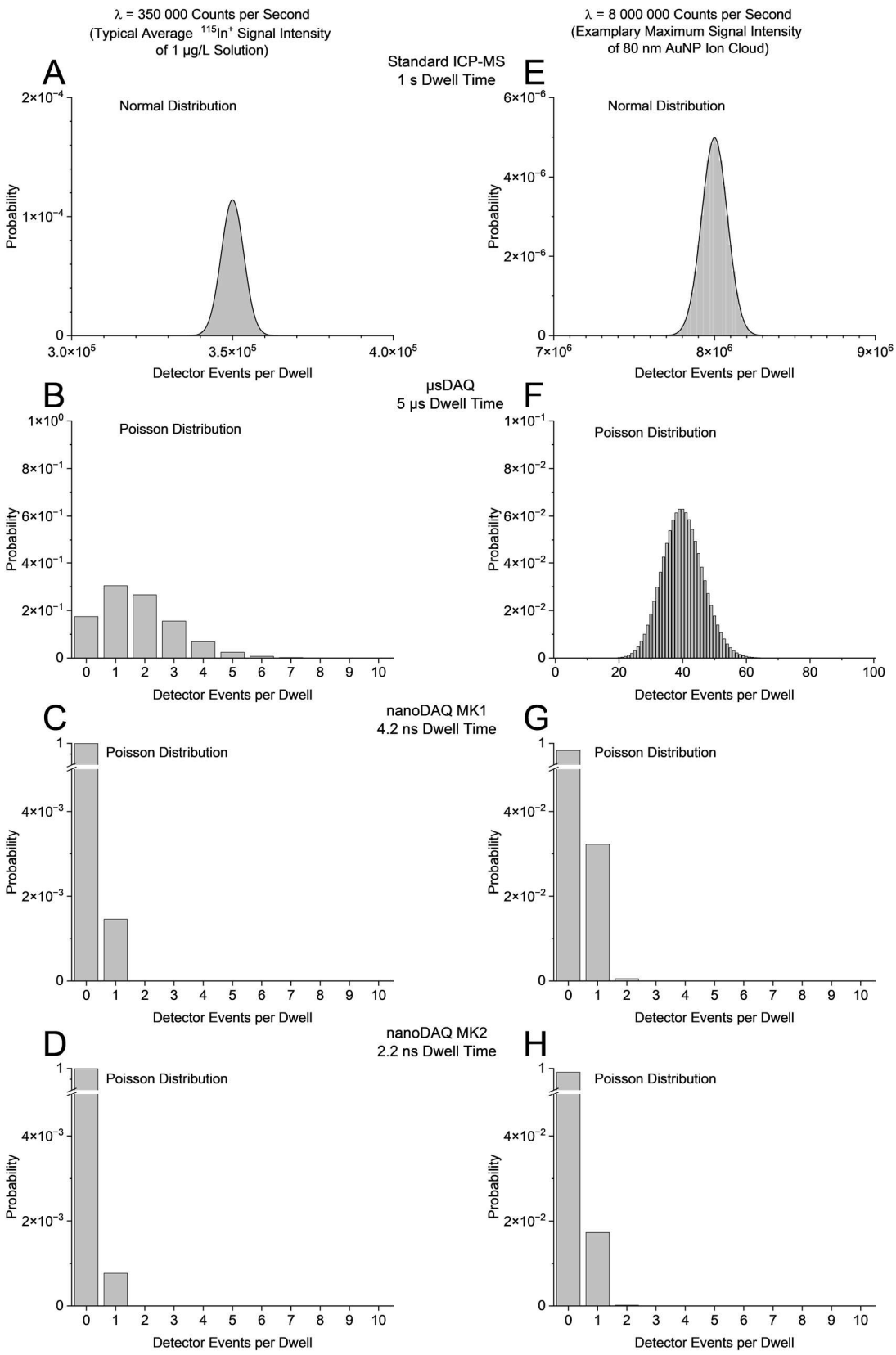


Figure 9. Probability distributions P(k,λ) for a number of k ions striking the SEM detector during a dwell time of 1s, 5 µs, 4.2 ns, and 2.2 ns for average exemplary signals corresponding to a 1 µg L^{-1} Indium solution (**A**–**D**) or a 80 nm AuNP (**E**–**H**). Calculated values for the distribution plots are presented in **Table S2**–**Table S6**.

Detector Dead Time. In addition to the consideration of counting statistics, it is important to consider the dead time of the SEM, which mainly depends on the pulse width and on the time the pulse-counting electronics requires to reset. From each ion that strikes the first dynode of the SEM, one electrical pulse is extracted from the multiplier output. This pulse has a certain width, *i.e.* certain duration (4–10 ns).[136] To separate the pulses from noise, the multiplier output signal is first fed into a pre-amplifier and then into a discriminator/comparator stage. Only signals above a certain discriminator threshold are subsequently counted by the pulse-counting electronics. After the complete detection process of one ion (*i.e*. electron multiplication, pre-amplification, noise reduction, pulse-counting), each stage requires a certain amount of time, before the next pulse can be processed; (i) the voltages of the dynodes have to re-charge, (ii) the amplified signal needs to fall below the discriminator threshold, and (iii) the counting electronics need to reset. Two main types of ion detection systems exist, which differ in their behaviour in the case that another ion strikes the detector during the dead time caused by the previous pulse: In paralyzable systems, the second pulse will be detected, but it creates a new dead time, which thereby extends the dead time of the first pulse. In nonparalyzable systems, the second pulse will not be detected and hence, the duration of the dead time after the first pulse is always constant. In this work, a nonparalyzable ion detection system is used, which had been tested in previous experiments.[137]

The dead time is an individual instrumental characteristic and it has to be determined specifically for each SEM. In practice, SEM are regularly exchanged when their lifetime is exceeded and it is laborious to re-determine the actual dead time after each exchange, for which several methods exist.[138] In order to avoid this, the ICP-MS instrument control software used in this work (Qtegra ISDS by Thermo Fisher Scientific) allows to specify a virtual dead time in the advanced detector settings. This virtual dead time is to be set reasonably close to the expected technical dead time, but in lieu of the correct value it can be chosen to be slightly higher. Since the dead times of SEM of the same series should be similar, the chosen dead time value should match most SEM that are installed into the mass spectrometer. In this case, the pre-set value for the detector dead time was 40 ns. This value can be used by the vendor software to mathematically correct for the ion signal loss during the dead time.

The home-built µsDAQ and nanoDAQs sample the detector signal directly at the discriminator stage, at which point the data has not been processed by the vendor software in any way and consequently, no dead time correction is applied to the sampled signal. For the µsDAQ, a fitting dead time correction approach has been described elsewhere, although it has not been incorporated into the routine data processing tool yet. This approach statistically considers the loss of ions during the assumed detector dead time τ at a certain experimentally determined count rate

R_{exp}. This count rate can then be used as a correction factor for the obtained sum of counts per dwell to calculate the true count rate R_{true}.[137] But as demonstrated above, the expected number of counts per dwell time during a nanoDAQ measurement is mostly 0 and never exceeds 1 count, which prohibits a 1:1 implementation of the µsDAQ dead time correction to the nanoDAQ.

Pulse Pile-Up. The probability that two ions strike the detector during one sampling interval of 2.2 ns is extremely low, as has been demonstrated above. However, two ions may strike the detector during the dead time of 40 ns with a considerably higher probability at high counts rates (*i.e*. during the detection of an ion cloud with a high ion density). The first ion will trigger the dead time of a nonparalyzable detection system and hence, the second pulse will not be counted. Nevertheless, both ions that strike the detector will create analog pulses that are transmitted to the amplifier and comparator/discriminator. If the signals of both pulses overlap (pile-up), the observed signal pulse is a convolution of both individual pulses. The convoluted pulse may be considerably broader (*i.e.* longer) and more intense (*i.e.* have a higher voltage maximum) than one individual pulse, if there is a certain temporal gap between the incident of the two ions. At the comparator/discriminator stage, the convoluted pulse signal intensity may fall below the set threshold later than after the signal produced by a single ion, which would results in a broader logic output pulse.

Conventional data acquisition systems for SEM with dwell times in the millisecond or even in the microsecond range are not affected by this pulse broadening due to pulse pile-up of two or more ions. The situation might be different, however, if the sampling rate is in the same order of magnitude as the duration of an individual pulse, which is the case for both nanosecond DAQs used in this work. As a consequence of the Nyquist-Shannon theorem, the sampling interval for a transient signal has to be less than half as long as the transient signal itself in order to sample at least one data point per analog pulse.[139] In the context of pulse-counting with the nanoDAQs, it is necessary that exactly one data point is sampled per pulse. To ensure this requirement is met, the pulse-counting signal of the SEM (behind the comparator/discriminator system) is transmitted to the nanoDAQ sampling electronics *via* a bustransceiver. Aside from signal transmission and maximum voltage reduction, this bustransceiver is used to adjust the width (duration) of a typical logic pulse so that, in combination with the constant sampling interval of 2.2 ns, in theory exactly one data point is sampled per pulse.

The analog signal broadening due to the convolution of several ions, however, could lead to a broader peak width of the output pulse, if the settings of the bustransceiver are not optimized for the broader convoluted pulse widths. Hence, the output pulse may be sampled twice by the high frequency sampling system, which would consequently acquire two data points per logic pulse.

The second data point that is counted by the nanoDAQ would be formally acquired within the detector dead time, which is only triggered after the convoluted pulse has already passed the SEM's detection system. Unfortunately, the number of convoluted pulses (incident ions) cannot be derived from the number of acquired data points, because the resulting convoluted peak width depends not only on the number of coinciding pulses, but also on the temporal gap between their arrival (which is neither constant nor known). *E.g*., the incident of a third ion might only result in an increased maximum signal intensity (*i.e*. higher voltage), but not in the further broadening of the convoluted peak width. At this point, pulse pile-up is not considered to affect the data acquisition with the system that was used in this work. However, future studies should include experimental set-ups to test and evaluate the occurrence of pulse pile-up in the measurement raw data.

3. Experimental Section

Based on:

A. Schardt, J. Schmitt, C. Engelhard, Single particle inductively coupled plasma mass spectrometry with nanosecond time resolution, *J. Anal. At. Spectrom*., 2024, **39**, 389–400.
DOI: 10.1039/D3JA00373F.

3.1. Chemicals and materials

Throughout the study, aqueous dispersions of monodisperse, metallic nanoparticles of various sizes, surface-coatings, and shapes from different manufacturers were diluted to the desired particle number concentration for each experiment. Here, the term “particle size” always refers to the particle diameter of an ideally spherical particle. The analysis certificates of the manufacturers provide a mean diameter, which is usually determined *via* TEM analysis of a certain number of particles from a random sample of each lot, as well as the analyte element mass concentration (*i.e.* the gold mass concentration in gold nanoparticle dispersion). For the experiments in this work, the certified diameter and mass concentration were used to calculate the particle number concentration of the originally purchased NP dispersion for the desired dilution steps, always assuming ideal geometry and the bulk density of the corresponding metal. The diameters of some selected particles were re-analyzed for this work using in-house S-TEM measurements to confirm the manufacturer`s size information. Fortunately, the in-house size values were found to be within the error range of the manufacturer’s size value. Therefore, the resulting error of the calculated particle number concentrations were assumed to be negligible and the PNCs were not adjusted to the in-house S-TEM diameters to correct the dilution factors of all particle solutions.

For the method development of size calibration, number concentration calibration, ionic background evaluation, and shape analysis, 14 spherical gold nanoparticles and two spherical types of silver nanoparticles were obtained from manufacturers that supplied an analysis certificate with the samples. In addition, two certified reference materials of spherical gold nanoparticles were purchased for method validation. The exact sizes of the used particle types are listed in **Table 2**.

Gold and silver nanoparticle stock solutions. Spherical AuNP with tannic acid coating were obtained from nanoComposix (San Diego, CA, USA) with nominal sizes of 5, 7, 10, 20, 40, and 100 nm in a mass concentration of 0.05 mg mL^{-1}. Citrate-coated AuNP were obtained from nanoComposix with nominal sizes of 5, 10, 30, 50, 80, and 100 nm in a mass concentration of 0.05 mg mL^{-1} and citrate-coated AuNP with nominal sizes of 70 nm (0.05 mg mL^{-1}) and 125 nm (0.06 mg mL^{-1}) were purchased from Nanopartz Inc. (Loveland, CO, USA). Quality control material LGCQC5050 spherical gold nanoparticles with a nominal diameter of 30 nm and a certified PNC of $1.47 \cdot 10^{11} \pm 2.8 \cdot 10^{10}$ NP g^{-1} in 1 mM citrate buffer was purchased from LGC Limited (Middlesex, UK) for PNC calibration experiments. Size calibration validation was performed with the NIST reference materials 8011 from NIST (Gaithersburg, MD, USA), which is a dispersion of spherical gold nanoparticles with a certified diameter of 8.9 ± 0.1 nm.

Citrate-coated AgNP with a nominal diameter of 20 nm, 40 nm and 60 nm (0.02 mg mL^{-1}) from nanoComposix were used for AgNP size calibration and polyvinylpyrrolidone (PVP)-coated AgNP with a nominal diameter of 40 nm were used for evaluation of the method's capabilities to recognize nanoparticles in the presence of high ionic background.

Table 2. AuNP diameters as declared by the manufacturer or as determined *via* in-house S-TEM analysis.

	Vendor Declaration (TEM)	In-House Analysis (S-TEM)		
LOT	Size / nm (± SD)	Mean size / nm (± SD)	Mode size / nm (± σ)	No. of analyzed Particles
Spherical Gold Nanoparticles				
DAC1299	4.7 ± 0.7	5.4 ± 0.9	5.1 ± 0.6	165
IAD0060	5.1 ± 0.6	5.3 ± 0.8	5.3 ± 0.6	356
DAC1294	6.5 ± 0.9	7.5 ± 0.7	7.4 ± 0.7	209
EAW1123	9.1 ± 0.8	9 ± 1	9.0 ± 0.7	648
IAD0033	10.3 ± 0.9	10 ± 2	9.8 ± 0.9	950
TJC0021	18 ± 1.5	n.d.	-	-
JCL0014	30 ± 3	30 ± 3	29 ± 2	509
CWW0039	41 ± 4	n.d.		-
JLC0019	51 ± 5	48 ± 5	48 ± 5	206
KDP0021	59 ± 5	n.d.		-
11H73-12430	70 ± 3	n.d.		-
JSD0015	75 ± 10	78 ± 14	85 ± 5; 68 ± 6	242
ZYR0003	83 ± 8	83 ± 9	86 ± 7	214
JME1085	100.9 ± 12.1	96 ± 13	99 ± 8	105
SCK0012	101 ± 11	100 ± 10	105 ± 4	174
11J311-12430	125 ± 4	n.d.	-	-
LGCQC5050	32.7 ± 2.0	n.d.	-	-
NIST RM 8011	8.9 ± 0.1	n.d.	-	-
Spherical Silver Nanoparticles				
TJC0126	20.8 ± 3.0	n.d.	-	-
ECP1469 (PVP)	41 ± 5	n.d.	-	-
TJC0084	41 ± 5	n.d.	-	-
DAG3489	59 ± 6	n.d.	-	-

n.d.: not determined

Chemicals. In all experiments, nanoparticle dispersions from the manufacturer were diluted in deionized, bi-distilled water without acidification to avoid dissolution of the particles. Bi-distilled water was freshly prepared using a bi-distillation apparatus from Heraeus Holding GmbH (Hanau, Germany). All highly concentrated nanoparticle dispersions from the manufacturers are buffered to prevent agglomeration and aggregation of the particles. During the necessary dilution steps, however, the buffer concentration decreases significantly, which might promote the formation of aggregates/agglomerates. Therefore, for some experiments, tri-sodium citrate dihydrate (p.a., >99%, Carl Roth GmbH + Co. KG, Karlsruhe, Germany) was added to bi-distilled water to obtain a 1 mM citrate buffered solution. The citrate buffer was used for gold nanoparticle dilution only.

Complementary, nitric acid (70%, analytical reagent grade from Fisher Scientific, Loughborough, UK) was diluted to a 2% HNO_3 solution to rinse the ICP-MS introduction system, because the acid quickly dissolves the metallic nanoparticles and therefore minimizes the analyte carry-over and hence the total wash and analysis time.

A dissolved silver ICP-MS standard stock solution with a concentration of 1 g L^{-1} was obtained from Inorganic Ventures (Christiansburg, VA, USA) and was diluted in deionized, bi-distilled water. Contrary to common practice for ICP-MS analysis of dissolved elements, the prepared dilutions of this stock solution were not acidified prior to the measurement, because this would lead to dissolution of the AgNP, which were spiked into the dilution. Dissolved titanium ICP-MS standard stock solution with a concentration of 1 g L^{-1} was obtained from Inorganic Ventures and diluted in 2% nitric acid for elevated background experiments.

Additionally, dissolved element stock solutions with concentrations of 1 g L^{-1} from Inorganic Ventures were diluted (and mixed) and acidified with nitric acid to 2% (w/v) to prepare solutions for performance tests/verification of the ICP-MS instrument. Stock solutions of Li, Co, In, Ba, Ce, Bi, and U were mixed and diluted in deionized, bi-distilled water to prepare a multi-element solution with 1 µg L^{-1} mass concentration of each element, acidified with 1% HNO_3 (diluted from 70%, Fisher Scientific) and 0.5% HCl (diluted from 37%, Carl Roth), which is analogous to the proprietary "Thermo Fisher iCAP Tune B" tuning solution. This tuning solution was used to perform mass calibrations and to observe and optimize the $^{115}In^+$ signal intensity, the oxide ratio ($^{156}CeO^+/^{140}Ce^+$ signal intensity ratio) as well as the doubly-charged ion ratio ($^{137}Ba^{2+}/^{137}Ba^+$ signal intensity ratio).

Materials. Liquid handling throughout this work was performed using almost exclusively plastic lab ware, *i.e.* micropipettes with plastic tips for pipetting, PP centrifuge tubes for storing and dilution, PFA and FEP bottles for storage, PP cryovials for freezing, and plastic safe-lock tubes for aliquoting of the stock solutions. The use of single-use plastic lab ware was chosen to prevent adsorption of the metallic nanoparticles to the container wall (which is expected when using glass ware) and to eliminate trace contaminations from pre-used containers. Only the deionized, bi-distilled water was stored in dedicated 2.5 L glass bottles and the citrate buffer was prepared in a thoroughly cleaned 1 L glass bottle.

3.2. Nanoparticle sample preparation

According to the recommendation of the vendors, all nanoparticle stock solutions were stored in darkness due to their photosensitivity. With one exception, all stock solutions were stored in the fridge at 4 °C. Only the NIST RM 8011 was stored at room temperature (r.t.) as advised by the manufacturer. Prior to further preparation, the stock solutions were let come to r.t. and were shaken thoroughly by hand for *ca*. 30 s to loosen agglomerates.

Sample preparation for spICP-MS. The stock solutions were diluted in either deionized, bi-distilled water or in citrate-buffered water. Depending on particle size, two or three dilution steps were required to obtain the desired particle number concentration (*e.g.* often 10^5 particles per mL). Dilutions were prepared in 50 mL and 15 mL PP centrifuge tubes. The final dilution step was calculated to yield 10 or 15 mL of sample volume, because each of the two sample racks of the ICP-MS autosampler can hold up to 60 of the 15 mL centrifuge tubes, which was necessary for the analysis of large sample series. Prior to the spICP-MS analysis, all diluted samples were shaken again and then placed onto the sample rack. The measurement was started as quickly as possible after sample dilution to prevent dissolution of the particles (due to exposure to light), agglomeration, or sedimentation in the tube. However, the longest analysis series took about 6 h of total measurement time and it could not be excluded that the last measured samples were subject to irradiation-induced dissolution. But since the data acquisition with the home-built systems µsDAQ and nanoDAQ (MK1 and MK2) has to be started manually for each individual sample, it was practically not feasible to start an automated analysis sequence and to dilute parts of the NP stock solutions during the measurement of the previous part. Therefore, sedimentation was prevented as well as possible by shaking the sample thoroughly again shortly before its analysis.

Sample preparation for S-TEM. For nanoparticle size determination *via* TEM, the stock solutions of selected spherical gold nanoparticles were directly pipetted onto TEM sample holder grids and dried before the measurement. Gold nanoparticles with sizes of 51, 75, 83, 100.9 and 101 nm (vendor specification) were each pipetted onto an individual 300 mesh nickel grid sample holder with a perforated carbon film (Plano GmbH, Wetzlar, Germany). The grid had been placed on a paper tissue to absorb any excess liquid that flows from the surface of the grid. Particles with sizes of 4.7, 5.1, 6.5, 9.1, and 10.3 nm were pipetted onto an ultrathin lacey-C-film on a 300 mesh gold grid sample holder (Plano GmbH), because it was assumed to adsorb smaller particles more efficiently than conventional grids. This should facilitate the search for a sufficient number of particles for a statistically significant size distribution determination. The grids were covered against contamination with dust and then air-dried over night before the TEM analysis.

3.3. Environmental water sampling campaign

The analysis of surface and waste water was implemented in this work as a feasibility study for the detection of nanoparticles with the nanoDAQ spICP-MS system in real water samples. Sample collection was performed as a part of another study on the total concentration of several relevant elements in the water samples.

For this thesis, water samples with a respective volume of 500 mL from each of 30 different points of interest in the area of Siegen were collected during a period of *ca*. 24 h. This sampling scheme was chosen to provide a quick screening of the nanoparticle content and composition in connected water bodies in a defined area and a short time period. The data derived from these individual samples are not intended to form conclusions on long-term nanoparticle flows in the water bodies nor to calculate reliable nanoparticle concentrations in the total water volume at a certain sampling site.

Sampling locations. Surface water samples from different rivers and streams in the extended area of Siegen were sampled as well as effluent water from 10 WWTP in the same area. The largest stream of interest in this study was the River Sieg, which was sampled at several spots from its spring and downstream through several villages, industrial areas, and the Siegen City area. Furthermore, confluences of other waterways were chosen as strategically important sampling sites, as well as spots upstream and downstream of WWTP discharges into the stream. The sampling points and their coordinates are listed in **Table 3** and marked on the map in **Figure 10**. Additionally, the effluent of the WWTP was collected inside the plant at the end of the complete water treatment process, but before the discharge into the designated surface waterway.

A field blank of deionized, bi-distilled water was filled in a 500 mL PFA sampling bottle and was stored and analyzed identically to the real samples for quality control of the method.

Table 3. Description and coordinates of water sampling sites displayed in Figure 10.

Sample I.D.	Site Description	Water body (discharge)	Coordinates
SW01	Sieg spring	Sieg	50.918081, 8.246354
SW02	DS of Sieg/Werthenbach CF, US of WWTP Netphen-Deuz	Sieg	50.881902, 8.140958
SW03	DS of WWTP Netphen-Deuz	Sieg	50.907452, 8.110900
SW04	DS of Obernau dam	Obernau	50.917182, 8.132928
SW05	DS of Sieg/Netphe CF, US of WWTP Netphen	Sieg	50.913000, 8.094296
SW06	DS of WWTP Netphen	Sieg	50.908871, 8.064891
SW07	US of WWTP Netphen-Eckmannshausen	Dreisbach	50.919339, 8.072805
SW08	DS of Sieg/Dreisbach CF	Sieg	50.908717, 8.035527
SW09	DS of Ferndorf/Zitzenbach CF, US of WWTP Hilchenbach-Ferndorftal	Ferndorf	50.958752, 8.027225
SW10	DS of WWTP Hilchenbach-Ferndorftal	Ferndorf	50.956352, 8.023019
SW11	US of Ferndorf/Littfe CF, US of WWTP Kreuztal	Littfe	50.956610, 7.990448
SW12	DS of WWTP Kreuztal	Ferndorf	50.951967, 7.989254
SW13	US of Sieg/Ferndorf CF	Ferndorf	50.895348, 8.023251
SW14	DS of Sieg/Ferndorf CF, US of WWTP Siegen-Weidenau	Sieg	50.889692, 8.025289
SW15	DS of WWTP Siegen-Weidenau	Sieg	50.886806, 8.025001
SW16	US of WWTP Wilnsdorf-Rinsdorf	Heckebach	50.824774, 8.053965
SW17	DS of WWTP Wilnsdorf-Rinsdorf	Heckebach	50.826443, 8.051120
SW18	US of WWTP Siegen	Sieg	50.850751, 7.992534
SW19	DS of WWTP Siegen	Sieg	50.850879, 7.991424
SW20	Ferndorf spring	Ferndorf	51.002145, 8.158924
WW-A	WWTP Netphen-Deuz	Wüste Beienbach (Sieg influent)	-
WW-B	WWTP Netphen	Sieg	-
WW-C	WWTP Netphen-Eckmannshausen	Dreisbach	-
WW-D	WWTP Hilchenbach-Ferndorftal	Ferndorf	-
WW-E	WWTP Kreuztal	Ferndorf	-
WW-F	WWTP Kreuztal-Buschhütten	Ferndorf	-
WW-G	WWTP Siegen-Weidenau	Sieg	-
WW-H	WWTP Wilnsdorf-Rinsdorf	Heckebach	-
WW-I	WWTP Siegen	Sieg	-
WW-J	WWTP Wilnsdorf-Niederdielfen	Weiß	-
FB	Field Blank		-

SW: surface water, WW: waste water, DS: downstream, US: upstream, CF: confluence, WWTP: waste water treatment plant

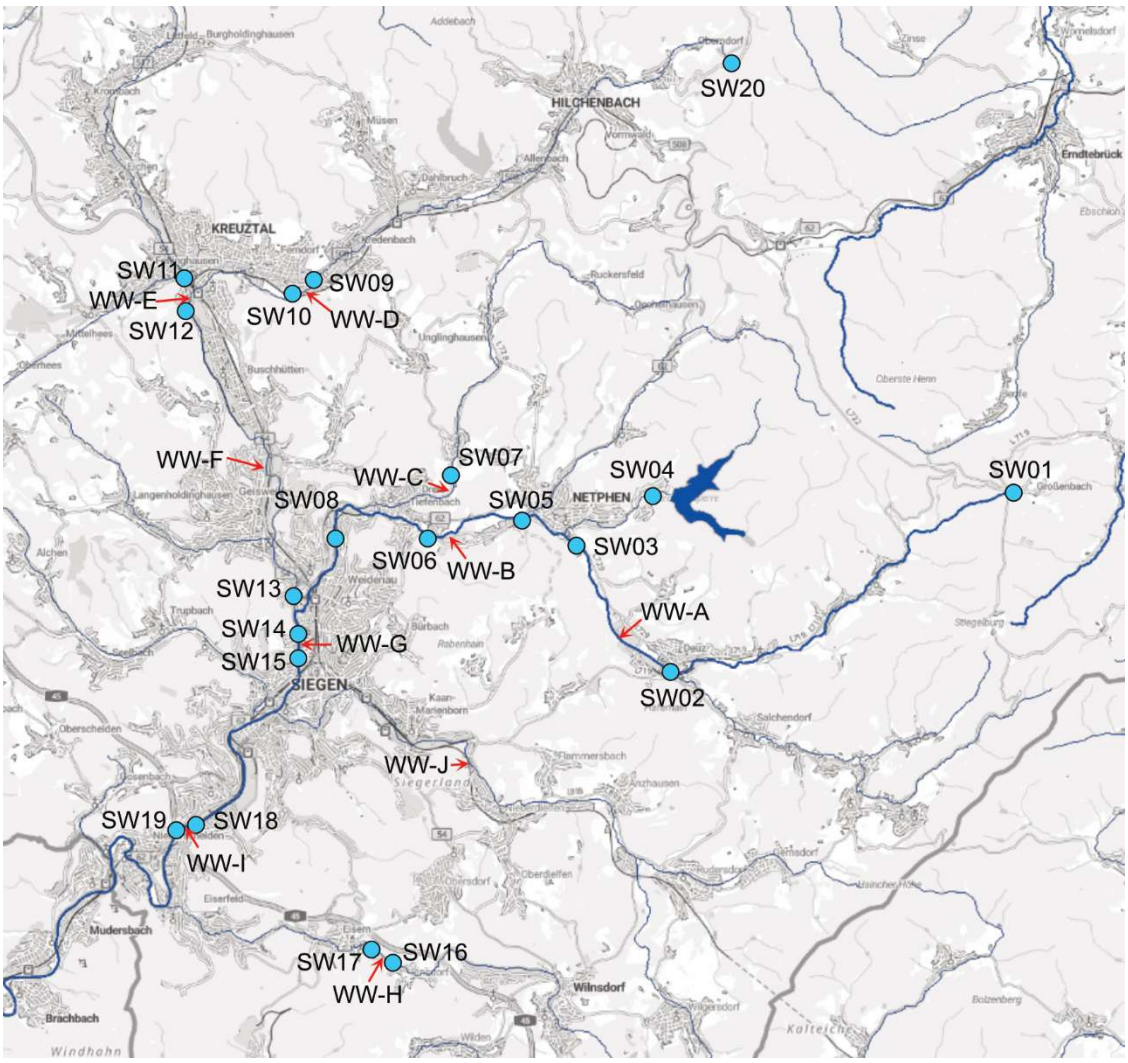


Figure 10. Schematic map showing the main waterways (dark blue) in the extended area of Siegen, the surface water sample locations (SW, cyan circles), and the points of waste water treatment plant discharges (WW, red arrows). The waterway map was taken from the website "Geoportal der Bundesanstalt für Gewässerkunde.[140] Sampling site coordinates were identified with Google Maps and visualized in Affinity Designer (V 1.10.4.1198).

Sampling Procedure. All surface water samples were collected on June 21, 2022. WWTP effluent samples were collected on the same day, except for effluents from WWTP Wilnsdorf-Niederdielfen and Wilnsdorf-Rinsdorf, which were sampled on the following day, June 22, 2022. On both days, it was sunny weather without rainfall, which at least excluded massively different conditions of the water bodies through dilution with rain water during this period.

At sampling sites which were easily accessible, *i.e.* the Sieg and Ferndorf springs, samples were filled directly into 500 mL PFA bottles (Savillex, LLC, Eden Prairie, MN, USA) after rinsing the bottle three times with sample water. At the other less accessible surface water sites, a sampling pole with an attached 1 L plastic beaker was first rinsed thrice with sample water and was then used to transfer the sample into the (also rinsed) PFA storage bottle. Effluent water of the WWTP was

sampled on the morning of June 21, 2022 (or June 22, see above) by the on-site staff, who were instructed to rinse the bottles similarly and to store them in the fridge until collection. All bottles were stored in a cooler box during transit time on the sampling days.

Sample Storage. After collection, subsamples for single particle analysis were refilled into 100 mL FEP bottles (Savillex) for storage in the fridge at 4 °C and for intermediate analysis, and additional aliquots were filled into two 5 mL and one 15 mL PP cryogenic tubes (Thermo Fisher Scientific) and frozen in liquid nitrogen for long-term storage in the freezer at -18 °C. Samples were frozen two days after collection and stored in the freezer. They were analyzed *ca*. 2.5 years after sample collection with the new nanoDAQ data acquisition software, which had just been completed by that time.

Sample Preparation. Frozen samples were slowly thawed overnight in the fridge. They were shaken to homogenize the sample liquid and *ca*. 10 mL were aspirated with a syringe (B. Braun, Melsungen, Germany) and filtered through a 0.45 µm pore size syringe filter with regenerated cellulose membrane into a 15 mL centrifuge vial for spICP-MS analysis. All surface and waste water samples prepared in this way were analyzed without further dilution or addition of any acid or internal standard.

3.4. Scanning transmission electron microscopy

Scanning transmission electron microscopy for size distribution determination of selected AuNP was carried out in high-angle annular dark-field imaging (HAADF) mode on a Talos F200X (former FEI, now Thermo Fisher Scientific, Bremen, Germany). Several images per sample were taken with a combined total number of at least 100 particles per size. The images were exported as PNG files to be further processed with the public domain software ImageJ Fiji.[141] The following workflow is visualized in **Figure S1** (Appendix). In Fiji, a color gradient threshold value was set to create black and white images from the original gray-scale S-TEM images. This was done to enable the automated shape recognition tool, which analyzes the spatial distribution of color contrasts and thereof derives the depiction of ellipses (here: the top down view on nanoparticle spheres) in the black and white image. After setting a threshold value for the circularity (because the AuNP do not, in fact, exhibit a perfect spherical shape), the software marks the calculated circumference of each recognized particle and additionally provides its area and diameter. This method of particle recognition bears the issue of over- or underestimating of the mean particle diameter, because both the choice of threshold for the black and white image creation is subjective, as well as the threshold for the circularity. The first factor influences the boundary, at which a gray-scale pixel is

displayed in white (particle signal) or black (background signal) in the processed image, which ultimately artificially broadens or narrows the calculated particle diameter. The circularity threshold determines the inclusion or exclusion of particles into the statistics depending on their shape. If, for example, many large particles exhibit a more circular shape than the smaller particles, the derived particle size distribution is falsely shifted to larger sizes, because the smaller particles do not contribute to the size distribution. Nevertheless, this automated process enabled the analysis of several thousands of particles in a reasonable amount of time, and it was taken care to optimize the threshold values as thoroughly as possible to minimize distortions of the size distribution. Additionally, the majority of the particles had a decent circular shape and few geometrical deviations were observed, which was taken as justification for the use of the above described method for images with many (*ca*. more than 25) particles. An alternative method is to manually determine the diameter of each nanoparticle in the original image (without setting of a color threshold), which is less prone to systematic underestimation of the diameter but much more elaborate and was therefore only used for images with less than *ca*. 25 particles.

A list of all detected particles and their diameters was exported to determine a size distribution for each AuNP size sample. For this purpose, two approaches were carried out. On the one hand, the list of particle diameters was imported into Origin 2017 (OriginLab Corporation, Northampton, MA, USA) and the “column statistics” tool was used to calculate average diameters of all particles and their standard deviations. On the other hand, particle size histograms were created for each size, to which a Gaussian function was fitted to obtain the mean particle size and the standard deviation. Both math functions yielded similar results within the respective error margin (see **Table 2**). Exemplary S-TEM images of 9.1 nm, 75 nm, and 83 nm AuNP are shown in **Figure S2** and represent the diverse image quality, which is a challenge for reliable NP size distribution determination. Nevertheless, sizes determined *via* in-house TEM analysis agree with the certified sizes from the manufacturer within the provided error margins (**Figure S3**), except for the 6.5 nm AuNP, for which the error margin was exceeded by 0.8% (average size value).

3.5. Single particle ICP-MS

3.5.1. Instrumentation and settings

Single particle ICP-MS experiments were performed on a model iCap Qc ICP-Q-MS (Thermo Fisher Scientific, Bremen, Germany). The instrument was controlled and tuned using the vendor software Qtegra ISDS (V 2.10.3324.131, Thermo Fisher Scientific). Semi-automated sample introduction was enabled by the ESI SC-2 DX autosampler (ESI Elemental Service & Instruments GmbH, Mainz, Germany). It was used for individual sample aspiration and rinsing, however, fully-automated sequence runs could not be triggered yet by the coupled home-built data acquisition system. A MicroFlow PFA-ST pneumatic nebulizer (Thermo Fisher Scientific) with a nominal flow rate of 100 µL min^{-1} was evaluated to be the most suitable nebulizer for fast and straightforward spICP-MS experiments. It is not as prone to clogging as *e.g.* the DS-5 nebulizer with flow rates of *ca*. 10 µL min^{-1},[65–67] but still can be operated on relatively low flow rates of *ca*. 100–400 µL min^{-1}, which is crucial for a high transport efficiency.[142] The Peltier-cooled quartz cyclonic spray chamber was operated at 3 °C. To increase instrument sensitivity, the high-sensitivity skimmer cone insert "2.8" (Glass Expansion, Melbourne, Australia) was used in combination with the nickel skimmer cone.

The sample flow rate and nebulizer gas flow rate were carefully optimized to find a compromise between high signal intensity, low oxide and doubly-charged ion ratio. Additionally, the nebulizer gas flow rate and RF generator power were specially tuned for the detection of nanoparticles, because the ionization efficiency of the solid particles is strongly dependent on the plasma parameters. For most experiments in this work, the nebulizer gas flow was set to 0.58 L min^{-1}, the sample was set to 165 ± 1 µL min^{-1} (determined gravimetrically), and the plasma power was set to 1450 W.

Another factor that influences the ionization of particles in the plasma is the distance of the plasma torch end to the sampler cone inlet, which with our system has proved to yield good results at the lowest possible distance (sampling position) of 1 mm. Voltages of the extraction lenses 1 and 2 were 0 V and -154 V. A second roughing pump had previously been attached to the vacuum outlet of the instrument *via* a high vacuum T-piece to achieve a reduced interface pressure of *ca*. 1.4 mbar, because a low interface pressure was shown to be beneficial for NP detection.[64] Argon (5.0, Messer Industriegase GmbH, Siegen, Germany) was used as nebulizer gas, auxiliary gas (0.8 L min^{-1}), and cooling gas (14 L min^{-1}).

3.5.2. Band pass mass filter settings to increase sensitivity

As a default, the iCap Qc ICP-MS is operated with "normal mass resolution", which provides unit mass resolution. However, as suggested by Meyer *et al*.[133], the sensitivity for a specific *m*/*z* value can be improved by lowering the mass resolution of the quadrupole. This beneficial effect is caused by the increased ion transmission of analyte ions within a certain *m*/*z* range through the quadrupole (*cf*. Chapter 2.2.3). If the isotope of the element of interest is not interfered by isobaric atoms or molecules, their signal intensity can be significantly enhanced by this approach, and the method is even more effective for poly-isotopic elements, because the signal intensity of all isotopes within the selected *m*/*z* range is cumulated.

For this work, the effect of decreased mass resolution was tested on AuNP (monoisotopic, *m*/*z* = 197) and AgNP (di-isotopic, *m*/*z* = 107 and 109). Two default mass resolution settings of the iCap Qc instruments are available for routine operation, namely "normal" and "high" mass resolution. The Qtegra software does, unfortunately, not provide direct control of the slope and offset of the mass scan line in the Mathieu diagram. However, extended parameter settings allowed the manual manipulation of the quadrupole voltages. In this case, the "DC Offset" voltage was lowered and the resulting signal intensity and peak width of continuous $^{115}In^+$ and $^{238}U^+$ ion signals were observed, because In and U are contained in the Tune solution and the masses are close to those of Ag and Au. The DC offset voltage was decreased from -109 V (default) to -189 V. The peaks widths widened from *ca*. $\Delta m/z$ = 0.6 to 1.2 ($^{115}In^+$) and from *ca*. $\Delta m/z$ = 0.5 to 1.0 ($^{238}U^+$). A voltage of -159 V provided 21% signal intensity increase for $^{115}In^+$ (+61% for $^{238}U^+$) and was chosen for further tests with gold and silver nanoparticles. Comparison of the number of detected particles during a set time span and the average number of detected atoms per particle confirmed that the low mass resolution (DC offset = -159 V) setting lead to higher ion transmission. For AuNP, which consist of monoisotopic gold atoms, the effect was moderate. Compared to the default setting, 6% more particles and 9% more ions per particle were detected in the low mass resolution mode. Although the mass peak width was not lowered enough to include both isotopic peaks of Ag completely, the signal enhancement on $^{107}Ag^+$ was significant. The low mass resolution mode enabled detection of 30% more ions per particle. Here, 6% fewer particles were detected during the run time as in the measurement employing normal resolution. This effect, however, might also be caused by slight inhomogeneity of the particle suspension or variations or the sample flow rate, which is a known source of error for (single particle) ICP-MS. The number of detected ions per particle is not influenced by these parameters. The DC offset voltage of -159 V was eventually used in experiments, which aimed to achieve lowest possible size detection limits for AuNP.

The lowered mass resolution was not applied during the analysis of surface water samples, because those were designed to provide a quick screening of nanoparticles in a broad mass range and the reduction of mass resolution would require careful examination of possible interferences on all analyte masses. For the surface water screening, the analyte ions $^{47}Ti^{+}$, $^{90}Zr^{+}$, $^{107}Ag^{+}$, $^{140}Ce^{+}$, and $^{208}Pb^{+}$ were successively analyzed in each sample.

3.5.3. Single particle ICP-MS data acquisition

In this work, data was acquired using three different spICP-MS data acquisition systems; namely the previously described microsecond data acquisition system (µsDAQ)[64] and two novel systems that acquire nanosecond time-resolved data[69]. The first version, nanoDAQ MK1, is mainly based on the µsDAQ hardware but achieves a dwell time of 4.2 ns (240 MHz sampling rate). Its successor nanoDAQ MK2 comprises a new board with a higher sampling frequency, more RAM, and a USB 3.0 connection. Because of the improved hardware, the nanoDAQ MK2 features a continuous acquisition of ICP-MS signals with a sampling rate of 520 MHz. This sampling rate would theoretically lead to a dwell time of 1.9 ns, however, experimental determination of the integration window resulted in a value of 2.2 ns. For further calculations, 2.2 ns was therefore used as the actual dwell time. The main method development part of this work was performed with the nanoDAQ MK1, while Chapter 4.3 is dedicated to a comparison of both nanosecond time resolution systems. The environmental water application study was carried out on the MK2.

All three data acquisition systems sample logic pulses behind the SEM's comparator/discriminator system, which requires the SEM to be operated in "pulse-counting mode". To that end, the "counting threshold" was to a maximum value of *ca*. 65 000 in the software. This prevents the detection system from switching to the "analog mode", which is designed to protect the SEM from damage at high ion currents. In practice, the gate electrode between the analog and pulse-counting output electrodes has to remain closed even at high count rates.

If the pulse-counting output signal of the SEM exceeds a specified threshold value at the time the signal is captured by the nanoDAQ, the software assigns this data point with the value 1. This usually occurs, if an individual ion hits the first SEM dynode and an output signal is produced at the pulse-counting output. This process and the recorded signal are denoted as detector event (DE) throughout this thesis. The alternative case is the recording of electrical noise without detection of an actual ion. If the SEM output signal intensity is below the specified threshold during nanoDAQ acquisition, the data point will be assigned with the value 0.

However, the integration intervals of both nanoDAQ versions are shorter than the SEM detector dead time, which was by default set to be 40 ns in the instrument control software (based

on an estimate of the real detector dead time). The dead time, during which no signals can be processed by the SEM electronics, starts again after each ion event. Hence, even if two or more ions hit the detector during this interval, the nanoDAQs should not record any detector events until the end of the dead time. One consequence to consider is that naturally the number of recorded detector events during a certain time span will not be proportional to the actual number of ions striking the SEM above a certain ion flux.

Upon inspection of the nanoDAQ MK1 raw data, successive detector events within an interval shorter than 40 ns were observed quite often. It was hypothesized that this phenomenon was caused by reflection of the electric signal pulses in the high-frequency cables within the experimental setup in combination with non-optimal settings of the bustransceiver. The bustransceiver transmits signal pulses above a manually set threshold to the signal processing chip of the respective DAQ and is mainly tuned to transmit every logic pulse of the comparator/discriminator. However, another important function of the bustransceiver is to prevent signals with high amplitudes from damaging the DAQ hardware. Reflection of one detected pulse may have led to the false detection of an additional signal by the DAQ, which had not been caused by an incident ion. As a consequence, the high-frequency signal acquisition of the nanoDAQ MK1 probably produced several successive data points with the value 1. These data points were therefore falsely labelled as detector events. Implications of this effect for the resulting particle size determination will be discussed. The data obtained from the successor nanoDAQ MK2 showed significantly fewer of those false detector events, which might be related to the different connection of the data acquisition units in the experimental setup (**Figure 11**). In future studies, experimental set-ups should by varied to asses whether reflected pulses indeed cause the observed artifacts or if pulse pile-up might contribute to the phenomenon, as well. The effect of pulse reflection on the data of the µsDAQ was not evaluated, because the sampling rate (dwell time of 5 µs) is too low to observe data points within the dead time of 40 ns.

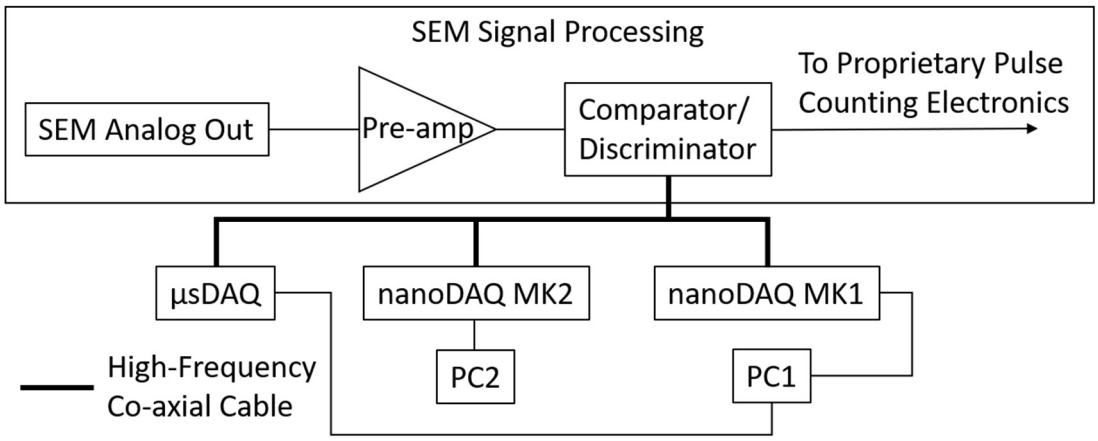


Figure 11. Schematic depiction of the experimental measurement set up for parallel data acquisition with three data acquisition systems and subsequent data storage on two different PCs. The digital pulse output signal was sampled by connecting the DAQs with a high-frequency cable. The signal was split by two different T-pieces to be acquired all three DAQs. Both the cable length and the number of branches might influence the occurrence of electronic signal reflection within the set up. Depending on the magnitude of this effect, the acquired signal might vary significantly from the true signal that was output by the SEM. The wiring of the three DAQs is not symmetrical, which probably causes a varying extent of the reflection among the systems.

For selected comparative measurements, two or three data acquisition systems were operated simultaneously, which had been enabled by two T-piece connectors between the high-frequency cables of the systems. Measurement starts with all systems had to be triggered manually, but the total run time could be set in advance. Mostly, it was sufficient to start all systems sequentially very quickly within a second (which was done on two separate computers), because the short time deviations would not influence the size or particle number concentration results of a 30 s (or 20 s) analysis noticeably. However, some experiments were designed to compare the ion cloud signals of identical ion clouds amongst the DAQs. For this purpose, operation of the SEM was first switched off in the instrument control software, so that no signal was recorded at the detector output at all. Then, data acquisition of all home-built DAQs was triggered to start (recording only electrical noise). Quickly hereafter, the instrument control software was used to switch on the SEM again. This procedure made sure that, while continuously aspirating a nanoparticle dispersion, theoretically the first detected ion cloud signal of all DAQs corresponds to the identical particle (as do all following ion clouds).

For most method development experiments, a total acquisition time between 15 and 30 s was sufficient, but especially the analysis of smaller nanoparticles required longer acquisition times of 60 s, because they consist of fewer atoms (**Figure S4**). An acquisition time of 30 s was chosen for real water samples to achieve a balance between sensitivity and sample throughput. Only one isotope was chosen for analysis for each element. The mechanism of the quadrupole mass analyzer

sets the condition that only one *m/z* ratio at a time can be observed for single particle ICP-MS analysis (*cf*. Chapter 2.2.3). Therefore, all isotopes of interest were analyzed successively during aspiration of each sample. After every sample, the introduction system was rinsed thoroughly for at least 1 min for real water samples or until no more particles could be detected in the live monitor for highly concentrated AuNP and AgNP dispersions.

3.5.4. Single particle ICP-MS data processing

Data processing of the novel nanosecond time-resolved data differs greatly from the processing of the previously described microsecond time-resolved data or the commonly known data obtained with millisecond dwell times. The development of a processing strategy and the evaluation of the derived information are the main part of this current work and will be explained in detail in the results and discussion part.

Specialized software was employed to process the data at different stages. The “raw data” obtained from the nanoDAQs is not to be confused with the raw signal from the SEM. The latter is transmitted by a bustransceiver, which slightly narrows the pulse width, and is subsequently sampled with the respective frequency (*i.e*. dwell times of 4.2 ns or 2.2 ns). The pulse-counting system provides data points with a time stamp and either the value 0 (no pulse) or 1 (pulse). It does not provide information on pulse duration or amplitude, neither does it produce output values higher than 1. This file can be opened with the Binary Viewer (V. 6.17.4.26, ProXoft LLC.) for quick visualization. Another software had been written to identify and extract ion signals from the raw data, which lowers the resulting file sizes immensely. This converted file could then be imported into Origin for further statistical analysis and graphical representation.

For high-throughput analysis, automated recognition of nanoparticle signals in the raw data is essential. Such a software had been developed specially for the new structure of the nanoDAQ data. In this work, the particle-by-particle analysis results from this new software were compared with figures of merit that were obtained from manual identification of ion clouds in the pre-processed data files.

3.5.5. Statistical analysis of variance

The significance of variations between groups of data points was tested for comparison of the duration, number of DE, and the ion detection efficiency among the three data acquisition units. Data groups were first tested for Normal distribution with the Kolmogorov-Smirnov test and

quantile-quantile plots (Q-Q plots). If the data points in all groups showed Normal distribution, the significance of the variance of their mean values was tested with the t-test (between two groups) or the ANOVA (among three groups). If the data points in one or more groups showed no Normal distribution, the significance of the variance of their median values was tested with the Mann-Whitney-U test (between two groups).

4. Results and Discussion

Chapters 4.1 and 4.2 are based on:

A. Schardt, J. Schmitt, C. Engelhard, Single particle inductively coupled plasma mass spectrometry with nanosecond time resolution, *J. Anal. At. Spectrom*., 2024, **39**, 389–400.
DOI: 10.1039/D3JA00373F.

In the following subchapters, the custom data acquisition systems with nanosecond time resolution for spICP-MS will be presented. Method development for the systems was performed with the use of model AuNP and AgNP suspensions with known particle sizes and (mostly) estimated particle concentrations. A suitable developed workflow for processing the raw data will be explained and discussed (**Figure 12**), as well as figures of merit for nanoparticle analysis capabilities and current shortcomings of both the method and the data treatment. Because the nanoDAQ MK1 had been revised during the course of this thesis, the performance of the new version with even higher time resolution and eliminated signal artifacts (nanoDAQ MK2) will be compared to the first prototype (MK1). In addition, a software developed by Johannes Schmitt[69,70], which includes an algorithm for automated particle identification, was tested and compared to results obtained from manual identification of identical, individual particles. The new nanoDAQ system with automated ion cloud recognition was implemented for the nanoparticle detection in environmental waters in the course of a field study in the area of Siegen. The validity and practicability of the current method for the application of NP analysis in environmental water samples will be assessed based on the results of this field study.

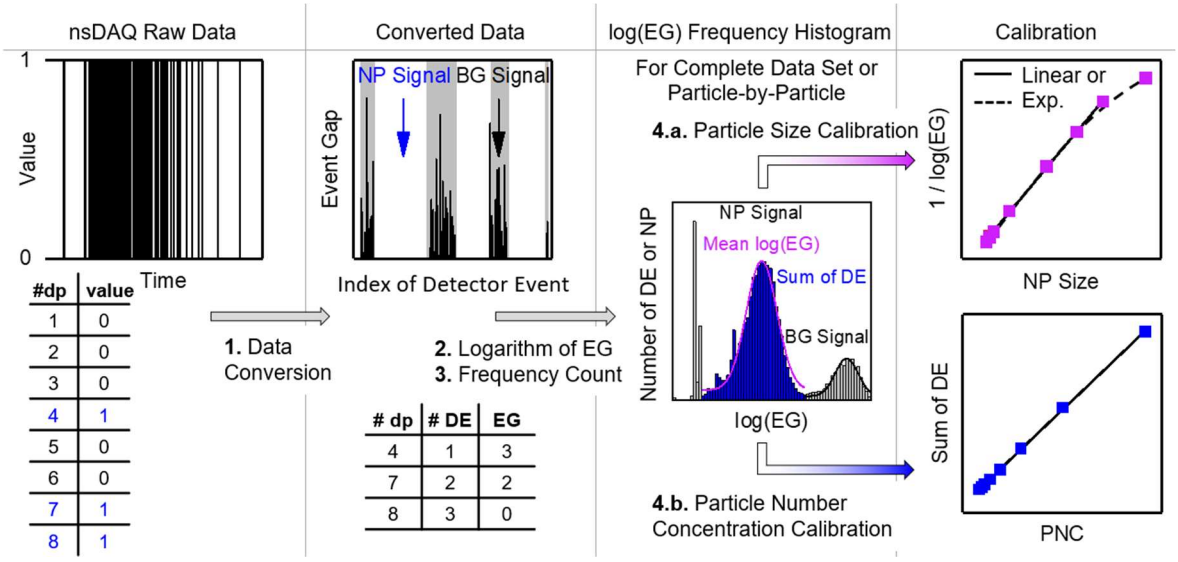


Figure 12. Workflow diagram for the processing of nanosecond time-resolved spICP-MS data. **1**. The nanoDAQ raw data is converted to remove data points (dp) with the value "0" and labels each detector event (DE) with the respective event gap (EG). **2**. The logarithm of the EG is calculated to obtain log(EG). **3**. The log(EG) values are binned and a frequency count is performed to create a histogram. **4.a** The inverse mean log(EG) of a Gaussian fit (purple curve) to the particle signal distribution in the histogram is used for size calibration. **4.b** The sum of DE of the particle signal distribution (blue) is used for particle number concentration calibration. Figure reprinted from Schardt *et al*. *J. Anal. Atom. Spectrom.* 39 (2), **2024**, 389–400.[68]

4.1. Structure of nanosecond time-resolved spICP-MS data

The data that was obtained from nanosecond time-resolved spICP-MS differs considerably from the data that is usually acquired with millisecond or microsecond dwell times (*cf*. Chapter 2.1.2). Therefore, the structure of the transient signals that were acquired and pre-processed by the nanoDAQ MK1 will be described and visualized in the following.

Only data points with 1 and 0 counts can be obtained with the nanoDAQ, which should be reliable according to Poisson statistics (*cf*. Chapter 2.2.4). Here, a value of 0 counts indicates that no detector event occurred during the dwell time, while a value of 1 is considered the result of an ion hit onto the detector (or that dark counts/electrical noise were recorded). Continuous signal acquisition of 30 s duration creates a data file containing *ca*. $7 \cdot 10^8$ dp, which corresponds to a file size of roughly 680 MB. Even during the analysis of ion clouds with temporarily high analyte ion densities, detector events are well spaced out on the nanosecond time scale and the majority of dp have the value 0 (*cf*. Chapter 2.2.4).

4.1.1. Binary viewer

Raw data of the nanoDAQ is visualized in this work with a binary viewer program (**Figure 13**). The acquired binary data, which is a succession of 0 and 1 (bits), is shown as bytes (8 bits) by the binary viewer program for visualization purposes. Depending on the value of each byte, its representative pixel in the graph is assigned with a customized colour. Here, each byte with a value of 0 (no DE) is represented by a white pixel and each byte with a value other than 0 (*i.e*. one or up to 8 DE) is represented in blue. The first dp of the data set is in the upper left corner, subsequent dp are shown as pixels from left to right to complete a row and the data rows fill down from top to bottom to the last dp. When the analyte ion density in the plasma is low, ions that emerge from the mass analyzer region are very likely to hit the SEM spaced out in time. Such temporal gaps will appear as a white space in the display. Contrarily, analyte ions arrive at the detector in quick succession over a limited time span if the analyte ion density is high. In spICP-MS, regions in the data display with a temporarily high density of blue pixels (*i.e*. representing DE) can be safely assumed to originate from the detection of an ion cloud with the SEM. Display settings can be changed to view a succession of ion clouds (**Figure 13A**) or to zoom into a singular ion cloud **Figure 13B**) by choosing how many bytes should be binned for one logical pixel.

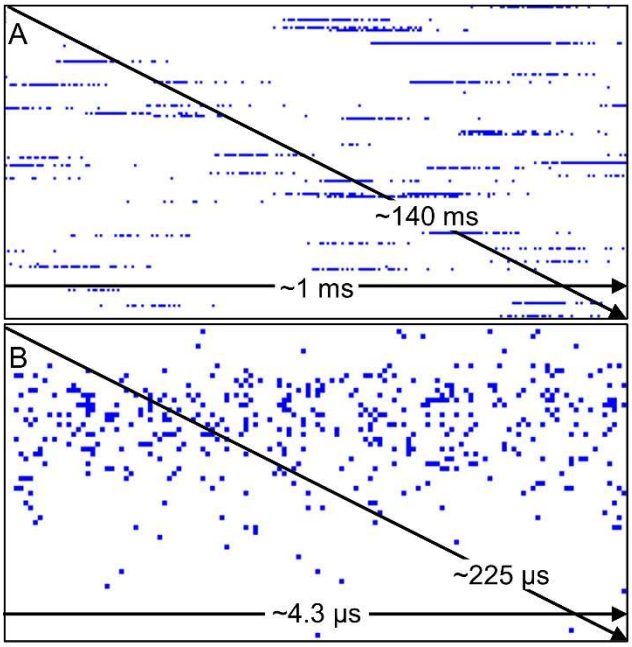


Figure 13. Simplified visualization of spICP-MS data of a dispersion of 41 nm AuNP with nanosecond time resolution (nanoDAQ MK1) with a binary viewer program. A. Several ion cloud signals during ~140 ms of acquisition. B. DE in one individual ion cloud during ~225 µs data acquisition. Note: Each blue logical pixel represents a byte with a value unequal to 0 (1 or more DE), each white logical pixel represents a byte with the value 0 (no DE). Figure reprinted from Schardt *et al*. *J. Anal. Atom. Spectrom.* 39 (2), **2024**, 389–400.[68]

In both representations, similarities can be observed between this data and transient signal profiles of ion clouds that were produced from colloids in an ICP with microsecond time-resolved analysis. In µs-spICP-MS, if an appropriate amount of data points across a peak is available, one typically observes a mass-to-charge number (m/z) signal trace with a fast "rising edge", *i.e*. the ion density in space increases rapidly until a maximum is reached, which then gradually tails off to the background level. With nanosecond time-resolved analysis, it was similarly observed that the SEM pulse density in time, *i.e.* the density of DE in **Figure 13**, seems to correlate with the ion density in space upstream the mass analyzer. Here, earlier studies using time-resolved measurements of particles and single droplets are helpful to understand these transient signals. Transient ion cloud signal profiles have been described earlier by Stewart and Olesik via experiments and simulations.[132] In their study, they introduced individual droplets containing dissolved Li^+ or Pb^+ (or both) into the ICP via a monodisperse dried microparticulate injector (MDMI) to investigate space-charge effects of Pb^+ ions on Li^+ ion detection in ICP-MS. The authors describe two major processes that determine the observable ICP-MS signal intensity trace profile, *i.e*. diffusion of ions in the plasma and their mass dependent acceleration through the ion optics. They analyzed the transient signals of Li^+ ion traces from droplets (~60 µm diameter) containing only 100 µg mL^{-1} dissolved lithium in 2% HNO_3 (to exclude matrix effects from Pb^+) and observed asymmetrical peak shapes

with a mean full width at the base of the peak of 344 ± 7 µs. Stewart and Olesik explain the asymmetry of the peak shape with results from simulations of the spatial ion concentration at the MS sampling orifice and experimental measurements of transient ICP-MS signal traces. They demonstrate that the signal intensity at the sampling orifice as a function of time depends on the initial analyte ion concentration in the droplet, the diffusion coefficient of the analyte ion in the plasma, and the total time the ion cloud spends in the plasma (which is determined by the distance between the point of vaporization and the sampling orifice, as well as the plasma gas flow velocity). The spatial ion concentration at the MS orifice is relatively dense shortly after vaporization and, in turn, the detected analyte signal intensity is high at the rising edge of the peak. However, the maximum of the signal peak is reached before the spatial center of the ion cloud passes the orifice, because the continuous diffusion leads to a steady 3-dimensional extension of the ion cloud and, consequently, a decrease of ion density. A continuously decreasing spatial ion concentration at the orifice is observed in the tailing of the signal intensity peak. Both simulated and measured ion cloud signal traces in Stewart and Olesik's study support the assumption that the data visualized with the binary viewer shows signals that originated from nanoparticles. Further evidence to support this was obtained by additional data processing, which is explained in the next sections.

4.1.2. Transient data

The number of successive dp with a value of 0 (0 counts) between two DE is proportional to the time gap between the two respective detector events. Further in the thesis, this will be referred to as "event gap (EG)". If the dwell time (4.2 ns) and other SEM settings are kept constant throughout an experiment, multiplication of the observed EG with the dwell time provides transient information on the gap between two DE (*e.g.*: an EG value of 1000 would correspond to a lag of ~4 µs between two ion impacts at the detector).

Acquired ns-spICP-MS data files are usually too large to be adequately processed with common data processing software as, for example, Origin and Excel. Therefore, a custom data processing software for ns-spICP-MS was developed that compresses the file size by removing all dp with the value 0 but preserving the timing information. Specifically, each individual dp with a value of 1 is now labelled with the number of preceding 0s as ordinate (*i.e*. the numerical value of the EG) and with its consecutive number of dp (#dp) in the data set as abscissa (*i.e*. the timing information). In the following example the pulse-counting raw data consisting of 8 dp would be converted to 3 dp in the new following format: raw: (1,0); (2,0); (3,0); (4,1); (5,0); (6,0); (7,1); (8,1) → converted: (4,3); (7,2); (8,0). The factor of data compression depends on the number of DE in the

data file, because only the dp with 0-values are removed, *i.e*., the higher the analyte ion concentration, the larger the processed file size.

The converted data can be imported into Excel or Origin for further processing, for which there are several options: One possibility for data visualization is to plot the dp value (1 or 0) versus the absolute measurement time, which is obtained by multiplication of the sequential number of the DE in the data set with the dwell time, as described above. The resulting graph resembles the structure of a barcode. Processed transient data of 60 s analysis of a AuNP dispersion with the nanoDAQ is shown in Figure 14**A**, while Figure 14**B** shows a zoom into a time window, during which an individual ion cloud was detected. Note that the line thickness in these graphs gives the impression as if most of the dp would represent DE, which is, in fact, not the case (*cf*. **Figure 13**). However, what can be readily observed in this type of visualization of individual ion clouds is in accordance with observations that were made earlier with microsecond time-resolved ICP-MS: the pulse count (resp. ion beam density) is high at the temporal "front" of the detection window and declines towards the "back", *i.e*. what would be the trailing edge of an ion cloud peak in a more customary visualization of microsecond time-resolved data. [64,65,130,132,137]

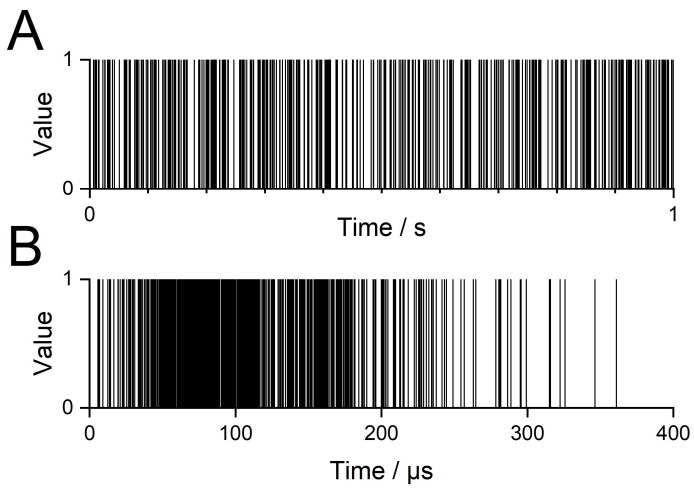


Figure 14 A. Transient signal of 1 s of measurement of a suspension of 59 nm AuNP. **B**. Transient signal of a singular ion cloud from an individual 59 nm AuNP in the same measurement. The ion cloud duration is approx. 360 µs. Figure adapted from Schardt *et al*. *J. Anal. Atom. Spectrom.* 39 (2), **2024**, 389–400. [68]

4.1.3. Event gap transient plots

An alternative data visualization approach compared to the one above is to plot the EG versus the sequential number of the DE **Figure 15A**). Here, sections on the x-axis with DE that show high EG values correspond to the background (BG) signal and sections with low EG values indicate the detection of an ion cloud with high analyte ion density (short temporal gaps between DE). The sections of the x-axis in **Figure 15B** that correspond to the background appear spatially "narrow" in

the plot, because DE occur rarely at low ion densities and few data points are extracted from the raw data files (raw data files contain all acquired data points with the values 0 or 1 of the complete measurement, while extracted data only contains the EG between DE). Sections that correspond to time spans, during which ion clouds were detected, are spatially "broader" on the abscissa in the plot, because each ion cloud consists of a large number of ions and many dp correspond to DE. Please note that, in contrast, the temporal duration of the BG sections is much longer compared to the short ion cloud events. A logarithmic scale of the EG (y-axis) helps to recognize the very low EG values during particle detection alongside the high EG of the background (**Figure 15B**).

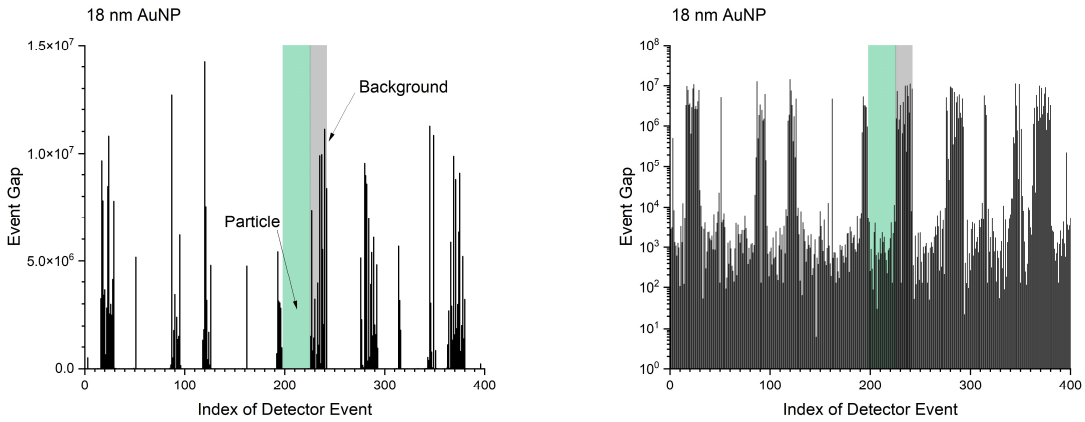


Figure 15 A. Plot of the EG (in data points, 1 dp 4.2 ns) *vs*. the consecutive number of the respective DE from the measurement of 18 nm AuNP (PNC =100 000 # mL^{-1}). The respective EG of each DE corresponds to the number of preceding data points with the value 0. Long EG between DE correspond to continuous BG with a low temporal ion density entering the detector (area highlighted in gray). Ion clouds from small colloids have higher temporal ion densities and, therefore, the gaps between detected ions are shorter (area highlighted in blue). **B**. Logarithmic scale on the y-axis enhances the visibility of the short EG. Figure adapted from Schardt *et al. J. Anal. Atom. Spectrom.* 39 (2), **2024**, 389–400.[68]

4.1.4. Event gap histograms

Because the described approach allows to qualitatively differentiate between background signal and particle signals, the EG data was further processed to obtain characteristics that can be utilized for quantitative NP size determination. A frequency histogram of the entire data set was created to distinguish between the two data populations with either high or low EG values. However, the resulting histogram of EG *vs*. DE does not show two clearly separated signal populations, but simply confirms that most of the dp have low EG values (**Figure S5A**).

We found, however, that a frequency histogram of the logarithm of the event gap (log(EG)) indeed allows to distinguish between a particle signal population (short log(EG)) and a background signal population (long log(EG)) (**Figure 16**). This visualization will be used further below in the

manuscript. Here, it is important to note that this style of representation is in contrast to typical spICP-MS size distribution data, in which the background signal is on the left and the particle signal is on the right. Also, the frequency histograms in this work are constructed from all detector events, so they only represent the merged information on ions from all nanoparticles (which was at this stage due to limitations in the data processing software, see Chapter 4.3 for particle-by-particle analysis). Hence, the mean log(EG) value of the NP signal population represents the mean temporal gap between two ions arriving at the detector, averaged over all ion clouds during the entire measurement. The calculation of the size resolution capability of the method is therefore not applicable.

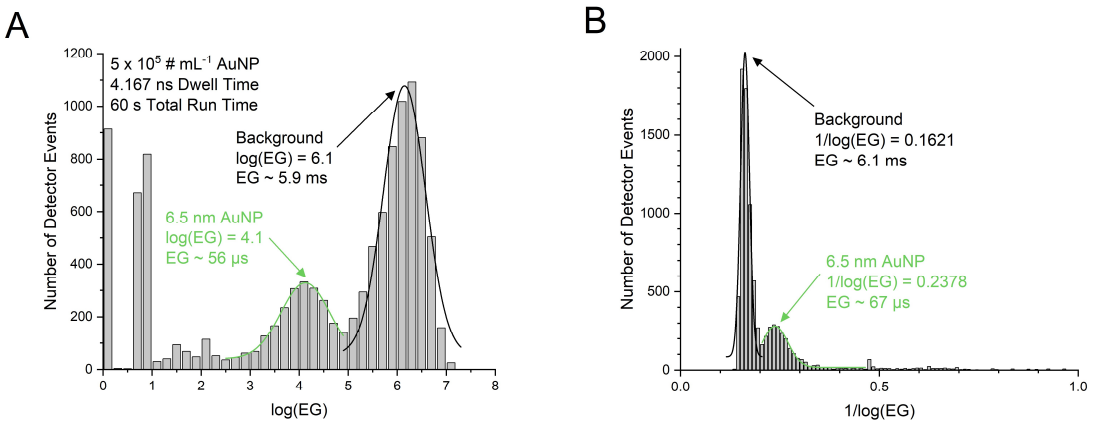


Figure 16. Histogram of the frequency of detector events *vs*. the logarithm of the event gap (log(EG)). In the bimodal distribution, the right peak with longer event gaps between detector events (avrg. ~5.9 ms) corresponds to the background (black) while the left shoulder with a shorter mean event gap (~56 µs) corresponds to ions from 6.5 nm AuNP (blue). Figure adapted from Schardt *et al*. *J. Anal. Atom. Spectrom.* 39 (2), **2024**, 389–400. [68]

4.2. Capabilities of nanoparticle characterization with the nanoDAQ MK1

4.2.1. Size calibration

We successively analysed dispersions of AuNP with different sizes and processed the nanosecond time-resolved data as described above. The nanoDAQ system in combination with decreased mass resolution allowed to distinguish signals from AuNP as small as 6.5 nm from the background in combination with a commercial single quadrupole ICP-MS (**Figure 16**). Signals from particles with a size of 4.7 nm were also detected but the separation from the background signal was considered to be not sufficient (**Figure 26B**).

Because of these promising results above, the mean log(EG) value of the particle population (Gauss fit) was calculated for each particle size and this showed that the mean log(EG) is inversely proportional to the particle size (**Figure 17A**). Ion clouds from small particles show a higher mean log(EG) than large particles, *i.e*. the mean time gap between two DE in an ion cloud from a small particle is longer. Smaller particles require less energy for complete vaporization, atomization, and ionization than larger particles and consequently, their ion clouds start to diffuse earlier in the plasma, which decreases their spatial ion density (in addition to broadening effects downstream). When an ion cloud with a low spatial ion density emerges from the mass analyzer, this results in the detection of ions with long temporal gaps between them. Based on this and the observation of the EG values one likely explanation is that the mean spatial ion density in ion clouds from small particles is lower at the detector than in ion clouds from large particles (assuming no other contributing factors such as space-charge effects, ion focusing *etc*.). Moreover, it was derived empirically that the correlation between inverse log(EG) (1/log(EG)) and original particle size (provided by the manufacturer) is linear over a range from 4.7–75 nm ($R^2 = 0.998$) and may, therefore, be a novel approach for NP size calibration (**Figure 17B**).

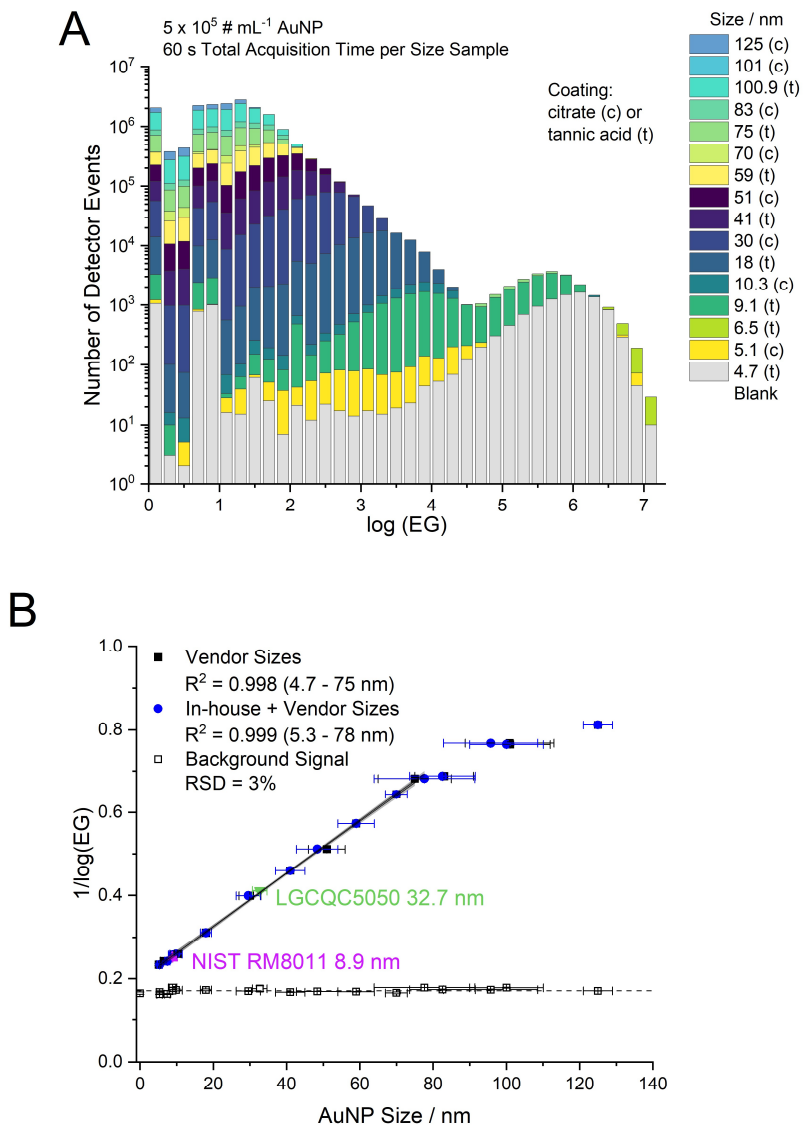


Figure 17 A. Frequency histograms of the logarithm of the event gap (log(EG)) of the individual measurements of AuNP with 16 different sizes and an approx. PNC of 10^5 # mL^{-1} and a blank solution. NP sizes as declared by the manufacturer. Please note the logarithmic scale on the y-axis. **B**. Plot of AuNP size versus the mean inverse logarithm of the event gap of 16 AuNP size standard solutions (black squares: Vendor sizes, blue circles: in-house TEM or vendor sizes) and two certified reference materials (NIST RM 8011: 8.9 nm; LGCQC5050: 32.7 nm). Mean values of three repetitive measurements (60 s) per size are shown. The x-error bars correspond to the SD of the particle size and the y-error bars indicate the SD of 1/log(EG) from three repetitive measurements. The mean inverse logarithm of the event gaps of the background signal distribution is independent of the particle size and varies by an RSD of ± 3% among the 17 samples (hollow black squares). Figure adapted from Schardt *et al. J. Anal. Atom. Spectrom.* 39 (2), **2024**, 389–400. [68]

The size calibration was validated by comparing the certified sizes of two CRMs to the sizes calculated with the calibration curves obtained from both the vendor sizes and the in-house determined mean sizes (**Table 4**). In both cases, the size deviation is well below10% for the small NIST RM with a diameter of 8.9 nm and for the medium-sized LGCQC5050 with a diameter of

32.7 nm. The relative standard deviation among three repetitive measurements during one experiment is 0.3% for the small particles. For the size determination of the LGCQC5050 particles, mean 1/log(EG) values of four separate solutions with four different particle number concentrations prepared from the same batch were used. Despite the varying PNC, the RSD does not exceed 0.3%, which showcases the robustness of the 1/log(EG) value for size determination.

Table 4. Validation of size calibration (linear fit calibration) with certified reference materials (RM).

	Vendor Calibration		In-house + Vendor Calibration	
	Size ± SD / nm[c]	Relative percent difference to RM	Size ± SD / nm[c]	Relative percent difference to RM
NIST RM8011 8.9 ± 0.1 nm[a]	8.3 ± 0.3	-7%	8.3 ± 0.3	-7%
LGCQC5050 32.7 ± 2.0 nm[b]	33.6 ± 0.1	+3%	33.3 ± 0.1	+2%

a. n = 3 repetitive measurements of the same sample, b. n = 4 different dilutions from the same batch. c. Arithmetic mean values of n measurements ± standard deviation (SD) of the mean.

The qualitative considerations on the relationship between particle size and average event gap of the corresponding detected ion clouds have been described. However, no mathematical rationale behind that linear correlation was found at this point. In the present work, a flattening of the size calibration curve above particle sizes larger than 75 nm was observed. In order to investigate the cause of this non-linearity, in-house S-TEM measurements of the nanoComposix particle standard solutions were conducted to confirm their sizes. We found that all of the analyzed batches are in agreement with the vendor´s specifications within the given error range (**Table 2**, **Figure S3**), which is why it was decided to use the vendor sizes for further calculations throughout the following sections of this work. It can be concluded that most probably the underestimation for larger particle sizes in the calibration curve stems from short lags during data acquisition, which were observed to occur both periodically and irregularly and statistically affect the detection of larger particles more than the detection of smaller particles. If ions from an ion cloud are not detected, the recorded event gap between the preceding and the subsequent ion artificially increases and the inverse log(EG) for size calibration is underestimated. In addition, a dead time correction approach that was already successfully used with the µsDAQ was not yet incorporated into the nanoDAQ.[137]

As mentioned before, Duffin *et al*. reported results from spICP-MS measurements with nanosecond time resolution with a multicollector detection system and showed that they were able to perform particle size calibration with the obtained data.[124] Their results resemble ours with respect to the limited linear dynamic range, but due to the higher sensitivity of the multicollector

they already observe a flattening of the size calibration curve above a AuNP size of 20 nm, which they attribute to pulse pile-up. With a time resolution of 0.5 ns, the group was able to determine the time difference between two incident ions (in this work referred to as “event gap”), as well. They used this timing information as a parameter for a boxcar-based algorithm that determines the beginning and the end of an ion cloud to enable particle-by-particle analysis. In contrast to the approach in this thesis, Duffin *et al*. do not use the time difference/ event gap information itself for the particle size determination, but instead use the cumulated number of detected counts per particle.

4.2.2. Particle number concentration calibration

When the particle size and the mass flow rate are kept constant, the number of DE can be used to perform a particle number concentration calibration (**Figure 18**). Because these two factors (particle size and PNC) co-dependently influence the sum of DE of the particle signal population, the mean particle size of an unknown sample should first be determined according to the mean log(EG) as described above. The mean log(EG) is not affected by the PNC and only varies by ± 3% among the analysis of LGCQC5050 30 nm AuNP with different PNC.

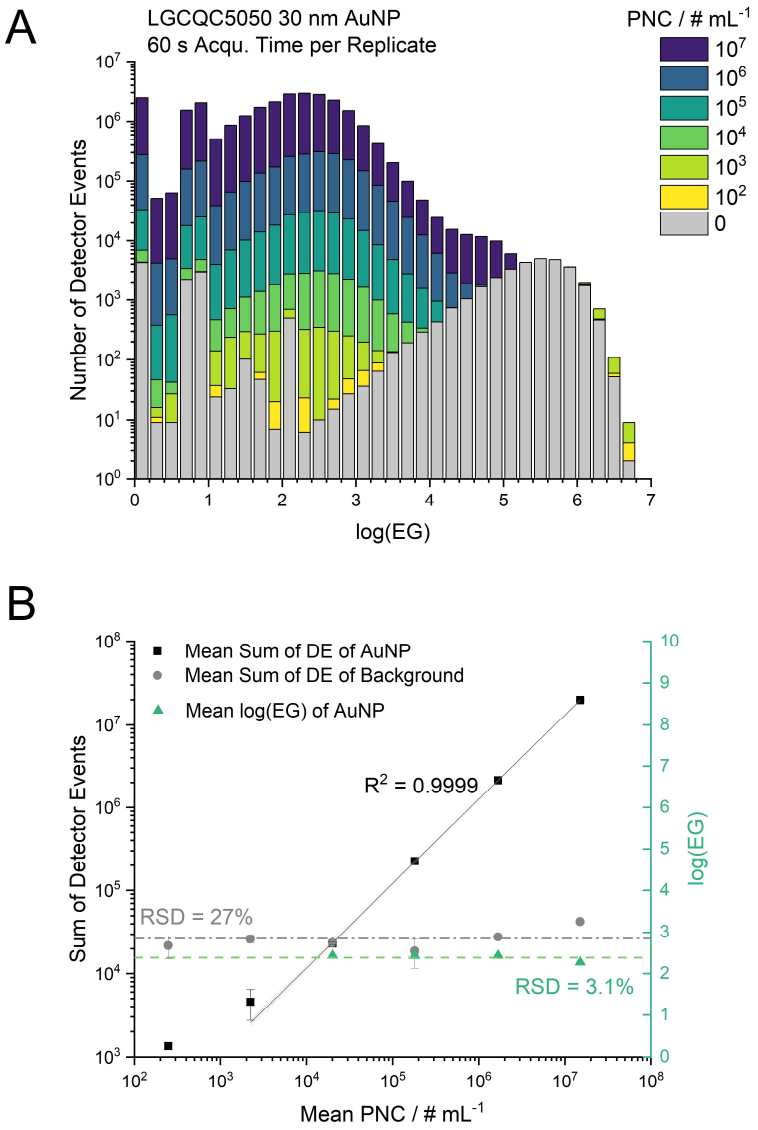


Figure 18. A. Frequency histograms of the logarithm of the event gap (log(EG)) of the individual measurements of 30 nm AuNP (LGCQC5050) with six different particle number concentrations and a blank sample (not shown in logarithmic plot). PNC [# mL^{-1}]: a. $(1.509 \pm 0.003) \cdot 10^7$, b. $(1.677 \pm 0.003) \cdot 10^6$, c. $(1.804 \pm 0.001) \cdot 10^5$, d. $(2.003 \pm 0.001) \cdot 10^4$, e. $(2.227 \pm 0.001) \cdot 10^3$, f. $(2.475 \pm 0.001) \cdot 10^2$, g. 0. Please note the logarithmic scale on the y-axis. B. The sum of detector events correlates linearly with the PNC between 10^3–10^7 # mL^{-1} (black squares), while the mean log(EG) remains constant throughout the measurement of six different PNC (3.1% RSD, green triangles). The sum of DE corresponding to the background distribution varies within ± 27% among the different PNC samples (gray circles). Mean values of 3 replicates are shown and error bars correspond to the standard deviation. Figure adapted from Schardt *et al. J. Anal. Atom. Spectrom.* 39 (2), **2024**, 389–400. [68]

4.2.3. Elevated ionic background

In environmental water samples it is to be expected that the background signal intensity of the analyte element is higher than in bi-distilled, deionized water. It is therefore important to test the NP analysis method's capability to detect NP in the presence of an elevated ionic background. Here, 40 nm AgNP were used as a model particle and were spiked into solutions with concentrations of dissolved silver between 0 and 7.5 µg L^{-1}. The particle distribution is only visible in the presence of 0, 0.01, and 0.05 µg L^{1} spiked Ag^{+} solution (**Figure 19A**). In the presence of higher concentrations, the particle signal is overlapped by the dissolved analyte signal. The mean log(EG) of the Ag^{+} distribution decreases exponentially (second order exponential decay) with increasing concentration because the temporal distance between the ions decreases (**Figure 19B**). As expected, the mean log(EG) of the particle distribution is not affected, because the ion density inside the ion clouds likely does not change in the presence of matrix in the sample medium. However, the chosen model particles already have a relatively large diameter of 40 nm and expected silver concentrations in environmental samples may be significantly higher than 0.05 µg L^{-1}. For example. In a previous study, a total concentration of 0.21 ± 0.05 µg L^{-1} dissolved silver was found in the influent of a WWTP in Austria.[47] Because the data processing of the nanoDAQ raw data does not distinguish between ions from particles and background, both signal distributions overlap significantly at higher background. While this processing method is not fit for purpose for environmental analysis at this stage yet, a particle-by-particle analysis approach is tested later (*cf*. Chapter 4.4) for its capability to solve this issue.

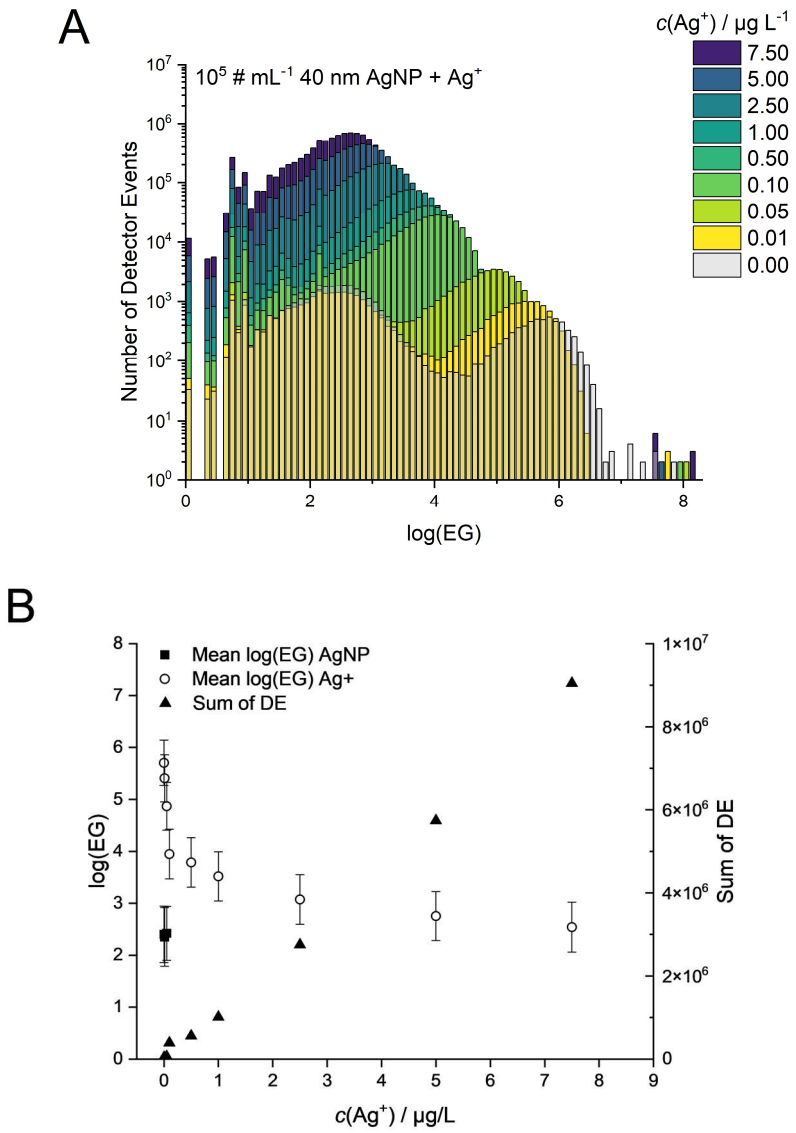


Figure 19 A. Frequency histograms of the logarithm of the event gap (log(EG)) of the individual measurements of mixtures of 40 nm AgNP with increasing concentration of spiked Ag^+ solution. **B**. Plot of the mean log(EG) of particle and dissolved analyte distribution *vs*. the Ag^+ concentration. Error bars indicate the FWHM of a Gaussian fit curve to the respective signal distribution (AgNP or dissolved Ag^+) in the histogram. The sum of total DE increases linearly with increasing Ag^+ ion concentration. Data was acquired with a dwell time of 4.2 ns and a total measurement time of 30 s.

4.2.4. Mixtures of particles with different sizes

Mixtures of AuNP with two different sizes with a PNC ratio of 1:1 were analyzed with the nanoDAQ to assess the methods capability to characterize more complex nanoparticle samples. As already outlined above, the log(EG) histograms obtained from the nanoDAQ data show the merged log(EG) values of all ions that were detected during the entire acquisition time. Results from the measurement of test mixtures confirm that the created log(EG) frequency histograms show a convolution of the event gaps between ions in the ion clouds from both types of particles, as well as the BG signal distribution (**Figure 20**). However, the log(EG) distributions are relatively broad in general, because the event gap is not even constant during the detection of one ion cloud (*cf*. **Figure 14**). As shown above, the ion density in an individual ion cloud is high at the rising edge (low EG) and decreases towards the end (high EG). Therefore, each ion cloud creates a respective distribution of log(EG) values, and the measurement of many ion clouds creates a cumulated distribution of log(EG) values. The range of log(EG) values from measurements of monodisperse particle solutions ranges from *ca*. 1–5.5 (*ca*. 40 ns–1.3 ms), which means that the distributions of all particle sizes overlap. Because smaller particles produce orders of magnitudes less ions than larger particles, the amplitudes of the log(EG) distribution of small particles are much lower than those of larger particles. Therefore, the mean of the log(EG) distribution of a suspension with small particles has a lower y-axis value than from a suspension with larger particles. Consequently, the resulting distribution of a 1:1 mixture of small and large nanoparticles mostly resembles the distribution of the larger particles, except for the fact that the amplitude of the maximum is *ca*. half as high due to the dilution. It is not possible to recognize a third log(EG) maximum of a peak shoulder between the log(EG) of the larger particles and the blank distribution. The issue might be solved to some extend by increasing the particle number concentration of the smaller particles and to ensure a large size discrepancy between the two different types, which would severely impede the applicability of this approach to unknown samples.

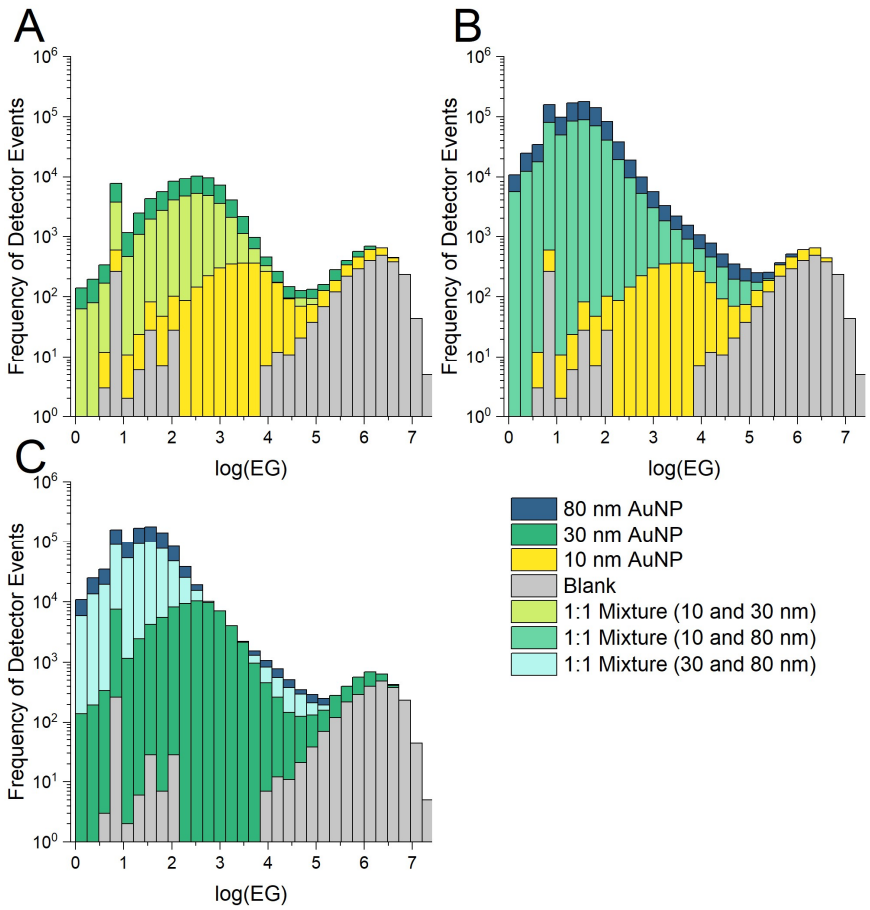


Figure 20. Frequency histograms of the logarithm of the event gap (log(EG)) of the individual measurements of AuNP with two different sizes and a PNC of 10^5 # mL^{-1}, a 1:1 mixture of the two respective samples, and a blank measurement. **A**. Measurements of a mixture of 10 and 30 nm AuNP, as well as individual size samples and a blank. **B**. Measurements of a mixture of 10 and 80 nm AuNP, as well as individual size samples and a blank. **C**. Measurements of a mixture of 30 and 80 nm AuNP, as well as individual size samples and a blank. Figure adapted from Schardt *et al*. *J. Anal. Atom. Spectrom.* 39 (2), **2024**, 389–400.[68]

4.3. Figures of merit of improved nanoDAQ MK2

In Chapter 4.2, the capabilities of spICP-MS with nanoDAQ MK1 were described and carefully evaluated. Specifically, the system provides a novel type of data of ion clouds from nanoparticles and the event gap between detector events was introduced as an additional parameter for nanoparticle sizing. However, some issues were recognized during the measurements that compromised the acquired data. Specifically, periodic and random lags during data acquisition and signal artifacts compromised the method's size calibration capability.

Consequently, a next generation DAQ system, nanoDAQ MK2, was developed by Johannes Schmitt to address some of the limitations of MK1.[69] The second prototype was designed to address the signal artifacts. In addition, software and hardware were refined to ensure continuous acquisition as well as to provide improved time resolution of 2.2 ns (versus 4.2 ns with MK1).

4.3.1. Artifacts in histograms of complete datasets

During the use of the prototype nanoDAQ MK1, it became apparent that gaps occurred during data acquisition in constant as well as random intervals. Additionally, strings of data points with event gaps shorter than 40 ns were frequently observed in the raw data, which should be impossible due to the detector dead time.

At a detector sampling rate of 4.2 ns of the nanoDAQ MK1, after each detector event, a pause of at least *ca*. 10 data points should follow (*e.g.*: 1000 0000 0001 0000 0000). Despite that technical limitation, sequences of data points with shorter event gaps were observed in the raw data, *e.g.*: 1101 0000 1000 0000 0001. In this example, the event gap between the first two detector events is "0", the EG between the second and third detector event is "1", the event gap to the next DE is "4", and the last EG is "10". The corresponding log(EG) values are "not valid", "0", "0.6", and "1.0". In the presented log(EG) histograms from the nanoDAQ MK1, the distribution of log(EG) below 1 is significant (**Figure 21A**), which introduces a bias to the Gauss curves that are fitted to log(EG) distributions, especially of larger nanoparticles. This issue may be corrected mathematically by excluding all data points with event gaps below 40 ns. However, this would lead to the exclusion of the first (true) detector event, and if this phenomenon would occur very often but irregularly during the analysis of an ion cloud, the exclusion of a large percentage of ions would distort the log(EG) histograms and hamper the size determination.

The above described observations are assumed to be symptoms of the reflection of electrical signal pulses in the high-frequency cables of the experimental set up for parallel data acquisition with three DAQs. Depending on the number of branches and cable length by which each

DAQ is connected to the pulse-counting output port, the magnitude of the signal reflection effect might vary (*cf*. Chapter 3.5). The effect appears to increase at high count rates during the analysis of ion clouds with high ion densities.

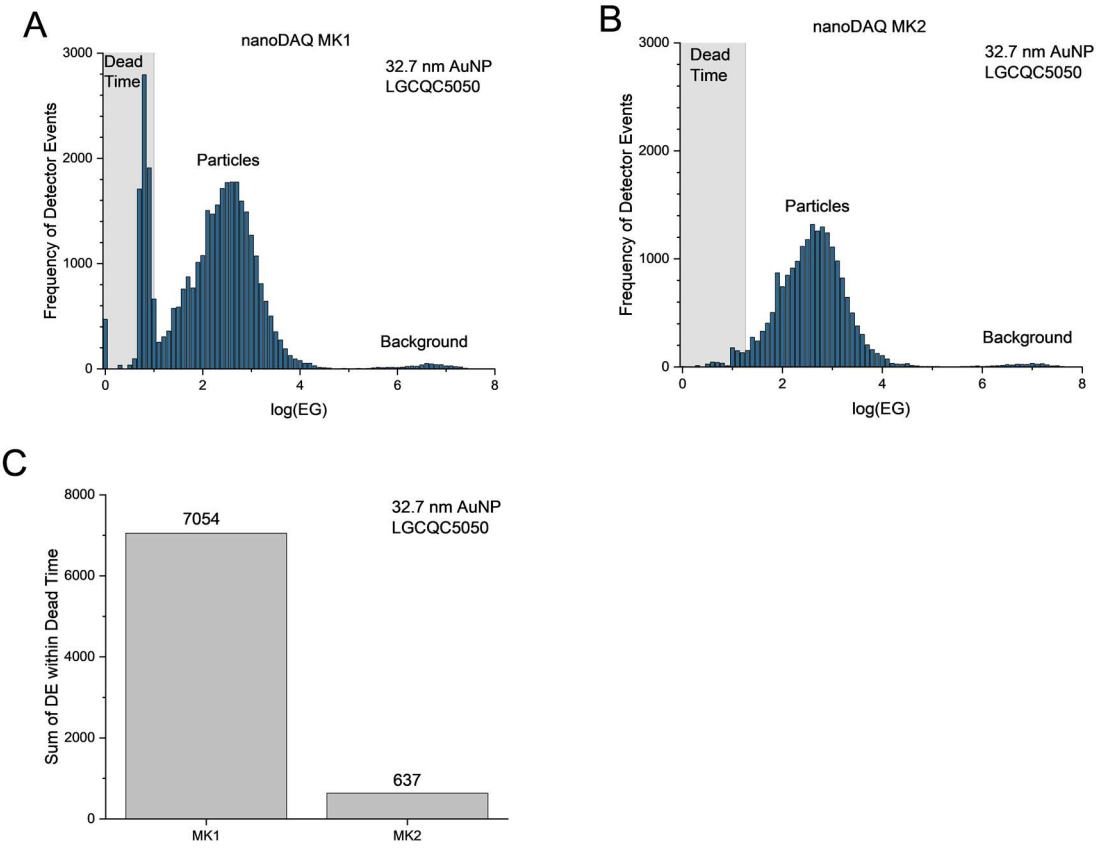


Figure 21. **A**. and **B**. Frequency histograms of the logarithm of the event gap (log(EG)) of 32.7 nm AuNP from simultaneous acquisition with the nanoDAQ MK1 and MK2. **C**. Comparison of the sum of detector events (DE) detected during the detector dead time of 40 ns in the data sets from A and B (MK1: log(EG) = 0–0.9, MK2: log(EG) = 0–1.2).

The data acquired with the improved nanoDAQ MK2, however, shows a significantly reduced distribution of DE within the detector dead time of 40 ns, which correspond to *ca*. 18 data points at a time resolution of 2.2 ns (**Figure 21B**). The sum of detector events within the dead time during 30 s of total analysis time of 30 nm AuNP with simultaneous data acquisition *via* nanoDAQ MK1 and MK2 was determined. By acquisition with the improved nanoDAQ MK2, the sum of detector events within the dead time was reduced by 91% (**Figure 21C**). The cause for the remaining false positives will be discussed in Chapter 4.4.5.

4.3.2. Ion detection efficiency in individual ion clouds

To achieve the goal of lowering the particle size detection limit in spICP-MS, it is crucial to provide the highest possible ion detection efficiency (DE_{eff}). As explained in the theory section, ions from particles are lost throughout the complete process from ionization to detection. The plasma and ion optics parameters may be optimized for each particle size to achieve maximum ion extraction, and the quadrupole mass resolution can be lowered to the same end (*cf*. Chapter 2.2.3).

However, even the data acquisition system has to be considered to avoid the non-detection of ions that actually reached the detector. Simultaneous acquisition of ions from a 30 nm AuNP suspension with microsecond (µsDAQ) and nanosecond time resolution (nanoDAQ MK1 and MK2) was performed to evaluate the influence of the data acquisition system under identical plasma and quadrupole conditions on the detection efficiency.

The identification of ion clouds and the extraction of signal profiles from the raw data is done using different pathways for the µsDAQ and nanoDAQs. The extraction of ion clouds from the µsDAQ data was described earlier. [123] In brief, a programmed shift register scans the complete data set from the first to last data point. Threshold parameters are chosen for the summed signal intensity within a certain number of data points, *e.g.* 5 data points, which corresponds to 25 µs at 5 µs time resolution. If the threshold signal intensity for the start of an ion cloud is exceeded within one shift size, the program extracts the following time and signal intensity information from the data until the summed signal intensity falls below the threshold for the end of an ion cloud.

Identification of ion clouds in the raw data from the nanoDAQs was performed manually by visually estimating the beginning and the end of each ion cloud in the Binary Viewer display of the raw data and correspondingly in the Origin list of DE *vs*. EG. Here, very long event gaps relatively clearly indicated the background in the bi-distilled water and were used as orientation point for particle beginning and end. The DE and EG data pairs belonging to each individual particle were marked and copied into an extra Origin sheet. From this, column statistics were used to count the number of data points per ion cloud.

For the following tests, 100 extracted ion clouds from identical particles were analyzed for 32.7 nm and 101 nm AuNP and 80 extracted ion clouds for 18 nm AuNP. To ensure that the ion clouds indeed stem from the exact same particle, the time between the incident of successively detected ion clouds (not individual ions) was compared. For all particles, the relative time gap between their detection matched very well among the three data acquisition systems.

For comparison, the duration of each ion cloud (start to end) was statistically analyzed for the data acquired with all three systems (**Figure 22**). The median ion cloud duration from all three

systems vary significantly, which underlines the influence of sampling rate, experimental set up and ion cloud extraction method on the reported results. Determined ion cloud duration values of 32.7 AuNP from µsDAQ data (550 µs) are ca 66% longer in duration (+218 µs) compared to nanoDAQ MK1 data (332 µs) and *ca*. 29% longer in duration (+123 µs) compared to nanoDAQ MK2 data (427 µs). Both ion cloud extraction methods (subjective visual estimation and setting of extraction parameters for automated extraction) are prone to errors. The extraction from the µsDAQ data is strongly influenced by the choice of threshold parameters and the background signal (*cf*. Chapter 2.1.2). If the parameters are chosen for a very low average background, but the background signal varies during the measurement, the parameters do not fit for all conditions throughout the data file. This may lead to the false identification of background signals as particle signals. If this occurs near the start or end of an actual particle, the false positives are assigned to the particles signal profile and artificially prolong its corresponding duration. Depending on the number of false positives, this contributes significantly to the determined duration of the extracted particles.

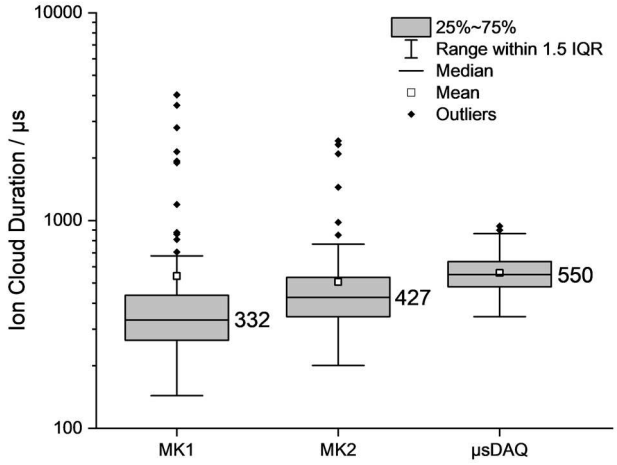


Figure 22. Comparison of the ion cloud duration of 32.7 nm AuNP acquired simultaneously with the µsDAQ and the nanoDAQs MK1 and MK2. False positive detector events are not removed from the data, but are not considered to have a significant influence on the ion cloud duration. Since the data points in the groups are not normally distributed, the median values of the groups were compared instead of mean values. The median duration (332, 427, 550 µs, respectively) varies significantly between all three data acquisition systems.

It is estimated that the visual identification of the ion cloud start and end is more exact than the automated method. However, it is also very subjective and extremely time consuming. Therefore, an adapted automated method for the processing of the event gap data from the nanoDAQs was developed and is compared to the manually extracted data in Chapter 4.4.

While the deviation of the ion cloud duration among the methods showcases the differences in the data processing pathway, it should not significantly affect the extracted sum of ions (detector events) per particle. It has a large influence on the ion cloud duration, if a background (or noise) data point is assigned to an ion cloud with an event gap of 50 µs. Nevertheless, an individual false positive ion does not significantly add to the sum of *e.g.* 150 ions in one ion cloud (*i.e*. 150 + 1).

This was tested experimentally using the same data files as described above by counting the total sum of counts for each of the 100 identical ion clouds acquired with all three systems (**Figure 23A**). The sum of detected counts does not vary significantly between the nanoDAQ MK2 and the µsDAQ data, while the nanoDAQ MK1 detected *ca*. 10% less ions per ion cloud. However, false positive detector events have to be subtracted from both nanoDAQ data files. If these artifacts are removed, it becomes apparent that the MK1 acquired on average even 41% fewer detector events per ion cloud than the MK2, which could be attributed to the lags during data acquisition mentioned earlier (**Figure 23B**). These lags may have been caused by electrical feedback loops in the connection and the signal splitting wiring of the set up for simultaneous acquisition with three DAQs. The slight plus of 7% more acquired detector events *via* µsDAQ compared to nanoDAQ MK2 may be explained by the few additional background ions that were assigned to the particle profiles, as explained above.

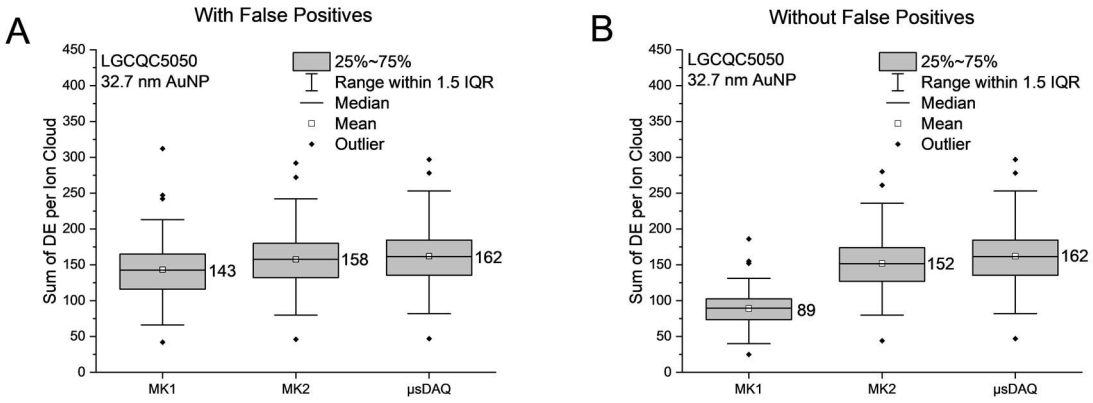


Figure 23. Comparison of the mean sum of detector events (DE) from the analysis of 32.7 nm AuNP acquired simultaneously with the µsDAQ and the nanoDAQs MK1 and MK2. **A**. Without correction of false positives. **B**. Corrected sum of DE per ion cloud (sum of DE within dead time subtracted from the total sum of DE). It appears that MK1 has a high false detection rate and detects significantly fewer true detector events (n = 100).

It was observed that the number of signal artifacts depends on the ion density. Consequently, it also depends on the particle size, because the increased density in ion clouds from larger particles manifests in the decrease of the event gap between detector events. This

relationship was utilized for the particle size calibration as explained in the previous chapter. False positive detector events within the detector dead time artificially shorten the true event gaps between two physically detected ions, which distorts the log(EG) distribution of the ion clouds toward smaller values (*i.e.* larger nanoparticle sizes). This would lead to an overestimation of the particle size, were it not for the fact that contrarily, a certain number of real ions are not detected, because they strike the SEM during the dead time. It is assumed that these contrary phenomena of ion loss due to dead time and false positive signal artifacts cancel each other out to some extent. However, the exact magnitudes of both effects need to be known to develop a suitable mathematical correction.

With the same data acquisition process as explained above, 100 ion clouds from 18 nm, 32.7 nm, and 101 nm AuNP were analyzed, respectively. Additionally, the ratio between false positive DE and total sum of DE per ion cloud was calculated (**Figure 24**). The comparison of this ratio between MK1 and MK2 data of two relatively medium-sized and one large particle type shows that 1) the number of false positive signal artifacts really does increase with increasing particle size, 2) the relative size-dependent influence is apparently higher for the MK2 and 3) the effect in total is much less significant with the MK2. The median false positive rate during the analysis of 18 nm AuNP with the nanoDAQ MK2 was *ca*. 1.3% (percentage of false positive DE per total sum of DE in each ion cloud). During the analysis of particles smaller than 18 nm with the nanoDAQ MK2, false positives were observed in even lower frequency. It is assumed that a false positive rate in this magnitude does not bias the size calibration significantly. Toward larger particles however, the effect is more severe (*ca*. 21% for 101 nm AuNP *via* nanoDAQ MK2). Therefore, a filtering feature that removes non-plausible events (*i.e.* DE within the dead time) from the data was implemented in the successive data processing software by Johannes Schmitt and will be described below (*cf*. Chapter 4.4).

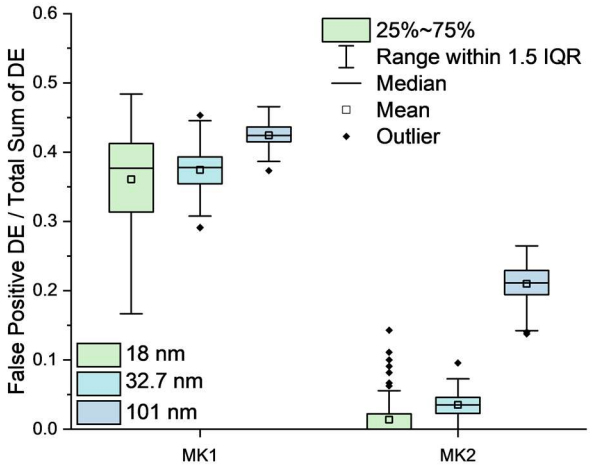


Figure 24. Ratio of false positive detector events (DE) *vs*. the total sum of DE per ion cloud determined for three AuNP sizes (18 nm, 32.7 nm, and 101 nm). Data was acquired simultaneously with the nanoDAQ MK1 and MK2 (n = 100 per size and per DAQ).

After subtraction of the false positive detector events from the total sum of detected ions per particle, the ion detection efficiencies of the three methods were estimated (**Figure 25**, **Table 5**). To that end, the theoretical number of atoms per particle was derived from the mass of a single gold atom and the sizes provided by the vendor under the assumption of an ideal spherical particle with the bulk density of gold. The corrected ion detection efficiency DE_{eff} was calculated from the mean total number of detector events per particle DE_{tot}, the mean number of detector events within the detector dead time DE_{dead}, and the theoretical number of atoms per particle n_{theor} according to Equation 7.

$$DE_{eff,corr} = \frac{(DE_{tot} - DE_{dead})}{n_{theor}} \qquad \text{Equation 7}$$

Table 5. Corrected mean ion detection efficiency per particle during data acquisition with µsDAQ, nanoDAQ MK1, and nanoDAQ MK2 for AuNP with different particles sizes.

	Corrected Ion Detection Efficiency DE_{eff} / % (± SD)				
	6.5 nm	8.9 nm	18 nm	32.7 nm	101 nm
MK1	n.d.	n.d.	$(1.1 \pm 0.4) \cdot 10^{-2}$	$(8.2 \pm 2.3) \cdot 10^{-3}$	$(3.6 \pm 0.7) \cdot 10^{-3}$
MK2	$(3.1 \pm 1.2) \cdot 10^{-2}$	$(2.3 \pm 1.0) \cdot 10^{-2}$	$(1.3 \pm 0.6) \cdot 10^{-2}$	$(1.4 \pm 0.3) \cdot 10^{-2}$	$(5.1 \pm 1.0) \cdot 10^{-3}$
µsDAQ	n.d.	n.d.	$(1.4 \pm 0.9) \cdot 10^{-2}$	$(1.5 \pm 0.4) \cdot 10^{-2}$	$(6.4 \pm 1.5) \cdot 10^{-3}$

n.d. not determined

Particles smaller than 18 nm could not be extracted with the µsDAQ, because they could not be distinguished from the background by the software. The manual identification and extraction of the ion clouds from the nanoDAQ MK1 data was also not possible, because most of them consisted of only one or two detector events, which made it impossible to label them as ion clouds or background. The DE_{eff} of the MK2, however, was high enough to allow the identification and analysis of AuNP as small as 6.5 nm (vendor size).

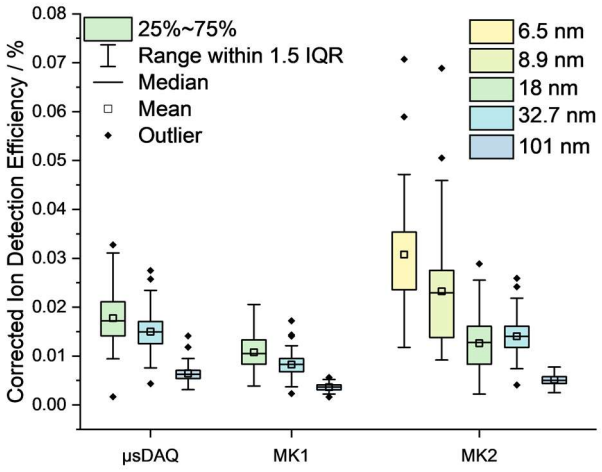


Figure 25. Corrected ion detection efficiency DE_{eff} *vs.* AuNP particle size (n = 100, except for 18 nm, µsDAQ; n = 80). All DAQs only provide a mean DE_{eff} below 10^{-2}% for the largest investigated particles (101 nm). For smaller particle sizes, the µsDAQ and the nanoDAQ MK2 detect ions more efficiently, but ion clouds from particles smaller than 18 nm could not be distinguished from the background with the default data extraction parameters. The nanoDAQ MK2 provided higher detection efficiency for the smallest nanoparticles and therefore enabled the identification of 6.5 and 8.9 nm AuNP.

It is readily visible that the DE_{eff} for all particle sizes is low, regardless of the data acquisition method, with a maximum median of *ca*. 0.03% for 6.5 nm AuNP acquired with the nanoDAQ MK2 and the dedicated data processing. The various reasons for this have been explained above (in brief, feedback loops of electric pulses in the high-frequency cables and T-pieces that connect the DAQs to the SEM output port presumably cause lags during the data acquisition with the MK1 and false positive detector events due to reflection of individual pulses). The slightly higher DE_{eff} of the µsDAQ might be ascribed to the incorporation of background ion signals, as mentioned above, which did not occur with the visual ion cloud identification method for the MK2 data. For 18 nm AuNP, the DE_{eff} of the MK1 system is approximately half of the DE_{eff} of the other two systems, which is again explained by the lags during data acquisition. During the detection of the 101 nm AuNP, however, all three systems only detect $(3–6) \cdot 10^{-3}$ % of the theoretical number of ions, which may be

attributed to the lack of a suitable dead time correction. This is in accordance with the observed flattening of the size calibration curve in previous tests with the nanoDAQ MK1 (**Figure 17**). The limitation of the linear dynamic range of spICP-MS methods towards larger NP or even microparticles is a subject of ongoing research in the community.[108,137,143]

4.3.3. Size calibration dynamic range and limit of detection

Considering the low DE_{eff} of the MK2 for large particles, the linear dynamic range is expected to end well below 100 nm. In contrast, the high detection efficiency for very small particles hints at a comparatively low size detection limit. Indeed, the signal distributions of ions from 5.1 nm and 6.5 nm (vendor sizes) can be visually distinguished from the background signal in a 1/log(EG) plot created from a measurement of 10^5 # mL^{-1} AuNP with 60 s total analysis time (**Figure 26**). The signal distribution of 4.7 nm particles, however, mostly convolutes with the background signal.

The common method to calculate a size detection limit is the 3σ-criterion. To adapt this criterion to the 1/log(EG) plots, a Gauss curve is fitted to the averaged signal distribution of three blank measurements (**Figure 26A**). The resulting 1/log(EG) LOD is 0.2032, which would correspond to a AuNP size of 2.9 nm (assuming exponential size correlation). However, the signal distribution of the background is different in each sample, because each sample might contain a different content of dissolved analyte ions. Consequently, the LOD should be determined for each sample. Unfortunately, the 1/log(EG) distributions for small particles always convolute with the BG signal and it is not straightforward to determine the mean background 1/log(EG) and the corresponding standard deviation σ (*e.g.*, the calculation of size LODs in the data sets of **Figure 26B**, **C**, and **D** results in negative values, which is not reasonable). An elaborate signal deconvolution would be necessary to solve this issue, which is beyond the scope of this thesis.

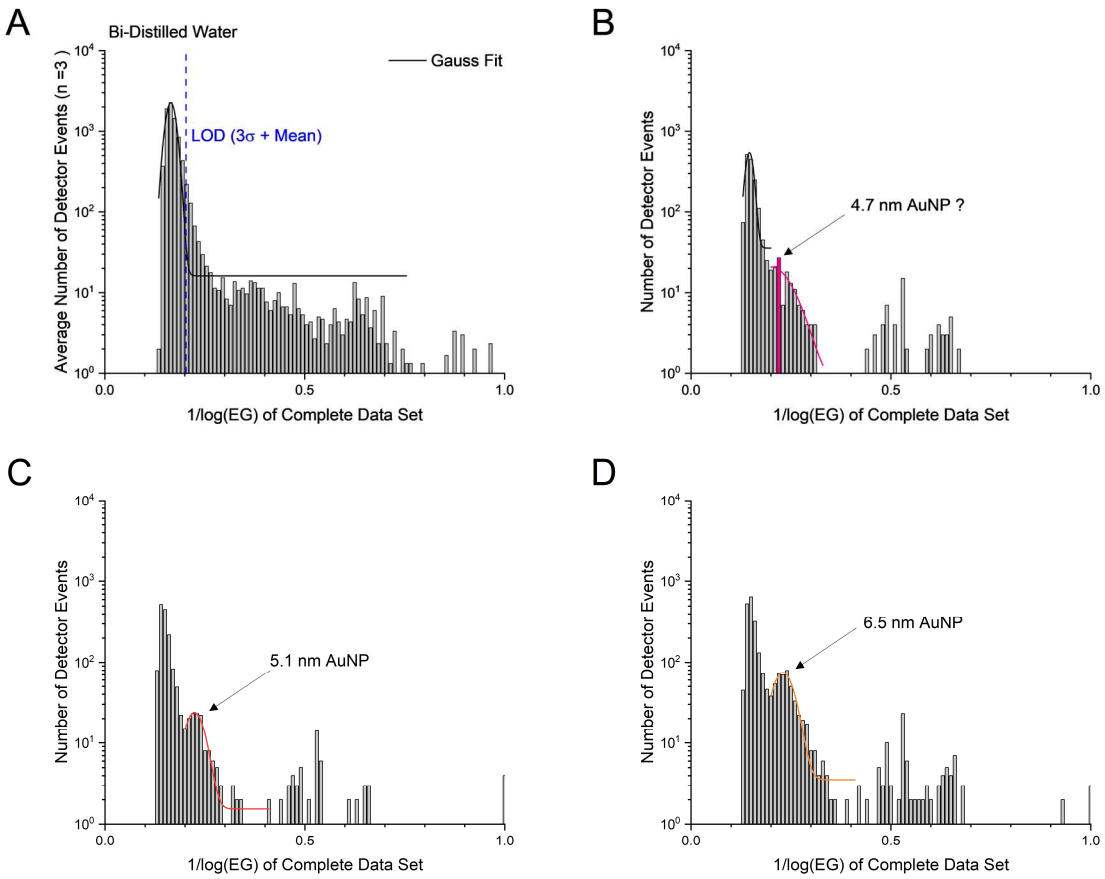


Figure 26. Histograms of the 1/log(EG) values of complete data sets from measurements acquired with the nanoDAQ MK2. **A**. A Gaussian fit to the averaged background (BG) distribution of three blanks of bi-distilled water can provide an estimate of the methods size detection limit (LOD) according to the 3σ-criterion. Nevertheless, the background distribution and signals of small particles usually convolute and does not allow the accurate determination of the size LOD for each analyzed sample. Signal distributions of AuNP with a diameter of 5.1 nm (**C**) and 6.5 nm (**D**) can be visually distinguished from the BG signals after 60 s total analysis time, while the signal distribution of 4.7 nm (**B**) AuNP is not clearly separated from the BG signal distribution. Note the logarithmic scale on the y-axis and that 1/log(EG) values above 1 have been cropped for better visualization.

If one applies the 3-σ criterion, one obtains a size LOD of 2.9 nm for the detection of AuNP with the nanoDAQ MK2 using the complete dataset method and the exponential fit function. However, the applicability of the 3-σ criterion to this novel data type, which was obtained from nanosecond time-resolution spICP-MS, has not been shown yet. The result that is obtained from the application of the 3-σ criterion to the experimental data in this work (2.9 nm) is not realistic and needs further refinement. It was therefore decided to adapt an alternative criterion, which is usually used in chromatography peak analysis, to the 1/log(EG) data. *I.e*. Gaussian curves were fit to the signal distributions of the BG and the NP, respectively. The center 1/log(EG) values and the base peak widths *w* were inserted in Equation 8[144] to obtain the peak resolution *R*:

$$R = \frac{1/\log(EG)_{\mathrm{NP}} \; - \; 1/\log(EG)_{\mathrm{BG}}}{{}^{1}/_{2} \cdot \; (w_{\mathrm{NP}} + \; w_{\mathrm{BG}})} \qquad \text{Equation 8}$$

A resolution of $R > 1.5$ is defined to be the minimum required resolution to state that two (chromatographic) peaks are resolved.[144] This definition was applied to the peak centers and widths of Gauss fits to the BG and NP signal distributions in the histograms in **Figure 26**. Accordingly, the signal distribution of 4.7 nm AuNP is not resolved from the BG ($R = 0.9$), while the NP signal distributions of 5.1 nm and 6.5 nm meet the minimum requirement ($R = 2.5$ and 2.4, respectively). This unconventional approach, which is usually applied to chromatographic peaks, may serve as a temporary aid to estimate the size detection limit of the nanoDAQ MK2 method. From the formally sufficient peak resolution, it may be concluded that the LOD_{size} of the method for AuNP is close to 5 nm. However, a designated size LOD calculation and the validation thereof should be the subject of further method development for nanosecond time resolution spICP-MS.

For the size calibration, two major processing methods were tested: 1) Analysis of the EG of each individual ion in the complete data set for each size (**Figure 27A** and **B**) and 2) analysis of the average EG per ion cloud for 100 particles per size (**Figure 27C** and **D**). All four graphs for each size were created from the same raw data set. Acquisition times were adapted to the particle size, because file sizes from analysis of larger particles (more ions) were very large and in contrast long analysis times did not provide advantages for the detection of large particles. In all cases, the signals produced within the detector dead time are indicated ($\log(EG) < 1.26$ and $1/\log(EG) > 0.79$).

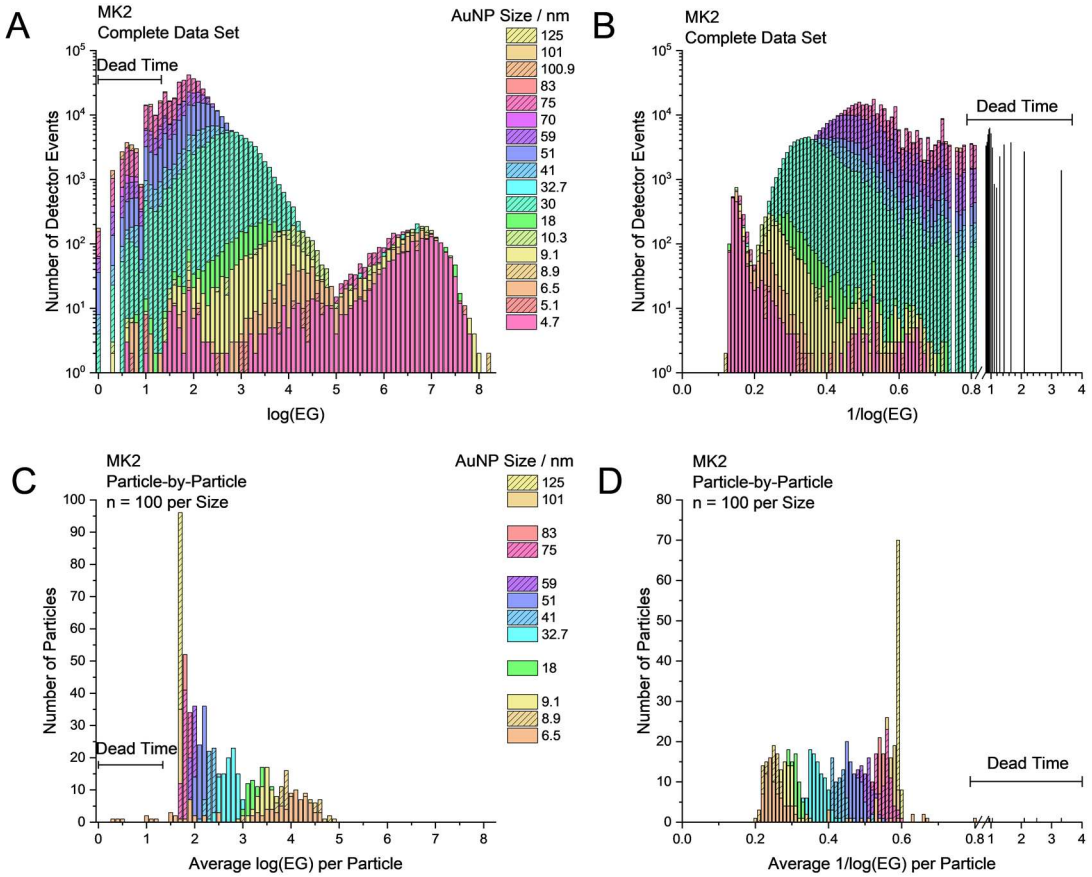


Figure 27. Comparison of data from nanosecond time-resolved spICP-MS analysis of AuNP *via* acquisition with the nanoDAQ MK2 and two different data processing approaches. **A** and **B.** Histograms of log(EG) and 1/log(EG) values obtained from each complete data set per size with size-dependent analysis time (15 s (83–125 nm AuNP), 30 s (41–75 nm), 60 s (4.7–30 nm)). **C** and **D**. Histograms of the average log(EG) and 1/log(EG) values per particle of 100 analyzed particles per size. The raw data files of the presented histograms in A–D are identical for each particle size, only the applied data processing method differs.

The distinction of the particle signal distributions from the background signal in the log(EG) graph is clearly visible, in contrast to the 1/log(EG) histogram. However, for particle size calibration, the mean 1/log(EG) of the ion cloud signals with the corresponding σ is required and is therefore determined from the 1/log(EG) plot. A linear scale on the y-axis showcases that the log(EG) values of ions from 32.7 nm-sized particles (125 nm) are fairly normally distributed (**Figure S6**) with a coefficient of determination R^2 of 0.98 (0.93). After conversion of the log(EG) data to the 1/log(EG) histogram, the R^2 of both a Normal distribution and a lognormal distribution are worse (R^2 = 0.92 and 0.96, respectively for 32.7 nm AuNP; 0.83 and 0.86 for 125 nm AuNP). The main assumption for the presented size calibration approach was that the mean 1/log(EG) of the ions from particles is proportional to the particle's size. If this is the case, the 1/log(EG) distribution should resemble the true size distribution of the nanoparticles. In literature, however, the size of engineered nanoparticles in suspension is reported to resemble a lognormal distribution.[145,146] From this

observed deviation it can be concluded that the 1/log(EG) distribution is distorted and that the mean 1/log(EG) from a Gauss fit to the distribution might not be proportional to the particle diameter.

Towards larger particle sizes, the ion density in the produced ion clouds is expected to increase further. As explained above, the detector dead time does not allow the detection of ions within shorter time spans than 40 ns, which leads to an overestimation of the true event gap between two ions (*i.e.* overestimation of the log(EG) and underestimation of the 1/log(EG) value).

The evaluation of the complete data set for particle size analysis is not ideal, as discussed above. Event gaps from background ions are incorporated and the detection of larger particles has an immense influence on the EG distribution. This is due to the fact that larger particles produce a relatively higher number of ions $\#_{ions}$ in the plasma compared to smaller particles ($\#_{ions} \propto r^3$). These ions can easily dominate the log(EG) distribution and distort it toward lower values (toward higher 1/log(EG) values) and, thus, disturb the size calibration.

It is therefore desirable to analyze the average event gap of each particle individually. This way, the log(EG) distribution is not affected proportionally to r^3, because the average EG from one large particle has the same statistical weight as the average EG from one small particle. To that end, histograms of the average log(EG) and 1/log(EG) from manually extracted ion clouds in the same data set were created and are depicted in **Figure 27C** and **D**. When comparing the two histograms, it is noticeable that the value of the y-axis is orders of magnitude lower compared to the analysis of the complete data set. In the particle-by-particle plots, the y-axis corresponds to complete ion clouds (*e.g.* from 100 AuNP with a diameter of 30 nm) and in the analysis of the complete data set it corresponds to individual ions (*e.g.* circa 77 000 detected ions from all 30 nm AuNP in the measurement). In addition, no background ion signal distribution is visible, because those ions were not extracted from the raw data. Some of the ion clouds that were extracted have average EG values that lie in the dead time region (see the distribution of 6.5 nm AuNP). This is because many of the visually identified ion clouds of the very small particles only consisted of two ions. At the time the ion cloud data was extracted, the exclusion of ions during the dead time was not yet considered and those ions were falsely extracted in addition to the main distribution with a mean log(EG) of 4.2 (1/log(EG) = 0.2299). Ion clouds of larger particles could be identified more clearly. Furthermore, apart from those short ion clouds discussed above, no false positive signals can be seen in the histograms even for larger particles. This is because the presented EG values per particle are the average values. If false positives are detected frequently during the detection of a large particle, the low EG values will shift the average to a lower EG, but the high number of truly detected ions with (slightly) higher EG shift the average to higher EG outside the dead time region.

Considering these advantages of the particle-by-particle approach it was assumed that the size calibration should provide more precise results using the data from individual particles instead of the complete data set. Indeed, the linear fit between 6.5–75 nm shows a better correlation with the average 1/log(EG) *vs*. size data from the particle-by-particle analysis (**Figure 28B**) with an R^2 of 0.993. For comparison, Duffin *et al*. achieved a linear dynamic range from 5–20 with their approach for nanosecond time-resolved spICP-MS (R^2 = 0.997).[124]

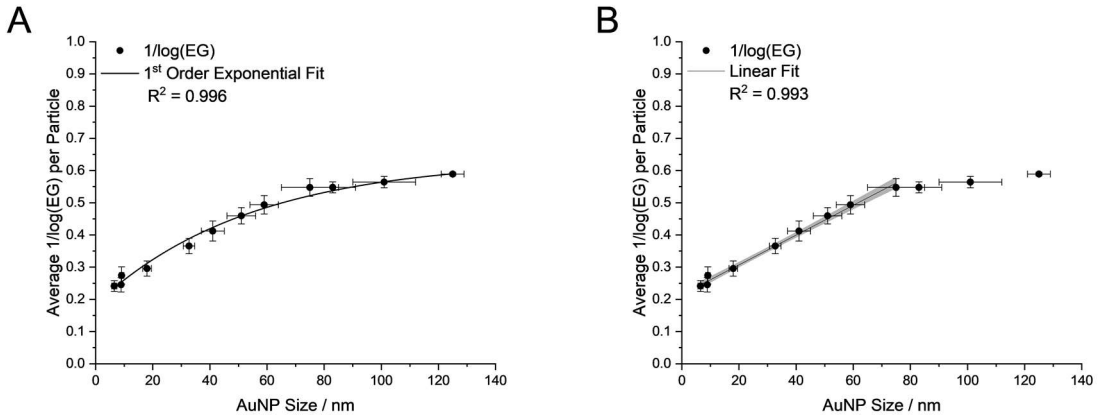


Figure 28. Particle size calibration for AuNP from 6.5–125 nm from spICP-MS analysis with the nanoDAQ MK2 and manual ion cloud recognition. The correlation between the average 1/log(EG) per particle and the AuNP size seems to be better described by (**A**) a 1st order exponential fit function compared to (**B**) a linear fit function. Across this large size range, the exponential fit does not lead to underestimation of the particle size as observed with a linear calibration approach in lieu of a detector dead time correction.

It can also be concluded that at this stage, without a suitable dead time correction for temporal event gap-based calibration, the correlation between average 1/log(EG) per ion cloud and particle size is better described by a first order exponential decay function over a relatively large size range of 6.5–125 nm with an R^2 of 0.996 (**Figure 28A**). It was therefore decided to test the exponential fit for size determination accuracy and to determine the size resolution capability of the particle-by-particle analysis with the nanoDAQ MK2 with manual ion cloud recognition.

4.3.4. Size accuracy and size resolution

The deviation between the particle sizes determined with all four presented nanosecond spICP-MS calibration methods and the average size given by the vendor was determined. Therefore, the experimental sizes were calculated according to Equation S1 and Equation S2 for the linear and exponential calibration method, respectively. The two-sided size deviations of those calculated diameters d_{calc} were determined *via* Equation S3 (**Figure 29**).

As expected, the size determination *via* linear calibration (circles) does not provide satisfactory values for larger particles. The calculated sizes of 101 nm and 125 nm AuNP deviate by more than 20% from the vendor specification, regardless of whether the complete data set was analyzed or individual particles. The size of the NIST RM8011 (8.9 nm) was overestimated by more than 20% with the linear calibration approach with both data processing methods, as well.

In contrast, the sizes determined with the exponential decay function to 1/log(EG) values from both the complete data set and the particle-by-particle method did not exceed a deviation of more than 20% across the complete size range, except for the 9.1 nm AuNP. The values of the 9.1 nm AuNP do not fit to the trend of the size deviation calculated from both calibration methods and both data processing pathways. In-house TEM analysis, however, confirmed a size distribution of 9.0 ± 1 nm. Therefore, the particles possibly agglomerated shortly before the spICP-MS analysis or issues occurred during the data acquisition of this individual sample.

Additionally, in-house TEM analysis of the 75 nm AuNP revealed a bimodal size distribution of the particles (68 ± 6 nm and 85 ± 5 nm). In contrast, data obtained from the analysis of a sufficiently large number of particles with the nanoDAQ and subsequent processing of the complete data set (*i.e.* averaging of the EG of all ions) do not lead to the bimodal distribution in the histograms. The mean of a Gauss fit to the particle signal distribution rather represent the corresponding average size and standard deviation of 78 ± 14 nm. This average size agrees well with the size specified by the vendor (75 ± 10 nm). The processing of only 100 individual ion clouds, however, bears the possibility that incidentally more of the larger particles were analyzed, which would increase the average determined size.

The trend of the size accuracy of the manual particle-by-particle method is fairly similar to the trend determined from the complete data set. It has to be considered, though, that only a maximum of 100 particles were observed per size for the manual extraction of ion cloud data. This probably adds to the observed shift of the average values, as explained by means of the extreme example of a bimodal size distribution above. Automated extraction of ion cloud data from longer measurements were expected to provide average 1/log(EG) values with more precision.

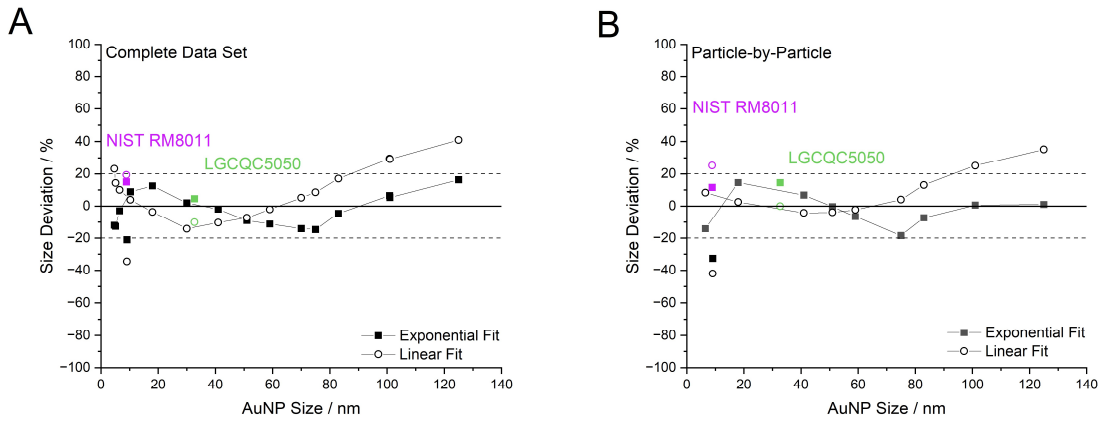


Figure 29. Percentual deviation of the AuNP sizes determined *via* nanosecond time-resolved spICP-MS (nanoDAQ MK2) from the sizes provided by the manufacturer. **A**. Size calibration performed using the 1/log(EG) of the complete data set. **B**. Size calibration performed with average 1/log(EG) values of 100 individual particles per AuNP size. Both the 1st order exponential fit function and the linear fit function were tested (*cf.* **Figure S7A–D**).

At this stage of the investigation of spICP-MS data acquisition with the nanoDAQ MK2 and without an appropriate dead time correction, the exponential fit to the mean or average 1/log(EG) values was assumed to perform best for the size calibration across a relatively broad range from 5.1–125 nm for gold nanoparticles with a size deviation below 20%. However, the manual ion cloud extraction is subjective, potentially irreproducible, prone to errors, and very time-consuming. To extract 100 ion cloud signals from one data file of one sample required several hours of searching for ion clouds, identifying ion cloud start and end times, and subsequently copying and pasting time *vs*. event gap data rows from one file to another.

For NP analysis with a higher throughput of samples, an ion cloud recognition algorithm (ICRA) was developed by Johannes Schmitt, which is able to process the large raw data files, recognize ion cloud transient profiles, and provide statistical analysis of the detected transients within a few minutes. The capabilities of this software will be presented and discussed in the following chapter.

4.4. Evaluation of an automated ion cloud recognition algorithm

The new nanoDAQ data visualization software and a tailored ion cloud recognition algorithm (ICRA) had been developed by Johannes Schmitt. The Python-based program initially extracts only the detector event (DE) data point pairs (time stamp vs event gap) from the raw data that was acquired with the nanoDAQ MK2 (2.2 ns dwell time) during spICP-MS analysis. This first step significantly reduces the processed data file size, when DE occur only rarely during the measurement. Secondly, DE that lie within the detector dead time of 40 ns are removed from the file. Depending on the total number of data points in a raw file (*i.e.* the total analysis time), the required time for this processing step varies. To process one raw file of a 30 s measurement took approximately 90 s in this study (compared to several hours for the analysis of only 100 ion clouds). After extraction of the DE data points, the processed file is stored and is available for further analysis. The new program was tested for its suitability to visualize the transient data and to provide quick information on ion cloud profiles for particle sizing and counting. The results are showcased below and are compared to the figures of merit of the "complete dataset" approach and the "manual ion cloud recognition" approach.

4.4.1. Data visualization and algorithm for peak detection

For visualization of the transient profiles of ion clouds in the acquired data, the recorded event gap corresponding to each detector event is converted into an "ion density" value. The ion density value of data point "x" relates it to the previous and the subsequent DE and is calculated using Equation 9, where EG_{x-1} is the EG to the previous data point and EG_{x+1} is the EG to the subsequent data point.

$$Ion\ Density\ (x) = \left(\frac{EG_{x-1} + EG_{x+1}}{2}\right)^{-1} \qquad \text{Equation 9}$$

As explained above, a large EG value is commonly associated with a low frequency of ions striking the detector and a low EG results from a high ion detection rate (as during the analysis of an individual ion cloud from a NP). In a transient plot of the EG *vs*. time (or data point index, *cf*. **Figure 15**), ion clouds can be discerned by a "dip" in the EG signal. However, this representation is somewhat counter-intuitive, because the frequency of detected ions in fact rises during analysis of an ion cloud. It was therefore decided to inverse the average EG and to denote this value as "ion density".

The transient ion density signal from 7 s of analysis of 32.7 nm-sized AuNP (10^5 # mL^{-1}) with the nanoDAQ MK2 is shown in **Figure 30A**, which is a graph created with the accompanying visualization software. Although this plot appears very similar to transient signals from common ms- or µs-spICP-MS analyses, it should be pointed out that the dimension on the y-axis is the ion density [s^{-1}] and not the usually displayed count rate [counts s^{-1}]. A zoom-in on the x-axis into an analysis time span of *ca*. 60 ms shows the successive detection of two ion clouds (**Figure 30B**) and a further zoom-in shows the transient ion density profile of an individual ion cloud, which lasts approximately 350 µs (**Figure 30C**).

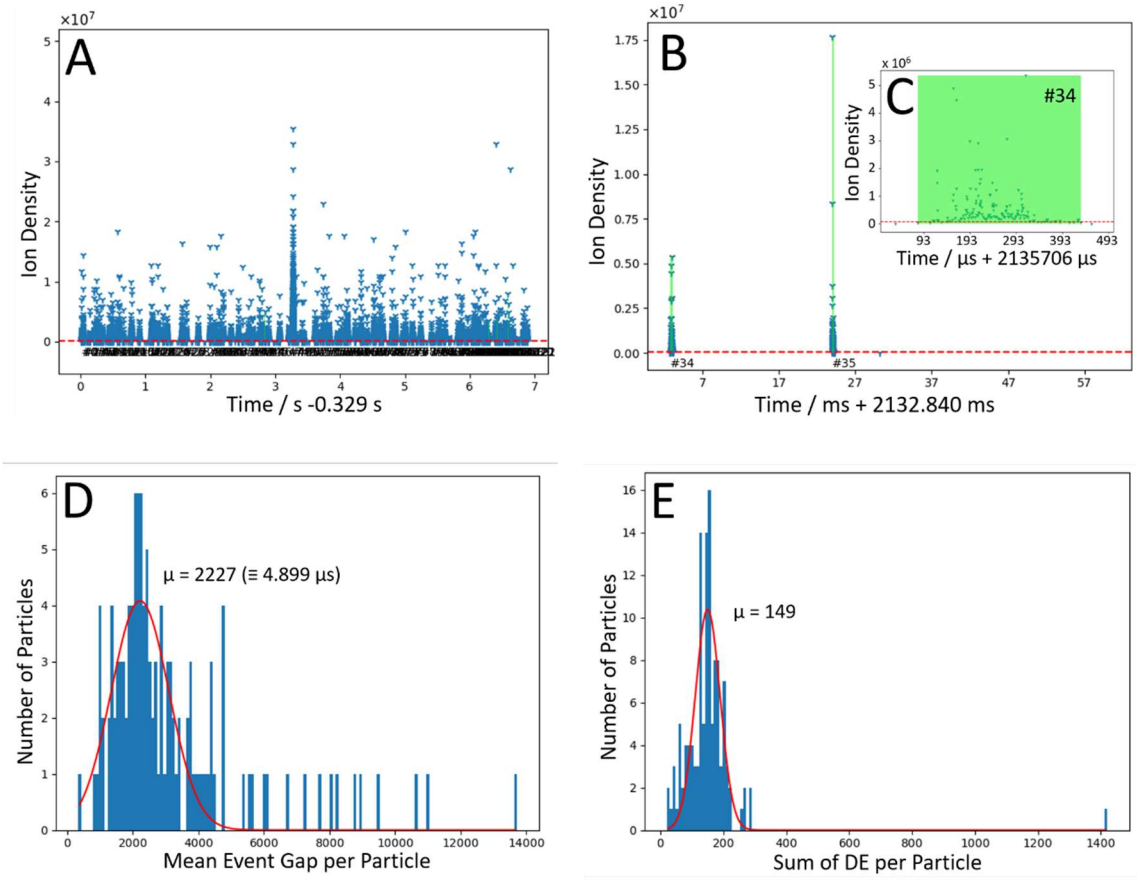


Figure 30. Exemplary processing and visualization possibilities of the ICRA software for spICP-MS data that was obtained with the nanoDAQ MK2. All graphs were created from a spICP-MS analysis of 32.7 nm AuNP (10^5 # mL^{-1}) with a total acquisition time of 7 s. **A**. Transient plot of the calculated ion density of each detector event *vs*. acquisition time. Magnifications on the time axis reveal peaks of two ion clouds (**B**) or the transient ion density profile of an individual ion cloud (**C**). Each identified peak is labelled in green. The consecutive index of each identified ion cloud is printed in black numbers beneath the peak (numbers overlap in A). The red dashed line indicates the calculated background ion density level, which is automatically determined by the ICRA. **D**. Frequency histogram of the mean event gap per identified particle. **E**. Frequency histogram of the total sum of detector events per identified particle. The red solid lines are the output curves of Gaussian fits to the histogram data with the mean µ.

The ion density is not only helpful for visualization, it is also required for the automatic identification of ion cloud peaks in the transient data. For this purpose, a "triple threshold" method was designed by Johannes Schmitt, which defines three independent criteria for the x- and y-data points that have to be met in order to identify a series of DE ("peak") as an ion cloud:

1) The peak has to overcome a minimum total duration (x-value).
2) Throughout the peak, a minimum ion density has to be exceeded (y-value).
3) The peak has to consist of a minimum number of DE (x-value).

Throughout this study, a minimum total duration of 50 µs (criterion 1) and a minimum number of 3 DE (criterion 3) were chosen as a default. The latter criterion is consistent with the condition that was applied during the manual identification of ion clouds. Based on the results from the manual ion cloud analysis, it was assumed that the requirements for criterion 1 and 3 are usually met for all analyzed particle types in this study, with the limitation that from very small particles below 6.5 nm only 1 or 2 ions might be detected in total and those therefore cannot be recognized with this algorithm. The minimum ion density (criterion 2) should be a variable parameter, as is it directly correlated to the ionic background of the analyte element in the sample solution. The implications of the chosen background threshold value on the peak analysis will be discussed in more detail in the next chapter.

If a series of DE meets all 3 criteria it is flagged as a peak and assigned with a continuous index. In the transient plot, the x-y-range from the peak start to end and from the minimum to the maximum ion density value is highlighted in green. The corresponding time stamp and EG (not ion density) of each DE in the peak are used to derive further information about the ion clouds:

1) The difference between the time stamp of the first and last DE in the peak provide the duration of the ion cloud (in ns).
2) The total sum of ions (counts) in the peak can be used to derive the particle mass/size analogously to the ms- and µs-spICP-MS methods.
3) The mean EG of all DE in the peak is used for the particle size calibration method presented in this study.
4) The total number of flagged peaks in the analysis file can be used to calculate the particle number concentration in the sample.

The values of duration, total sum of ions, and mean event gap per ion cloud are automatically binned within variable bin sizes and displayed in corresponding frequency count histograms. As shown above, the center value µ of a Gaussian fit to *e.g*. the mean EG (**Figure 30D**)

or the total sum of DE (**Figure 30E**) is determined and displayed in the graph, as well. In addition to the graphs, all parameters from the Gaussian fits, as well as the number of detected peaks per file, is also printed in the command line output of the program.

Before the provided information was used for particle sizing and counting methods, the programs ability to recognize ion clouds from NP with different sizes in solutions with little to no dissolved analyte was tested, as described in the following chapter.

4.4.2. Setting of the background threshold parameter

The described ion cloud recognition algorithm provides the option to manually set an arbitrary ion density background threshold value, or to automatically calculate the threshold value, which is used to distinguish between background signal and ion cloud signal during peak identification (criterion 2). The workflow that is implemented in the software to calculate the threshold value is depicted schematically in **Figure 31**:

A. The transient measurement is divided into subdivisions (bins) of equal time span.
B. The sum of ions (DE) per subdivision is counted.
C. The bins are sorted by increasing sum of ions per bin.
D. The sum of ions per bin is reconverted into the ion density per bin according to Equation 9. A smooth function is used to create a curve from the maxima of the bins.
E. The turning point of the curve is calculated. The respective ion density value of the turning point is divided by 2 to obtain the background threshold value.
F. The ion density threshold value depends on the ratio between ion density in the ion clouds (high values on the right) and ion density in the background (low values on the left).

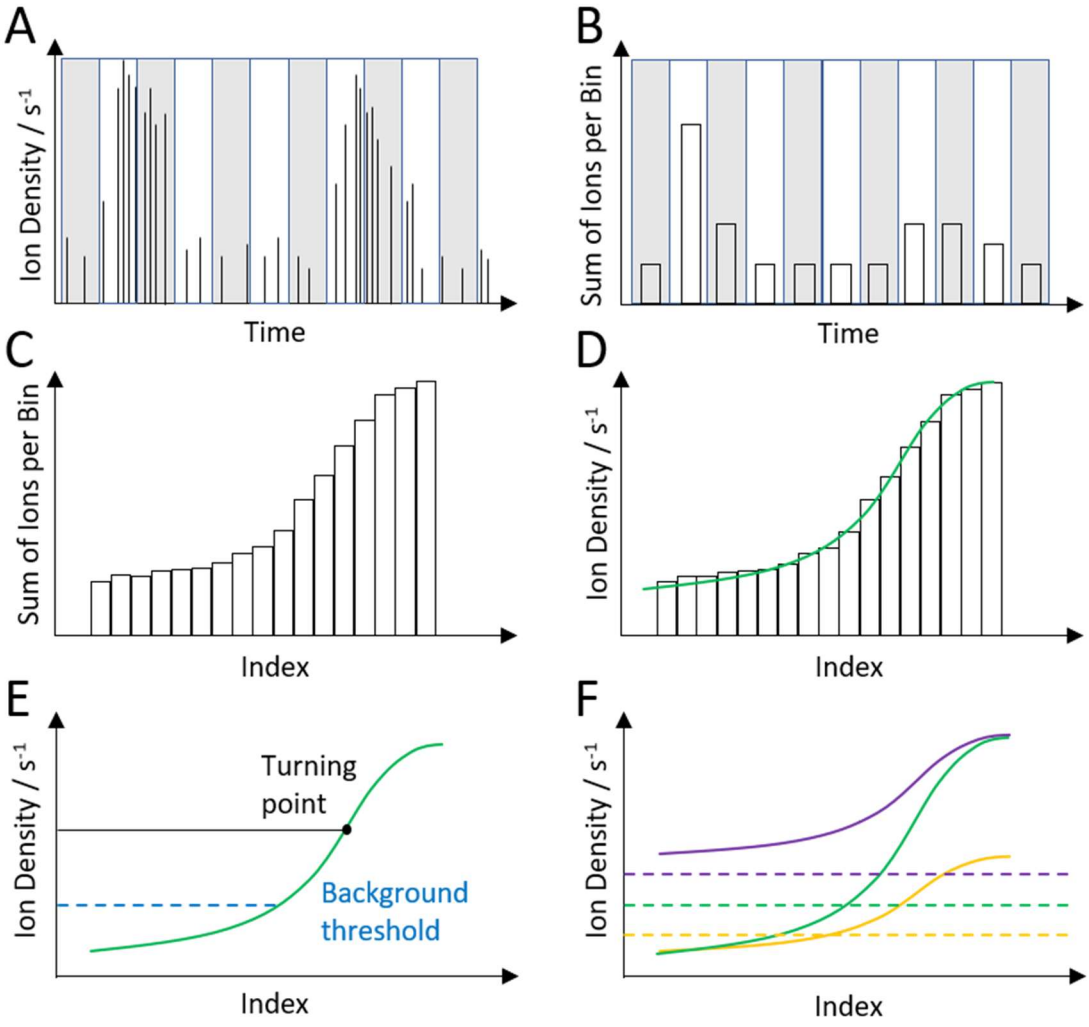


Figure 31. Schematic representation of the ion cloud recognition algorithm to determine the ion density background threshold. **A**. The transient measurement is divided into bins (blue rectangles). **B**. The sum of counts per bin is counted. **C**. The bins are sorted by increasing sum of counts. **D**. The sum of counts per bin is reconverted into the ion density value. The maxima of the bins are smoothed to obtain a curve. **E**. The first turning point of the smoothing curve is determined and the respective y-value is divided by 2 to obtain the ion density background threshold. **F**. Smoothed bin curves for BG threshold determination of three hypothetical NP solutions: Low BG ion density with high NP ion density (green), low BG ion density with medium NP ion density (yellow), and medium BG ion density with high NP ion density (purple). Even though the BG ion density of the green and yellow curve is equal, the calculated BG threshold (dotted blue line) is different due to its dependency on the NP ion density.

By following this workflow, the ion density background threshold value is calculated from all DE that were recorded during the measurement. Instead of using the transient ion density profiles of each ion cloud to determine signal-to-noise thresholds, which are then averaged, the algorithm uses the background DE and ion cloud DE of the complete measurement.

This method of setting a background threshold value in the prototype software is not based on counting statistics. It is merely an approach to quickly, automatically, and reproducibly determine a threshold value between signal and noise in each individual data set. For AuNP model samples with low background, the threshold value seemed to produce ion density threshold values, which were too high to reliably identify ion clouds from small particles. Additionally, the calculation pathway using the turning point of a curve implies that the obtained threshold value not only depends on the ion density of the background DE, but also on the ion density of the analyte DE, *i.e*. on particle size (**Figure 31F**). Consequently, the BG threshold value increases with increasing particle size, even though the concentration of dissolved analyte stays constant (*cf*. **Figure 32**). In future versions of the software, alternative calculation pathways based on counting statistics would help to derive a size-independent determination of the BG threshold to attain more accuracy for particle counting and sizing.

In order to evaluate the algorithm in its current version, the measurement files from spICP-MS analysis of AuNP with the nanoDAQ MK2 acquisition were processed with the peak analysis software (default values for criterion 1 and 3) and the automatic background threshold determination.

Representative transient profiles of ion clouds from 6.5 nm, 32.7 nm, and 125 nm-sized AuNP indicate that the algorithm is able to identify the ion clouds from 6.5 nm AuNP (**Figure 32A**), which was not possible with previous data acquisition systems for spICP-MS. However, the BG threshold determination appears to be not yet optimized for larger particles. If the ion density threshold is set too high, the start and end time of the ion cloud is not determined correctly (**Figure 32D**). In addition, temporarily decreased ion densities within the long ion cloud of a large particle falsely lead to the recognition of two separate, shorter peaks (**Figure 32G**). Both cases lead to an underestimation of the sum of ions per ion cloud and its duration, as well as an underestimation of the average event gap, because only the time sections with the highest ion densities (low EG) are identified as a peak. The splitting of one ion cloud into two peaks is already known from millisecond time-resolution spICP-MS and additionally leads to the problem of false particle counting results.

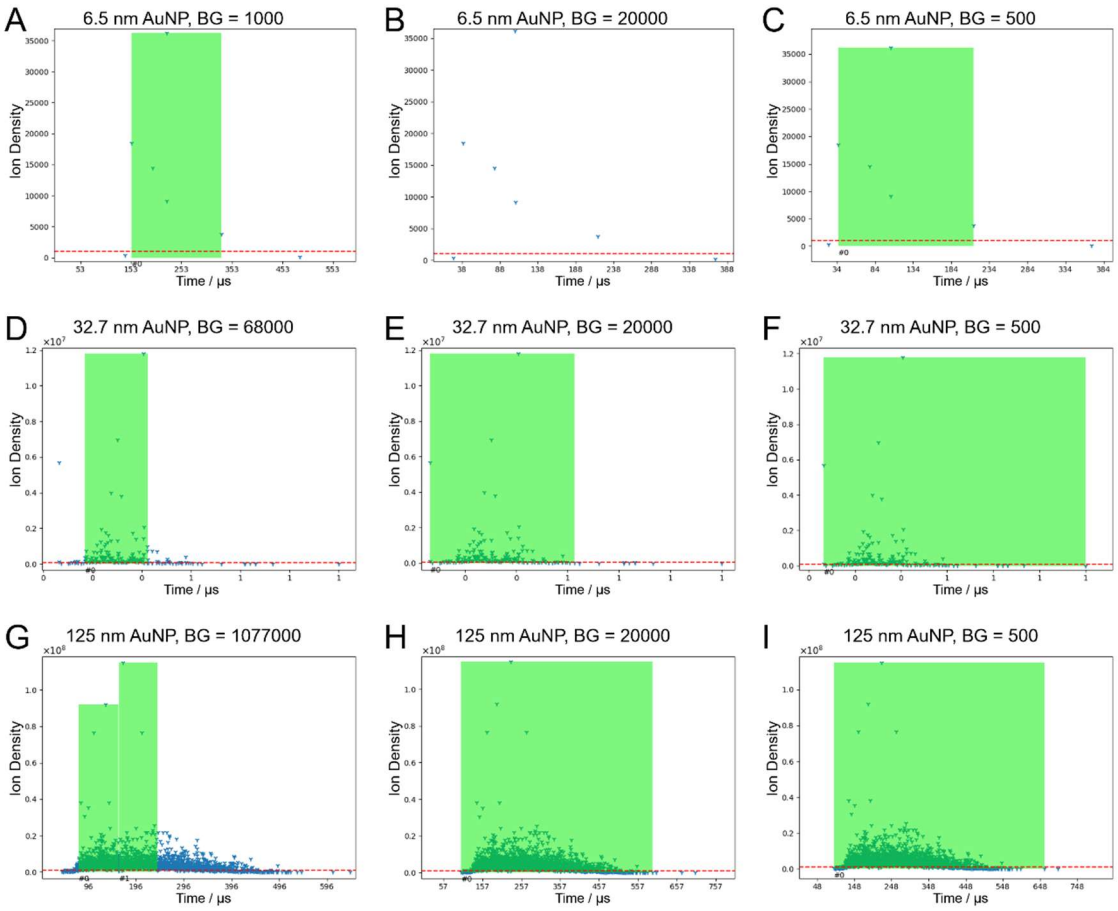


Figure 32. Transient ion density profiles of 6.5 nm AuNP (top row), 32.7 nm AuNP (mid row), and 125 nm AuNP (bottom row) from spICP-MS analysis with the nanoDAQ MK2 and data processing using ICRA. Three different setting for the ion density background threshold determination were tested: Automatic calculation by ICRA (left column), manual setting of 20000 (mid column), and manual setting of 500 (right column). Successions of DE (blue marks) that were identified as one continuous ion cloud by ICRA with the respective setting are labelled in green. Non-optimal BG threshold setting lead to failure to recognize an ion cloud (B), underestimation of the ion cloud duration (D), or split-particle events (G). With optimized settings the beginning and end of the complete ion cloud are successfully recognized.

Due to these challenges with the automatic variable threshold calculation, it was decided to empirically determine a low constant threshold that is suitable for the complete range of particle sizes for the model AuNP samples with low dissolved analyte concentration. While the peaks of large and medium sized NP are satisfactorily recognized when setting the BG threshold value to 20 000, the algorithm fails to detected the smallest particles (**Figure 32B**, **E**, **H**). In contrast, a BG threshold value of 500 enables the algorithm to identify the ion clouds of all three particles sizes and even to include the characteristic “tail” of the ion cloud profile (**Figure 32C**, **F**, **I**).

Analysis of the complete data sets of all particle sizes confirms that especially at smaller particle sizes, the algorithm finds more peaks with the ion density BG threshold value of 500 than

with the automatically determined threshold or the value of 20 000 (**Figure 33**). It has to be mentioned, though, that the original number of particles per mL in all AuNP sample solutions was equal. However, none of the BG threshold parameters enabled the recognition of the same number of particles per minute for the smaller sized particles (6.5–18 nm) as for the larger particles (32.7–125 nm), which might have several causes. First, the distinction of the smaller particles from the background by the ICRA is more efficient for ion clouds with higher density (*i.e.* larger particles), and second, the overall transport efficiency of particles smaller than 18 nm might be less effective than for the larger size range.

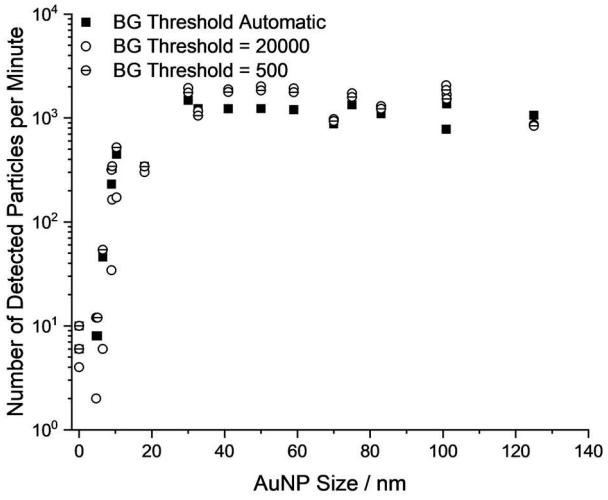


Figure 33. Evaluation of the influence of three different BG threshold settings on ICRA's capability to recognize ion clouds in data sets from spICPMS analysis (nanoDAQ MK2) of differently-sized AuNP. Measurement files were identical per AuNP size. With the highest BG threshold of 20 000, fewer particles were identified in the lower size region (circles), while the automatically-determined BG threshold led to an underestimation of the particle numbers in samples with larger AuNP (squares). The BG threshold of 500 enabled the recognition of the highest number of ion clouds per minute for most AuNP sizes (crossed circles). Note the logarithmic scale on the y-axis.

Quantitative analysis of the mean sum of counts and mean ion cloud durations per particle size were determined using the three different threshold settings and confirm the observations that were made based upon the transient ion cloud profiles in **Figure 32**. Above a particle size of 83 nm, the automatic BG threshold calculation leads to a significant decrease of the determined average sum of ions (detector events) per particle (**Figure 34A**). In contrast, the expected continuous positive correlation between sum of DE and particle size is observed when the two lower BG threshold values are used. Similarly, the ion cloud duration does not extend with increasing particle size based on the data from the automatically calculated BG threshold (**Figure 34B**). The usage of the other threshold values rather effectively prevents the observed splitting of ion clouds and thus

leads to the expected positive correlation between particle size and ion cloud duration. In conclusion, out of the three tested settings, the lower BG threshold value of 500 provides the most reliable recognition of complete ion cloud transients in the studied data sets with low dissolved background.

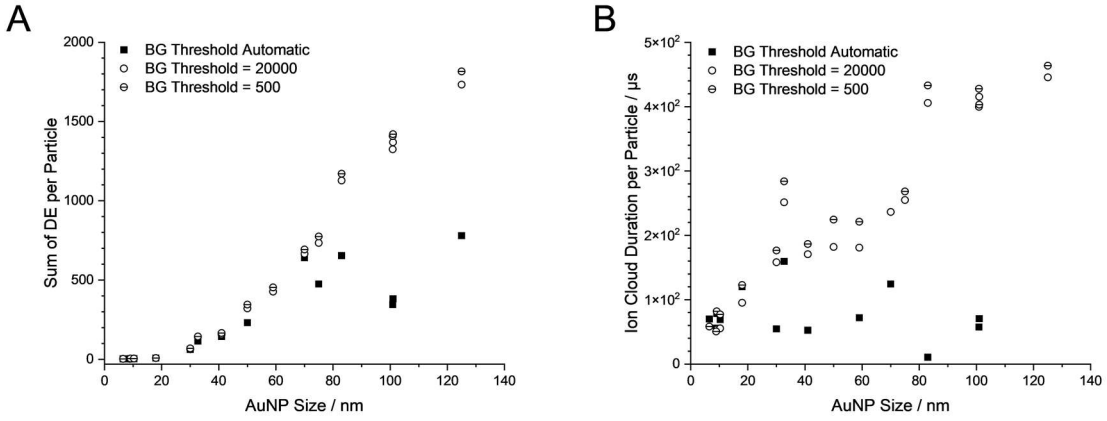


Figure 34. Evaluation of the influence of three different BG threshold settings in ICRA on **A**. the average total sum of DE per ion cloud and **B**. the average ion cloud duration in data sets from spICPMS analysis (nanoDAQ MK2) of differently-sized AuNP. Measurement files were identical per AuNP size. The automatically-determined BG threshold results in a drastic underestimation of the Sum of DE at particle sizes above 75 nm and the respective ion cloud duration does not correlate with the particle size. Using the manually set BG threshold of 500, ICRA recognizes more DE and longer durations per ion cloud than the other tested settings and both parameters correlate positively with the particle size.

Naturally, this empirically chosen BG threshold value is only valid for pure NP samples, in which the ion density of the background is low and it might not provide accurate ion cloud detection for unknown samples. However, it is sufficient for the comparison of the particle sizing and counting capabilities of the different processing pathways for nanoDAQ MK2 data of the model NP solutions, which will be discussed below.

4.4.3. Comparison of ion detection efficiency

The average (or most frequent) DE_{eff} of the ion cloud recognition algorithm was determined for 16 monodisperse AuNP suspensions between 6.5–125 nm and was compared to the figures that had been obtained from manual ion cloud recognition (**Figure 35**). Expectedly, the correlation between DE_{eff} and particle size is similar for both methods and the DE_{eff} are in the same order of magnitude. For 18.5 nm-sized particles, the ICRA found a smaller number of ions (DE) per ion cloud (18.5 nm: -0.7% DE), while the difference between ICRA and manual recognition is below 0.4% for the other analyzed sizes.

One explanation for this deviation might be increased dissolved background which hampered the equal identification of ion clouds by the algorithm and *via* subjective, visual determination of ion cloud start and end. Especially at small particle sizes with only tens of DE per ion cloud, a false judgement of the ion cloud temporal limits leads to significant percentual false positives (and negatives). Additionally, only 100 ion clouds were analyzed for manual identification.

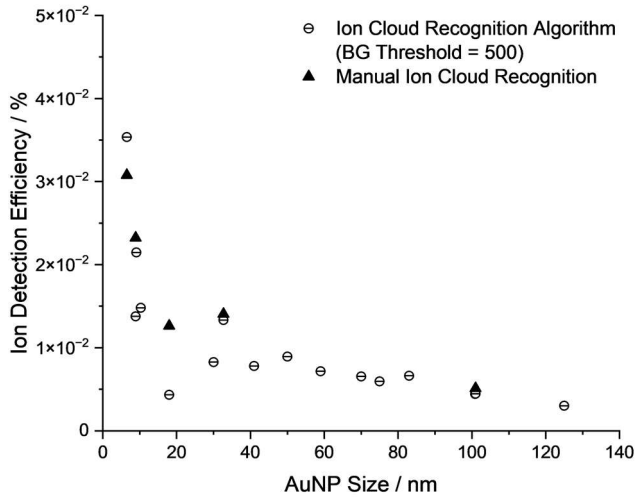


Figure 35. Comparison of the ion detection efficiency per AuNP particle size obtained with the ICRA software using a BG threshold of 500 (crossed circles) and *via* manual ion cloud recognition (triangles). The ion detection efficiencies obtained with both methods follow the same decreasing trend towards larger particle sizes due to dead time-related losses, although deviations from the trend were observed. Measurement files were identical per AuNP size.

The experiment confirms that an overall DE_{eff} between *ca*. $(0.3–3.5) \cdot 10^{-2}$% can be achieved with the nanoDAQ MK2, which means that at small particles sizes approximately 1 in 3000 ions is detected (6.5 nm) and at large sizes only 1 in 30000 ions is detected (125 nm). Assuming the highest determined DE_{eff} of $3.5 \cdot 10^{-2}$% and absolutely no background noise (which is of course not achievable), the detection of 1 DE would correspond to a size detection limit of 4.5 nm, if a count-based size calibration would be performed. The event gap-based size calibration approach, however, requires the detection of at least two DE per ion cloud, because their difference in arrival time is used for calibration. This would correspond to a size detection limit (in terms of DE_{eff}) of 5.7 nm for gold NP, which agrees well with the LOD_{size} that was postulated before for manual ion cloud recognition.

However, the ICRA is programmed in such a way that, according to criterion 3, only ion clouds consisting of at least 3 DE are even considered for extraction. Currently, the smallest AuNP size that could be extracted with the ICRA is 6.5 nm, which infers that only 3 ions from initially *ca*. 8500 atoms in the NP were detected. Therefore, to lower the LOD_{size}, the ion transmission of the

MS system would have to be increased *via* instrumental modifications in order to ensure that at least 3 ions from AuNP that are even smaller than 6.5 nm arrive at the detector.

4.4.4. Particle size calibration capability

While low ion transmission is not an issue for the detection of larger particles, the DE_{eff} is lowered by a factor of 10 (from 6.5 nm to 125 nm AuNP). This is most probably caused by the loss of ions during the detector dead time, as already explained extensively above, and limits the upper size calibration range of spICP-MS methods.

The correlation between the log(EG) per particle and particle size that was determined from the complete dataset, manual ion cloud recognition, and ICRA with a constant BG threshold of 500 is shown in **Figure 36.** The information of interest here is the particle size sensitivity that can be achieved with the different methods. The particle size sensitivity is characterized by the signal response with regard to the particle size, which is here the decrease of the log(EG) value with increasing particle size. The response should be high to ensure that even small changes of the particle size lead to significant changes of the log(EG). Ideally, the response (here: log(EG)) is linearly proportional to the particle size and corresponds to the slope of a linear regression.

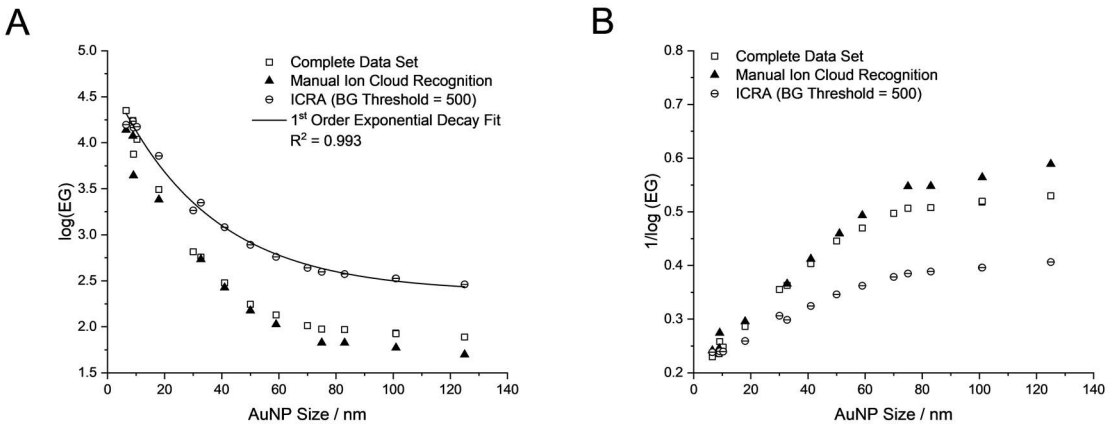


Figure 36. Comparison of three data processing pathways for the size characterization of different sizes of AuNP *via* spICP-MS with the nanoDAQ MK2 system: The analysis of the average EG of the complete data set (squares), particle-by-particle analysis after manual ion cloud recognition (triangles), and particle-by-particle analysis using the ICRA (crossed circles). **A**. Plot of log(EG) *vs*. AuNP size. Average log(EG) values per AuNP type that were obtained with ICRA appear to decrease logarithmically with particle size. **B**. Plot of 1/log(EG) *vs*. AuNP size. The sensitivity for size calibration *via* 1/log(EG) seems to be lowest for the data obtained with ICRA. Measurement files were identical per AuNP size.

As shown in **Figure 32A**, the log(EG) value does not have a linear correlation with the particle size over the observed size range of 6.5–125 nm AuNP for none of the tested data

processing methods for the nanoDAQ MK2, which had been demonstrated before for the data from the complete data set and from manual ion cloud recognition (**Figure S7**). However, it had been unclear whether the non-linear correlation had been caused by influences from dissolved background (complete data set) or from weak statistics due to an insufficient number of analyzed particles (manual ion cloud recognition). Additionally, false positive DE had not been removed from those results, which artificially lead to shorter EG between DE (*i.e.* lower log(EG)).

The ICRA, however, provides particle-by-particle information on all ion clouds that were analyzed during the complete measurement run time. It should also feature an automatic filter for DE within the detector dead time to avoid false positives, which results in higher log(EG) values compared to the previous two methods. Unfortunately, while this feature improves the accuracy of the method, it also reveals that its size sensitivity is lower than expected. Specifically, the decrease of log(EG) upon increase of particle size is lower at high particle sizes than at small particle sizes. Instead of a linear correlation, log(EG) appears to decrease exponentially with increasing particle size, which confirms the assumption that had been made earlier (*cf*. Chapter 4.3.3) based on the manual ion cloud recognition data.

For vizualization purposes, plots of 1/log(EG) *vs*. particle size had been presented before to obtain a positive relationship between signal and particle size, because it is easily comparable to particle size calibrations from conventional count-based spICP-MS approaches. While the non-dead time corrected values from the complete data set and manual ion cloud recognition feature an approximately linear increase of 1/log(EG) between AuNP sizes of 6.5–83 nm, this is not the case for the more accurate data obtained with the ICRA (**Figure 36B**).

If a detector dead time of 40 ns is assumed for the type of detector used in this work, this is the minimum possible time gap between two detected events, which corresponds to 18 data points with 2.2 ns dwell time, a log(EG) value of 1.26 and 1/log(EG) = 0.79. Should the detector dead time be the sole limit for the detection rate of ion clouds from larger particles with a high ion density, it would be expected that the curve of 1/log(EG) *vs*. particle size approaches this value of 1.26 and then levels off due to saturation. However, the curve obtained from the ICRA already seems to approach saturation at 1/log(EG) = 0.4 (125 nm), which corresponds to *ca*. 550 ns, *i.e*. event gaps that are 10 times longer than the theoretical limit.

At this point it is also very important to remember that the plotted 1/log(EG) values are averaged over each individual ion cloud. It is known that the ion density is not constant within the ion cloud. On the contrary, is rather high in the beginning and trails off toward the end. So even if

a maximum 1/log(EG) of 0.79 may be reached within the densest parts of the ion cloud, the average value will always be much lower due to the ion cloud tail with low ion density.

In addition to the factors discussed above, the ion cloud recognition method of the algorithm might set false limits to the temporal extension of the ion cloud and thus neglect DE at its beginning or end. This should affect a count-based size calibration to the same extend. However, the correlation between radius units per particle ($(\text{Sum of DE})^{1/3}$) and particle size is linear between 6.5–83 nm, which means that at least within this size range, only a negligible number of DE is excluded from the ion cloud by the ICRA (**Figure 37**).

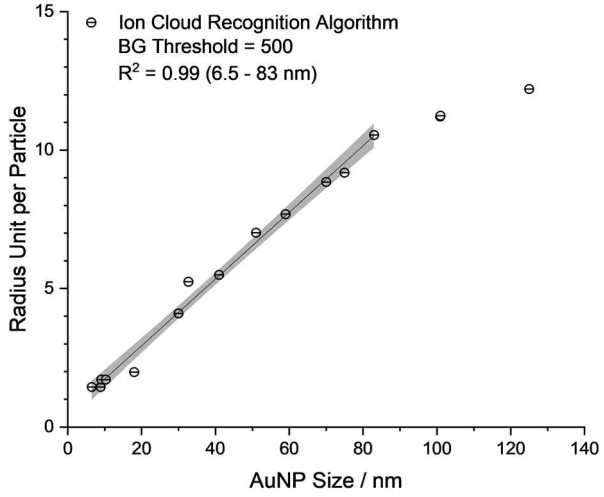


Figure 37. Evaluation of a count-based size calibration approach for data obtained *via* spICP-MS analysis of differently-sized AuNP after processing with the ICRA software. Radius units were derived from the average sum of DE per particle size $\left((\text{Sum of DE})^{1/3}\right)$. The correlation between radius units and particle size was found to be linear in the range between 6.5–83 nm. Toward larger particle sizes, the sum of DE per ion cloud is increasingly affected by detector dead time losses, which causes a flattening of the response signal.

In summary, it can be derived from the ICRA results that the ion density (1/log(EG)) shows a non-linear response to the particle size and the exact causes should be elucidated in detail in further studies. The potentially incomplete vaporization of large particles at the plasma conditions used in this work should be taken into consideration for size calibration in the upper size range. At the lower end of the size range, however, a size detection limit of *ca*. 5 nm can be achieved for gold nanoparticles in pure model solutions with the combination of the high time resolution of the nanoDAQ MK2 and the ICRA. In addition to the short analysis time and fast data processing, the ICRA also provides the total number of detected particles during the measurement time, which is essential for a comprehensive particle characterization in real samples. At this point, the count-

based particle size calibration (radius unit) or the ion cloud density-based calibration (1/log(EG)) using interpolation with a linear regression should only be used as an estimate and within a narrow size range.

4.4.5. False positive detector events during detector dead time

The influence of false positive detector events during the detector dead time on the particle sizing capability of the nanoDAQ MK1 was already discussed (*cf*. Chapter 4.3.2). It was also observed that the magnitude of false positive DE was significantly lower in the data acquired with the nanoDAQ MK2, which is presumably attributed to the connection of the MK2 within the parallel acquisition set up (**Figure 21**). Nevertheless, the histogram in **Figure 21** shows that some (although few) false positive DE were detected, anyway. In this case, the total number of false positives was low, because the histogram corresponds to the analysis of a medium-sized 32.7 nm AuNP with a moderate ion density. To further reduce the number of false positives in the processed data, a filter algorithm was additionally implemented in the ICRA software to identify DE within the dead time of 40 ns, omit them from being transferred to the processed data file, and to adapt the respective EG from the first DE to the next "valid" DE after the dead time passed.

According to Equation 9, the ion density of a detector event x is obtained from its EG to the preceding and following DE. The minimum EG is limited to 40 ns by the detector dead time. If EG_{x-1} and EG_{x+1} are both 40 ns due to a very high analyte ion concentration, this results in an ion density of $1.25 \cdot 10^{-7}$. In other words, a value of $1.25 \cdot 10^{-7}$ should be the highest ion density value, if the dead time filter function is applied. However, the transient plot of ion density *vs*. time that was obtained from the analysis of a 125 nm-sized AuNP (**Figure 38A** and **B**) reveals that this theoretical maximum limit (indicated as black solid line) is exceed very often, even by a factor of 10. A zoom into the transient profile of a singular ion cloud shows that this technical threshold of the SEM appears to be exceeded only during the time in which ions from the "body" of the ion cloud strike the detector, *i.e.* the part with the highest ion density. At times during the ion cloud arrival, in which the ion density is lower, *i.e*. the "head" and "tail" of the ion cloud, the ions arrive with EG longer than the dead time (above 40 ns).

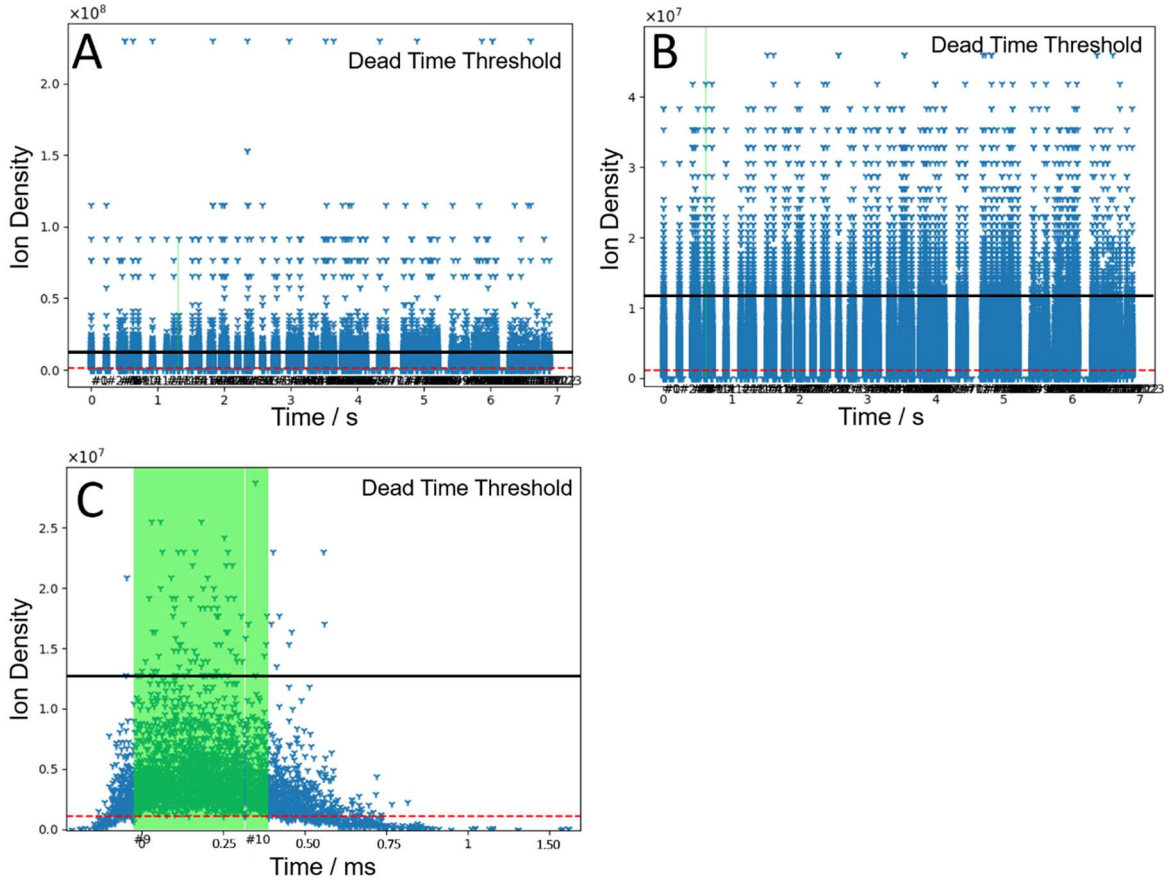


Figure 38. Transient plots of the calculated ion density *vs.* acquisition time obtained from spICP-MS analysis of 125 nm AuNP with the nanoDAQ MK2 system and subsequent processing and visualization with the ICRA software. **A**. Acquisition time of 7 s showing the total ion density range. **B**. Acquisition time of 7 s showing a lower ion density range. **C**. Magnification of an individual ion cloud profile from the same measurement file. The dead time threshold (black solid line) indicates the theoretical maximum ion density that should be obtained from data acquisition with the nanoDAQ at the output of the secondary electron multiplier with a dead time of 40 ns. However, false positive detector events and a non-optimal data filter function in the ICRA, signals above the theoretical ion density limit distort the true ion cloud profiles. The red dashed line indicates the calculated background ion density level, which is automatically determined by the ICRA.

The current explanation for this unexpected observation is that that the filter function fails to completely remove all of those false positives. In this version of the prototype ICRA, the filter function most probably recognizes the first false positive value and removes it from further processing, but it does not yet correctly identify another false positive within the same dead time period. This issue can potentially be resolved by adapting the filter algorithm appropriately, which is already considered for a future modified version of the ICRA.

4.4.6. Capability of peak recognition in elevated ionic background

Ideally, the ICRA should be able to automatically adapt the background threshold in samples with higher content of dissolved analyte. However, the analysis of particle-free model samples with different concentrations of dissolved titanium from 0–5 µg L^{-1} revealed that the ion density distribution is not monomodal with one average value and a certain SD (**Figure 39**). With increasing analyte concentration, the event gaps between many ions approach the detector dead time-dependent threshold ion density of $1.25 \cdot 10^{-7}$, which is exceeded by a few false positive DE *(cf.* Chapter 4.4.5). Here, it is important to note that the maximum threshold value is only obtained, if the EG to both the previous and the successive DE is 40 ns. If only one EG is 40 ns and the other EG is higher, the calculated ion density of the respective DE is anywhere between $1.25 \cdot 10^{-7}$ and 0.

In conventional ICP-MS, the mass concentration of an analyte in solution is obtained *via* calibration of the analyte response, *i.e*. the signal intensity within a certain integration time (average number of DE within dwell time) *vs*. the mass concentration. If the analyte concentration is high, many DE will occur within the detector dead time, which would cause a non-linear response. However, a dead time correction based on counting statistics is usually automatically applied to the raw data within the proprietary software.

The ion density data that is obtained from the nanoDAQ and visualized with the ICRA is based on temporal gaps between DE and not on the number of DE within a certain dwell time. Therefore, the commonly used dead time correction approaches cannot be applied. The software version of the ICRA that was used in this work is, as demonstrated above, not yet capable of adjusting the background level in model samples with elevated ionic background. This also implies that the detection of particles in real water samples is only possible under the condition of a low analyte background.

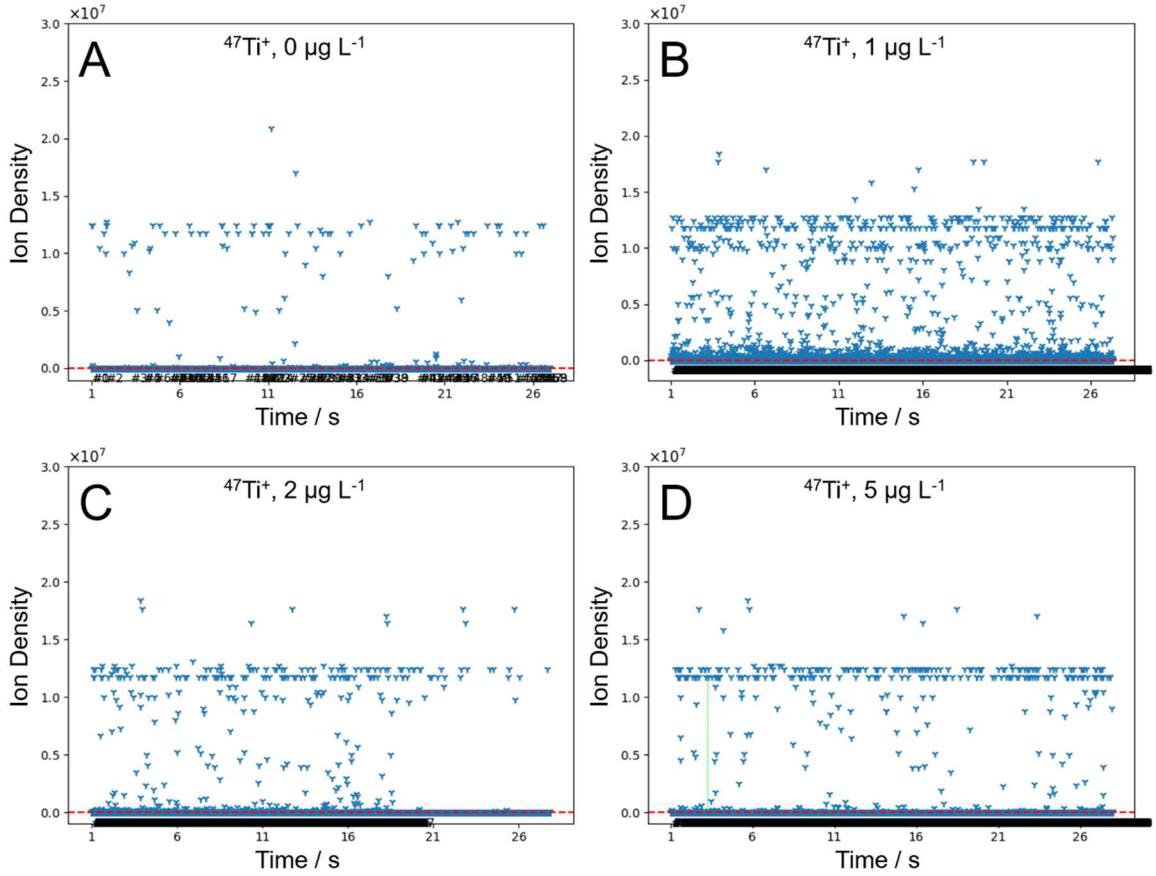


Figure 39. Transient plots of ion density *vs*. acquisition time from analyses of solutions with mass concentrations of dissolved titanium of **A**. 0 µL L^{-1}, **B**. 1 µg L^{-1}, **C**. 2 µg L^{-1}, and **D**. 5 µg L^{-1} acquired with the nanoDAQ MK2 system and subsequent data processing with the ICRA software. The dead time-dependent maximum ion density of $1.25 \cdot 10^7$ is exceeded at high count rates and the ion density distribution is not correlated to the mass concentration of the dissolved titanium standard solution, which restricts the capability of the ICRA to recognize particles in solutions with high background analyte signal.

Plausible particle counting results are obtained for titanium-containing NP in real water samples with sufficiently low background levels (**Figure 40A**), as demonstrated at the example of the Sieg spring water sample (SW01). The number of detected ion clouds (64) is higher than the ion cloud profiles of presumably large particles that can be identified visually in the ion density plot (*ca*. 12–13 large peaks), but it is reasonable that the ICRA detected additional, much smaller and shorter ion clouds. Even though the counted number of particles is most probably not accurate, the order of magnitude is reasonable (hence the PNC).

In contrast, elevated background levels in the effluent of a waste water treatment plant (sample WWA) impede the particle recognition and counting of the ICRA and result in an unrealistically high number of detected titanium-containing particles (12208 particles), which do not match at all with the number of large visible ion cloud peaks in the transient ion density plot

(**Figure 40B**). Clearly, the distinction between ionic background and very short ion clouds with few ions is not effective in this case.

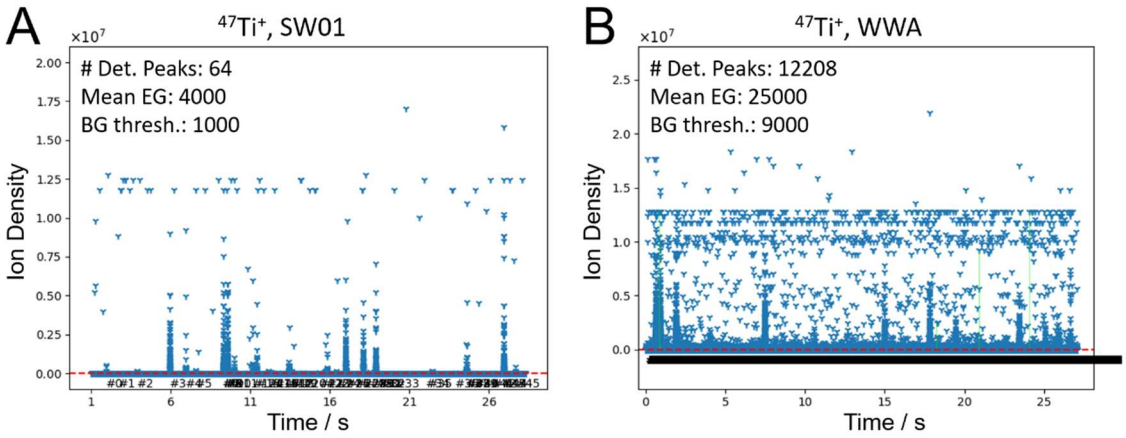


Figure 40. Transient plots of ion density *vs*. acquisition time from analyses of **A**. the Sieg spring water sample S01 and **B**. the WWTP Netphen-Deuz effluent sample WWA acquired with the nanoDAQ MK2 system and subsequent data processing with the ICRA software (automatic BG threshold calculation). The $^{47}Ti^+$ ion was selected for analysis. The dissolved background in the surface water sample is sufficiently low to allow the recognition of a plausible number of ion clouds by the ICRA, but the higher dissolved titanium content in the waste water effluent sample leads to the identification of an unreasonably high number of ion clouds.

Based on the observations described above, it was decided to refrain from applying the ICRA to analyte ions that show elevated background levels in at least one of the samples. A partial evaluation of selected samples of one analyte element was not performed, because the obtained incomplete PNC data would not be meaningful for a comparison of different sampling sites in the area of Siegen. Therefore, only the spICPMS measurements of $^{90}Zr^+$, $^{107}Ag^+$, and $^{140}Ce^+$ that were acquired with the nanoDAQ MK2 were processed using the prototype ICRA.

4.5. Feasibility test: Nanoparticle screening in surface and waste waters

Surface water samples from 20 sampling sites in the area of Siegen and waste water treatment plant effluent samples from ten local WWTP with discharges into the respective waterbodies were analyzed *via* spICP-MS with the new nanoDAQ MK2 and the matching ICRA to test the feasibility of the established workflow for nanoparticle characterization. The water samples were screened for the presence of nanometer-sized particles containing Ti, Ag, Zr, Ce, or Pb. In the following, the term "Ag-c-NP" will be used to account for the fact that the detected unknown particles are most likely not pure AgNP, but potentially contain other elements and/or a surface coating (which cannot be detected simultaneously during spICP-MS with a quadrupole ICP-MS (ICP-Q-MS), *cf*. Chapter 2.2.3). Due to the high content of dissolved analyte, the evaluation of the measurements with the selected analyte ions of $^{47}Ti^{+}$ and $^{208}Pb^{+}$ could not be performed with the current state of the ICRA.

The level of dissolved Zr, Ag, and Ce was sufficiently low in the analyzed samples to allow a reasonable ion cloud recognition with the ICRA and automatic BG threshold calculation. The number of detected particles during the measurement of each sample was counted automatically, followed by an approximate one-point particle number concentration calibration using the PNC standard LGCQC5050, which had been analyzed with the same measurement parameters directly after the real water samples. It has to be noted, tough, that the detected ion clouds were mostly very small, consisting of only 3–10 DE on average. Due to the non-optimal background calculation algorithm it is likely that an unknown number of background signals were falsely identified as ion clouds. Consequently, the presented estimated PNC are most probably biased. Additionally, only one technical replicate of only one environmental sample was analyzed for the feasibility screening test with the nanoDAQ MK2. Therefore, all obtained figures should be regarded with utmost caution and only serve as indicators for areas of interest for future, more extensive studies. Additionally, a two-point-calibration with AgNP size standards (40 and 60 nm) was carried out to roughly estimate the particle size of detected Ag-c-NP.

4.5.1. Spatial distribution of particle number concentrations

The obtained nanosecond spICP-MS results show that, on average, the PNC of all three particle types is lower in the WWTP effluent (WW) than in the surface water samples (SW), but there is significant variation within both sample types (**Figure 41**). Among the surface waters, especially the sample SW01, SW02, SW04, and SW20 exhibit lower concentrations of Zr- and Ce-containing NP (Zr-c-NP, Ce-c-NP). This observation seems plausible because these sampling sites correspond to the relatively pristine water of the Sieg spring (SW01), a sampling location not too

far downstream the Sieg spring (SW02), the effluent of the Obernau damn (SW04), and the Ferndorf spring (SW20).

Surprisingly, the PNC of Ag-c-NP in the Ferndorf spring water is not significantly lower than in the other water samples, which might be a hint to a non-anthropogenic source of AgNP. However, the overall determined PNC of Ag-c-NP is *ca*. 10 times lower than the PNCs of Zr-c-NP and Ce-c-NP.

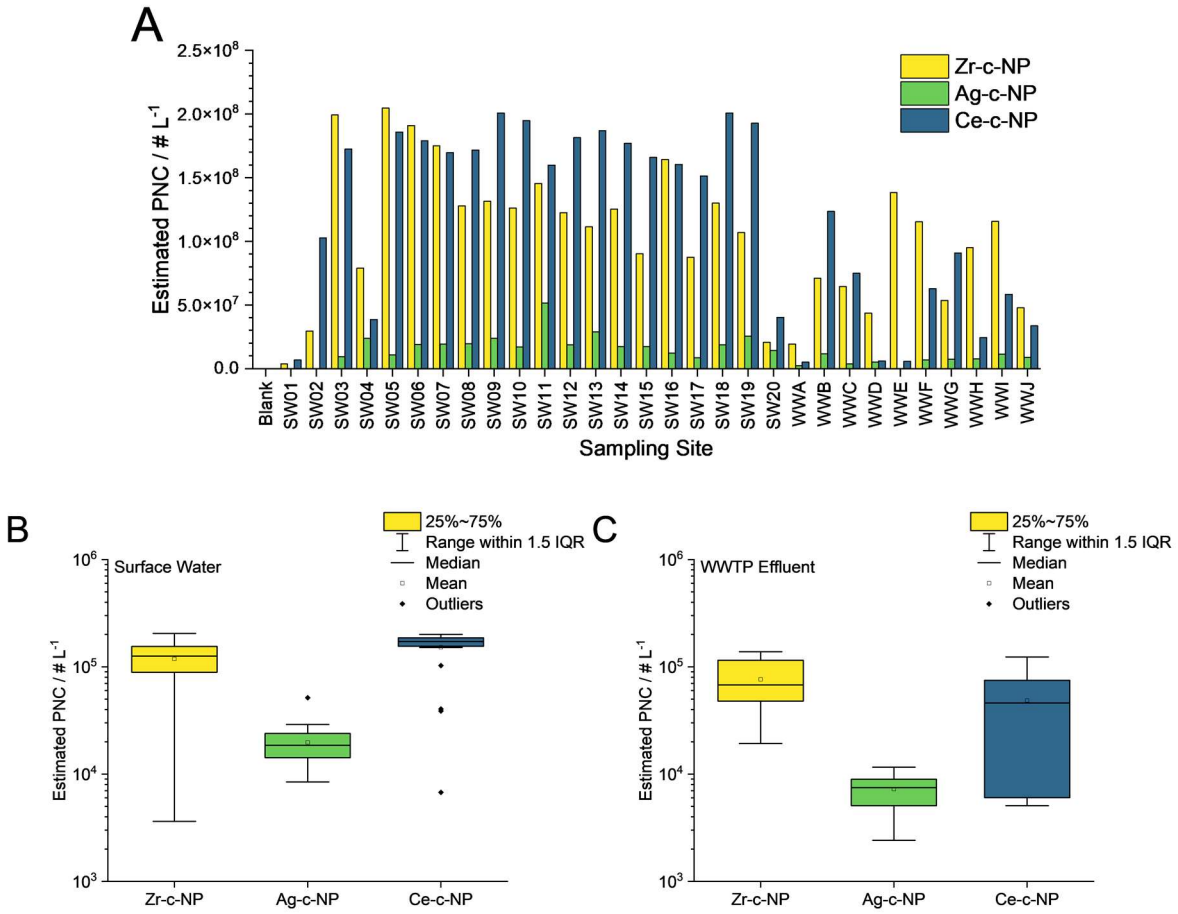


Figure 41. Feasibility test of the spICP-MS measurements with nanosecond time resolution using the nanoDAQ MK2 system and subsequent data processing with the ICRA software to estimate particle number concentrations (PNC) of Zr-, Ag-, and Ce-containing particles in environmental water samples. **A**. Samples were taken on June 21st or June 22^{nd,} 2022 in 20 surface water sampling sites and from the effluent of ten local WWTP in the area of Siegen (n =1, respectively). Boxplots diagrams showcase that the median and mean estimated PNC of the respective NP type in the surface waters (**B**, n = 20) is significantly higher than in the WWTP effluent samples (**C**, n = 10).

The spatial differences of the estimated PNC of particles containing Ce, Zr, and Ag are visualized in **Figure 42**–**Figure 44**. One goal of the screening campaign was to assess whether the occurrence of metal-containing nanoparticles in the surface water streams might be linked to the high prevalence of metal-processing industries in the area of Siegen and especially in close vicinity to the streams. The map in **Figure S8** highlights areas with industrial activity, which helps to interpret the estimated PNC in this regard. The second question was whether the discharge of waste water effluent from municipal WWTP might act as a vector for nanoparticles into the surface water streams.

The estimated PNC of Ce-c-NP in the investigated area seems to correlate with the distribution of industrially-used land surrounding the sampling site. Both water samples taken from the pristine springs of Sieg (SW01) and Ferndorf (SW20) and from the Obernau damn (SW04) contain significantly fewer Ce-c-NP than all other surface water samples. The second sampling point downstream of the Sieg spring (SW02) is situated in-midst the first larger industrial area along the Sieg and already indicates an increase in Ce-c-NP concentration. Throughout the following sampling sites along the Sieg, the PNC increases further. The same trend is observed for the Ferndorf, which appears to gain in Ce-c-NP concentration in the industrially-active areas of Hilchenbach and Kreuztal. The sample of the inflow of the Littfe into the Ferndorf (SW11) in Kreuztal, however, has a lower PNC of Ce-c-NP and does not seem to add to the contamination of the Ferndorf (which flows into the Sieg later).

As a comparison, two water samples were taken from the Heckebach, which only passed a small industrial area downstream its spring before the points of sampling. These two sampling sites themselves were, unlike the others, not situated directly in an industrial area (except for the two springs). Analysis results show that the PNC of Ce-c-NP in both samples (SW16 and SW17) are indeed lower than in the water samples from (downstream) Sieg, Ferndorf, and Littfe. The observations give rise to the assumption that the detected Ce-c-NP in the surface water samples might have anthropogenic origins and are not naturally occurring colloids.

The PNC that were determined for the waste water effluents indicate that the municipal WWTP in the area of Siegen do not contaminate their receiving surface water streams with Ce-c-NP, because the concentrations found in the effluents was always lower than in the sampling points upstream and downstream of the discharge in the respective water body.

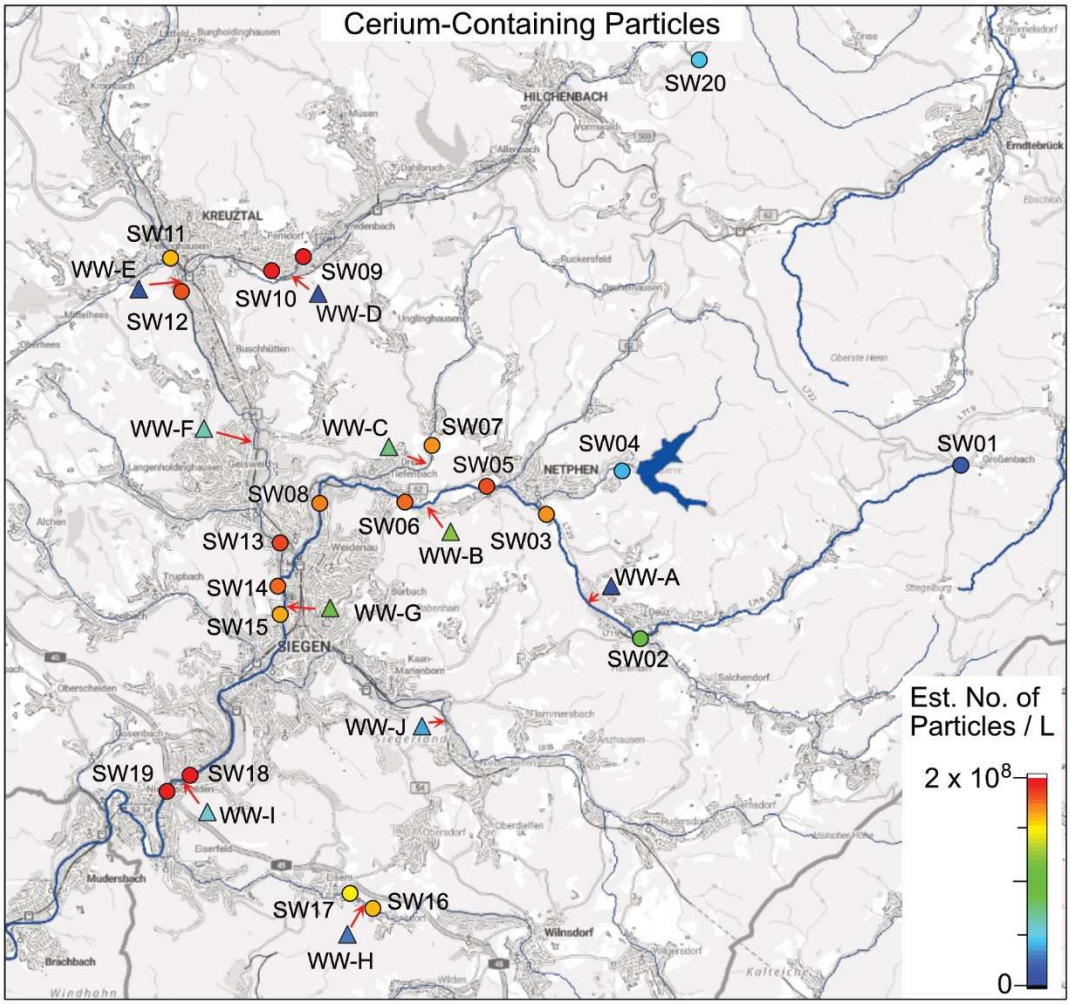


Figure 42. Spatial distribution of the estimated particle number concentration of Ce-c-NP in the investigated area. The estimated PNC in the surface water samples (circles) and WWTP effluent samples (triangles) are indicated by the color scale. The points of discharge of WWTP effluent into the receiving water bodies are marked by red arrows.

As shown in **Figure 41**, the estimated PNC of Zr-c-NP and Ce-c-NP were found to be roughly in the same order of magnitude. However, the local distribution of Zr-c-NP differs noticeably from the distribution of Ce-c-NP. While the Zr-c-NP concentrations are low in in the spring water samples, as well, the PNC only moderately increases in most samples that are located in the industrial areas (**Figure 43**). Solely the samples from the stretch of the Sieg in the area between Netphen and Dreis-Tiefenbach (SW03, SW05, SW06) show significantly increased PNC of Zr-c-NP, which fall back to a relatively moderate level throughout the remaining investigated section of the Sieg. Individual samples from the Dreisbach (SW07), Littfe (SW11), and Heckebach (SW16) were found to have comparatively slightly higher contents of Zr-c-NP, but waters of those sampling sites do not seem to have a contaminative influence on the downstream water or the receiving river. Most waste water effluents contained more Zr-c-NP in comparison to the Ce-c-NP, but again, WWTP effluent

discharges into the surface waters do not appear to release Zr-c-NP in a higher concentration than that of the receiving surface water.

For future investigations, the elevated content of Zr-c-NP in the vicinity to the industrial area in Netphen should be confirmed over a longer time span in order to derive valid conclusions from this preliminary observation and to link the contamination to possible sources of pollution.

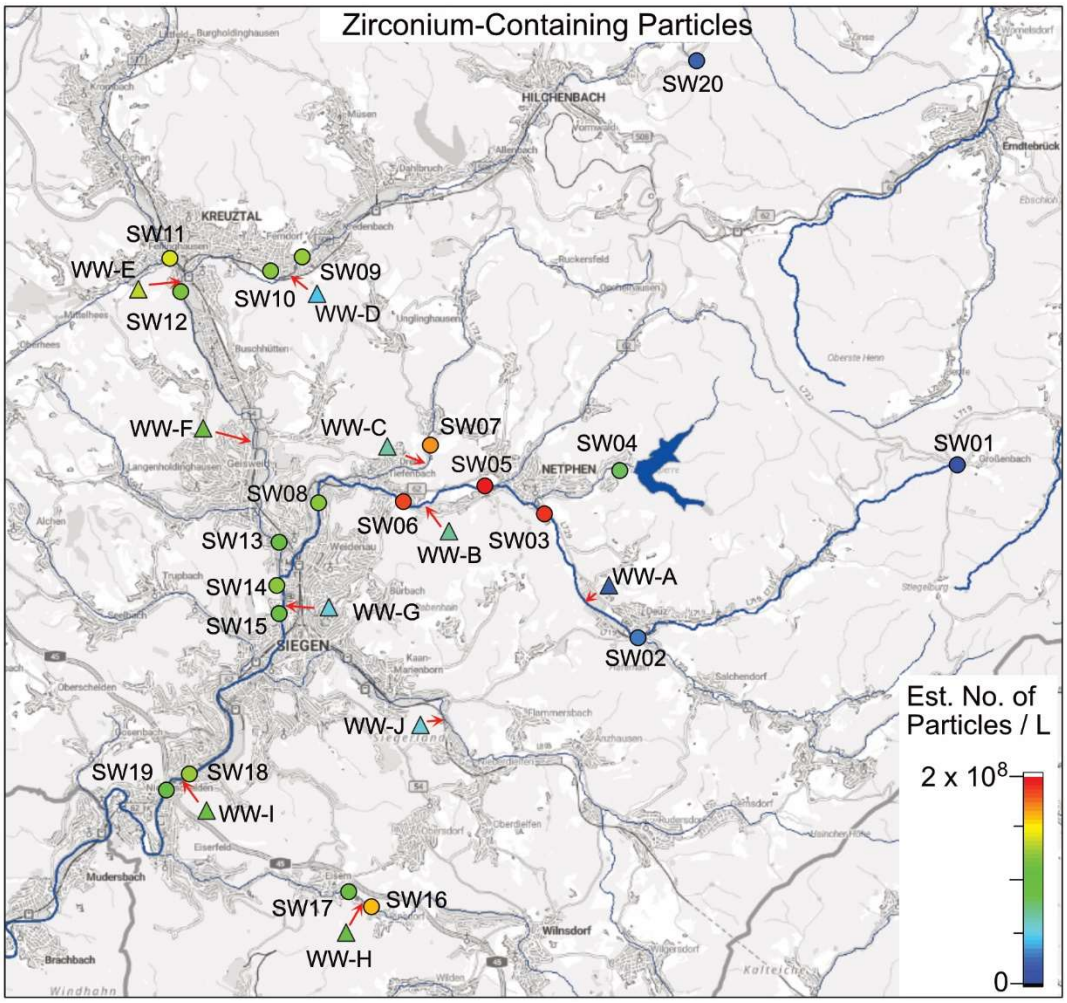


Figure 43. Spatial distribution of the estimated particle number concentration of Zr-c-NP in the investigated area. The estimated PNC in the surface water samples (circles) and WWTP effluent samples (triangles) are indicated by the color scale. The points of discharge of WWTP effluent into the receiving water bodies are marked by red arrows.

Ag-c-NP were detected in ten times lower concentrations in all analyzed samples on average. As expected, concentrations are low in the spring water samples, in areas with low industrial activity, and in the waste water effluent samples (**Figure 44**). PNC steadily increase further downstream, while the Sieg and Ferndorf pass inhabited and industrially-used areas. The water sample from the Obernau (SW07) contained more Ag-c-NP than the sample from the Sieg after the

merging of the two streams, which might indicate that the comparatively low amount of water from the Obernau is significantly diluted after flowing into the Sieg.

Interestingly, in the water sample SW11 from the Littfe in Kreuztal, right before the confluence with the Ferndorf, a significantly higher number of Ag-c-NP was detected. This should be a further point of interest for future investigation in order to verify, whether this result is reproducible and, if so, whether the Ag-c-NP were released into the Littfe further upstream or in close vicinity to the sampling spot (which is also located inside an industrial area). Apparently, the water from the Littfe did not seem to have led to an elevated PNC at the downstream sampling point of the Sieg (SW12) at the time of the sampling campaign, though.

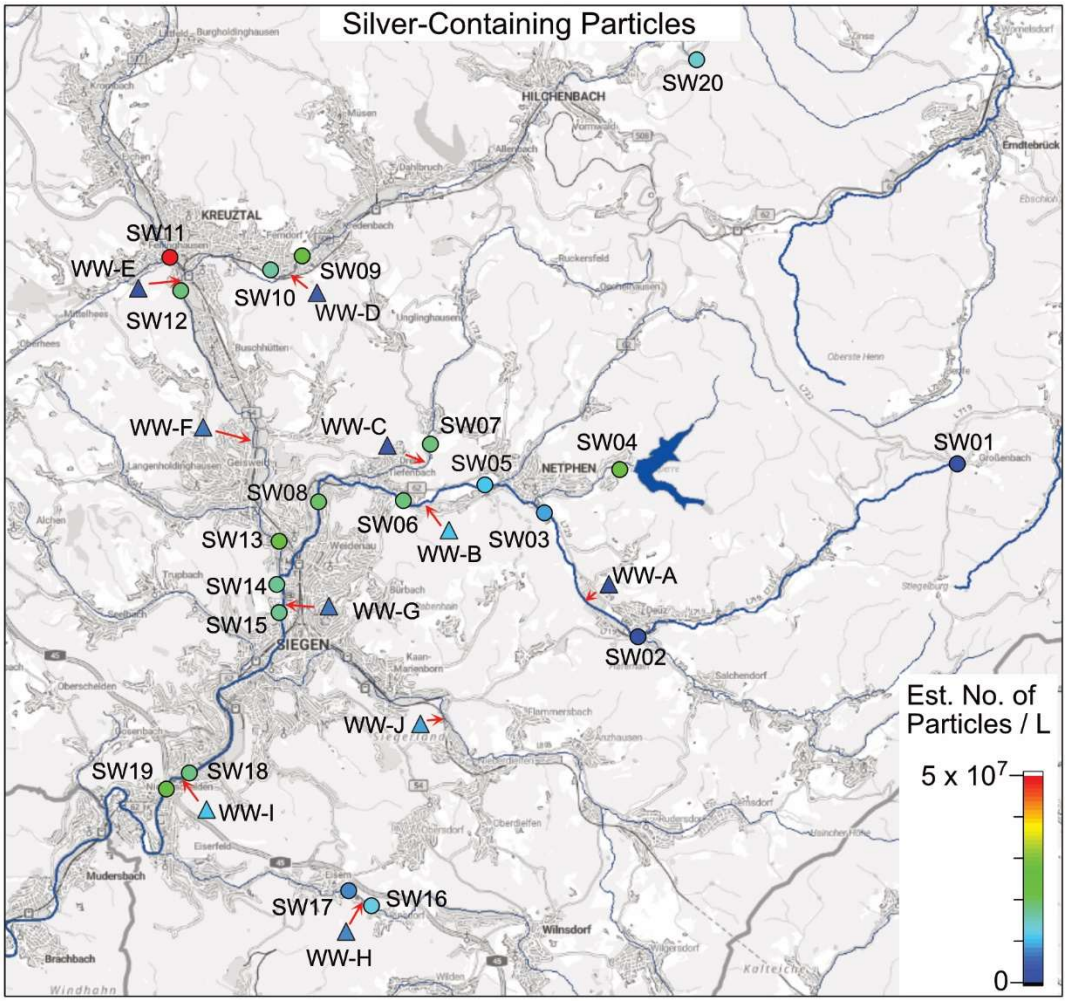


Figure 44. Spatial distribution of the estimated particle number concentration of Ag-c-NP in the investigated area. The estimated PNC in the surface water samples (circles) and WWTP effluent samples (triangles) are indicated by the color scale. The points of discharge of WWTP effluent into the receiving water bodies are marked by red arrows.

As already pointed out, the particle number concentrations that were determined in this feasibility study are only estimates. Only one sample (500 mL) per sampling site was taken, only

one technical replicate was analyzed (15 mL aliquot), and only one measurement was carried out (*ca*. 80 µL), because the measurements that were conducted for this study served only as a pilot feasibility test for the nanoDAQ MK2 and for developing a data processing strategy with the ICRA. The remaining aliquots of the samples are kept frozen for further investigations with an optimized method. Additionally, samples were filtered through 0.45 µm membrane filters prior to spICP-MS analysis, but the determination of the recovery of NP was beyond the scope of this feasibility study. A comprehensive study of the NP recovery after membrane filtration needs to be carried out for each sample (due to varying matrix compositions) and across a large NP size range (*e.g*. 5–125 nm) of all NP types of interest (*e.g*. Ag-c-NP, Ce-c-NP, *etc*.). It also has to be considered that the use of commercially available size standard materials of NP (*e.g*. AgNP) for the recovery determination does not account for the actual composition nor the size of Ag-c-NP (or other NP) in real samples, which may have been altered due to oxidation, sulfidation, or formation of a corona at the particle's surface.[40] However, the surface properties of the particle influence its retention by the membrane material.[147] Therefore, the (elemental) composition and the hydrodynamic diameter of the detected NP in the real samples needs to be elucidated (*e.g*. *via* spICP-ToF-MS and HDC, respectively), as well. The exact determination of the specific recovery of each investigated NP type should be a crucial part of future studies that are conducted to provide validated PNC of NP in the surface waters or waste waters in the area of Siegen.

It is therefore surprising that, nevertheless, the relative values of the estimated PNC of all three particle types display spatial distributions, which indeed seem plausible with regard to the colocalization with industrial areas. Naturally, this interesting observation has to be confirmed by a more extensive sampling campaign, ideally over an extended time span. Points of interest for potential sources of NP could already be identified within the scope of this feasibility study.

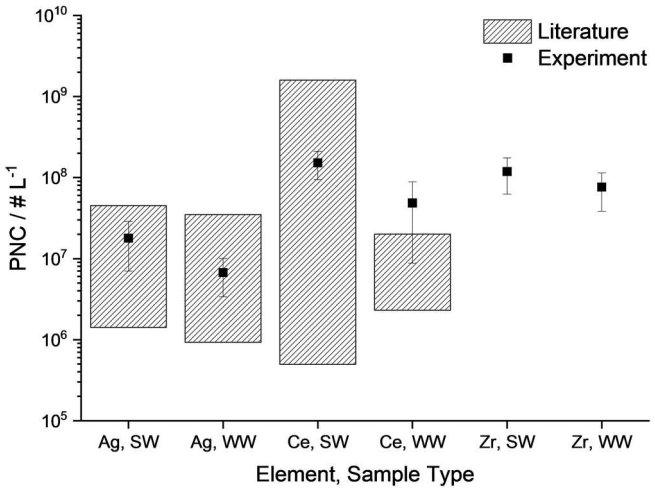


Figure 45. Comparison between the average estimated particle number concentrations that were obtained for surface water (SW) and waste water effluent (WW) in the feasibility experiment within the scope of this thesis (squares) and PNC ranges that were reported for the respective particle types (Ag-, Ce-, and Zr-containing NP) in comparable water samples in the literature (hatched bars). References of the literature size ranges are listed in **Table S1** and **Table 6**.

The PNC that were obtained within the scope of this study only serve as indicative values. Nevertheless, the order of magnitude of the determined average particle number concentration of Ag-c-NP and Ce-c-NP agrees well with the concentration ranges that were reported for those particle types in similar surface waters in the literature (**Figure 45**, **Table 6**). PNC that were found in waste water effluent within this study differed slightly from reported values; Ce-c-NP concentrations were elevated in comparison to the PNC reported in other studies. Unfortunately, the only study that was found to investigate the occurrence of Zr-c-NP in surface water and waste water effluent only determined the mass concentration of the Zr-c-NP fraction after filtration (<450 nm), but not the particle number concentration.[148]

Table 6. Reported size, particle number concentration, and mass concentration of different nanomaterial types in surface waters.

NM	Water Body	Size / nm	PNC / # L^{-1} ($x10^6$)	*c* / µg L^{-1}	Reference
Ag	Besòs River Basin	14–18	17.9–45.1	-	75
Ag	River Dommel	-	-	$(3.0–27) \cdot 10^{-3}$	149
Ag	Verde River	19.2	1.83	$0.2 \cdot 10^{-3}$	150
Ag	Salt River	17	1.42	$0.1 \cdot 10^{-3}$	150
Ag	River Isar, Germany	-	-	$(2.0–8.6) \cdot 10^{-3}$	46
Al	River Dommel			2.84–5.94	148
Ce	Besòs River Basin	37	18–280	-	75
Ce	River Dommel	-	-	0.5–1.4	149
Ce	River Dommel	-	-	$(82–270) \cdot 10^{-3}$	148
Ce	Missouri River	29–44	0.496–0.578	-	72
Ce	Seine River	5–80	470	-	151
Ce	Marne River	5–80	1590	-	151
Ce	Verde River	41	48.3	$18 \cdot 10^{-3}$	150
Ce	Salt River	25	38.5	$6.9 \cdot 10^{-3}$	150
Cu	North Fork of Clear Creek	-	100	-	152
Fe	North Fork of Clear Creek	180	10000	-	152
Ti	Besòs River Basin	37	23.2–298	-	75
Ti	Shijiazhuang Area	-	-	$(52–86) \cdot 10^{-3}$	76
Ti	River Dommel	-	-	0.62–1.80	149
Ti	UK Rivers	-	-	0.4–13.5	153
Ti	River Dommel	-	-	0.68–1.15	148
Ti	Missouri River	153–170	425–451	-	73
Ti	Melbourne Area	79.8	14600	-	154
Ti	Seine River	60–300	1350	-	151
Ti	Marne River	60–300	5890	-	151
Ti	Verde River	225	35.3	$895 \cdot 10^{-3}$	150
Ti	Salt River	144	8.92	$67.0 \cdot 10^{-3}$	150
Ti	Salt River,	68-92	22-310	-	155
Ti	Clear Creek	68-69	46-80	-	155
Ti	Truckee River	68-90	170-250	-	155
Zn	Missouri River	81–114	0.111–0.144	-	72
Zr	River Dommel	-	-	$(74–227) \cdot 10^{-3}$	148
Pb	Melbourne Area	-	395	-	154

4.5.2. Size estimation of detected silver-containing nanoparticles

After the successful detection and estimation of the PNC and the spatial distribution of Ag-c-NP, Ce-c-NP, and Zr-c-NP using the novel nanoDAQ and ICRA, it was attempted to determine the NP size in the real samples, as well. While the method promisingly achieved a very low size detection limit for AuNP in bi-distilled water, some challenges were faced during the analysis of NP with a different elemental composition in samples with a more complex matrix.

Well characterized size standards were not available for Ce-c-NP and Zr-c-NP, which limited the calibration to Ag-c-NP using AgNP size calibration standards. An alternative sizing method (based on dissolved elemental standards instead of NP dispersions) suggested by Pace *et al*.[57] could not be implemented, because the prototype version of the ICRA does not yet provide the average

count rates (counts per second) of dissolved elemental solutions, which are crucial for this calibration approach.

Consequently, it was decided to apply the size estimation test to Ag-c-NP during this feasibility study using size calibration standards of 20, 40, and 60 nm diameter. However, the signal distribution of 20 nm AgNP could not be distinguished from the background signal by the ICRA and therefore, a two-point-calibration with 40 nm and 60 nm AgNP was attempted. One known reason for the apparently much higher size detection limit of AgNP in comparison to AuNP is that silver has two stable isotopes with approx. equal natural abundance, of which only one can be selected for analysis in spICP-Q-MS. This leads to a reduced number of ions that are detected per particle, and indeed, the ICRA only assigned 17 ions on average to one ion cloud (n = 377) for 60 nm-sized AgNP. This value, however, is substantially lower than previously obtained numbers of ions per ion cloud that had been acquired with the same ICP-MS system using microsecond time resolution (approx. 730 counts per ion cloud, n = 10).[65] Evidently, the fact that the instrumental method used in the present study (nebulizer gas flow, ion lenses, sample flow rate, *etc.*) had been optimized for the comparatively heavy $^{197}Au^{+}$ analyte ion comes at a loss of sensitivity for the lighter $^{107}Ag^{+}$. For future analyses of real water samples, it should be considered to develop separate instrumental methods for groups of certain elements to ensure highest sensitivity for each type of NP. Within the scope of this pilot screening study, however, the use of one set of instrumental parameters served the aim to develop a fast screening method for multiple elements in multiple real water samples.

In Chapter 4.4.4, two different particle sizing approaches for the data obtained from the nanoDAQ had been compared and discussed. It was suggested that the count-based approach might be favourable for the current version of the ICRA, because the mathematical correlation between the average 1/log(EG) per ion cloud and the particle size has not been elucidated yet. However, the low number of counts per ion cloud that were detected in the AgNP size standards and in the Ag-c-NP severely hinder the conventional count-based size calibration *via* the radius units (**Figure 46B**). The number of DE per ion cloud of almost all samples was below the calibration range Note that only *ca*. 4 DE were detected for the 40 nm AgNP size standard and *ca*. 3 DE per ion cloud were most frequently detected in the environmental water samples. These values are very close to the minimum number of DE that are required for the ICRA to label a succession of DE as an ion cloud (3rd criterion).

Consequently, the size calibration method based on the average 1/log(EG) value was tested instead (**Figure 46A**). The advantage of the nanosecond time-resolved data is that the 1/log(EG) parameter provides additional information, even though the number of detected ions alone would not be sufficient to distinguish particle sizes. The variance of the 1/log(EG) values (*i.e.* the ion cloud

density) seems to be sufficiently high to distinguish between ion clouds with the same number of DE (here: 3). It is assumed that the original Ag-c-NP had different sizes. Those were ionized in the plasma and created ion clouds with different average ion densities, but only a small fraction of these ions was transmitted to the detector. However, the number of detected ions per ion cloud cannot be lower than 3 (due to the 3rd criterion of the ICRA), even though the original ratios of the number of atoms per particle size was not equal. In contrast, the average 1/log(EG) values of NP in the water samples (**Figure 46A**) have a higher variance in comparison to the narrow distribution of the average number of DE per ion cloud (**Figure 46B**).

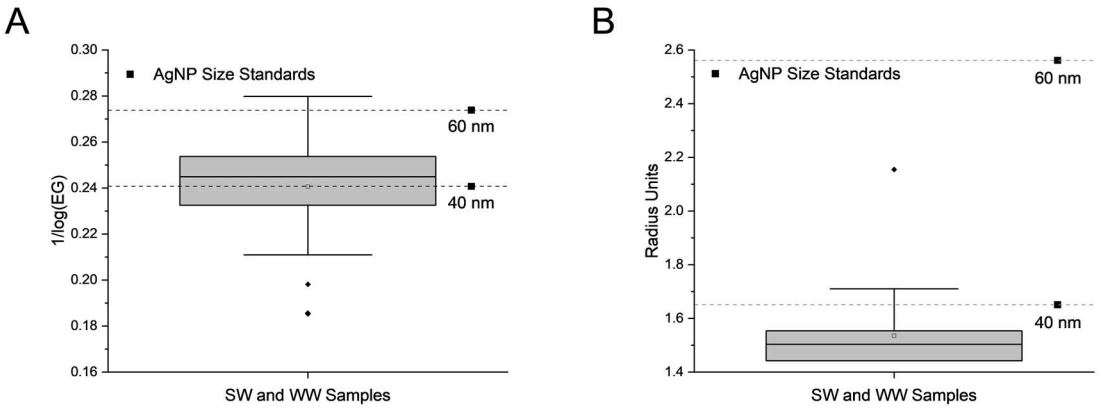


Figure 46. Comparison of two size calibration approaches for the determination of Ag-c-NP in environmental water samples based on **A**. the average 1/log(EG) and **B**. the average radius unit per particle in each sample. For both methods, a 2-point size calibration was carried out using 40 nm and 60 nm AgNP standard solutions from nanoComposix and they were performed with identical measurement files. Most Ag-c-NP in the water sample have average 1/log(EG) values within the calibrated range and their deviation is large enough to determine size differences. The deviation of the average radius unit per Ag-c-NP in the observed size range is too small to determine their size with sufficient sensitivity and most of the determined radius units are below the calibrated range.

Therefore it was decided to perform a size calibration using the 1/log(EG) values to roughly estimate the sizes of the Ag-c-NP that were detected in the surface water and waste water effluent samples of the campaign (**Figure 47**). Only samples in which more than ten particles were detected during 30 s of measurement were considered and only Ag-c-NP that did not exceed the calibration range by more than ±5 nm are shown. The estimated average particle sizes apparently vary between the water samples from different sampling locations, but no obvious trend can be derived from the available data. As discussed above, the number of samples and replicates needs to be higher to obtain representative data and the instrumental settings need to be optimized to obtain a higher sensitivity for Ag-c-NP in order to create a valid size calibration. It also should be kept in mind that the presented particle sizes are probably biased toward larger sizes, because the smaller particles in the water samples could not be recognized by the ICRA.

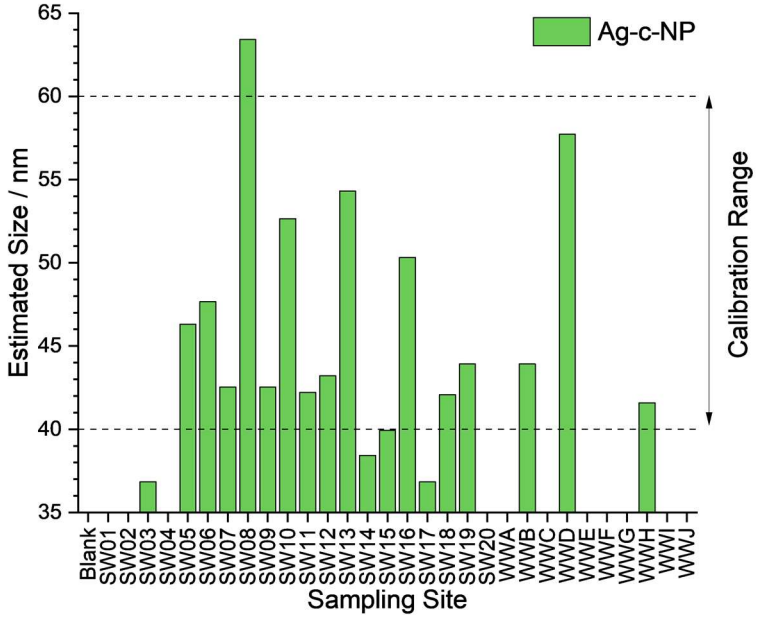


Figure 47. Estimated sizes of Ag-c-NP that were detected in surface water (SW) and waste water effluent (WW) samples *via* spICP-MS with the nanoDAQ MK2 system and subsequent data processing with the ICRA software. Size estimation was carried out *via* 2-point calibration of the 1/log(EG) value using 40 nm and 60 nm AgNP size standards from nanoComposix. Sizes correspond to solid, spherical particles bearing exclusively silver atoms with the bulk density of silver. Only samples with more than ten detected particles within the measurement time of 30 s were considered.

Nevertheless, the size calibration test revealed challenges that arise from data processing with the ICRA and from using "one-size-fits-all" instrumental settings for spICP-MS screening of multiple elements. These observations provide important information for future surface water screening campaigns with subsequent nanosecond spICP-MS analysis with the nanoDAQ MK2 and point out the need for additional features, which should be implemented into an advanced version of the ICRA. Specifically, a tool for the determination of background or dissolved standard concentrations, an automatic size calibration tool, and an export function for histogram data from the ICRA will expand the application range of the software and are already planned for the next version. When the above described optimizations of the instrumental tune settings and of the software features are considered for the development of a successive method, the full potential of the nanoDAQ and ICRA can be utilized to achieve low size detection limits, short data acquisition times, and fast data processing for high-throughput NP screenings.

4.5.3. Evaluation of the NP screening results

Potential sources of Ag-c-NP, Ce-c-NP, and Zr-c-NP that were detected in the surface water samples from the studied area are manifold. Anthropogenic sources of intentionally produced

nanomaterials into the environment are the direct or indirect release during production or use of the ENM, or at the end of the material's life cycle.[156] Nanomaterials can also be produced unintentionally, *e.g*. by mining, welding, or industrial processes in general.[71]

Specifically, Ce-c-NP are used for chemical-mechanical polishing in some electronic industries, as an additive to diesel fuel to improve combustion efficiency, and in automobile catalysts.[157] Another element that is commonly used in catalysts is Zr, and indeed both particulate Zr and Ce have been detected in road runoff sediments.[158] It can therefore be assumed that surface water bodies in areas with industrial activity and/or high traffic are potentially vulnerable to contamination with Ce-c-NP and Zr-c-NP, which agrees with the observations in this study. It should also be noted that many metal processing companies are situated in the area of Siegen in close vicinity to the surface water streams. Those might potentially act as unintentional sources of NP that were incidentally created *via* degradation from bulk materials during metal processing or *via* powder coating. Airborne particles might directly enter surface waters or accumulate on nearby surfaces (*e.g*. rooftops, roads, plants *etc*.). During rainfalls, the particles might then be washed into the water streams. The possibility that NP are released into the environment *via* this route despite preventive actions of the companies should be evaluated very carefully after further confirmational sampling campaigns and analyses. However, certain companies (*e.g*. several steel plants and metal processing plants) in the area are known to directly discharge industrially used water into nearby surface water streams.[159] They are obliged to test and report the chemical composition of their industrial waste water and are subject to regular federal inspections. A potential correlation between the observed increased PNC of NP in the industrial areas and the discharge of these companies should be closely examined and confirmed.

In addition, the detected NP may also be naturally occurring nanomaterials, as *e.g*. the cerium-containing mineral allanite, which has been found in riverbed sediments.[160] In general, geogenic sources of nanometer-sized particulates can be (among others) forest fires, (past) volcano eruptions, or erosions.[71] Natural NP and engineered NP can sometimes be differentiated by their elemental fingerprint, because natural NP usually contain several trace elements (*e.g*. La, Ba, Pr, Nd, and Th) or certain elements in specific ratios (*e.g*. Ce/La).[75,84,149] Due to the limitation to only one analyte isotope per measurement, the spICP-Q-MS method that was used in this work is not capable to distinguish between naturally occurring and engineered particles. However, future investigations on the NP content in surface waters in the area of Siegen could be supported by simultaneous spICP-ToF-MS analysis of several isotopes to classify the origin of the detected NP. This would aid to confirm the observed increase of the PNC of Ce-c-NP and Zr-c-NP in the industrially active areas, which are usually accompanied by increased automobile traffic.

Silver can be used in batteries, bearings, catalysts, electronics, during brazing and soldering,[161] and as all nanomaterials, Ag-c-NP might be formed and released into the environment during any stage of the product life cycle, or leach from deposited waste on landfills.[39] In consumer products, AgNP are often used due to their antimicrobial properties, and may *e.g*. be released into the waste water system during the washing of sports clothing.[150,162] However, the low concentrations of Ag-c-NP in the WWTP effluent that were detected within this work and previous studies[47] suggest that the WWTP remove the NP from the waste water efficiently. As shown above, the concentrations of Ag-c-NP in the surface water samples were mostly *ca*. 10 times lower than the PNC of Ce-c-NP and Zr-c-NP (*cf*. **Figure 41**), which indicates that their release occurs on a much lower scale.

The elucidation of the origins of the three detected different nanomaterial types is beyond the scope of this NP screening study, however, points of interest for future studies could be identified successfully, as *e.g*. the significant increase of the Ag-c-NP PNC in sample SW11 in Kreuztal.

5. Concluding Remarks and Future Perspectives

Based on:

A. Schardt, J. Schmitt, C. Engelhard, Single particle inductively coupled plasma mass spectrometry with nanosecond time resolution, *J. Anal. At. Spectrom*., 2024, **39**, 389–400.
DOI: 10.1039/D3JA00373F.

Single particle inductively coupled plasma mass spectrometry is an important tool for the characterization of nanoparticles in environmental water samples. Previously, spICP-MS with milli- or microsecond time resolution was used to detect transient signals of individual NP in suspensions. In this thesis, two novel data acquisition units (nanoDAQ MK1 and MK2) for the characterization of NP were carefully developed, optimized, and evaluated regarding their capability to analyze NP in environmental samples. For the first time, nanosecond time-resolved spICP-MS was used to detect and analyze NP in river water and waste water treatment plant effluent water. A novel data processing approach for high-throughput analysis of the nanosecond time-resolved spICP-MS data was developed. The potentials and future challenges of the novel data acquisition hardware and tailored software were evaluated in the field study and provide insights into possible improvements of the systems.

In Chapter 4.1 it is showcased that the nanoDAQ MK1 enabled the recording of individual ion clouds at the SEM detector of the mass spectrometer with a dwell time of 4.2 ns. Time-resolved pulse-counting signals (detector events, DE) were obtained and provide information on ion arrival times at the detector. Time spans with no or very little counts were assumed to be background noise and time spans with a high event density were assumed to originate from dense ion clouds. With a tailored data processing method, it was possible to visualize and quantify the temporal gap or event gap, with which the ions arrive at the detector during the analysis of gold nanoparticle dispersions.

In Chapter 4.2, it was found that the average inverse logarithm of the EG (1/log) of the ions that stem from ion clouds is proportional to the mean of the original particle's size. This proportionality was utilized for a particle size calibration for unknown particle dispersions. The nanoDAQ MK1 enabled the distinction of 6.5 nm-sized AuNP from the background signal in a pure model solution within 60 s of net measurement time. Furthermore, the total number of DE in the measurement data file of a monodisperse NP suspension was found to be proportional to the particle number concentration. However, the methods capability to distinguish particle size distributions in a mixture of two NP types or to detect NP in the presence of elevated ionic background was found to be limited. Additionally, signal artifacts were observed in the processed data files, which hampered NP sizing and gave cause for improvement of the data acquisition hardware and software.

Consequently, the improved successor nanoDAQ MK2 with an effective time resolution of 2.2 ns and a manual particle-by-particle analysis approach were presented in Chapter 4.3. Simultaneous measurements with the established µsDAQ, the novel nanoDAQ MK1, and nanoDAQ MK2 were conducted to compare their figures of merit, *i.e.* the ion detection efficiency

per individual NP and the suitability of the obtained data to perform NP size determination with optimum size accuracy and across a maximum dynamic range. The nanoDAQ MK2 was empirically found to enable an improved particle size detection limit of 5 nm for AuNP in a pure model solution. It was also demonstrated that ion density-dependent signal artifacts due to reflections of electronic pulses within the experimental set up for the parallel measurements affect the signal intensity distributions (and consequently the particle size distributions).

To achieve the goal of a high-throughput analysis method for NP in water samples, a newly developed ion cloud recognition algorithm (ICRA) was tested and evaluated in Chapter 4.4. The software was developed to enable direct visualization of the transient raw data and to provide quick data processing and output of results for NP sizing and counting, without the need for additional data processing software. ICRA was also developed to automatically calculate a background threshold based on the ion density in transient measurement files, which is indispensable for the analysis of NP in environmental water samples. While ICRA already succeeded enabling fast data analysis for NP in pure samples and environmental water samples with low background, the detection of false positive DE by the nanoDAQ MK2 hardware still limited its applicability to samples with high matrix content. A data filtering feature that removes non-plausible false positive DE within the detector dead time was already implemented. However, the settings need to be further improved for optimum results.

Because the nanoDAQ MK2 in combination with ICRA already provided satisfactory results for NP suspensions with low background, the system was tested on river water and waste water treatment plant effluent water within a field study in Chapter 4.5. The method could be utilized to estimate the particle number concentrations of NP containing Ag, Ce, or Zr, while the size calibration approach requires further optimization and additional software features. The average PNC of all three NP types was found to be significantly higher in the surface water samples than in the WWTP effluent samples. The spatial distribution of the PNC of the three NP types in surface waters from the area of Siegen was determined. Low concentrations of NP were detected in the pristine water of two springs compared to relatively increased PNC in river sections that are located in industrially active areas, which might indicate anthropogenic origins of the NP. However, the field sampling campaign was not designed to supply statistically reliable data, but rather served as a proof-of-principle study for the nanoDAQ MK2 and to highlight sampling areas of interest that should be carefully examined in future studies.

In the future, the need for fast, high-throughput analysis methods for nanomaterials with lowest possible size detection limits will grow further to meet the demands of potential future federal regulations. Because spICP-MS enables both NP size and PNC determination in a direct-

injection manner with minimum sample preparation, it has already become a routine tool for the characterization of NP in a variety of consumer products and environmental samples. The prototype hardware modifications and data processing software for conventional single quadrupole mass spectrometers presented in this work have contributed to further decrease the effective size detection limit of spICP-MS and to extend the PNC dynamic range by avoiding particle-coincidence, while maintaining short measurement times and minimum sample preparation.

In the opinion of the author, the application range of spICP-MS may be significantly expanded by the implementation of artificial intelligence into the data processing workflow to identify and characterize NP signals in the raw data in future developments. The use of nanosecond time resolution for spICP-MS provides size and concentration information on a statistically relevant number of particles in a significantly shorter data acquisition time than microscopy-based techniques and therefore may be used increasingly as a complementary tool for analyses at the nanoscale. Furthermore, the combination of the nanosecond time-resolved data acquisition and the rising field of multi-elemental fingerprinting using time-of-flight mass spectrometers could provide interesting new possibilities for the classification and characterization of nanomaterials.

After addressing the challenges of the nanoDAQ MK2 and ICRA mentioned above, *i.e*. filtering of false positive detector events and optimization of the background threshold calculation, the system should have the potential to be used as a routine method for NP analysis in a variety of relevant environmental liquid samples with minimal hardware modifications on commercially available, low-cost quadrupole mass analyzers and a tailored software package.

Appendix

I. Supplementary tables

Table S1. Reported size, particle number concentration, and mass concentration of different nanomaterial types in waste water treatment plant effluents.

NM	Size / nm	PNC / # L^{-1} ($x10^6$)	*c* / µg L^{-1}	Reference
Ag		9.57		157
Ag		35		75
Ag			$0.9 \cdot 10^{-3}$	163
Ag	13.4		$1.77 \cdot 10^{-3}$	164
Ag			0.1	165
Ag			$7 \cdot 10^{-3}$	149
Ag	19–25	0.929–10.4	$(0.1–2.1) \cdot 10^{-3}$	150
Ag	15.3		$(0.7–11.1) \cdot 10^{-3}$	46
Al			$0.4 \cdot 10^{-3}$	163
Al	55		$16.2 \cdot 10^{-3}$	164
Al			3.19	148
Au			$0.2 \cdot 10^{-3}$	163
Au	43		$3.8 \cdot 10^{-3}$	164
Cd			$0.5 \cdot 10^{-3}$	163
Cd	60.1		$0.24 \cdot 10^{-3}$	164
Ce		20		75
Ce		2.31		157
Ce			$8 \cdot 10^{-3}$	163
Ce			$52 \cdot 10^{-3}$	149
Ce	24		$0.75 \cdot 10^{-3}$	164
Ce	19–31	5.53–6.95	$(42–85) \cdot 10^{-3}$	150
Ce			0.102	148
Co			$1.5 \cdot 10^{-3}$	163
Co	52.4		$2.56 \cdot 10^{-3}$	164
Cu			0.3	163
Cu	94.5		$25.6 \cdot 10^{-3}$	164
Fe			0.2	163
Fe	168.8		0.35	164
Mg			1	163
Mg	1734		70.2	164
Mn			$20 \cdot 10^{-3}$	163
Mn	322.1		0.65	164
Ni			$15 \cdot 10^{-3}$	163
Ni	102.9		$37 \cdot 10^{-3}$	164
Ti		78		75
Ti		32.7		157
Ti			0.5	163
Ti	86.1		0.24	164
Ti			0.84	148
Ti			26.9–43.1	76
Ti			1.6	166
Ti			0.41	149
Ti			1.6–3.6	153
Ti	4–30		$(0.18–1.23) \cdot 10^{3}$	167
Ti	143-174	5.61–12.2	$(57.0–124) \cdot 10^{-3}$	150
Zn			$8 \cdot 10^{-3}$	163
Zn	101.7		$7.38 \cdot 10^{-3}$	164
Zr			$33 \cdot 10^{-3}$	148

Table S2. Calculation of the probability distribution P(k,λ) for a number of k ions striking the SEM detector during a dwell time of 5 µs with an expectation value λ =1.75 (corresponding to average $^{115}In^{+}$ signal intensity of exemplary 1 µg L^{-1} Indium solution).

k	P(k,λ)	P(k,λ) cumulated	1 – P(k,λ) cumulated
0	1.74E-01	1.74E-01	8.26E-01
1	3.04E-01	4.78E-01	5.22E-01
2	2.66E-01	7.44E-01	2.56E-01
3	1.55E-01	8.99E-01	1.01E-01
4	6.79E-02	9.67E-01	3.29E-02
5	2.38E-02	9.91E-01	9.13E-03
6	6.93E-03	9.98E-01	2.20E-03
7	1.73E-03	1.00E+00	4.68E-04
8	3.79E-04	1.00E+00	8.90E-05
9	7.37E-05	1.00E+00	1.53E-05
10	1.29E-05	1.00E+00	2.40E-06

Table S3. Calculation of the probability distribution P(k,λ) for a number of k ions striking the SEM detector during a dwell time of 4.2 ns with an expectation value $\lambda = 1.46 \cdot 10^{-3}$ (corresponding to average $^{115}In^{+}$ signal intensity of exemplary 1 µg L^{-1} Indium solution).

k	P(k,λ)	P(k,λ) cumulated	1 – P(k,λ) cumulated
0	9.99E-01	9.99E-01	1.46E-03
1	1.46E-03	1.00E+00	1.06E-06
2	1.06E-06	1.00E+00	5.16E-10
3	5.16E-10	1.00E+00	1.88E-13
4	1.88E-13	1.00E+00	0.00E+00
5	5.49E-17	1.00E+00	0.00E+00
6	1.33E-20	1.00E+00	0.00E+00
7	2.78E-24	1.00E+00	0.00E+00
8	5.07E-28	1.00E+00	0.00E+00
9	8.22E-32	1.00E+00	0.00E+00
10	1.20E-35	1.00E+00	0.00E+00

Table S4. Calculation of the probability distribution P(k,λ) for a number of k ions striking the SEM detector during a dwell time of 1.9 ns with an expectation value $\lambda = 6.65 \cdot 10^{-4}$ (corresponding to average $^{115}In^{+}$ signal intensity of exemplary 1 µg L^{-1} Indium solution).

k	P(k,λ)	P(k,λ) cumulated	1 – P(k,λ) cumulated
0	9.99E-01	9.99E-01	6.65E-04
1	6.65E-04	1.00E+00	2.21E-07
2	2.21E-07	1.00E+00	4.90E-11
3	4.90E-11	1.00E+00	7.99E-15
4	8.14E-15	1.00E+00	0.00E+00
5	1.08E-18	1.00E+00	0.00E+00
6	1.20E-22	1.00E+00	0.00E+00
7	1.14E-26	1.00E+00	0.00E+00
8	9.48E-31	1.00E+00	0.00E+00
9	7.00E-35	1.00E+00	0.00E+00
10	4.66E-39	1.00E+00	0.00E+00

Table S5. Calculation of the probability distribution P(k,λ) for a number of k ions striking the SEM detector during a dwell time of 4.2 ns with an expectation value $\lambda = 3.33 \cdot 10^{-2}$ (corresponding to maximum signal intensity of exemplary 80 nm AuNP).

k	P(k,λ)	P(k,λ) cumulated	1 – P(k,λ) cumulated
0	9.67E-01	9.67E-01	3.28E-02
1	3.22E-02	9.99E-01	5.43E-04
2	5.37E-04	1.00E+00	6.02E-06
3	5.97E-06	1.00E+00	5.01E-08
4	4.98E-08	1.00E+00	3.34E-10
5	3.32E-10	1.00E+00	1.85E-12
6	1.84E-12	1.00E+00	8.88E-15
7	8.78E-15	1.00E+00	0.00E+00
8	3.66E-17	1.00E+00	0.00E+00
9	1.36E-19	1.00E+00	0.00E+00
10	4.52E-22	1.00E+00	0.00E+00

Table S6. Calculation of the probability distribution P(k,λ) for a number of k ions striking the SEM detector during a dwell time of 1.9 ns with an expectation value $\lambda = 1.52 \cdot 10^{-2}$ (corresponding to maximum signal intensity of exemplary 80 nm AuNP).

k	P(k,λ)	P(k,λ) cumulated	1 – P(k,λ) cumulated
0	9.85E-01	9.85E-01	1.51E-02
1	1.50E-02	1.00E+00	1.14E-04
2	1.14E-04	1.00E+00	5.79E-07
3	5.76E-07	1.00E+00	2.20E-09
4	2.19E-09	1.00E+00	6.68E-12
5	6.66E-12	1.00E+00	1.68E-14
6	1.69E-14	1.00E+00	0.00E+00
7	3.66E-17	1.00E+00	0.00E+00
8	6.96E-20	1.00E+00	0.00E+00
9	1.18E-22	1.00E+00	0.00E+00
10	1.79E-25	1.00E+00	0.00E+00

Table S7. Calculation of the probability distribution P(k,λ) for a number of k ions striking the SEM detector during a dwell time of 5 µs with an expectation value λ = 40 (corresponding to maximum signal intensity of exemplary 80 nm AuNP).

k	P(k,λ)	P(k,λ) cumulated	1 – P(k,λ) cumulated	k	P(k,λ)	P(k,λ) cumulated	1 – P(k,λ) cumulated
0	4.25E-18	4.25E-18	1.00E+00	continued:			
1	1.70E-16	1.74E-16	1.00E+00	61	4.45E-04	9.99E-01	7.56E-04
2	3.40E-15	3.57E-15	1.00E+00	62	2.87E-04	1.00E+00	4.69E-04
3	4.53E-14	4.89E-14	1.00E+00	63	1.82E-04	1.00E+00	2.87E-04
4	4.53E-13	5.02E-13	1.00E+00	64	1.14E-04	1.00E+00	1.73E-04
5	3.63E-12	4.13E-12	1.00E+00	65	7.01E-05	1.00E+00	1.03E-04
6	2.42E-11	2.83E-11	1.00E+00	66	4.25E-05	1.00E+00	6.00E-05
7	1.38E-10	1.66E-10	1.00E+00	67	2.54E-05	1.00E+00	3.47E-05
8	6.91E-10	8.57E-10	1.00E+00	68	1.49E-05	1.00E+00	1.97E-05
9	3.07E-09	3.93E-09	1.00E+00	69	8.65E-06	1.00E+00	1.11E-05
10	1.23E-08	1.62E-08	1.00E+00	70	4.94E-06	1.00E+00	6.15E-06
11	4.46E-08	6.08E-08	1.00E+00	71	2.78E-06	1.00E+00	3.36E-06
12	1.49E-07	2.10E-07	1.00E+00	72	1.55E-06	1.00E+00	1.81E-06
13	4.58E-07	6.67E-07	1.00E+00	73	8.48E-07	1.00E+00	9.67E-07
14	1.31E-06	1.98E-06	1.00E+00	74	4.58E-07	1.00E+00	5.08E-07
15	3.49E-06	5.46E-06	1.00E+00	75	2.44E-07	1.00E+00	2.64E-07
16	8.72E-06	1.42E-05	1.00E+00	76	1.29E-07	1.00E+00	1.35E-07
17	2.05E-05	3.47E-05	1.00E+00	77	6.68E-08	1.00E+00	6.86E-08
18	4.56E-05	8.03E-05	1.00E+00	78	3.43E-08	1.00E+00	3.43E-08
19	9.60E-05	1.76E-04	1.00E+00	79	1.74E-08	1.00E+00	1.70E-08
20	1.92E-04	3.68E-04	1.00E+00	80	8.68E-09	1.00E+00	8.28E-09
21	3.66E-04	7.34E-04	9.99E-01	81	4.28E-09	1.00E+00	4.00E-09
22	6.65E-04	1.40E-03	9.99E-01	82	2.09E-09	1.00E+00	1.91E-09
23	1.16E-03	2.56E-03	9.97E-01	83	1.01E-09	1.00E+00	8.98E-10
24	1.93E-03	4.48E-03	9.96E-01	84	4.80E-10	1.00E+00	4.18E-10
25	3.08E-03	7.57E-03	9.92E-01	85	2.26E-10	1.00E+00	1.93E-10
26	4.74E-03	1.23E-02	9.88E-01	86	1.05E-10	1.00E+00	8.78E-11
27	7.03E-03	1.93E-02	9.81E-01	87	4.83E-11	1.00E+00	3.96E-11
28	1.00E-02	2.94E-02	9.71E-01	88	2.19E-11	1.00E+00	1.76E-11
29	1.38E-02	4.32E-02	9.57E-01	89	9.86E-12	1.00E+00	7.77E-12
30	1.85E-02	6.17E-02	9.38E-01	90	4.38E-12	1.00E+00	3.39E-12
31	2.38E-02	8.55E-02	9.14E-01	91	1.93E-12	1.00E+00	1.46E-12
32	2.98E-02	1.15E-01	8.85E-01	92	8.37E-13	1.00E+00	6.24E-13
33	3.61E-02	1.51E-01	8.49E-01	93	3.60E-13	1.00E+00	2.63E-13
34	4.25E-02	1.94E-01	8.06E-01	94	1.53E-13	1.00E+00	1.10E-13
35	4.85E-02	2.42E-01	7.58E-01	95	6.45E-14	1.00E+00	4.56E-14
36	5.39E-02	2.96E-01	7.04E-01	96	2.69E-14	1.00E+00	1.88E-14
37	5.83E-02	3.55E-01	6.45E-01	97	1.11E-14	1.00E+00	7.66E-15
38	6.14E-02	4.16E-01	5.84E-01	98	4.53E-15	1.00E+00	3.11E-15
39	6.29E-02	4.79E-01	5.21E-01	99	1.83E-15	1.00E+00	0.00E+00
40	6.29E-02	5.42E-01	4.58E-01	100	7.32E-16	1.00E+00	0.00E+00
41	6.14E-02	6.03E-01	3.97E-01				
42	5.85E-02	6.62E-01	3.38E-01				
43	5.44E-02	7.16E-01	2.84E-01				
44	4.95E-02	7.66E-01	2.34E-01				
45	4.40E-02	8.10E-01	1.90E-01				
46	3.82E-02	8.48E-01	1.52E-01				
47	3.25E-02	8.80E-01	1.20E-01				
48	2.71E-02	9.08E-01	9.25E-02				
49	2.21E-02	9.30E-01	7.03E-02				
50	1.77E-02	9.47E-01	5.26E-02				
51	1.39E-02	9.61E-01	3.87E-02				
52	1.07E-02	9.72E-01	2.81E-02				
53	8.06E-03	9.80E-01	2.00E-02				
54	5.97E-03	9.86E-01	1.40E-02				
55	4.34E-03	9.90E-01	9.68E-03				
56	3.10E-03	9.93E-01	6.58E-03				
57	2.18E-03	9.96E-01	4.40E-03				
58	1.50E-03	9.97E-01	2.90E-03				
59	1.02E-03	9.98E-01	1.88E-03				
60	6.79E-04	9.99E-01	1.20E-03				

II. Supplementary figures

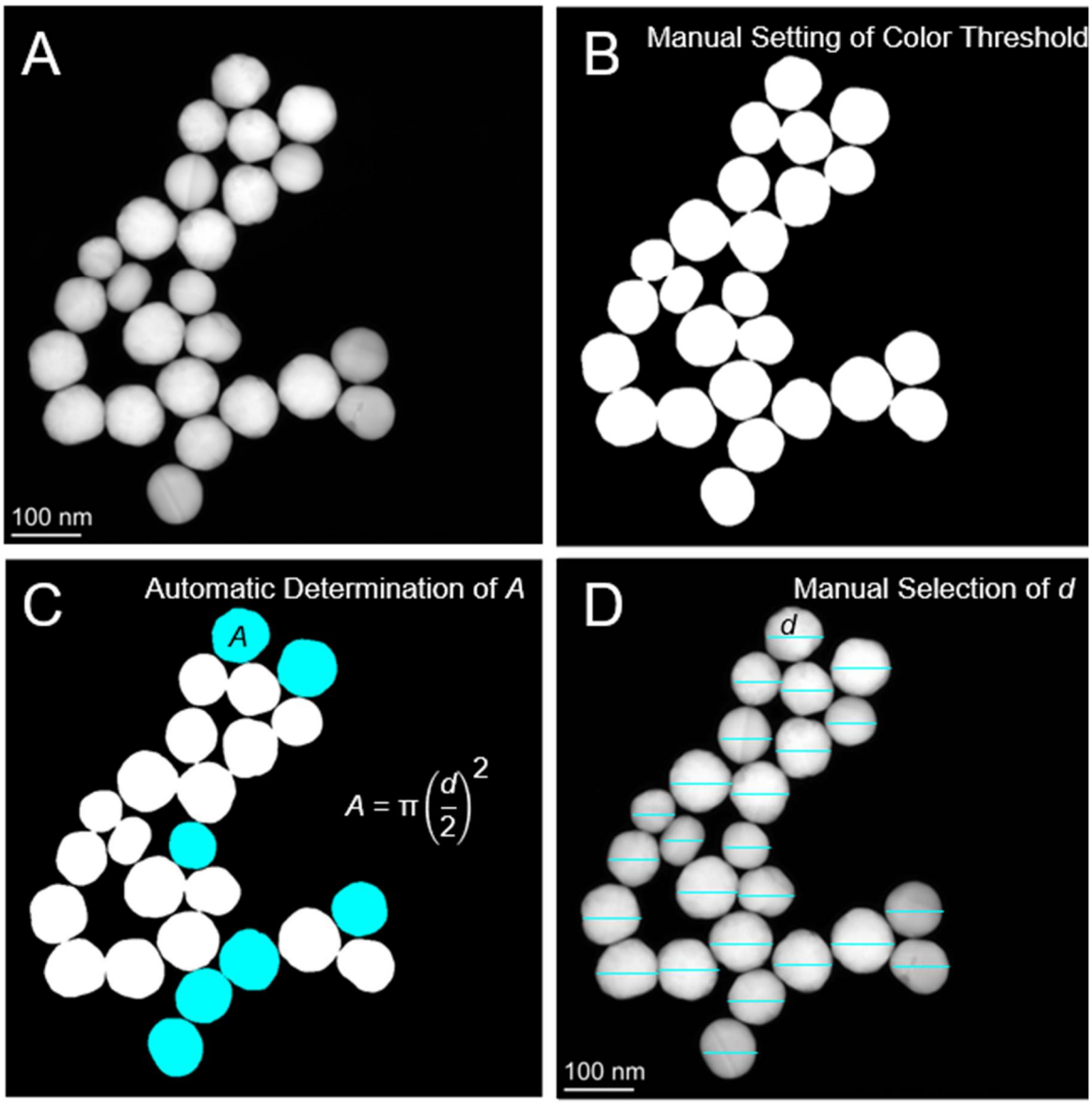


Figure S1. TEM image data processing workflow for particle size determination using Fiji by ImageJ. **A**. TEM image (.jpg) is opened with Fiji and the scale bar is used to determine a pixel/nm conversion factor. **B**. The monochrome image is first converted to an 8-bit grayscale image and then a color threshold is set to create a black-and-white image. The setting of the threshold is subjective and especially affects the pixels at the outer circumference of the particles. Threshold settings directly influence the determined area and diameter of the cross sections. **C**. The areas of the cross sections can be determined automatically in Fiji by setting reasonable parameters for the expected circularity and area range. If two or more cross sections are "connected" by at least one pixel, the respective shapes will not be recognized as circles within the set parameter range. The corresponding areas will not be reported as a result, which reduces the number of analyzed particles. **D**. The length of each cross section's diameter can be determined manually, which circumvents the issue of connected cross sections. Manual determination of the diameter is subjective and time-consuming and not efficient for TEM images showing hundreds of particles.

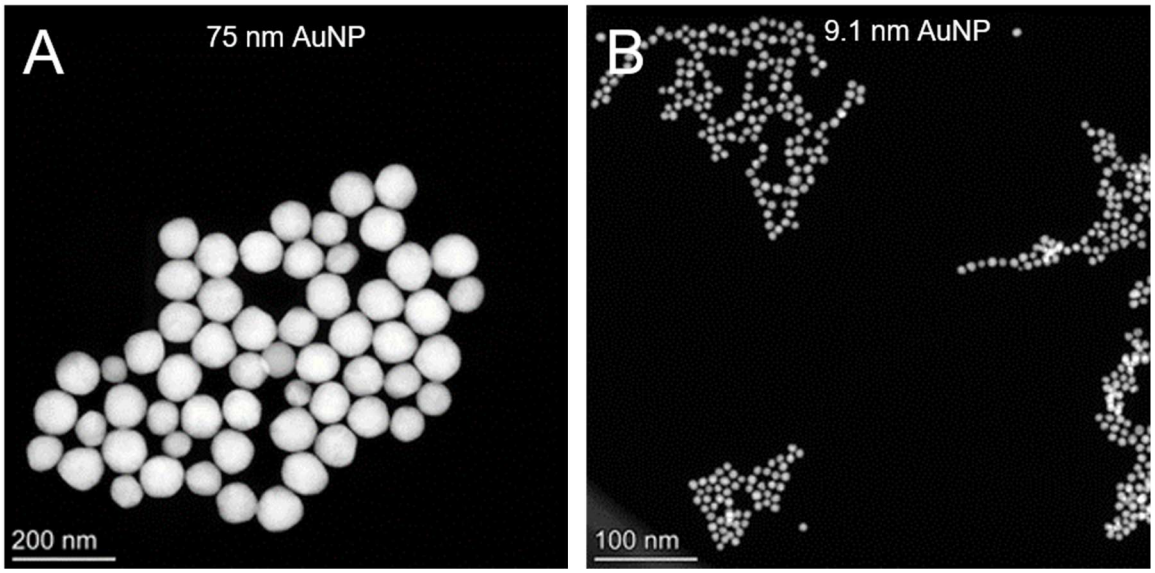


Figure S2. Exemplary TEM images of (A) 75 nm AuNP and (B) 9.1 nm AuNP. The number of particles per image varied significantly due to different agglomeration behaviour of the particles, and due to different magnification factors that were required to visualize differently sized particles. The manual determination of the particles' diameters is possible in A, but not efficient in B.

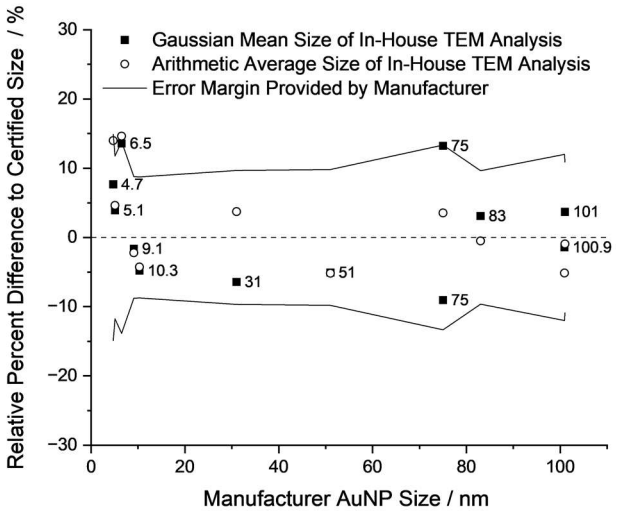


Figure S3. Deviation of the sizes determined *via* in-house TEM analysis from the sizes provided by the manufacturer. In-house sizes were either determined as the mean of a Gaussian fit function to the size distribution histogram of all analyzed particles or as arithmetic average values of the sizes of all analyzed particles. Percentual deviation of both approaches from the size provided by the manufacturer are displayed as black squares (mean) or circles (average). The dashed line indicates 0% deviation from the manufacturer size, the black lines correspond to the percentual size error provided by the manufacturer. Almost all in-house determined sizes (average and mean) fall within those error margins. Only the average size value determined for the (6.5 ± 0.9) nm AuNP (average: (7.5 ± 0.7) nm) exceeds the error margin by 0.8%. The size histogram of the 75 nm AuNP reveals a bimodal size distribution with two maxima at 68 nm and 85 nm, but the average value of 78 nm is much closer to the size provided by the manufacturer.

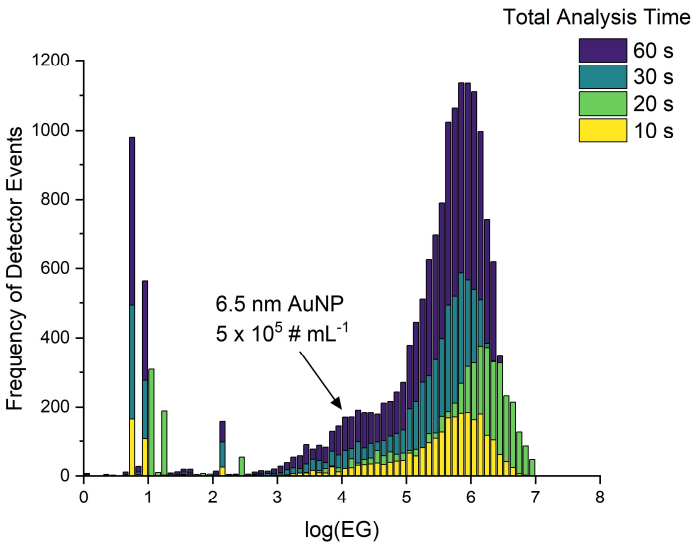


Figure S4. Histograms of the log(EG) of ions from 6.5 nm AuNP from the complete data set of spICP-MS analysis using the nanoDAQ MK2. The total analysis time was varied from 10 to 60 s to estimate a minimum analysis time for small particles at the default concentration of 10^5 # mL^{-1} for method development in this work. A measurement time of 60 s was necessary to distinguish the NP signal from the background (BG) signal distribution.

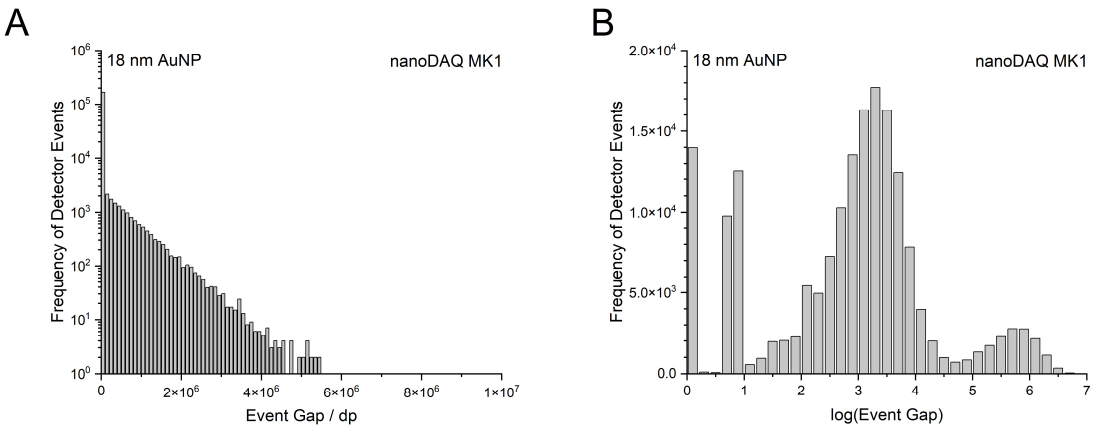


Figure S5. Histograms of detector events (DE) acquired with the nanoDAQ MK1 during analysis of a suspension of 18 nm AuNP. **A**. Frequency counts of the event gap (EG) between detector events. **B**. Frequency count of the logarithm of the event gap (log(EG)) between detector events. Both histograms were created from identical raw data sets. Note the logarithmic scale on the y-axis of the histogram in A. Frequency counts of the determined EG between DE merely show that the event gaps are very short between most of the detected ions. In the logarithmic display in B, however, a bimodal distribution is visible, which reflects the short event gaps between ions within ion clouds from particles (left distribution) and long event gaps between ions from the background (right distribution).

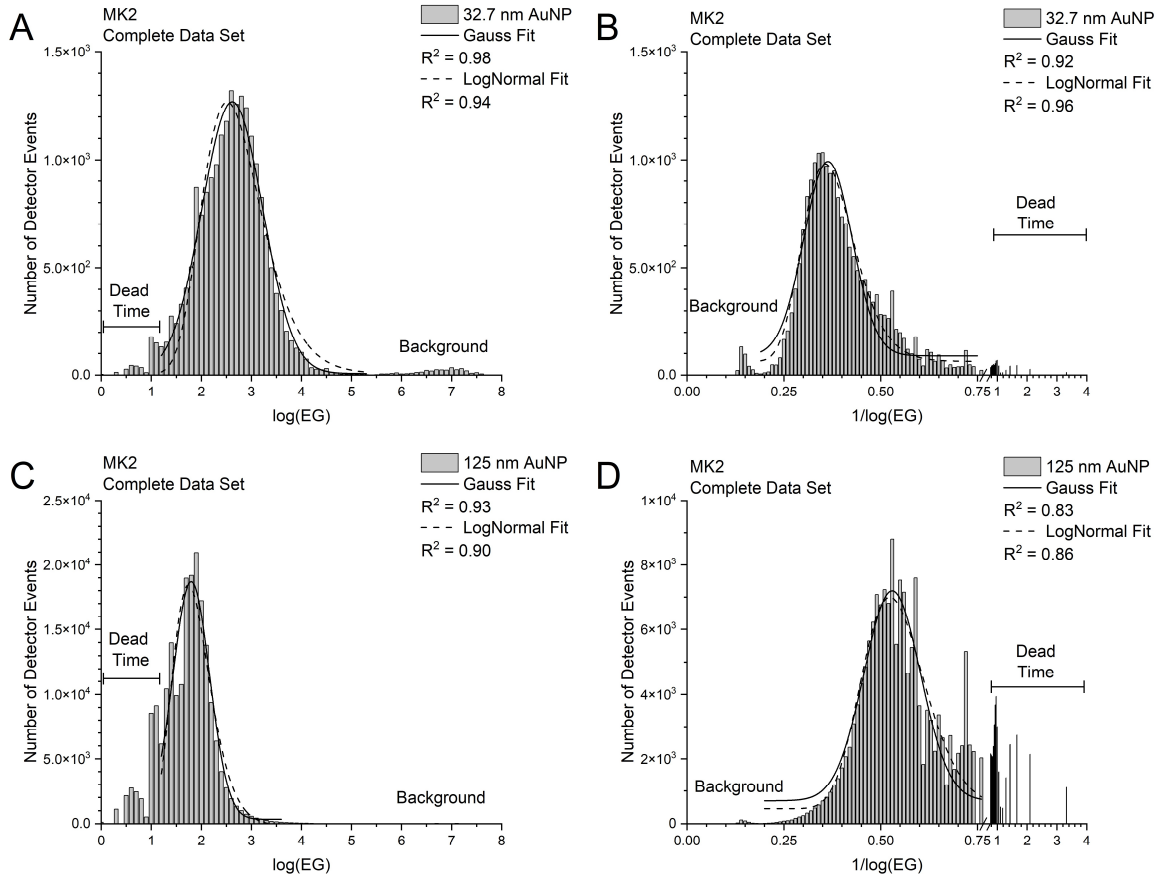


Figure S6. Histograms of the log(EG) and 1/log(EG) values of ions from complete data sets of the analysis of 32.7 nm and 125 nm-sized AuNP. Gaussian (Normal) and logarithmic Normal curve functions were fitted to the particle ion signal distributions in all graphs, taking care that signals corresponding to the background or detector dead time are not included. The best coefficient of determination for both particle sizes is obtained from a Gaussian fit to the log(EG) signal distribution.

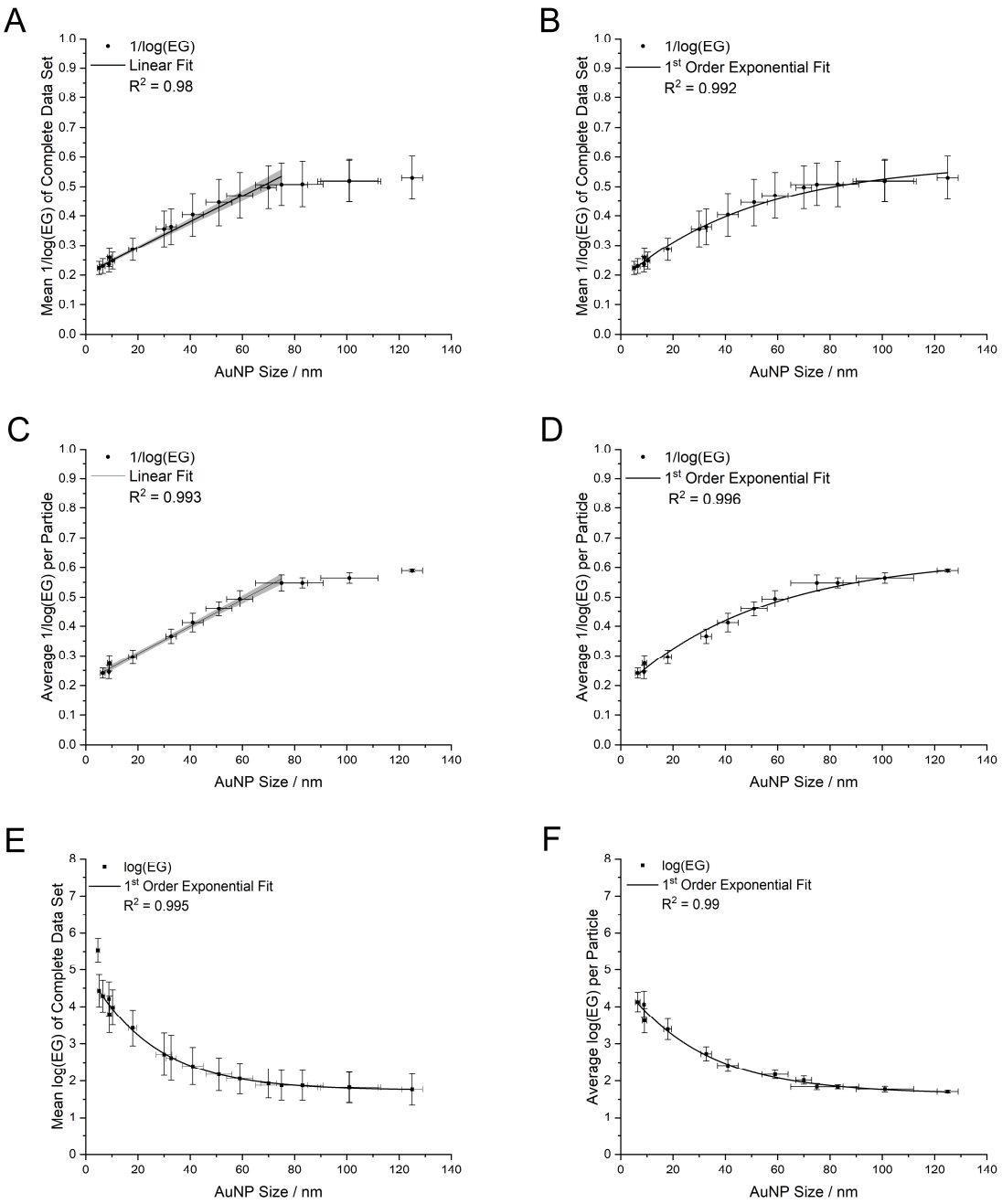


Figure S7. Particle size calibration approaches for AuNP *via* spICP-MS analysis with the nanoDAQ MK2 (values of 4.7 nm AuNP are shown, but are not included in the calculation). Linear fit functions were tested within the range of 5.1–75 nm (complete data set) and 6.5–75 nm (particle-by-particle). Exponential fit functions were tested within the range of 5.1–125 nm (complete data set) and 6.5–125 nm (particle-by-particle).
Error bars in the plots of complete data sets indicate the σ value of the Gaussian fit function to the log(EG) or 1/log(EG) distribution of the ion cloud DE. Error bars in the plots of particle-by-particle analysis indicate the SD of the average log(EG) and 1/log(EG) values of 100 analyzed particles.

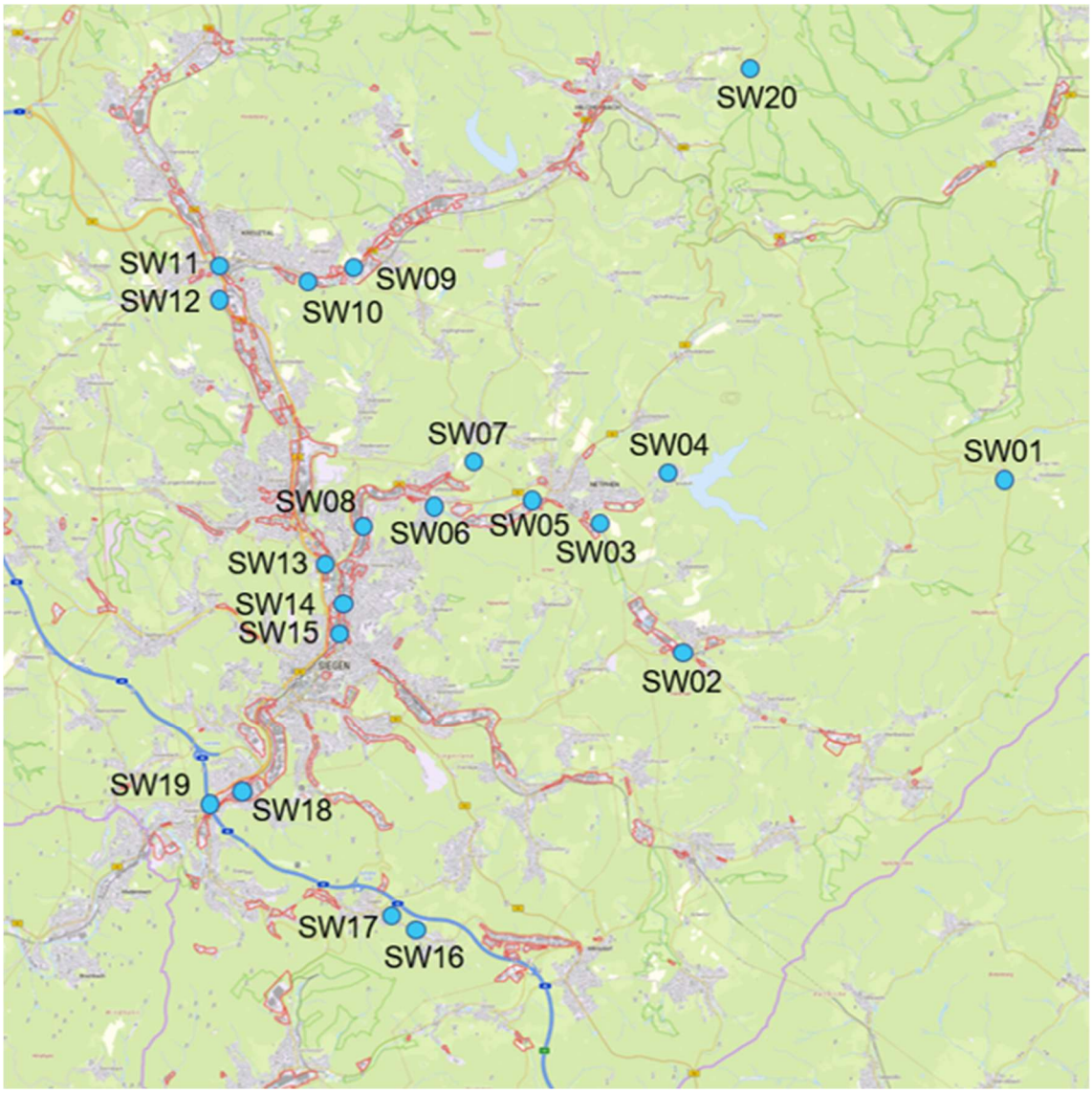


Figure S8. Schematic map showing industrially-used areas (marked in red) in the extended area of Siegen and the surface water sample locations (SW, cyan circles). The map was created on the website "Geoportal.de", which is provided by the "Bundesamt für Kartographie und Geodäsie".[168] Sampling site coordinates were identified with Google Maps and visualized in Affinity Designer (V 1.10.4.1198).

III. Supplementary equations

The NP diameter $d_{calc,lin}$ [nm] was calculated from the linear fit function in Equation S1,

$$d_{\mathrm{calc,lin}} = \frac{y - b}{m} \qquad \text{Equation S1}$$

where *y* is 1/log(EG) [dimensionless], *b* is the y-axis offset 1/log(EG), and *m* is the slope [1/nm].

In addition, the NP diameter $d_{calc,exp}$ [nm] was calculated from the 1st order exponential decay function in Equation S2,

$$d_{\mathrm{calc,exp}} = -\ln\left(\frac{y - b}{A_1}\right) \cdot d_1 \qquad \text{Equation S2}$$

where *y* is 1/log(EG) [dimensionless], *b* is the y-axis offset 1/log(EG), A_1 is the amplitude [dimensionless], and d_1 is a constant [nm].

The two-sided size deviation [%] of the calculated diameter d_{calc} [nm] from the vendor size d_{vendor} [nm] was determined *via* Equation S3:

$$Size\ deviation = \frac{d_{\mathrm{vendor}} - d_{\mathrm{calc}}}{d_{\mathrm{vendor}}} \cdot 100\% \qquad \text{Equation S3}$$

References

(1) Nanotechnology Products Database. *https://product.statnano.com/* (accessed 01.05.2025).

(2) Malik, S.; Muhammad, K.; Waheed, Y. Nanotechnology: A revolution in modern industry. *Molecules* **2023**, *28:661.* DOI: 10.3390/molecules28020661.

(3) Hansen, S. F.; Hansen, O. F. H.; Nielsen, M. B. Advances and challenges towards consumerization of nanomaterials. *Nat. Nanotechnol.* **2020**, *15*, 964–965. DOI: 10.1038/s41565-020-00819-7.

(4) Joseph, T. M.; Kar Mahapatra, D.; Esmaeili, A.; Piszczyk, Ł.; Hasanin, M. S.; Kattali, M.; Haponiuk, J.; Thomas, S. Nanoparticles: Taking a unique position in medicine. *Nanomaterials* **2023**, *13:574.* DOI: 10.3390/nano13030574.

(5) Singh, R. P.; Handa, R.; Manchanda, G. Nanoparticles in sustainable agriculture: An emerging opportunity. *J. Controlled Release* **2021**, *329*, 1234–1248. DOI: 10.1016/j.jconrel.2020.10.051.

(6) Usman, M.; Farooq, M.; Wakeel, A.; Nawaz, A.; Cheema, S. A.; Rehman, H. U.; Ashraf, I.; Sanaullah, M. Nanotechnology in agriculture: Current status, challenges and future opportunities. *Sci. Total Environ.* **2020**, *721:137778.* DOI: 10.1016/j.scitotenv.2020.137778.

(7) Shafique, M.; Luo, X. Nanotechnology in transportation vehicles: An overview of its applications, environmental, health and safety concerns. *Materials* **2019**, *12:2493.* DOI: 10.3390/ma12152493.

(8) Piluk, T.; Faccio, G.; Letsiou, S.; Liang, R.; Freire-Gormaly, M. A critical review investigating the use of nanoparticles in cosmetic skin products. *Environ. Sci.: Nano* **2024**, *11*, 3674–3692. DOI: 10.1039/D4EN00489B.

(9) Dubey, S. K.; Dey, A.; Singhvi, G.; Pandey, M. M.; Singh, V.; Kesharwani, P. Emerging trends of nanotechnology in advanced cosmetics. *Colloids Surf., B* **2022**, *214:112440.* DOI: 10.1016/j.colsurfb.2022.112440.

(10) Onyeaka, H.; Passaretti, P.; Miri, T.; Al-Sharify, Z. T. The safety of nanomaterials in food production and packaging. *Curr. Res. Food Sci.* **2022**, *5*, 763–774. DOI: 10.1016/j.crfs.2022.04.005.

(11) Yetisen, A. K.; Qu, H.; Manbachi, A.; Butt, H.; Dokmeci, M. R.; Hinestroza, J. P.; Skorobogatiy, M.; Khademhosseini, A.; Yun, S. H. Nanotechnology in textiles. *ACS Nano* **2016**, *10*, 3042–3068. DOI: 10.1021/acsnano.5b08176.

(12) DTU Environment, The Danish Ecological Council, The Danish Consumer Council. *The Nanodatabase, https://nanodb.dk/* (accessed 16.04.2025).

(13) Labuda, J.; Barek, J.; Gajdosechova, Z.; Goenaga-Infante, H.; Johnston, L. J.; Mester, Z.; Shtykov, S. Analytical chemistry of engineered nanomaterials: Part 1. Scope, regulation, legislation, and metrology (IUPAC Technical Report). *Pure Appl. Chem.* **2023**, *95*, 133–163. DOI: 10.1515/pac-2021-1001.

(14) Asha, A. B.; Narain, R. Nanomaterials properties. In *Polymer Science and Nanotechnology*; Elsevier, 2020; pp 343–359. DOI: 10.1016/B978-0-12-816806-6.00015-7.

(15) Ogunsona, E. O.; Muthuraj, R.; Ojogbo, E.; Valerio, O.; Mekonnen, T. H. Engineered nanomaterials for antimicrobial applications: A review. *Appl. Mater. Today* **2020**, *18:100473.* DOI: 10.1016/j.apmt.2019.100473.

(16) Lombardo, D.; Kiselev, M. A.; Caccamo, M. T. Smart nanoparticles for drug delivery application: Development of versatile nanocarrier platforms in biotechnology and nanomedicine. *J. Nanomater.* **2019**, *2019*, 1–26. DOI: 10.1155/2019/3702518.

(17) European Commission. Commission Recommendation of 18 October 2011 on the definition of nanomaterial Text with EEA relevance **2011**, 38–40.

(18) Mu, Q.; Jiang, G.-B.; Chen, L.; Zhou, H.; Fourches, D.; Tropsha, A.; Yan, B. Chemical basis of interactions between engineered nanoparticles and biological systems. *Chem. Rev.* **2014**, *114*, 7740–7781. DOI: 10.1021/cr400295a.

(19) Nguyen, T.-D. From formation mechanisms to synthetic methods toward shape-controlled oxide nanoparticles. *Nanoscale* **2013**, *5*, 9455–9482. DOI: 10.1039/c3nr01810e.

(20) Khodashenas, B.; Ghorbani, H. R. Synthesis of silver nanoparticles with different shapes. *Arabian J. Chem.* **2019**, *12*, 1823–1838. DOI: 10.1016/j.arabjc.2014.12.014.

(21) Dahoumane, S. A.; Jeffryes, C.; Mechouet, M.; Agathos, S. N. Biosynthesis of inorganic nanoparticles: A fresh look at the control of shape, size and composition. *Bioengineering* **2017**, *4:14.* DOI: 10.3390/bioengineering4010014.

(22) Xia, Y.; Xiong, Y.; Lim, B.; Skrabalak, S. E. Shape-controlled synthesis of metal nanocrystals: simple chemistry meets complex physics? *Angew. Chem., Int. Ed.* **2009**, *48*, 60–103. DOI: 10.1002/anie.200802248.

(23) Ghosh Chaudhuri, R.; Paria, S. Core/shell nanoparticles: Classes, properties, synthesis mechanisms, characterization, and applications. *Chem. Rev.* **2012**, *112*, 2373–2433. DOI: 10.1021/cr100449n.

(24) Wang, X.; Feng, J.; Bai, Y.; Zhang, Q.; Yin, Y. Synthesis, properties, and applications of hollow micro-/nanostructures. *Chem. Rev.* **2016**, *116*, 10983–11060. DOI: 10.1021/acs.chemrev.5b00731.

(25) Piccinno, F.; Gottschalk, F.; Seeger, S.; Nowack, B. Industrial production quantities and uses of ten engineered nanomaterials in Europe and the world. *J. Nanopart. Res.* **2012**, *14:1109.* DOI: 10.1007/s11051-012-1109-9.

(26) Hartmann, S.; Louch, R.; Zeumer, R.; Steinhoff, B.; Mozhayeva, D.; Engelhard, C.; Schönherr, H.; Schlechtriem, C.; Witte, K. Comparative multi-generation study on long-term effects of pristine and wastewater-borne silver and titanium dioxide nanoparticles on key lifecycle parameters in Daphnia magna. *NanoImpact* **2019**, *14:100163.* DOI: 10.1016/j.impact.2019.100163.

(27) Galhano, V.; Hartmann, S.; Monteiro, M. S.; Zeumer, R.; Mozhayeva, D.; Steinhoff, B.; Müller, K.; Prenzel, K.; Kunze, J.; Kuhnert, K.-D.; Schönherr, H.; Engelhard, C.; Schlechtriem, C.; Loureiro, S.; Soares, A. M. V. M.; Witte, K.; Lopes, I. Impact of wastewater-borne nanoparticles of silver and titanium dioxide on the swimming behaviour and biochemical markers of Daphnia magna: An integrated approach. *Aquat. Toxicol.* **2020**, *220:105404.* DOI: 10.1016/j.aquatox.2020.105404.

(28) Gottschalk, F.; Sun, T.; Nowack, B. Environmental concentrations of engineered nanomaterials: Review of modeling and analytical studies. *Environ. Pollut.* **2013**, *181*, 287–300. DOI: 10.1016/j.envpol.2013.06.003.

(29) Behzadi, S.; Serpooshan, V.; Tao, W.; Hamaly, M. A.; Alkawareek, M. Y.; Dreaden, E. C.; Brown, D.; Alkilany, A. M.; Farokhzad, O. C.; Mahmoudi, M. Cellular uptake of nanoparticles: Journey inside the cell. *Chem. Soc. Rev.* **2017**, *46*, 4218–4244. DOI: 10.1039/c6cs00636a.

(30) Sela, H.; Cohen, H.; Elia, P.; Zach, R.; Karpas, Z.; Zeiri, Y. Spontaneous penetration of gold nanoparticles through the blood brain barrier (BBB). *J. Nanobiotechnol.* **2015**, *13:71.* DOI: 10.1186/s12951-015-0133-1.

(31) de Jong, W. H.; Hagens, W. I.; Krystek, P.; Burger, M. C.; Sips, A. J. A. M.; Geertsma, R. E. Particle size-dependent organ distribution of gold nanoparticles after intravenous administration. *Biomaterials* **2008**, *29*, 1912–1919. DOI: 10.1016/j.biomaterials.2007.12.037.

(32) Zha, S.; Liu, H.; Li, H.; Li, H.; Wong, K.-L.; All, A. H. Functionalized nanomaterials capable of crossing the blood-brain barrier. *ACS Nano* **2024**, *18*, 1820–1845. DOI: 10.1021/acsnano.3c10674.

(33) Baroli, B.; Ennas, M. G.; Loffredo, F.; Isola, M.; Pinna, R.; López-Quintela, M. A. Penetration of metallic nanoparticles in human full-thickness skin. *J. Invest. Dermatol.* **2007**, *127*, 1701–1712. DOI: 10.1038/sj.jid.5700733.

(34) Khabir, Z.; Guller, A. E.; Rozova, V. S.; Liang, L.; Lai, Y.-J.; Goldys, E. M.; Hu, H.; Vickery, K.; Zvyagin, A. V. Tracing upconversion nanoparticle penetration in human skin. *Colloids Surf., B* **2019**, *184:110480.* DOI: 10.1016/j.colsurfb.2019.110480.

(35) Zhang, N.; Xiong, G.; Liu, Z. Toxicity of metal-based nanoparticles: Challenges in the nano era. *Front. Bioeng. Biotechnol.* **2022**, *10:1001572.* DOI: 10.3389/fbioe.2022.1001572.

(36) Khanna, P.; Ong, C.; Bay, B. H.; Baeg, G. H. Nanotoxicity: An interplay of oxidative stress, inflammation and cell death. *Nanomaterials* **2015**, *5*, 1163–1180. DOI: 10.3390/nano5031163.

(37) Čapek, J.; Roušar, T. Detection of oxidative stress induced by nanomaterials in cells-The roles of reactive oxygen species and glutathione. *Molecules* **2021**, *26:4710.* DOI: 10.3390/molecules26164710.

(38) Hochella, M. F.; Mogk, D. W.; Ranville, J. F.; Allen, I. C.; Luther, G. W.; Marr, L. C.; McGrail, B. P.; Murayama, M.; Qafoku, N. P.; Rosso, K. M.; Sahai, N.; Schroeder, P. A.; Vikesland, P. J.; Westerhoff, P.; Yang, Y. Natural, incidental, and engineered nanomaterials and their impacts on the Earth system. *Science* **2019**, *363:1414.* DOI: 10.1126/science.aau8299.

(39) Bundschuh, M.; Filser, J.; Lüderwald, S.; McKee, M. S.; Metreveli, G.; Schaumann, G. E.; Schulz, R.; Wagner, S. Nanoparticles in the environment: where do we come from, where do we go to? *Environ. Sci. Eur.* **2018**, *30:6.* DOI: 10.1186/s12302-018-0132-6.

(40) Abbas, Q.; Yousaf, B.; Amina; Ali, M. U.; Munir, M. A. M.; El-Naggar, A.; Rinklebe, J.; Naushad, M. Transformation pathways and fate of engineered nanoparticles (ENPs) in distinct interactive environmental compartments: A review. *Environ. Int.* **2020**, *138:105646.* DOI: 10.1016/j.envint.2020.105646.

(41) Vale, G.; Mehennaoui, K.; Cambier, S.; Libralato, G.; Jomini, S.; Domingos, R. F. Manufactured nanoparticles in the aquatic environment-biochemical responses on freshwater organisms: A critical overview. *Aquat. Toxicol.* **2016**, *170*, 162–174. DOI: 10.1016/j.aquatox.2015.11.019.

(42) Tran, T.-K.; Nguyen, M.-K.; Lin, C.; Hoang, T.-D.; Nguyen, T.-C.; Lone, A. M.; Khedulkar, A. P.; Gaballah, M. S.; Singh, J.; Chung, W. J.; Nguyen, D. D. Review on fate, transport, toxicity and health risk of nanoparticles in natural ecosystems: Emerging challenges in the modern age and solutions toward a sustainable environment. *Sci. Total Environ.* **2024**, *912:169331.* DOI: 10.1016/j.scitotenv.2023.169331.

(43) Kiser, M. A.; Westerhoff, P.; Benn, T.; Wang, Y.; Perez-Rivera, J.; Hristovski, K. Titanium nanomaterial removal and release from wastewater treatment plants. *Environ. Sci. Technol.* **2009**, *43*, 6757–6763. DOI: 10.1021/es901102n.

(44) Bitragunta, S. P.; Palani, S. G.; Gopala, A.; Sarkar, S. K.; Kandukuri, V. R. Detection of TiO_2 nanoparticles in municipal sewage treatment plant and their characterization using single particle ICP-MS. *Bull. Environ. Contam. Toxicol.* **2017**, *98*, 595–600. DOI: 10.1007/s00128-017-2031-8.

(45) Gómez-Rivera, F.; Field, J. A.; Brown, D.; Sierra-Alvarez, R. Fate of cerium dioxide (CeO_2) nanoparticles in municipal wastewater during activated sludge treatment. *Bioresour. Technol.* **2012**, *108*, 300–304. DOI: 10.1016/j.biortech.2011.12.113.

(46) Li, L.; Stoiber, M.; Wimmer, A.; Xu, Z.; Lindenblatt, C.; Helmreich, B.; Schuster, M. To what extent can full-scale wastewater treatment plant effluent influence the occurrence of silver-based nanoparticles in surface waters? *Environ. Sci. Technol.* **2016**, *50*, 6327–6333. DOI: 10.1021/acs.est.6b00694.

(47) Vogt, R.; Mozhayeva, D.; Steinhoff, B.; Schardt, A.; Spelz, B. T. F.; Philippe, A.; Kurtz, S.; Schaumann, G. E.; Engelhard, C.; Schönherr, H.; Lamatsch, D. K.; Wanzenböck, J. Spatiotemporal distribution of silver and silver-containing nanoparticles in a prealpine lake in relation to the discharge from a wastewater treatment plant. *Sci. Total Environ.* **2019**, *696:134034.* DOI: 10.1016/j.scitotenv.2019.134034.

(48) Kunhikrishnan, A.; Shon, H. K.; Bolan, N. S.; El Saliby, I.; Vigneswaran, S. Sources, distribution, environmental fate, and ecological effects of nanomaterials in wastewater streams. *Crit. Rev. Environ. Sci. Technol.* **2014**, *45*, 277–318. DOI: 10.1080/10643389.2013.852407.

(49) Loosli, F.; Wang, J.; Rothenberg, S.; Bizimis, M.; Winkler, C.; Borovinskaya, O.; Flamigni, L.; Baalousha, M. Sewage spills are a major source of titanium dioxide engineered (nano)-particles into the environment. *Environ. Sci.: Nano* **2019**, *6*, 763–777. DOI: 10.1039/C8EN01376D.

(50) Leopold, K.; Philippe, A.; Wörle, K.; Schaumann, G. E. Analytical strategies to the determination of metal-containing nanoparticles in environmental waters. *TrAC, Trends Anal. Chem.* **2016**, *84*, 107–120. DOI: 10.1016/j.trac.2016.03.026.

(51) Howard, A. G. On the challenge of quantifying man-made nanoparticles in the aquatic environment. *J. Environ. Monit.* **2010**, *12*, 135–142. DOI: 10.1039/B913681A.

(52) Zhang, M.; Yang, J.; Cai, Z.; Feng, Y.; Wang, Y.; Zhang, D.; Pan, X. Detection of engineered nanoparticles in aquatic environments: current status and challenges in enrichment, separation, and analysis. *Environ. Sci.: Nano* **2019**, *6*, 709–735. DOI: 10.1039/C8EN01086B.

(53) Sukhanova, A.; Bozrova, S.; Sokolov, P.; Berestovoy, M.; Karaulov, A.; Nabiev, I. Dependence of nanoparticle toxicity on their physical and chemical properties. *Nanoscale Res. Lett.* **2018**, *13:44*. DOI: 10.1186/s11671-018-2457-x.

(54) Metch, J. W.; Burrows, N. D.; Murphy, C. J.; Pruden, A.; Vikesland, P. J. Metagenomic analysis of microbial communities yields insight into impacts of nanoparticle design. *Nat. Nanotechnol.* **2018**, *13*, 253–259. DOI: 10.1038/s41565-017-0029-3.

(55) Lai, R. W. S.; Yeung, K. W. Y.; Yung, M. M. N.; Djurišić, A. B.; Giesy, J. P.; Leung, K. M. Y. Regulation of engineered nanomaterials: current challenges, insights and future directions. *Environ. Sci. Pollut. Res.* **2018**, *25*, 3060–3077. DOI: 10.1007/s11356-017-9489-0.

(56) Labuda, J.; Barek, J.; Gajdosechova, Z.; Jacob, S.; Johnston, L. J.; Krystek, P.; Mester, Z.; Moreira, J.; Svitkova, V.; Wilkinson, K. J. Analytical chemistry of engineered nanomaterials: Part 2. analysis in complex samples (IUPAC Technical Report). *Pure Appl. Chem.* **2023**, *95*, 1159–1196. DOI: 10.1515/pac-2022-0401.

(57) Pace, H. E.; Rogers, N. J.; Jarolimek, C.; Coleman, V. A.; Higgins, C. P.; Ranville, J. F. Determining transport efficiency for the purpose of counting and sizing nanoparticles via single particle inductively coupled plasma mass spectrometry. *Anal. Chem.* **2011**, *83*, 9361–9369. DOI: 10.1021/ac201952t.

(58) Nomizu, T.; Kaneco, S.; Tanaka, T.; Yamamoto, T.; Kawaguchi, H. Determination of femto-gram amounts of zinc and lead in individual airborne particles by inductively-coupled plasma-mass spectrometry with direct air-sample introduction. *Anal. Sci.* **1993**, *9*, 843–846. DOI: 10.2116/analsci.9.843.

(59) Zhou, Z.; Beauchemin, D. Single particle inductively coupled plasma mass spectrometry and its variations for the analysis of nanoparticles. *Chem. Commun.* **2024**, *60*, 1826–1839. DOI: 10.1039/d3cc04974d.

(60) Mozhayeva, D.; Engelhard, C. A critical review of single particle inductively coupled plasma mass spectrometry – A step towards an ideal method for nanomaterial characterization. *J. Anal. At. Spectrom.* **2020**, *35*, 1740–1783. DOI: 10.1039/c9ja00206e.

(61) Meermann, B.; Nischwitz, V. ICP-MS for the analysis at the nanoscale – A tutorial review. *J. Anal. At. Spectrom.* **2018**, *33*, 1432–1468. DOI: 10.1039/C8JA00037A.

(62) International Standardization Organization. *Nanotechnologies*: *Size distribution and concentration of inorganic nanoparticles in aqueous media via single particle inductively coupled plasma mass spectrometry* (Technical Specification ISO/TS 19590:2017), 2017.

(63) International Standardization Organization. *Nanotechnologies*: *Characterization of nano-objects using single particle inductively coupled plasma mass spectrometry* (Technical Specification ISO/TS 19590:2024), 2024.

(64) Strenge, I.; Engelhard, C. Capabilities of fast data acquisition with microsecond time resolution in inductively coupled plasma mass spectrometry and identification of signal artifacts from millisecond dwell times during detection of single gold nanoparticles. *J. Anal. At. Spectrom.* **2016**, *31*, 135–144. DOI: 10.1039/c5ja00177c.

(65) Mozhayeva, D.; Strenge, I.; Engelhard, C. Implementation of online preconcentration and microsecond time resolution to capillary electrophoresis single particle inductively coupled plasma mass spectrometry (CE-SP-ICP-MS) and its application in silver nanoparticle analysis. *Anal. Chem.* **2017**, *89*, 7152–7159. DOI: 10.1021/acs.analchem.7b01185.

(66) Mozhayeva, D.; Engelhard, C. Separation of silver nanoparticles with different coatings by capillary electrophoresis coupled to ICP-MS in single particle mode. *Anal. Chem.* **2017**, *89*, 9767–9774. DOI: 10.1021/acs.analchem.7b01626.

(67) Mozhayeva, D.; Engelhard, C. CE coupled to ICP-MS and single particle ICP-MS for nanoparticle analysis. *Methods Mol. Biol.* **2022**, *2531*, 243–257. DOI: 10.1007/978-1-0716-2493-7_16.

(68) Schardt, A.; Schmitt, J.; Engelhard, C. Single particle inductively coupled plasma mass spectrometry with nanosecond time resolution. *J. Anal. At. Spectrom.* **2024**, *39*, 389–400. DOI: 10.1039/D3JA00373F.

(69) Johannes Schmitt. Portierung und Erweiterung eines Datenerfassungssystems für die Einzelpartikel-Massenspektrometrie mit induktiv gekoppeltem Plasma (spICP-MS). Master Thesis, Universität Siegen, Siegen, 2023.

(70) Johannes Schmitt. Datenerfassung und Datenverarbeitung von Nanopartikelmessungen an einem Massenspektrometer mit induktiv gekoppeltem Plasma. Bachelor Thesis, Universität Siegen, Siegen, 2020.

(71) Hendricks, N.; Olatunji, O.; Ofori, I.; Gumbi, B. P. Occurrence, fate, and impact of engineered metal/carbonaceous nanomaterials in the environment, detection, and quantitation methods. *Int. J. Environ. Sci. Technol.* **2023**, *20*, 12937–12954. DOI: 10.1007/s13762-023-04977-8.

(72) Donovan, A. R.; Adams, C. D.; Ma, Y.; Stephan, C.; Eichholz, T.; Shi, H. Detection of zinc oxide and cerium dioxide nanoparticles during drinking water treatment by rapid single particle ICP-MS methods. *Anal. Bioanal. Chem.* **2016**, *408*, 5137–5145. DOI: 10.1007/s00216-016-9432-0.

(73) Donovan, A. R.; Adams, C. D.; Ma, Y.; Stephan, C.; Eichholz, T.; Shi, H. Single particle ICP-MS characterization of titanium dioxide, silver, and gold nanoparticles during drinking water treatment. *Chemosphere* **2016**, *144*, 148–153. DOI: 10.1016/j.chemosphere.2015.07.081.

(74) Kim, B.; Park, C.-S.; Murayama, M.; Hochella, M. F. Discovery and characterization of silver sulfide nanoparticles in final sewage sludge products. *Environ. Sci. Technol.* **2010**, *44*, 7509–7514. DOI: 10.1021/es101565j.

(75) Sanchís, J.; Jiménez-Lamana, J.; Abad, E.; Szpunar, J.; Farré, M. Occurrence of cerium-, titanium-, and silver-bearing nanoparticles in the Besòs and Ebro Rivers. *Environ. Sci. Technol.* **2020**, *54*, 3969–3978. DOI: 10.1021/acs.est.9b05996.

(76) Shi, X.; Li, Z.; Chen, W.; Qiang, L.; Xia, J.; Chen, M.; Zhu, L.; Alvarez, P. J. Fate of TiO_2 nanoparticles entering sewage treatment plants and bioaccumulation in fish in the receiving streams. *NanoImpact* **2016**, *3-4*, 96–103. DOI: 10.1016/j.impact.2016.09.002.

(77) Steinhoff, B.; Müller, J.; Mozhayeva, D.; Spelz, B. T. F.; Engelhard, C.; Butz, B.; Schönherr, H. Investigation of the fate of silver and titanium dioxide nanoparticles in model wastewater effluents via selected area electron diffraction. *Environ. Sci. Technol.* **2020**, *54*, 8681–8689. DOI: 10.1021/acs.est.9b07840.

(78) Prasad, A.; Lead, J. R.; Baalousha, M. An electron microscopy based method for the detection and quantification of nanomaterial number concentration in environmentally relevant media. *Sci. Total Environ.* **2015**, *537*, 479–486. DOI: 10.1016/j.scitotenv.2015.07.117.

(79) Bolea-Fernandez, E.; Jimenez, M. S.; Perez-Arantegui, J.; Vidal, J. C.; Bakir, M.; Ben-Jeddou, K.; Gimenez-Ingalaturre, A. C.; Ojeda, D.; Trujillo, C.; Laborda, F. Analytical applications of single particle inductively coupled plasma mass spectrometry: A comprehensive and critical review. *Anal. Methods* **2021**, *13*, 2742–2795. DOI: 10.1039/d1ay00761k.

(80) Resano, M.; Aramendía, M.; García-Ruiz, E.; Bazo, A.; Bolea-Fernandez, E.; Vanhaecke, F. Living in a transient world: ICP-MS reinvented via time-resolved analysis for monitoring single events. *Chem. Sci.* **2022**, *13*, 4436–4473. DOI: 10.1039/d1sc05452j.

(81) Gross, J. H. *Massenspektrometrie*; Springer Berlin Heidelberg, 2013. DOI: 10.1007/978-3-8274-2981-0.

(82) Borovinskaya, O.; Hattendorf, B.; Tanner, M.; Gschwind, S.; Günther, D. A prototype of a new inductively coupled plasma time-of-flight mass spectrometer providing temporally resolved, multi-element detection of short signals generated by single particles and droplets. *J. Anal. At. Spectrom.* **2013**, *28*, 226–233. DOI: 10.1039/C2JA30227F.

(83) Baalousha, M.; Wang, J.; Erfani, M.; Goharian, E. Elemental fingerprints in natural nanomaterials determined using SP-ICP-TOF-MS and clustering analysis. *Sci. Total Environ.* **2021**, *792:148426.* DOI: 10.1016/j.scitotenv.2021.148426.

(84) Praetorius, A.; Gundlach-Graham, A.; Goldberg, E.; Fabienke, W.; Navratilova, J.; Gondikas, A.; Kägi, R.; Günther, D.; Hofmann, T.; von der Kammer, F. Single-particle multi-element fingerprinting (spMEF) using inductively-coupled plasma time-of-flight mass spectrometry (ICP-TOFMS) to identify engineered nanoparticles against the elevated natural background in soils. *Environ. Sci.: Nano* **2017**, *4*, 307–314. DOI: 10.1039/c6en00455e.

(85) Karkee, H.; Gundlach-Graham, A. Two-stage hierarchical clustering for analysis and classification of mineral sunscreen and naturally occurring nanoparticles in river water using single-particle ICP-TOFMS. *Environ. Sci.: Nano* **2024**, *11*, 4162–4173. DOI: 10.1039/D4EN00288A.

(86) Greenfield, S.; Jones, I. L.; Berry, C. T. High-pressure plasmas as spectroscopic emission sources. *Analyst* **1964**, *89*, 713–720. DOI: 10.1039/an9648900713.

(87) Wendt, R. H.; Fassel, V. A. Induction-coupled plasma spectrometric excitation source. *Anal. Chem.* **1965**, *37*, 920–922. DOI: 10.1021/ac60226a003.

(88) Houk, R. S.; Fassel, V. A.; Flesch, G. D.; Svec, H. J.; Gray, A. L.; Taylor, C. E. Inductively coupled argon plasma as an ion source for mass spectrometric determination of trace elements. *Anal. Chem.* **1980**, *52*, 2283–2289. DOI: 10.1021/ac50064a012.

(89) Kawaguchi, H.; Fukasawa, N.; Mizuike, A. Investigation of airborne particles by inductively coupled plasma emission spectrometry calibrated with monodisperse aerosols. *Spectrochim. Acta, Part B* **1986**, *41*, 1277–1286. DOI: 10.1016/0584-8547(86)80006-4.

(90) Degueldre, C.; Favarger, P. Y. Colloid analysis by single particle inductively coupled plasma-mass spectroscopy: A feasibility study. *Colloids Surf., A* **2003**, *217*, 137–142. DOI: 10.1016/s0927-7757(02)00568-x.

(91) Degueldre, C.; Favarger, P. Y. Thorium colloid analysis by single particle inductively coupled plasma-mass spectrometry. *Talanta* **2004**, *62*, 1051–1054. DOI: 10.1016/j.talanta.2003.10.016.

(92) Degueldre, C.; Favarger, P. Y.; Bitea, C. Zirconia colloid analysis by single particle inductively coupled plasma–mass spectrometry. *Anal. Chim. Acta* **2004**, *518*, 137–142. DOI: 10.1016/j.aca.2004.04.015.

(93) Degueldre, C.; Favarger, P. Y.; Wold, S. Gold colloid analysis by inductively coupled plasma-mass spectrometry in a single particle mode. *Anal. Chim. Acta* **2006**, *555*, 263–268. DOI: 10.1016/j.aca.2005.09.021.

(94) Degueldre, C.; Favarger, P. Y.; Rosse, R.; Wold, S. Uranium colloid analysis by single particle inductively coupled plasma-mass spectrometry. *Talanta* **2006**, *68*, 623–628. DOI: 10.1016/j.talanta.2005.05.006.

(95) Laborda, F.; Jiménez-Lamana, J.; Bolea-Fernandez, E.; Castillo, J. R. Selective identification, characterization and determination of dissolved silver(I) and silver nanoparticles based on single particle detection by inductively coupled plasma mass spectrometry. *J. Anal. At. Spectrom.* **2011**, *26*, 1362–1371. DOI: 10.1039/c0ja00098a.

(96) Laborda, F.; Bolea-Fernandez, E.; Jiménez-Lamana, J. Single particle inductively coupled plasma mass spectrometry: a powerful tool for nanoanalysis. *Anal. Chem.* **2014**, *86*, 2270–2278. DOI: 10.1021/ac402980q.

(97) Yang, Y.; Long, C.-L.; Li, H.-P.; Wang, Q.; Yang, Z.-G. Analysis of silver and gold nanoparticles in environmental water using single particle-inductively coupled plasma-mass spectrometry. *Sci. Total Environ.* **2016**, *563-564*, 996–1007. DOI: 10.1016/j.scitotenv.2015.12.150.

(98) Reed, R. B.; Martin, D. P.; Bednar, A. J.; Montaño, M. D.; Westerhoff, P.; Ranville, J. F. Multi-day diurnal measurements of Ti-containing nanoparticle and organic sunscreen chemical release during recreational use of a natural surface water. *Environ. Sci.: Nano* **2017**, *4*, 69–77. DOI: 10.1039/C6EN00283H.

(99) Venkatesan, A. K.; Rodríguez, B. T.; Marcotte, A. R.; Bi, X.; Schoepf, J.; Ranville, J. F.; Herckes, P.; Westerhoff, P. Using single-particle ICP-MS for monitoring metal-containing particles in tap water. *Environ. Sci.: Water Res. Technol.* **2018**, *4*, 1923–1932. DOI: 10.1039/C8EW00478A.

(100) Lee, S.; Bi, X.; Reed, R. B.; Ranville, J. F.; Herckes, P.; Westerhoff, P. Nanoparticle size detection limits by single particle ICP-MS for 40 elements. *Environ. Sci. Technol.* **2014**, *48*, 10291–10300. DOI: 10.1021/es502422v.

(101) Montaño, M. D.; Badiei, H. R.; Bazargan, S.; Ranville, J. F. Improvements in the detection and characterization of engineered nanoparticles using spICP-MS with microsecond dwell times. *Environ. Sci.: Nano* **2014**, *1*, 338–346. DOI: 10.1039/c4en00058g.

(102) Bazo, A.; Bolea-Fernandez, E.; Rua-Ibarz, A.; Aramendía, M.; Resano, M. Intensity- and time-based strategies for micro/nano-sizing via single-particle ICP-mass spectrometry: A comparative assessment using Au and SiO2 as model particles. *Anal. Chim. Acta* **2024**, *1331:343305.* DOI: 10.1016/j.aca.2024.343305.

(103) Hobbs, S. E.; Olesik, J. W. Inductively coupled plasma mass spectrometry signal fluctuations due to individual aerosol droplets and vaporizing particles. *Anal. Chem.* **1992**, *64*, 274–283. DOI: 10.1021/ac00027a007.

(104) Nomizu, T.; Hayashi, H.; Hoshino, N.; Tanaka, T.; Kawaguchi, H.; Kitagawa, K.; Kaneco, S. Determination of zinc in individual airborne particles by inductively coupled plasma mass spectrometry with digital signal processing. *J. Anal. At. Spectrom.* **2002**, *17*, 592–595. DOI: 10.1039/b111444a.

(105) Managh, A. J.; Douglas, D. N.; Makella Cowen, K.; Reid, H. J.; Sharp, B. L. Acquisition of fast transient signals in ICP-MS with enhanced time resolution. *J. Anal. At. Spectrom.* **2016**, *31*, 1688–1692. DOI: 10.1039/c6ja00140h.

(106) Gschwind, S.; Flamigni, L.; Koch, J.; Borovinskaya, O.; Groh, S.; Niemax, K.; Günther, D. Capabilities of inductively coupled plasma mass spectrometry for the detection of nanoparticles carried by monodisperse microdroplets. *J. Anal. At. Spectrom.* **2011**, *26*, 1166–1174. DOI: 10.1039/c0ja00249f.

(107) Koch, J.; Flamigni, L.; Gschwind, S.; Allner, S.; Longerich, H.; Günther, D. Accelerated evaporation of microdroplets at ambient conditions for the on-line analysis of nanoparticles by inductively-coupled plasma mass spectrometry. *J. Anal. At. Spectrom.* **2013**, *28*, 1707–1717. DOI: 10.1039/c3ja50052g.

(108) Rush, L. A.; Endres, M. C.; Liezers, M.; Ward, J. D.; Eiden, G. C.; Duffin, A. M. Collisional dampening for improved quantification in single particle inductively coupled plasma mass spectrometry. *Talanta* **2018**, *189*, 268–273. DOI: 10.1016/j.talanta.2018.06.071.

(109) Shigeta, K.; Traub, H.; Panne, U.; Okino, A.; Rottmann, L.; Jakubowski, N. Application of a micro-droplet generator for an ICP-sector field mass spectrometer – Optimization and analytical characterization. *J. Anal. At. Spectrom.* **2013**, *28*, 646–656. DOI: 10.1039/c2ja30207a.

(110) Liu, J.; Murphy, K. E.; MacCuspie, R. I.; Winchester, M. R. Capabilities of single particle inductively coupled plasma mass spectrometry for the size measurement of nanoparticles: a case study on gold nanoparticles. *Anal. Chem.* **2014**, *86*, 3405–3414. DOI: 10.1021/ac403775a.

(111) Newman, K.; Metcalfe, C. D.; Martin, J.; Hintelmann, H.; Shaw, P.; Donard, A. Improved single particle ICP-MS characterization of silver nanoparticles at environmentally relevant concentrations. *J. Anal. At. Spectrom.* **2016**, *31*, 2069–2077. DOI: 10.1039/c6ja00221h.

(112) Shaw, P.; Donard, A. Nano-particle analysis using dwell times between 10 μs and 70 μs with an upper counting limit of greater than 3×10^7 cps and a gold nanoparticle detection limit of less than 10 nm diameter. *J. Anal. At. Spectrom.* **2016**, *31*, 1234–1242. DOI: 10.1039/c6ja00047a.

(113) Lamsal, R. P.; Hineman, A.; Stephan, C.; Tahmasebi, S.; Baranton, S.; Coutanceau, C.; Jerkiewicz, G.; Beauchemin, D. Characterization of platinum nanoparticles for fuel cell applications by single particle inductively coupled plasma mass spectrometry. *Anal. Chim. Acta* **2020**, *1139*, 36–41. DOI: 10.1016/j.aca.2020.09.021.

(114) Montaño, M. D.; Majestic, B. J.; Jämting, Å. K.; Westerhoff, P.; Ranville, J. F. Methods for the detection and characterization of silica colloids by microsecond spICP-MS. *Anal. Chem.* **2016**, *88*, 4733–4741. DOI: 10.1021/acs.analchem.5b04924.

(115) Kálomista, I.; Kéri, A.; Ungor, D.; Csapó, E.; Dékány, I.; Prohaska, T.; Galbács, G. Dimensional characterization of gold nanorods by combining millisecond and microsecond temporal resolution single particle ICP-MS measurements. *J. Anal. At. Spectrom.* **2017**, *32*, 2455–2462. DOI: 10.1039/c7ja00306d.

(116) Kéri, A.; Kálomista, I.; Ungor, D.; Bélteki, Á.; Csapó, E.; Dékány, I.; Prohaska, T.; Galbács, G. Determination of the structure and composition of Au-Ag bimetallic spherical nanoparticles using single particle ICP-MS measurements performed with normal and high temporal resolution. *Talanta* **2018**, *179*, 193–199. DOI: 10.1016/j.talanta.2017.10.056.

(117) Lee, Y. J.; Ahn, E.-Y.; Park, Y. Shape-dependent cytotoxicity and cellular uptake of gold nanoparticles synthesized using green tea extract. *Nanoscale Res. Lett.* **2019**, *14:129*. DOI: 10.1186/s11671-019-2967-1.

(118) Steckiewicz, K. P.; Barcinska, E.; Malankowska, A.; Zauszkiewicz-Pawlak, A.; Nowaczyk, G.; Zaleska-Medynska, A.; Inkielewicz-Stepniak, I. Impact of gold nanoparticles shape on their cytotoxicity against human osteoblast and osteosarcoma in in vitro model. Evaluation of the safety of use and anti-cancer potential. *J. Mater. Sci.: Mater. Med.* **2019**, *30:22*. DOI: 10.1007/s10856-019-6221-2.

(119) Liu, X.; Sui, B.; Sun, J. Size- and shape-dependent effects of titanium dioxide nanoparticles on the permeabilization of the blood-brain barrier. *J. Mater. Chem. B* **2017**, *5*, 9558–9570. DOI: 10.1039/c7tb01314k.

(120) Bolea-Fernandez, E.; Rua-Ibarz, A.; Velimirovic, M.; Tirez, K.; Vanhaecke, F. Detection of microplastics using inductively coupled plasma-mass spectrometry (ICP-MS) operated in single-event mode. *J. Anal. At. Spectrom.* **2020**, *35*, 455–460. DOI: 10.1039/C9JA00379G.

(121) Liu, Z.; Zhu, Y.; Lv, S.; Shi, Y.; Dong, S.; Yan, D.; Zhu, X.; Peng, R.; Keller, A. A.; Huang, Y. Quantifying the dynamics of polystyrene microplastics UV-aging process. *Environ. Sci. Technol. Lett.* **2021**, *9*, 50–56. DOI: 10.1021/acs.estlett.1c00888.

(122) Gonzalez de Vega, R.; Goyen, S.; Lockwood, T. E.; Doble, P. A.; Camp, E. F.; Clases, D. Characterisation of microplastics and unicellular algae in seawater by targeting carbon via single particle and single cell ICP-MS. *Anal. Chim. Acta* **2021**, *1174:338737.* DOI: 10.1016/j.aca.2021.338737.

(123) Mozhayeva, D.; Engelhard, C. A quantitative nanoparticle extraction method for microsecond time resolved single-particle ICP-MS data in the presence of a high background. *J. Anal. At. Spectrom.* **2019**, *34*, 1571–1580. DOI: 10.1039/c9ja00042a.

(124) Duffin, A. M.; Hoegg, E. D.; Sumner, R. I.; Cell, T.; Eiden, G. C.; Wood, L. S. Temporal analysis of ion arrival for particle quantification. *J. Anal. At. Spectrom.* **2021**, *36*, 133–141. DOI: 10.1039/d0ja00412j.

(125) Hill, S. J.; Fisher, A.; Liezers, M. Plasma generation, ion sampling and focusing. In *Inductively coupled plasma mass spectrometry handbook*; Nelms, S. M., Ed.; Blackwell Pub, 2005; pp 1–25. DOI: 10.1002/9781444305463.ch1.

(126) Fréchette-Viens, L.; Hadioui, M.; Wilkinson, K. J. Practical limitations of single particle ICP-MS in the determination of nanoparticle size distributions and dissolution: Case of rare earth oxides. *Talanta* **2017**, *163*, 121–126. DOI: 10.1016/j.talanta.2016.10.093.

(127) Löschner, K.; Brabrand, M. S. J.; Sloth, J. J.; Larsen, E. H. Use of alkaline or enzymatic sample pretreatment prior to characterization of gold nanoparticles in animal tissue by single-particle ICPMS. *Anal. Bioanal. Chem.* **2014**, *406*, 3845–3851. DOI: 10.1007/s00216-013-7431-y.

(128) Corte-Rodríguez, M.; Álvarez-Fernández, R.; García-Cancela, P.; Montes-Bayón, M.; Bettmer, J. Single cell ICP-MS using on line sample introduction systems: Current developments and remaining challenges. *TrAC, Trends Anal. Chem.* **2020**, *132:116042.* DOI: 10.1016/j.trac.2020.116042.

(129) Niu, H.; Houk, R. S. Fundamental aspects of ion extraction in inductively coupled plasma mass spectrometry. *Spectrochim. Acta, Part B* **1996**, *51*, 779–815. DOI: 10.1016/0584-8547(96)01506-6.

(130) Olesik, J. W.; Gray, P. J. Considerations for measurement of individual nanoparticles or microparticles by ICP-MS: determination of the number of particles and the analyte mass in each particle. *J. Anal. At. Spectrom.* **2012**, *27*, 1143–1155. DOI: 10.1039/c2ja30073g.

(131) Peters, R.; Herrera-Rivera, Z.; Undas, A.; van der Lee, M.; Marvin, H.; Bouwmeester, H.; Weigel, S. Single particle ICP-MS combined with a data evaluation tool as a routine technique for the analysis of nanoparticles in complex matrices. *J. Anal. At. Spectrom.* **2015**, *30*, 1274–1285. DOI: 10.1039/C4JA00357H.

(132) Stewart, I. I.; Olesik, J. W. Time-resolved measurements with single droplet introduction to investigate space-charge effects in plasma mass spectrometry. *J. Am. Soc. Mass Spectrom.* **1999**, *10*, 159–174. DOI: 10.1016/s1044-0305(98)00136-6.

(133) Meyer, S.; Gonzalez de Vega, R.; Xu, X.; Du, Z.; Doble, P. A.; Clases, D. Characterization of upconversion nanoparticles by single-particle ICP-MS employing a quadrupole mass filter with increased bandpass. *Anal. Chem.* **2020**, *92*, 15007–15016. DOI: 10.1021/acs.analchem.0c02925.

(134) Hunter, K.; Stresau, D. Ion detection. In *Inductively coupled plasma mass spectrometry handbook*; Nelms, S. M., Ed.; Blackwell Pub, 2005; pp 117–146. DOI: 10.1002/9781444305463.ch3.

(135) Tuoriniemi, J.; Cornelis, G.; Hassellöv, M. A new peak recognition algorithm for detection of ultra-small nano-particles by single particle ICP-MS using rapid time resolved data acquisition on a sector-field mass spectrometer. *J. Anal. At. Spectrom.* **2015**, *30*, 1723–1729. DOI: 10.1039/c5ja00113g.

(136) Nelms, S. M., Ed. *Inductively coupled plasma mass spectrometry handbook*; Blackwell Pub, 2005. DOI: 10.1002/9781444305463.

(137) Strenge, I.; Engelhard, C. Single particle inductively coupled plasma mass spectrometry: Investigating nonlinear response observed in pulse counting mode and extending the linear dynamic range by compensating

for dead time related count losses on a microsecond timescale. *J. Anal. At. Spectrom.* **2020**, *35*, 84–99. DOI: 10.1039/c9ja00327d.

(138) Nelms, S. M.; Quétel, C. R.; Prohaska, T.; Vogl, J.; Taylor, P. D. P. Evaluation of detector dead time calculation models for ICP-MS. *J. Anal. At. Spectrom.* **2001**, *16*, 333–338. DOI: 10.1039/B007913H.

(139) Shannon, C. E. Communication in the presence of noise. *Proc. IEEE* **1998**, *86*, 447–457. DOI: 10.1109/JPROC.1998.659497.

(140) Bundesanstalt für Gewässerkunde. *Geoportal der Bundesanstalt für Gewässerkunde https://geoportal.bafg.de/mapapps/resources/apps/HAD/index.html* (accessed 29.07.2024).

(141) Schindelin, J.; Arganda-Carreras, I.; Frise, E.; Kaynig, V.; Longair, M.; Pietzsch, T.; Preibisch, S.; Rueden, C.; Saalfeld, S.; Schmid, B.; Tinevez, J.-Y.; White, D. J.; Hartenstein, V.; Eliceiri, K.; Tomancak, P.; Cardona, A. Fiji: An open-source platform for biological-image analysis. *Nat. Methods* **2012**, *9*, 676–682. DOI: 10.1038/nmeth.2019.

(142) Olesik, J. W.; Hartshorne, J. A.; Casey, N.; Linard, E.; Dettman, J. R. Further insight into analyte transport processes and water vapor, aerosol loading in ICP-OES and ICP-MS. *Spectrochim. Acta, Part B* **2021**, *176:106038.* DOI: 10.1016/j.sab.2020.106038.

(143) Lee, W.-W.; Chan, W.-T. Calibration of single-particle inductively coupled plasma-mass spectrometry (SP-ICP-MS). *J. Anal. At. Spectrom.* **2015**, *30*, 1245–1254. DOI: 10.1039/c4ja00408f.

(144) Gerhard Werner; Tobias Werner, Eds. *Lehrbuch der quantitativen Analyse*, 8th ed.; Springer Spektrum, 2014.

(145) Granqvist, C.-G.; Buhrman, R. A. Ultrafine metal particles. *J. Appl. Phys.* **1976**, *47*, 2200–2219. DOI: 10.1063/1.322870.

(146) Kiss, L. B.; Söderlund, J.; Niklasson, G. A.; Granqvist, C.-G. New approach to the origin of lognormal size distributions of nanoparticles. *Nanotechnology* **1999**, *10*, 25–28. DOI: 10.1088/0957-4484/10/1/006.

(147) van Koetsem, F.; Verstraete, S.; Wallaert, E.; Verbeken, K.; van der Meeren, P.; Rinklebe, J.; Du Laing, G. Use of filtration techniques to study environmental fate of engineered metallic nanoparticles: Factors affecting filter performance. *J. Hazard. Mater.* **2017**, *322*, 105–117. DOI: 10.1016/j.jhazmat.2016.05.098.

(148) de Klein, J. J. M.; Quik, J. T. K.; Bäuerlein, P. S.; Koelmans, A. A. Towards validation of the NanoDUFLOW nanoparticle fate model for the river Dommel, The Netherlands. *Environ. Sci.: Nano* **2016**, *3*, 434–441. DOI: 10.1039/C5EN00270B.

(149) Markus, A. A.; Krystek, P.; Tromp, P. C.; Parsons, J. R.; Roex, E. W. M.; de Voogt, P.; Laane, R. W. P. M. Determination of metal-based nanoparticles in the river Dommel in the Netherlands via ultrafiltration, HR-ICP-MS and SEM. *Sci. Total Environ.* **2018**, *631-632*, 485–495. DOI: 10.1016/j.scitotenv.2018.03.007.

(150) Yang, Y.; Westerhoff, P. Presence in, and release of, nanomaterials from consumer products. In *Nanomaterial*:*Advances in Experimental Medicine and Biology*; Capco, D., Chen, Y., Ed., Vol. 811; Springer, 2014; pp 1–17. DOI: 10.1007/978-94-017-8739-0_1.

(151) Phalyvong, K.; Sivry, Y.; Pauwels, H.; Gélabert, A.; Tharaud, M.; Wille, G.; Bourrat, X.; Ranville, J. F.; Benedetti, M. F. Assessing CeO_2 and TiO_2 nanoparticle concentrations in the Seine River and its tributaries Near Paris. *Front. Environ. Sci.* **2021**, *8:549896.* DOI: 10.3389/fenvs.2020.549896.

(152) Rand, L. N.; Ranville, J. F. Characteristics and stability of incidental iron oxide nanoparticles during remediation of a mining-impacted stream. *Environ. Sci. Technol.* **2019**, *53*, 11214–11222. DOI: 10.1021/acs.est.9b03036.

(153) Neal, C.; Jarvie, H.; Rowland, P.; Lawler, A.; Sleep, D.; Scholefield, P. Titanium in UK rural, agricultural and urban/industrial rivers: geogenic and anthropogenic colloidal/sub-colloidal sources and the significance of within-river retention. *Sci. Total Environ.* **2011**, *409*, 1843–1853. DOI: 10.1016/j.scitotenv.2010.12.021.

(154) Gonzalez de Vega, R.; Lockwood, T. E.; Xu, X.; Gonzalez de Vega, C.; Scholz, J.; Horstmann, M.; Doble, P. A.; Clases, D. Analysis of Ti- and Pb-based particles in the aqueous environment of Melbourne (Australia) via single particle ICP-MS. *Anal. Bioanal. Chem.* **2022**, *414*, 5671–5681. DOI: 10.1007/s00216-022-04052-0.

(155) Rand, L. N.; Bi, Y.; Poustie, A.; Bednar, A. J.; Hanigan, D. J.; Westerhoff, P.; Ranville, J. F. Quantifying temporal and geographic variation in sunscreen and mineralogic titanium-containing nanoparticles in three recreational rivers. *Sci. Total Environ.* **2020**, *743:140845.* DOI: 10.1016/j.scitotenv.2020.140845.

(156) Part, F.; Berge, N.; Baran, P.; Stringfellow, A.; Sun, W.; Bartelt-Hunt, S.; Mitrano, D. M.; Li, L.; Hennebert, P.; Quicker, P.; Bolyard, S. C.; Huber-Humer, M. A review of the fate of engineered nanomaterials in municipal solid waste streams. *Waste Manage.* **2018**, *75*, 427–449. DOI: 10.1016/j.wasman.2018.02.012.

(157) Tuoriniemi, J.; Cornelis, G.; Hassellöv, M. Size discrimination and detection capabilities of single-particle ICPMS for environmental analysis of silver nanoparticles. *Anal. Chem.* **2012**, *84*, 3965–3972. DOI: 10.1021/ac203005r.

(158) Baur, S.; Reemtsma, T.; Stärk, H.-J.; Wagner, S. Surfactant assisted extraction of incidental nanoparticles from road runoff sediment and their characterization by single particle-ICP-MS. *Chemosphere* **2020**, *246:125765.* DOI: 10.1016/j.chemosphere.2019.125765.

(159) Ministerium für Umwelt, Naturschutz und Verkehr des Landes Nordrhein-Westfalen. *ELWAS-WEB https://www.elwasweb.nrw.de/elwas-web/index.xhtml#: Wasserdaten NRW* (accessed 02.05.2025).

(160) Plathe, K. L.; von der Kammer, F.; Hassellöv, M.; Moore, J.; Murayama, M.; Hofmann, T.; Hochella, M. F. Using FlFFF and aTEM to determine trace metal–nanoparticle associations in riverbed sediment. *Environ. Chem.* **2010**, *7*, 82–93. DOI: 10.1071/en09111.

(161) Whiteley, C. M.; Dalla Valle, M.; Jones, K. C.; Sweetman, A. J. Challenges in assessing release, exposure and fate of silver nanoparticles within the UK environment. *Environ. Sci.:Processes Impacts* **2013**, *15*, 2050–2058. DOI: 10.1039/c3em00226h.

(162) Mitrano, D. M.; Rimmele, E.; Wichser, A.; Erni, R.; Height, M.; Nowack, B. Presence of nanoparticles in wash water from conventional silver and nano-silver textiles. *ACS Nano* **2014**, *8*, 7208–7219. DOI: 10.1021/nn502228w.

(163) Cervantes-Avilés, P.; Keller, A. A. Incidence of metal-based nanoparticles in the conventional wastewater treatment process. *Water Res.* **2021**, *189:116603.* DOI: 10.1016/j.watres.2020.116603.

(164) Huang, Y.; Keller, A. A.; Cervantes-Avilés, P.; Nelson, J. Fast multielement quantification of nanoparticles in wastewater and sludge using single-particle ICP-MS. *ACS ES&T Water* **2021**, *1*, 205–213. DOI: 10.1021/acsestwater.0c00083.

(165) Mitrano, D. M.; Lesher, E. K.; Bednar, A. J.; Monserud, J.; Higgins, C. P.; Ranville, J. F. Detecting nanoparticulate silver using single-particle inductively coupled plasma-mass spectrometry. *Environ. Toxicol. Chem.* **2012**, *31*, 115–121. DOI: 10.1002/etc.719.

(166) Khosravi, K.; Hoque, M. E.; Dimock, B.; Hintelmann, H.; Metcalfe, C. D. A novel approach for determining total titanium from titanium dioxide nanoparticles suspended in water and biosolids by digestion with ammonium persulfate. *Anal. Chim. Acta* **2012**, *713*, 86–91. DOI: 10.1016/j.aca.2011.11.048.

(167) Westerhoff, P.; Song, G.; Hristovski, K.; Kiser, M. A. Occurrence and removal of titanium at full scale wastewater treatment plants: implications for TiO_2 nanomaterials. *J. Environ. Monit.* **2011**, *13*, 1195–1203. DOI: 10.1039/c1em10017c.

(168) Bundesamt für Kartographie und Geodäsie. *Geoportal des Bundesamts für Kartographie und Geodäsie https://geoportal.de/map.html?map=tk_07-bodenrichtwert-nrw* (accessed 17.01.2025).

List of Abbreviations

AC	Alternating current
AF4	Asymmetric flow-field flow fractionation
AgNP	Silver nanoparticle
AuNP	Gold nanoparticle
BPEI	Branched polyethylenimine
CCT	Collision cell technology
CE	Capillary electrophoresis
CPE	Cloud-point extraction
CRM	Certified reference material
DAQ	Data acquisition unit
DC	Direct current
DE	Detector event
DE_{eff}	Ion detection efficiency
DLS	Dynamic light scattering
dp	Data point
EDX	Energy dispersive X-ray spectroscopy
ENM	Engineered nanomaterial
FEP	Fluorinated ethylene propylene
FFF	Field flow fractionation
GF-AAS	Graphite furnace atomic absorption spectroscopy
HAADF	High-angle annular dark-field imaging
HDC	Hydrodynamic chromatography
HR-TEM	High-resolution transmission electron microscopy
ICP	Inductively coupled plasma
ICP-OES	Inductively coupled plasma optical emission spectrometry
ICRA	Ion cloud recognition algorithm
IQR	Interquartile range
IUPAC	International Union of Pure and Applied Chemistry
LOD	Limit of detection
LPE	Liquid phase extraction
MALS	Multi angle light scattering
MS	Mass spectrometry
µsDAQ	Data acquisition unit with microsecond time resolution
m/*z*	mass-to-charge number
nanoDAQ	Data acquisition unit with nanosecond time resolution
NOM	Natural organic matter
NP	Nanoparticle
NTA	Nanoparticle tracking analysis
OES	Optical emission spectrometry
PE	Polyethylene
PEG	Polyethylene glycol
PFA	Perfluoroalkoxy alkane
PNC	Particle number concentration
PP	Polypropylene
PVP	Polyvinylpyrrolidone
Q	Quadrupole
QQQ	Triple quadrupole
RF	Radio frequency

RM	Reference material
ROS	Reactive oxygen species
RSD	Relative standard deviation
r.t.	Room temperature
SD	Standard deviation
SEM	Secondary electron multiplier *or* scanning electron microscopy
SF	Sector-field
spICP-MS	Single particle inductively coupled plasma mass spectrometry
spICP-Q-MS	Single quadrupole spICP-MS
SPE	Solid phase extraction
S-TEM	Scanning transmission electron microscopy
SW	Surface water sample
TE	Transport efficiency
TEM	Transmission electron microscopy
TiO_2NP	Titanium dioxide nanoparticle
ToF-MS	Time-of-flight mass spectrometry
UV-Vis	Ultraviolet/Visible light spectroscopy
WW	Waste water effluent sample
WWTP	Waste water treatment plant
XPS	X-ray photoelectron spectroscopy

Contributions to this Thesis

- The design, construction, and programming of the nanoDAQ MK1 and MK2 hardware, software, and data acquisition systems were performed by Johannes Schmitt.
- The design and installation of the experimental set up for parallel measurements with three data acquisition units (µsDAQ, nanoDAQ MK1, and MK2) were performed by Johannes Schmitt
- The design and programming of the data processing and visualization software for nanoDAQ MK1 and MK2 raw data and of the ion cloud recognition algorithm ICRA including automatic background threshold calculation were performed by Johannes Schmitt
- The data processing workflow for nanoparticle size analysis was conceptualized by Johannes Schmitt and the author
- The experimental measurements with the nanoDAQ MK1 for the published paper were carried out by the author
- Under the supervision of Johannes Schmitt and the author, the experimental measurements for simultaneous data acquisition with multiple data acquisition units were performed by Alexander Herrmann during his Bachelor thesis project
- Under the author's supervision, the selection of sampling sites for the water sampling campaign was conceptualized by Guillaume Woodcock during his Master thesis project
- The water samples were collected by Guillaume Woodcock and the author
- The experimental measurements of the water samples were carried out by the author
- TEM measurements were carried out by Dr.-Ing Julian Müller and selected TEM measurements were carried out by the author
- The design of experiments, and the processing, analysis, visualization, and interpretation of all experimental data obtained in this work was carried out by the author
- The initial draft of the published paper was prepared by the author. The paper was refined in collaboration with the co-authors Prof. Dr. Carsten Engelhard and Johannes Schmitt and was finally edited by Prof. Dr. Carsten Engelhard
- Funding for this project in the form of a Kekulé scholarship was acquired by Prof. Dr. Carsten Engelhard and the author
- Under the conceptual guidance of Prof. Dr. Carsten Engelhard, the project was initiated by Johannes Schmitt and the author

Acknowledgements

I gratefully acknowledge Prof. Dr. Carsten Engelhard for his support and supervision and for the opportunity to complete my PhD in his research group.

I thank Johannes Schmitt for the close collaboration and fruitful discussions during the work on this thesis and for our valuable friendship. I'd also like to thank all my past and present co-workers in the Analytical Chemistry lab, especially Darya Mozhayeva for the supervision of my Master thesis and Maximilian Heide, the Spaß-Büro (Désirée Schütz, Manuel Heinelt, Cristian Escobar), Narmina Heupel, Ulrike Koch, and Aly Hafez for their constant support and friendship during the past years.

Alexander Herrmann is gratefully acknowledged for conducting spICP-MS measurements with simultaneous data acquisition with different DAQ systems within the scope of his Bachelor Thesis and Guillaume Woodcock is gratefully acknowledged for his work on the water sampling campaign within the scope of his Master Thesis.

I gratefully acknowledge Ingo Strenge for his work on the microsecond time resolution data acquisition system for spICP-MS and for his support of Johannes Schmitt, as well as Dr. Julian Müller for creating the S-TEM images in cooperation with the Micro- and Nanoanalytics Facility (MNaF Siegen). I thank the machine shop team in the Department of Chemistry and Biology of the University of Siegen (especially Bernd Meyer and Markus Rabe) for their valuable advice and for meeting every challenge to keep the ICP-MS running.

Financial support by the FCI (chemical industry fund within the German Chemical Industry Association VCI) in the form of a Kekulé fellowship is gratefully acknowledged.

Besonders möchte ich mich bei meiner Familie, Margit, Gerold und Alex, und bei Jochen für eure Unterstützung und Geduld bedanken.